Design and Analysis of Microthermal Accelerometer

by

Lin Lin

M.A.Sc. Simon Fraser University, Canada, 1997
B.A.Sc. XIDIAN University, China, 1990

THESIS SUBMITTED IN PARTIAL FULFILLMENT OF
THE REQUIREMENTS FOR THE DEGREE OF
DOCTOR OF PHILOSOPHY

in the School
of
Engineering Science

SIMON FRASER UNIVERSITY
March, 2004

Approval

Name: Lin Lin

Degree: Doctor of Applied Science

Title of Thesis: Design and Analysis of Microthermal Accelerometer

Examining Committee:

Chair: Dr. Glenn H. Chapman
Professor, School of Engineering Science
Simon Fraser University

Dr. John D. Jones
Senior Supervisor
Associate Professor, School of Engineering Science
Simon Fraser University

Dr. Albert M. Leung
Supervisor
Professor, School of Engineering Science
Simon Fraser University

Dr. Ash Parameswaran
Examiner
Associate Professor, School of Engineering Science
Simon Fraser University

Dr. Ted Hubbard
External Examiner
Associate Professor, Department of Mechanical Engineering
Dalhousie University

Date Approved: March 19, 2004

Abstract

A novel design of accelerometer based on differential buoyancy of a heated fluid in a micromachined enclosure has been developed at Simon Fraser University. This project focuses on theoretical and experimental studies aimed at optimizing the design of such an accelerometer. In particular, the consequences of using a liquid as the working fluid are explored. The current single-axis and double-axis accelerometer designs can be modeled as convective laminar flow within the space enclosed by horizontal concentric annuli and concentric spheres respectively. Both steady state and transient solutions to the convective laminar fluid flow are investigated by analytical methods and numerical simulations to predict such performance parameters as: maximum differential temperature, location at which maximum differential temperature occurs, and response time. Experimental studies are then performed to verify the results of theoretical study. Some conclusions for accelerometer design are drawn.

Acknowledgments

I would like to express my sincere gratitude to my senior academic supervisor Dr. John Jones for his guidance and insightful advice throughout this thesis project. My special thanks go to Dr. Albert Leung for his suggestions and the chips he supplied. I would like also to acknowledge Mr. Fred Heep and Mr. Bill Woods for their advice on experimental technique.

Table of Contents

List of Figures

List of Tables

Nomenclature

Note:

1. For all dimensional quantities, their corresponding nondimensional quantities are marked by "hat", such as $\hat{x}$, or $\tilde{x}$;
2. Subscript *o* represents variable evaluated at outer-sphere or outer-cylinder, and subscript *i* represents variables evaluated at inner-sphere or inner-cylinder.

Dimensional Quantities

c	Specific heat, J/kgK.
a	Acceleration, m/s^2.
g	Gravity, $g = 9.8\ m/s^2$.
h	Convective heat transfer coefficient, W/m^2K.
k	Thermal conductivity, W/mK.
L	Gap distance between inner cylinder/sphere and outer cylinder/sphere, $L = r_o - r_i$, m.
D_i, D_o	Diameter of inner cylinder/sphere and outer cylinder/sphere, m.
p	Gas or fluid pressure, Pa.
q_s	Volumetric heat generation, W/m^3.
r	Radial distance, m.
r_i, r_o	Radii of inner and outer spheres (or cylinders) respectively, m.
t	Time, s.
T_i, T_o	Temperature of inner and outer spheres (or cylinders) respectively, K.
v_r	Superficial fluid velocity in radial direction, cylindrical coordinates /

spherical coordinates, m/s.

v_θ Superficial fluid velocity, in circumferential direction, cylindrical coordinates / spherical coordinates, m/s.

v_z Superficial fluid velocity, in axial direction, cylindrical coordinates, m/s.

v_ϕ Superficial fluid velocity, in azimuthal direction, spherical coordinates, m/s.

z Cylindrical coordinate, axial direction.

Greek Letters

α Fluid diffusivity, $\alpha = k/(\rho c_p)$, m^2/s.

β Coefficient of thermal expansion of fluid, K^{-1}.

δT Temperature difference between symmetrically placed sensors, K.

θ Colatitude or polar angle, measured from the upward vertical, $\theta = 0$.

μ Viscosity, Ns/m^2.

ρ Density, kg/m^3.

τ The characteristic response time.

τ_v The characteristic response time for the final flow field to develop.

τ_T The characteristic response time for the final temperature field to develop.

ϕ Spherical coordinate, azimuthal direction.

ψ Stokes stream function.

ω Vorticity, defined as $\omega = -\nabla^2\hat{\psi}$.

Φ Dissipation function, s^{-2}.

Dimensionless Quantities

$\hat{t}$ Dimensionless time variable, $\hat{t} = \frac{t}{\tau}$.

$\hat{r}$ Dimensionless radial distance $\hat{r} = r/r_i$.

$\tilde{r}$ Dimensionless radial distance, defined as $\tilde{r} = r/L$.

R Radius ratio, r_o/r_i.

$\hat{T}$ Dimensionless temperature, defined as $\hat{T} = T/T_o$.

$\tilde{T}$ Dimensionless temperature, defined as $\tilde{T} = (T - T_o)/(T_i - T_o)$.

$\tilde{T}_j$ jth-order term in expansion of $\tilde{T}$.

$\hat{P}$ Dimensionless gas or fluid pressure, $\hat{P} = \frac{P}{\rho(r_i/\tau)^2}$.

$\hat{v}_r$ Dimensionless superficial fluid velocity in radial direction, cylindrical coordinates / spherical coordinates, defined as: $\hat{v}_r = v_r\frac{\tau}{r_i}$

$\tilde{v}_r$ Dimensionless superficial fluid velocity in radial direction, cylindrical coordinates / spherical coordinates, defined as: $\tilde{v}_r = \frac{v_r L}{\alpha}$

$\hat{v}_\theta$ Dimensionless superficial fluid velocity, in circumferential direction, cylindrical coordinates / spherical coordinates, defined as $\hat{v}_\theta = v_\theta\frac{\tau}{r_i}$

$\tilde{v}_\theta$ Dimensionless superficial fluid, in circumferential direction, cylindrical coordinates / spherical coordinates, defined as $\tilde{v}_\theta = \frac{v_\theta L}{\alpha}$

Greek Letters

$\tilde{\psi}$ Dimensionless Stokes stream function, defined as $\tilde{\psi} = \frac{\psi}{\alpha}$

Dimensionless Groups

F_o Fourier number, $F_o = \frac{\tau\alpha}{r_i^2}$.

F_{ov} Velocity Fourier number; $F_{ov} = \frac{\alpha\tau_v}{r_i^2}$.

F_{oT}	Thermal Fourier number; $F_{oT} = \frac{\alpha \tau_T}{r_i^2}$.
Pr	Prandtl number, $\frac{\mu c}{k}$.
G	Gravity number $G = \frac{\rho^2 r_i^3 g}{\mu^2}$.
Gr	Grashof number $\frac{\rho^2 r_i^3 g \Delta T \beta}{\mu^2}$.
Ra	Rayleigh number, $Ra = GrPr$.
Ra^*	Rayleigh number based on gap thickness, $Ra^* = \frac{g\beta(r_o - r_i)^3(T_i - T_o)}{\nu\alpha}$ or $Ra^* = \frac{\rho g \beta (r_o - r_i)^3 (T_i - T_o)}{\mu \alpha}$
Ra_{lim}, Ra^*_{lim}	Limiting Rayleigh number.
Nu	Nusselt number, defined as $Nu = hd_c/k_f$.
Nu_i	Inner-sphere local Nusselt number.
Nu_o	Outer-sphere local Nusselt number.
$\overline{Nu}$	Overall Nusselt number.

Chapter 1 Introduction to the Microthermal Accelerometer

Recently, a novel design of microthermal accelerometer based on the buoyancy of a heated air bubble enclosed within a chamber has been developed at Simon Fraser University (Leung, Jones, Czyzewska, Chen, and Pascal 1997). One major potential application for this microthermal accelerometer is as an air-bag trigger in the automobile industry, particularly roll-over air-bag deployment. This microthermal accelerometer is completely different in operating principle from traditional accelerometers such as electro-mechanical accelerometers, and the conventional micro-electro-mechanical accelerometers now commonly used in air-bag trigger sensors. Compared with traditional accelerometers, the microthermal accelerometer contains no mechanical moving parts. Manufacture of such devices makes use of micromachining technology and can thus be integrated with other signal processing circuitry in the IC fabrication process. Therefore, this microthermal accelerometer is preferable to traditional accelerometers for such features as: sensitive to small acceleration, compact design, light weight, and yet inexpensive to manufacture. Its significant advantage over the micro-electro-mechanical accelerometer is that it does not face the same compromise between device sensitivity and device robustness.

1 - 1 A Glance at the Conventional Accelerometers

An accelerometer is a device or a transducer which can be used to determine acceleration. We can generally classify them into two categories: traditional electro-mechanical accelerometers and conventional micro-electro-mechanical system (MEMS) accelerometers. The microthermal accelerometer should fit into the category of MEMS

accelerometers since it also makes use of micromachining technology. However, in this thesis it is listed as a separate category from conventional MEMS accelerometer due to its unique operational principle. Before investigating the microthermal accelerometer in detail, it is necessary for us to take a glance at traditional electro-mechanical accelerometer and conventional micro-electro-mechanical accelerometers.

1 - 1.1 Traditional Electro-Mechanical Accelerometer

Though traditional electro-mechanical accelerometers come with a variety of designs for different applications, they commonly consist of three elements: a mass, often called "proof mass"; a suspension, which locates the mass; and a pickoff, which delivers a signal related to the acceleration. Some closed-loop designs also include a "forcer", which is an electric or magnetic force generator designed to oppose the inertial force; and an automatic controller, by which a signal from the pickoff is returned through a feedback amplifier to the forcer, to control the input condition so that the pickoff output can be held at null.

A traditional accelerometer operates by measuring the inertia force generated when the proof mass accelerates. Depending on the mechanism of each actual accelerometer design, this inertial force might deflect a spring, for example, in mass-spring model, whose deflection can be measured; or it might change the torque of a pendulum or change the capacitance of pairs of electrode plates, etc.

In this section, to understand various traditional electro-mechanical accelerometer designs, we will give brief descriptions for a few typical types, such as mass-spring, electrostatic, and pendulum-type accelerometer.

1 - 1.1.1 A Spring-Mass Accelerometer

A common spring-supported accelerometer design is illustrated in Figure 1 - 1, (based on Lawrence, 1998).

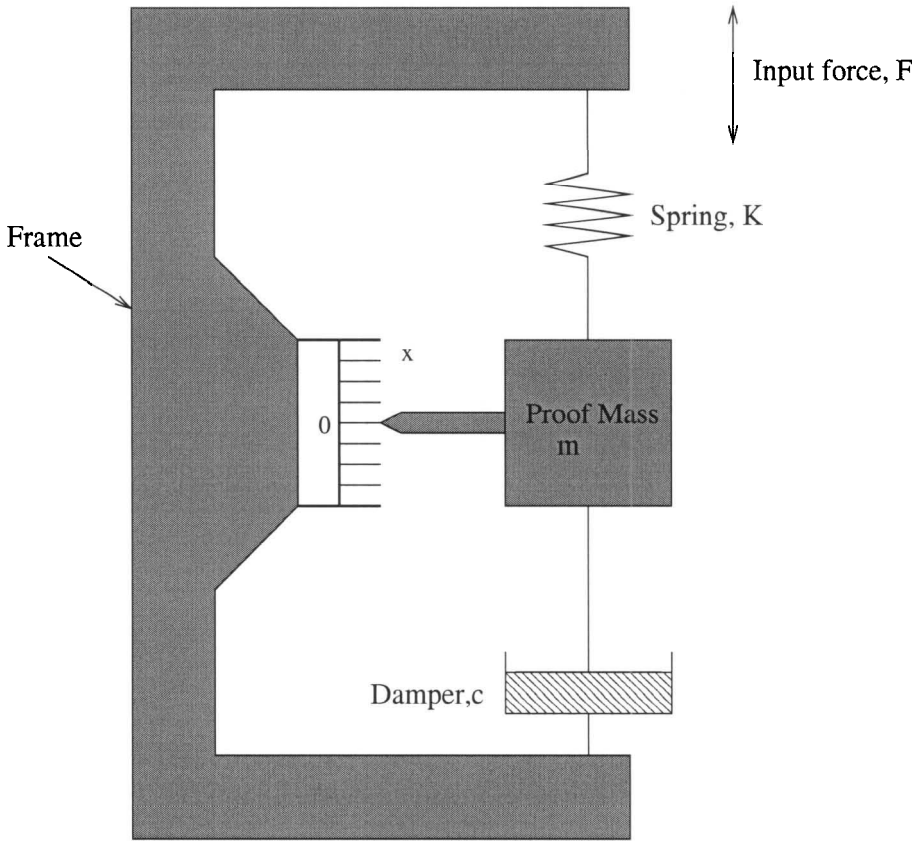

Figure 1 - 1 A common mass-spring accelerometer design

Here, a proof-mass block is suspended by a spring and a damper, all of which are then mounted inside a frame. This is a basic single-degree-of-freedom accelerometer, and its characteristics can be determined by the size of the proof mass, the damping and the stiffness K of the suspension. Considering the response of such a system to a force applied to the frame along the spring's axis, we can sum the initial force of proof-mass, fluid damping, and equate the spring displacement to the applied force. We have:

$$F = m\left(\frac{d^2x}{dt^2}\right) + c\left(\frac{dx}{dt}\right) = -Kx \qquad \textbf{(Eq 1 - 1)}$$

where

x = displacement from the rest position of the proof-mass

c = damping coefficient

K = spring stiffness

As the system reaches equilibrium, $c\frac{dx}{dt} = 0$. And if the acceleration is steady and mass displacement is steady,

$$m\left(\frac{d^2x}{dt^2}\right) = -Kx \qquad \textbf{(Eq 1 - 2)}$$

Hence, the inertia force is balanced by the opposing spring force, and acceleration can be obtained by measuring x.

1 - 1.1.2 A Closed-loop Electrostatic Accelerometer

Another type of traditional accelerometer is the electrostatic accelerometer illustrated in Figure 1 - 2, (based on Lawrence, 1998). Here, a metallic cube (proof mass) is placed inside a box with six electrode plates, each spaced a small distance from a cube face. The cube is suspended electrostatically by charging the plates with voltages V_x, V_y, V_z. The capacitance of each plate to the cube(C_x, C_y, C_z) is a measure of the gap between the plate and cube (pickoff). Three automatic controllers, one per pair of opposite plates, can adjust the plate voltages so that the cube is supported with equal gaps on all faces, and the voltages are a measure of the acceleration. The electrostatic field serves both as the suspension and the forcer, and this is a closed-loop sensor. This instrument has been used to study small acceleration effects in spacecraft. (Bernard, Foulon and Le Clerc, 1985).

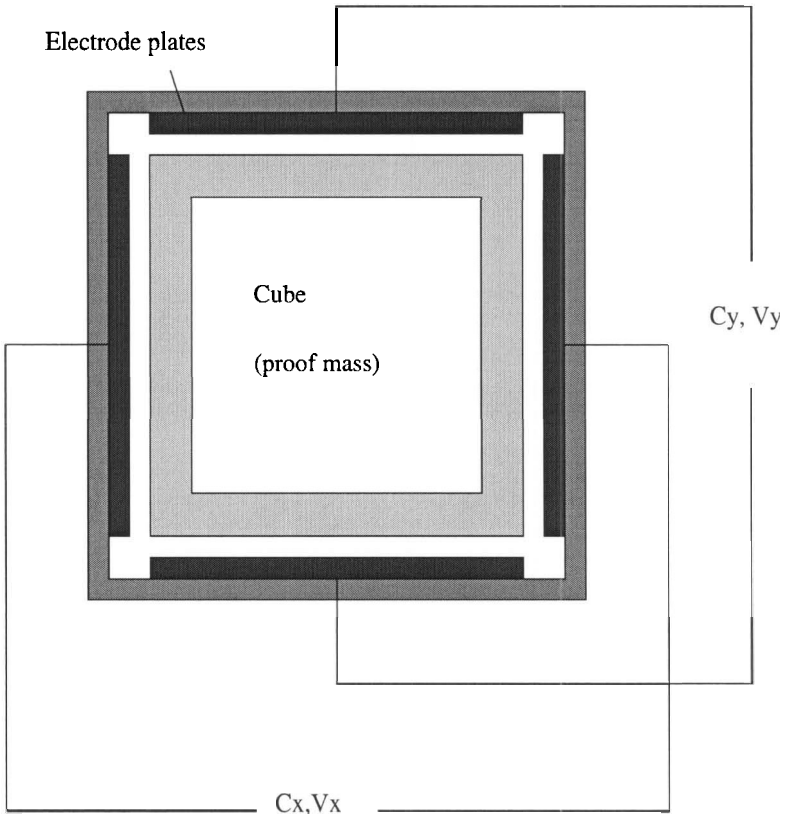

Figure 1 - 2 An electrostatic accelerometer

1 - 1.1.3 A Pendulous Accelerometer

A generic closed-loop pendulous accelerometer is illustrated in Figure 1 - 3, (based on Lawrence, 1998). This accelerometer consists of a proof mass, a hinge, pickoff and a feedback control loop.

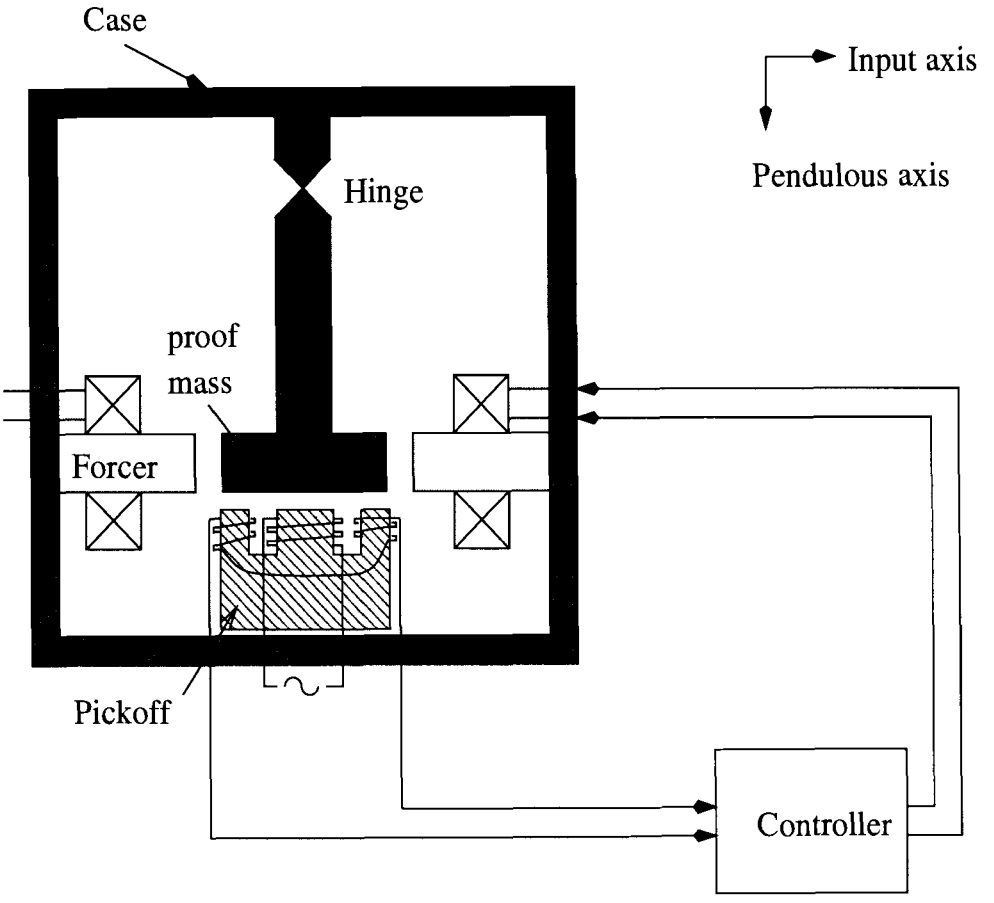

Figure 1 - 3 A pendulous accelerometer

The relation between acceleration and torque can be describe as:

$$T = F \times l = m \times a \times l \qquad \textbf{(Eq 1 - 3)}$$

where

F = inertia force

l = length from hinge to proof mass

m = proof mass

a = acceleration

Many types of traditional accelerometers, operating on a variety of technologies, have been developed and are commercially available, including mass-spring, electro-

static, and pendulum-based designs, as above mentioned. Operating principles for such devices have been discussed in detail by (Lawrence, 1998). In addition, two new technologies applied to accelerometry worthy of note are those of surface acoustic wave (Hartermann, Meunier and Jocobelli, 1985), (Bower, Cracknell and Harrison, 1987) and optical fiber sensors (Tveten, Dandrige, Davis and Giallorenzi, 1980).

To summarize, a traditional electro-mechanical accelerometer generally consists of three elements, including a proof-mass, a suspension and a pickoff. The operating principles of such accelerometers are based on a variety of mechanical, optical and electronic technologies. Such devices usually include delicate moving parts, hence they are complicated in design and expensive to produce. One typical application of conventional accelerometer is for inertial navigation system.

1 - 1.2 Conventional Silicon Micro-Electro-Mechanical Accelerometers

Single-crystal silicon has been made readily available in the microelectronics field. Silicon has excellent mechanical properties, for instance, it is harder than most metals and its elastic limits in both tension and compression are higher than steel. With the advance of micromachining technology, silicon has been used to make a variety of micro-electro-mechanical systems (MEMS), including accelerometer.

There are also a variety of designs of conventional silicon micro-electro-mechanical accelerometers. First of all, some of the traditional electro-mechanical accelerometers have made their way into MEMS. For example, the simple pendulum design works well in its MEMS version. There are several design of micromachined pendulous accelerometer already commercially available, such as by Northrop-Grumman (Blanco and Geen, 1993), Draper Laboratories (Babour et al., 1996) and Rockwell. Such

MEMS accelerometers have started to replace their traditional counterparts in navigation applications.

Specifically, a competitive accelerometer to the microthermal accelerometer of interest to us is the MEMS capacitive accelerometer, which is now commonly used as an air-bag trigger sensor. This type of accelerometer is produced in millions annually. In this section, we introduce the technology of micromachining; we will then go on to describe the MEMS capacitive accelerometer and compare it with the microthermal accelerometer.

1 - 1.2.1 Micromachining Technology

Micromachining and micro-electromechanical system (MEMS) technologies can be used to produce complex structures, devices and systems on the scale of microns. Initially, micromachining techniques were borrowed directly from the integrated circuit (IC) industry, but now many unique MEMS-specific micromachining processes are being developed.

Since most of the production steps used in MEMS manufacture are borrowed from silicon chip manufacturing technologies, micromachining silicon techniques are the basis for various device types. Though details vary for each specific device, the fundamental process of MEMS involves the following steps (Vigna, STMicroelectronics 2003).

"First, a layer of sacrificial silicon oxide is grown onto a silicon wafer. It's called 'sacrificial' because it will be mostly removed later on to free the moving parts. Second, the sacrificial layer is etched with holes at points corresponding to the supports for fixed elements and anchors for moving elements respectively. Third, a thicker eptitaxial polysilicon layer is grown in the holes and on the top of the second layer. Then we etch the structure for the moving and fixed elements of the device for this layer. Finally, the sacrificial oxide layer beneath the structures is removed by an isotropic etching operation

to free the moving parts. At the end, the open space around the structures is filled with gas, normally dry nitrogen, to avoid effects by humidity or variations in gas density, which would affect resonant frequencies."

1 - 1.3 MEMS Capacitive Accelerometer

One competitive accelerometer to the microthermal accelerometer is the MEMS capacitive accelerometer. This MEMS capactive accelerometer is an inertial sensor which can be used to measure linear and rotational accelerations. The technology used to produce such devices is the most common MEMS technology. Typically, the MEMS capactive accelerometer consists of interlocking fingers which are alternately movable and fixed. Acceleration is sensed by measuring the capacitance of the structure, which varies in proportion to changes in acceleration. For a linear accelerometer, the fixed and moving elements can be arranged like interlocking combs. A MEMS capacitive accelerometer made by surface micromachining technology is shown in Figure 1 - 4, (based on Bao, 2000) (Kuehnel and Sherman, 1994)

As seen in Figure 1 - 4, from (a) and its simplified version (b), the movement of the plate caused by the acceleration along the central line of the movable plate changes the capacitance of the two capacitors, with one increasing and other decreasing, the acceleration can be measured by the differential capacitance.

This type of accelerometer with operation range of 2g to 50g has been mass produced and widely used in applications such as airbag-triggers in automobile industry.

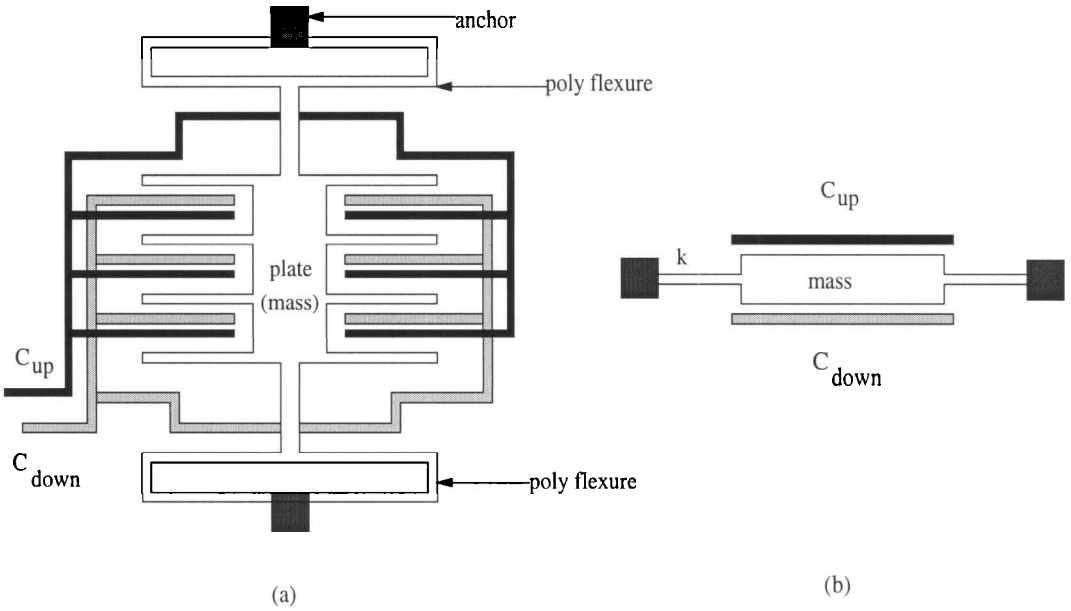

Figure 1 - 4 A MEMS capactive accelerometer (a) top view of the schematic structure (b) a simplified model

1 - 2 Introduction to the Microthermal Accelerometer

The focus of this thesis is a novel design of accelerometer based on the buoyancy of a heated fluid in an enclosure. The first example of such a device was developed recently by Leung et. al. (Leung, Jones, Czyzewska, Chen, and Pascal 1997). This accelerometer has also been developed under micromachining technology, hence it inherits the same desirable features as MEMS device; however, unlike the MEMS capacitive accelerometer, it contains no moving parts, therefore it can stand much higher shock. Its operational principle is completely different from conventional MEMS capacitive accelerometers. For the microthermal accelerometer, when an acceleration is applied to a contained fluid having an initially symmetric temperature distribution, buoyancy forces produce a temperature asymmetry, from which the magnitude of the

acceleration can be deduced.

1 - 2.1 Device Structure of the Microthermal Accelerometer

Figure 1 - 5 is a photograph of the prototype microthermal accelerometer chip used for the experimental work that will be described in Chapter 5, "Experimental Studies" of this thesis. The photograph shows a cavity 230 microns deep etched in silicon, spanned by a single heater bridge in one direction, and by eight sensor bridges in the orthogonal direction. The length of the heater bridge is 970 microns, and the sensor bridges are 915 microns long. Thermocouple junctions were created on each of the sensor bridges during the micromachining process, and are symmetrically placed to either side of the heater bridge, about one-third of the way from the heater bridge to the walls. During operation, the cavity is covered by a cap, giving a clearance of about 1000 microns above the heater plane.

Figure 1 - 6 shows a simplified version of the device.

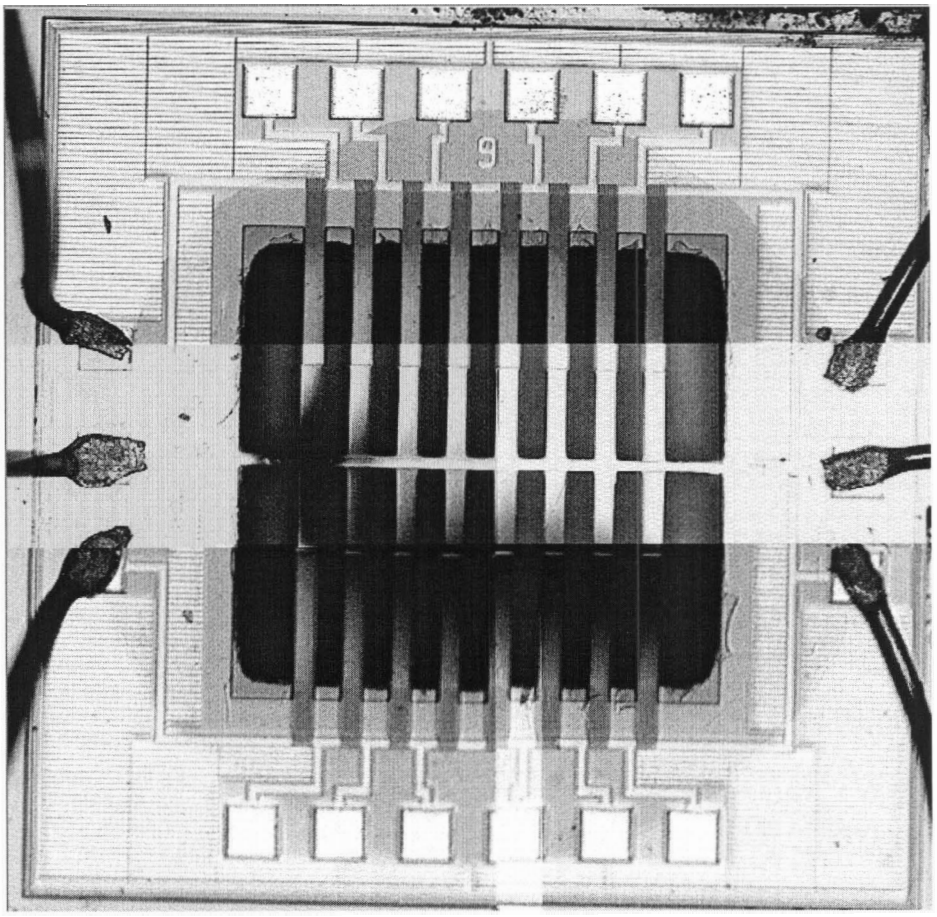

Figure 1 - 5 Photograph of the prototype microthermal accelerometer chip

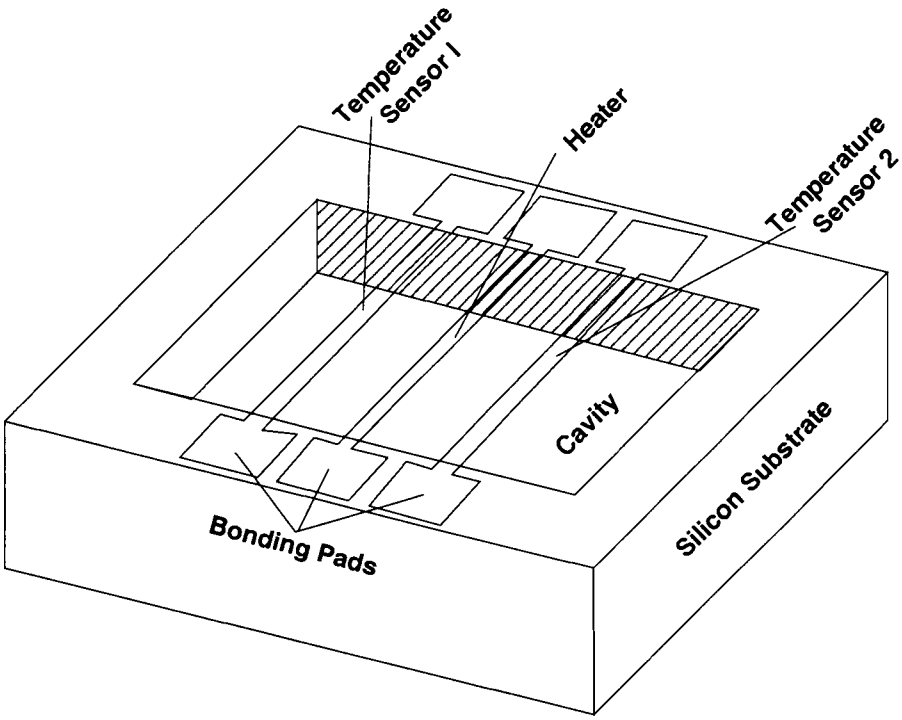

Figure 1 - 6 Structure of a single-axis microthermal accelerometer

1 - 2.2 Operation of the Microthermal Accelerometer

The operating principle of the microthermal accelerometer is based on the buoyancy of a heated fluid. Before the device supplies power to the heater, no heated fluid is developed. Temperature distribution is uniform along the axis. After the device is powered, but with no acceleration, the fluid around the heater will warm up. This warmed fluid produces a temperature gradient between the heater and the temperature sensors. At this stage, the temperature profiles on both sides are symmetrical. The heated fluid bubble is centered on the heater bar. Therefore the two temperature sensors will produce zero differential output. When acceleration is applied, acceleration causes the heated fluid to move in the same direction as the applied force, the temperature profile will be disturbed by this buoyancy force, hence, a differential temperature between the temperature sensors

is produced, corresponding to the applied acceleration, as shown in Figure 1 - 7. This differential temperature increases with the acceleration applied.

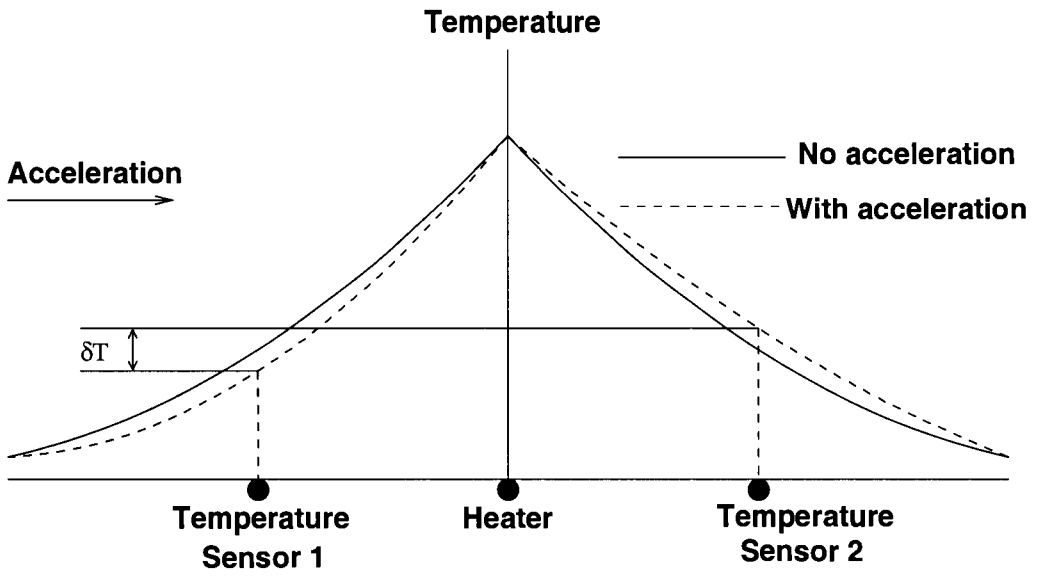

Figure 1 - 7 Schematic of operating principle

For the device that will be studied in Chapter 5, "Experimental Studies", using air as a working fluid, a typical power supply to the heater would be about 10 mW, leading to a heater temperature of about 100 K above ambient. When exposed to an acceleration of 1g, the buoyancy-induced temperature differential is about 0.1K, which induces a voltage of about 10 microvolts in each of the thermocouple junctions, for a total voltage of 100 microvolts. This voltage is then amplified 1000 times, to about 100 millivolts.

1 - 2.3 Comparison of the Microthermal Accelerometer and the MEMS Capacitive Accelerometer

In this section, a detailed comparison is made between commercially available microthermal accelerometers (e.g. MXR7210GL by MEMSIC Inc.) and the alternative MEMS capacitive accelerometer (e.g. ADXL50 by Analog Devices and Siemens.) used in

air-bag control systems, in terms of typical resolution, response time and operation range, as listed in Table 1 - 1. Since a major objective of this thesis is to demonstrate that the performance limits of the currently available microthermal accelerometer can be greatly extended by use of working fluids other than air, we will re-visit this comparison in Chapter 8, "Size Limitations, Design Implications, and Future Work", after the limits of the novel, liquid-filled accelerometer have been established in Chapter 5, "Experimental Studies".

Table 1 - 1 Comparison of the microthermal accelerometer and the MEMS capacitive accelerometer

Accelerometer type	Microthermal accelerometer	MEMS capacitive accelerometer
Sensitivity	100 mV/g	20 mV/g
Typical resolution Voltage Noise Density	$1 mg/(\sqrt{Hz})$ 4mg rms noise for a 10 Hz bandwidth	$(6.6mg)/(\sqrt{Hz})$ 60mg rms noise for 100Hz Bandwidth 20mg rms noise for 10 Hz Bandwidth
Response time/bandwidth	160Hz	1 KHz
Operational range	below ±1g to above ±100g	±2g to above ±50g
Maximum acceleration	50,000g	1450g
Commercialized device	MXR7210GL by MEMSIC	ADXL50 by Analog Device and Siemens

1 - 2.3.1 Device Structure and Signal Processing Circuitry

In Section 1 - 1.3 and in Section 1 - 2 we have discussed the operational principle and micro-electro-mechanical structure of the MEMS capacitive accelerometer,

commercially available from Analog Device and Siemens, and the microthermal accelerometer, commercially available from MEMSIC, respectively. Compared with MEMS capacitive accelerometer, the microthermal accelerometer is much simpler in its device structure: it consists of no mechanical moving parts, and the output signals from the thermal sensors can be differentially amplified, relatively simpler than that of MEMS capacitive accelerometer. For the MEMS capacitive accelerometer ADXL50 discussed in this section, it has been calculated that for 1g acceleration, the mass displacement is only 7.9×10^{-10} m. The original capacitance of the sensing capacitors is only 0.1pF, so the capacitance change is about 6.2×10^{-5} pF. To detect such small capacitance changes, an opposite driving or amplitude modulation technique is employed for signal processing. Therefore, the signal processing circuit must be very sophisticated and has to be monolithically integrated with the sensing elements, and special care must be taken with the circuit design. (Bao, 2000) (Kuehnel and Sherman, 1994)

1 - 2.3.2 Sensitivity

Sensitivity is defined as Vout (output voltage of accelerometer) per g unit of acceleration applied, specified at the Vout pin in mV/g.

The sensitivity of MEMS capacitive accelerometer is typically at 20mV/g, for example for ADXL50, and has almost reached the limit. Attempting to increase the displacement by using thinner fingers will increase the fragility of the device.

By comparison, the microthermal accelerometer has much higher sensitivity: for the prototype accelerometer described in Chapter 5, "Experimental Studies", using air as working fluid and operating with heater power of 10mW and amplification of 1000, the sensitivity is at 100mV/g level, and still can be improved. More important, as will be demonstrated in this thesis, by using different working fluids such as isopropanol, the sensitivity can be further improved by between two and three orders of magnitude.

1 - 2.3.3 Operational Range

Microthermal accelerometers, such as those produced by MEMSIC are capable of measuring acceleration with a full-scale range from below ±1 g to above ±100 g. And the MEMS capacitive accelerometer developed by Analog Devices and Siemens, has an operation range of ±2 g to above ±50 g. So by comparison, microthermal accelerometers can measure acceleration of wider range than the MEMS capacitive accelerometer.

1 - 2.3.4 Resolution

The resolution of an accelerometer, or the smallest detectable increment in acceleration, is limited by the signal to noise ratio. For the microthermal accelerometer, such as MEMSIC accelerometer, the typical noise floor is below $1\text{mg}/(\sqrt{\text{Hz}})$, allowing sub milli-g signal to be measured at very low frequency. The MEMSIC accelerometer is capable of resolving less than 1° of tilt angle. When using a simple RC low pass filter to reduce the noise by limiting the bandwidth, the noise floor of the MEMSIC accelerometer can be calculated by $\text{Noise}_{(\text{rms})} = (1\text{mg}/\sqrt{\text{Hz}}) \times (\sqrt{\text{BW} \times 1.6})$ (MEMSIC Inc. 2004).

For the MEMS capacitive accelerometer, such as ADXL50 discussed in this section, in early stages, the preamplifier noise was considered to dominate the sensor noise floor. But with steady progress in the design of sensing electronics and in the miniaturization of the sensing elements, the inherent thermal-mechanical noise of the mechanical structure may play an important role or even dominate the noise floor of the sensor. The thermal mechanical noise for a bandwidth of 100Hz at 300K is 2.6×10^{-3} m/s^2 (Bao, 2000). In Table 1 - 1, the typical reading of noise floor for ADXL50 is listed as $(6.6\text{mg})/(\sqrt{\text{Hz}})$, and the noise reading is 20mg rms noise in 10 Hz bandwidth and 60mg in 100Hz bandwidth. The later version of ADXL150 has some improvement in reducing noise level. Because of lower noise floor, microthermal accelerometer can

generally achieve better resolution than MEMS capacitive accelerometer.

1 - 2.3.5 Response Time

As will be shown in Chapter 5, "Experimental Studies", for a microthermal accelerometer with geometry similar to that described in Section 1 - 2.1, the response time for the thermocouples is several milliseconds, therefore, the current response time for microthermal accelerometer is limited by the thermocouple response. The measured bandwidth of MEMSIC accelerometer is about 60Hz, and is expandable to 160Hz by frequency compensation circuit. Improving the response time of thermal sensors can reduce the overall response time of the microthermal accelerometer. For MEMS capacitive accelerometer, such as ADXL50, the free vibration frequency is 17.7KHz. Since the resonant frequency is very high, the overall bandwidth of the device will be determined by the low pass filter, which is 1KHz.

1 - 2.3.6 Robustness

One of the most important advantages of the microthermal accelerometer compared with the micro-electro-mechanical alternative is that the micro-electro-mechanical accelerometer fails by the same mechanism that it uses to measure acceleration: for it to make a measurement, the imposed acceleration must cause sufficient flexing of the silicon cantilevers to change the capacitance of the device. But if a larger acceleration is imposed, the cantilevers will bend further and ultimately break. Thus there is necessarily a trade-off between sensitivity and robustness for this design.

For the microthermal accelerometer, by contrast, no solid part of the device need move in response to an acceleration. As will be proven in the course of this thesis, there are a variety of ways to increase the sensitivity of the accelerometer, for example,

pressurizing the working fluid, which do not compromise its robustness. This advantage over the micro-electro-mechanical accelerometer is important in applications which require both the sensitive measurement of an acceleration and exposure to incidental high accelerations -- for example, an instrumentation package in a spacecraft that is designed to measure microgravities, but which must survive the stresses of launch and re-entry. An independent mechanical shock test has been performed on a MEMSIC commercially available microthermal accelerometer. In that test, it has been demonstrated that the microthermal accelerometer has an inherent capability to survive high shocks of up to 50,000g (MEMSIC Inc. 2004), whereas the MEMS capacitive accelerometer is only rated to 1,450g (Bao, 2000).

1 - 2.4 Microthermal Accelerometer and Applications

The accelerometer can measure both dynamic acceleration (e.g. vibration) and static acceleration. (e.g. gravity). The device is also sensitive to changes in position, or tilt, when the accelerometer's axis is perpendicular to the force of gravity, or parallel to the Earth's surface.

The microthermal accelerometer is targeted for a wide variety of applications, including:

1. Vehicle airbags and fail-safe system,
2. Medical and industrial sensors,
3. Computer game "joysticks" and portable computers

Several applications have developed based on the microthermal accelerometer (MEMSIC Inc. 2003). For example, one type of MEMSIC accelerometer has been used as the multifunction sensor for a vehicle security system, capable of acting simultaneously as a shock/vibration detector and a tilt sensor. Another example of application is to use

thermal accelerometer as a human motion sensor.

Light Truck Vehicles including Sports Utility Vehicles (SUV) possess rollover problems. Many lives can be saved with the introduction of rollover warning and prevention system, hence development of early predictive rollover sensor systems becomes an important issue. One important potential application of the microthermal accelerometer under development is to be used in "roll-over" sensor for vehicles to detect imminent roll-overs and instantly deploy side airbags.

1 - 3 Summary

To summarize, the microthermal accelerometer has many desirable features over traditional electro-mechanical accelerometer and conventional MEMS capacitive accelerometer such as sensitivity to small acceleration, compact design, light weight, resistant to mechanical shock and yet inexpensive to manufacture. For a full comparison, though, we need to determine the performance limits of the entire class of microthermal accelerometers, not just the single example that has been reported in the literature (Leung, Jones, Czyzewska, Chen, and Pascal 1997). Microthermal accelerometers built on the basis of buoyancy principle have so far used air as the working fluid. It is important to investigate the possible advantages of using other fluids, including liquids. This is one of the major motivations for this thesis project, and will be pursued by literature search, by CFD modelling, and by experiment. Once the governing equations have been established, both steady-state solution and transient solutions will be sought to establish limits on sensitivity and on response time. At the conclusion of this thesis, we expect to be able to answer such questions as:

1. How does the choice of working fluid affect sensitivity and response time?
2. How do the dimensions of the accelerometer affect sensitivity and response time?

3. How does the heater temperature affect performance?

Chapter 2 Microthermal Accelerometer Designs and Modeling

As stated in the previous chapter, all that is currently known about microthermal accelerometers is that one particular design, that described in (Leung, Jones, Czyzewska, Chen, and Pascal 1997), has been shown to work. The theory of their operation is limited to the conjecture, in the same paper, that the sensitivity of the accelerometer is proportional to the Grashof number:

$$Gr = \frac{g\rho^2 l^3 \beta \Delta T}{\mu^2} \qquad \textbf{(Eq 2 - 1)}$$

where ρ is the density of the working fluid, l a characteristic dimension of the device, β the thermal expansion coefficient of air, ΔT the temperature difference between the heater and the ambient temperature, and μ is the viscosity of the working fluid. The significance of Gr and other relevant non-dimensional numbers will be discussed at the end of this chapter.

To study the fundamental operational physics of the microthermal accelerometer and to provide guidelines for its development and improvement, we will develop an idealized model. Our goal is to establish the limits that the design can achieve in accuracy, sensitivity and speed of response, and how these things depend on the design parameters; in other words, in this thesis, we will predict the 'performance envelope' of each design, which means the upper and lower bounds on its performance parameters. Also, we want to find out, from our models, what advantages there might be using fluids other than air.

2 - 1 Assumptions

To design and calibrate a microthermal accelerometer device, it is necessary to predict the magnitude of the temperature asymmetry as a function of the system parameters and the applied acceleration. The first two performance parameters sought are: the magnitude of the maximum differential temperature output, and the location at which this maximum differential temperature occurs. The third performance parameter is the response time of this design.

We will begin by setting out a set of assumptions, then formulate equations based on these assumptions. By non-dimensionalising the equations, we will determine the non-dimensional numbers governing device operation. These equations will then be solved, using computational fluid dynamics, to yield correlations to be used as a basis for design. Lastly, we will verify our assumptions by comparing performance predictions based on the models with the results of experiment.

2 - 1.1 Idealized Geometry

The geometry represented in Figure 1 - 5 will be idealized as a pair of infinitely long concentric cylinders, the inner cylinder being the heater, the outer cylinder being the side walls of the cavity. This corresponds to Figure 2 - 1, except that the thermocouples will not be modeled.

This is a drastic simplification of the geometry of the device shown in Figure 1 - 5. We make this simplification because we are interested in the performance limits of the entire class of microthermal accelerometers, rather than modeling a particular device. The simplification allows us to compare the results of our modeling with analytic and experimental results in the prior literature. We can apply the results of modeling the simplified geometry to more realistic geometries via a scaling argument: if changing the

working fluid from air to a liquid increases the sensitivity of the idealized accelerometer by a factor of N, we expect the same change to increase the sensitivity of an actual accelerometer by a similar factor.

The temperature profile of the heater element is derived in Appendix II, as a function of the properties of the heater material and dimensions. It is shown that the heater temperature profile will consist of a central, isothermal portion, falling off towards the wall temperature to either side. If the central portion is large, the concentric-cylinder model is a good description; if it is short, the accelerometer is better modeled as two concentric spheres, the inner sphere representing the heater, the outer sphere representing the cavity walls. This latter idealization also corresponds to an alternative accelerometer design, in which the central heater is a point source rather than a line source, and in which thermocouples can be symmetrically placed on two or three orthogonal axes as shown in Figure 2 - 2. No results for such a design have been published, but its appeal is that it would permit measurement of the magnitude and direction of an acceleration along any axis.

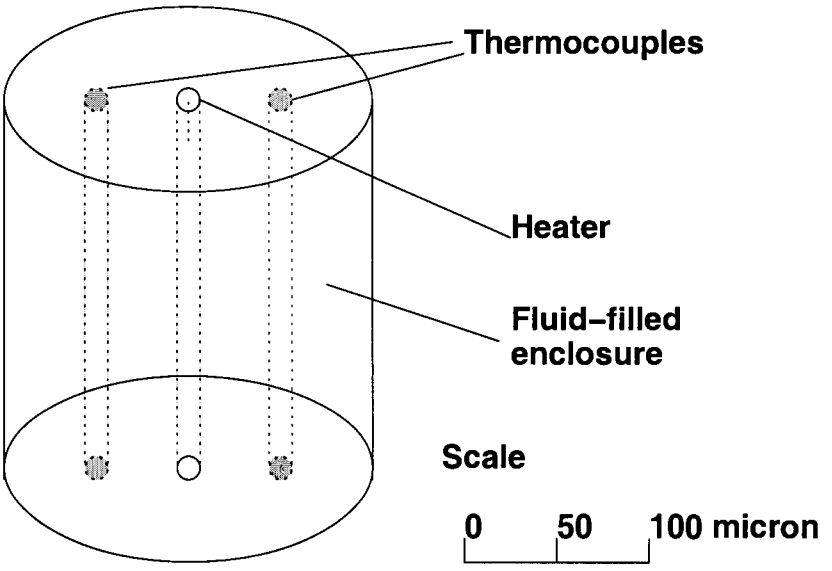

Figure 2 - 1 Idealized concentric-cylinder model of accelerometer

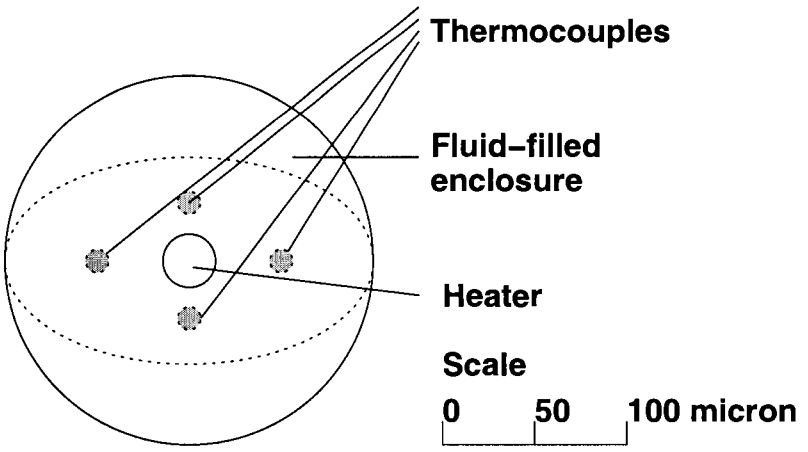

Figure 2 - 2 Idealized concentric-sphere model of accelerometer

2 - 1.2 Assumptions

In this section, we derive equations for the natural convection induced by the buoyancy force in enclosures bound by concentric cylinders and concentric spheres.

Since we are modeling heat transfer, we must consider which of the three heat transfer mechanisms -- radiation, convection, and conduction -- are relevant. A simple order-of-magnitude calculation will show that radiation can be neglected:

Consider two concentric cylinders, the inner of radius 10 microns, the outer of radius 1000 microns, the inner maintained at 400 K and the outer at 300 K. Suppose the space between them to be filled with air. The heat flow by conduction from the inner to the outer is given by

$$\frac{Q}{L} = \frac{2\pi k(T_i - T_o)}{\ln\left(\frac{r_o}{r_i}\right)} = \frac{2\pi k(400-300)}{\ln\left(\frac{0.001000}{0.000010}\right)} \qquad \textbf{(Eq 2 - 2)}$$

Taking k, the conductivity of air, to be 0.03 W/(mK), this evaluates to 4.1 W/m. If we now calculate the radiative heat transfer from the inner cylinder to the outer, we obtain:

$$\frac{Q}{L} = 2\pi(r_i)\sigma T_i^4 = 2\pi \times 0.000010 \times \sigma \times 400^4 \qquad \textbf{(Eq 2 - 3)}$$

Taking σ, the Stefan-Boltzmann constant, to be $5.66 \times 10^{-8}\ W/(m^2K^4)$, this evaluates to $0.09\ W/m$. We note also that most potential working fluids will be more conductive than air, so we conclude that radiative heat transfer may be neglected.

By starting from the equations of continuity, momentum and energy, we make no initial assumption about the relative importance of conduction and convection: the magnitudes of conductive and convective heat transfer will emerge from the solution to the equations.

We further assume that:

- all flows are laminar
- there are no heat sources within the annular space between the bounding cylinders or spheres;
- the enclosed fluid is incompressible;
- the variations in gas density, ρ may be ignored, except insofar as they give rise to a buoyancy force (this is the Boussinesq approximation).
- the fluid conductivity, specific heat and viscosity do not vary with temperature. (The consequences of departures from this assumptions will be discussed in Chapter 8.)

2 - 2 Governing Equations

The conservation equations of mass, momentum, and energy will be examined for both the cylindrical and spherical cases.

2 - 2.1 The Equation of Continuity

The general form of continuity equation is:

$$\frac{D\rho}{Dt} = -\rho(\nabla \bullet V) \qquad \textbf{(Eq 2 - 4)}$$

Where V is the local velocity.

With Boussinesq approximation, for a fluid of constant density (incompressible fluid), the equation of continuity becomes:

$$\nabla \bullet (\rho V) = \rho \nabla \bullet V = \nabla \bullet V = 0 \qquad \textbf{(Eq 2 - 5)}$$

The following gives the equation of continuity in different coordinate systems for incompressible flow:

Cylindrical coordinates (r, θ, z)

$$\frac{1}{r}\frac{\partial(rv_r)}{\partial r} + \frac{1}{r}\frac{\partial v_\theta}{\partial \theta} + \frac{\partial v_z}{\partial z} = 0 \qquad \textbf{(Eq 2 - 6)}$$

Spherical coordinates (r, θ, ϕ)

$$\frac{1}{r^2}\frac{\partial(r^2 v_r)}{\partial r} + \frac{1}{r\sin\theta}\frac{\partial(v_\theta \sin\theta)}{\partial \theta} + \frac{1}{r\sin\theta}\frac{\partial v_\phi}{\partial \phi} = 0 \qquad \textbf{(Eq 2 - 7)}$$

2 - 2.2 The Equation of Motion

The general form of conservation of momentum equation is given as:

$$\rho\frac{DV}{Dt} = -\nabla P + \nabla \bullet S + \rho g \qquad \textbf{(Eq 2 - 8)}$$

Where S is the stress tensor of the fluid.

For the flow of a Newtonian fluid with varying density but constant viscosity μ, the above equation becomes:

$$\rho\frac{DV}{Dt} = -\nabla P + \frac{1}{3}\mu\nabla(\nabla\bullet\boldsymbol{V}) + \mu\nabla^2\boldsymbol{V} + \rho\boldsymbol{g} \qquad \textbf{(Eq 2 - 9)}$$

For the flow of a Newtonian fluid, where both density ρ and viscosity μ are constant, the above equation may be simplified by means of the continuity equation $\nabla\bullet\boldsymbol{V} = 0$ to give the famous Navier-Stokes equation in vector form:

$$\rho\frac{DV}{Dt} = -\nabla P + \mu\nabla^2\boldsymbol{V} + \rho\boldsymbol{g} \qquad \textbf{(Eq 2 - 10)}$$

More specifically for natural convection due to buoyancy forces caused by temperature differences,

$$\rho\frac{DV}{Dt} = -\nabla P + \mu\nabla^2\boldsymbol{V} + \rho\beta\boldsymbol{g}(T - T_o) \qquad \textbf{(Eq 2 - 11)}$$

which can be written in the following coordinate systems:

Cylindrical coordinate (r, θ, z)

r direction:

$$\rho\left(\frac{\partial v_r}{\partial t} + v_r\frac{\partial v_r}{\partial r} + \frac{v_\theta}{r}\frac{\partial v_r}{\partial\theta} - \frac{v_\theta^2}{r} + v_z\frac{\partial v_r}{\partial z}\right) \qquad \textbf{(Eq 2 - 12)}$$
$$= -\frac{\partial P}{\partial r} + \mu\left[\frac{\partial}{\partial r}\left(\frac{1}{r}\frac{\partial(rv_r)}{\partial r}\right) + \frac{1}{r^2}\frac{\partial^2 v_r}{\partial\theta^2} - \frac{2}{r^2}\frac{\partial v_\theta}{\partial\theta} + \frac{\partial^2 v_r}{\partial z^2}\right] + \rho\beta(T - T_o)g_r$$

θ direction:

$$\rho\left(\frac{\partial v_\theta}{\partial t} + v_r\frac{\partial v_\theta}{\partial r} + \frac{v_\theta}{r}\frac{\partial v_\theta}{\partial\theta} + \frac{v_r v_\theta}{r} + v_z\frac{\partial v_\theta}{\partial z}\right) \qquad \textbf{(Eq 2 - 13)}$$
$$= -\frac{1}{r}\frac{\partial P}{\partial\theta} + \mu\left[\frac{\partial}{\partial r}\left(\frac{1}{r}\frac{\partial(rv_\theta)}{\partial r}\right) + \frac{1}{r^2}\frac{\partial^2 v_\theta}{\partial\theta^2} + \frac{2}{r^2}\frac{\partial v_r}{\partial\theta} + \frac{\partial^2 v_\theta}{\partial z^2}\right] + \rho\beta(T - T_o)g_\theta$$

z direction:

$$\rho\left(\frac{\partial v_z}{\partial t} + v_r\frac{\partial v_z}{\partial r} + \frac{v_\theta}{r}\frac{\partial v_z}{\partial \theta} + v_z\frac{\partial v_z}{\partial z}\right) \qquad \textbf{(Eq 2 - 14)}$$

$$= -\frac{\partial P}{\partial z} + \mu\left[\frac{1}{r}\frac{\partial}{\partial r}\left(r\frac{\partial v_z}{\partial r}\right) + \frac{1}{r^2}\frac{\partial^2 v_z}{\partial \theta^2} + \frac{\partial^2 v_z}{\partial z^2}\right] + \rho\beta(T - T_o)g_z$$

Spherical coordinates (r, θ, ϕ)*

r direction:

$$\rho\left(\frac{\partial v_r}{\partial t} + v_r\frac{\partial v_r}{\partial r} + \frac{v_\theta}{r}\frac{\partial v_r}{\partial \theta} + \frac{v_\phi}{r\sin\theta}\frac{\partial v_r}{\partial \phi} - \frac{v_\theta^2 + v_\phi^2}{r}\right) \qquad \textbf{(Eq 2 - 15)}$$

$$= -\frac{\partial P}{\partial r} + \mu\left(\nabla^2 v_r - \frac{2v_r}{r^2} - \frac{2}{r^2}\frac{\partial v_\theta}{\partial \theta} - \frac{2v_\theta\cot\theta}{r^2} - \frac{2}{r^2\sin\theta}\frac{\partial v_\phi}{\partial \phi}\right) + \rho\beta(T - T_o)g_r$$

θ direction:

$$\rho\left(\frac{\partial v_\theta}{\partial t} + v_r\frac{\partial v_\theta}{\partial r} + \frac{v_\theta}{r}\frac{\partial v_\theta}{\partial \theta} + \frac{v_\phi}{r\sin\theta}\frac{\partial v_\theta}{\partial \phi} - \frac{v_r v_\theta}{r} - \frac{v_\phi^2\cot\theta}{r}\right) \qquad \textbf{(Eq 2 - 16)}$$

$$= -\frac{1}{r}\frac{\partial P}{\partial \theta} + \mu\left(\nabla^2 v_\theta + \frac{2}{r^2}\frac{\partial v_r}{\partial \theta} - \frac{v_\theta}{r^2\sin^2\theta} - \frac{2\cos\theta}{r^2\sin^2\theta}\frac{\partial v_\phi}{\partial \phi}\right) + \rho\beta(T - T_o)g_\theta$$

ϕ direction:

$$\rho\left(\frac{\partial v_\phi}{\partial t} + v_r\frac{\partial v_\phi}{\partial r} + \frac{v_\theta}{r}\frac{\partial v_\phi}{\partial \theta} + \frac{v_\phi}{r\sin\theta}\frac{\partial v_\phi}{\partial \phi} - \frac{v_r v_\phi}{r} - \frac{v_\theta v_\phi\cot\theta}{r}\right) \qquad \textbf{(Eq 2 - 17)}$$

$$= -\frac{1}{r\sin\theta}\frac{\partial P}{\partial \phi} + \mu\left(\nabla^2 v_\phi + \frac{2}{r^2\sin\theta}\frac{\partial v_r}{\partial \phi} - \frac{v_\phi}{r^2\sin^2\theta} + \frac{2\cos\theta}{r^2\sin^2\theta}\frac{\partial v_\theta}{\partial \phi}\right) + \rho\beta(T - T_o)g_\phi$$

*For spherical coordinates the Laplacian is

$$\nabla^2 = \frac{1}{r^2}\frac{\partial}{\partial r}\left(r^2\frac{\partial}{\partial r}\right) + \frac{1}{r^2\sin\theta}\frac{\partial}{\partial \theta}\left(\sin\theta\frac{\partial}{\partial \theta}\right) + \frac{1}{r^2\sin^2\theta}\left(\frac{\partial^2}{\partial \phi^2}\right)$$

2 - 2.3 The Energy Equation

The general relation for energy for a Newtonian fluid is given as:

$$\rho\frac{Du}{Dt} = \nabla\bullet k\nabla T - P(\nabla \bullet V) + \mu\Phi + q_s \qquad \textbf{(Eq 2 - 18)}$$

Where $\boldsymbol{u}$ is internal energy, Φ is the dissipation function.

Using continuity equation, for an incompressible fluid, the above equation can be rewritten:

$$\rho\frac{D\boldsymbol{u}}{Dt} = \nabla\bullet k\nabla T + \mu\Phi + q_s \qquad \textbf{(Eq 2 - 19)}$$

For an ideal gas or for a liquid,

$$\boldsymbol{u} = c_v T \qquad \textbf{(Eq 2 - 20)}$$

For incompressible fluid with specific heat $c = c_p = c_v$, from (Eq 2 - 19), and $d\boldsymbol{u} = cdT$, we obtain:

$$\rho c\frac{DT}{Dt} = \nabla\bullet k\nabla T + \mu\Phi + q_s \qquad \textbf{(Eq 2 - 21)}$$

The term $\mu\Phi$ in above equation represents the dissipation of work to produce frictional heating. It is reasonable to assume it is negligible. Hardee calculates this term in Appendix D of his thesis (Hardee, 1966), and shows that it is about 10^{-10} times smaller than the other terms for typical cases.

Therefore, since the heat source term $q_s = 0$, with Boussinesq approximation and $k \neq k(T)$, also assuming viscous heat generation is zero, the equation can be further simplified as:

$$\rho c\frac{DT}{Dt} = k\nabla^2 T \qquad \textbf{(Eq 2 - 22)}$$

Written in the following coordinate systems:

Cylindrical coordinates (r, θ, z):

$$\rho c\left(\frac{\partial T}{\partial t} + v_r\frac{\partial T}{\partial r} + \frac{v_\theta}{r}\frac{\partial T}{\partial \theta} + v_z\frac{\partial T}{\partial z}\right) = k\left[\frac{1}{r}\frac{\partial}{\partial r}\left(r\frac{\partial T}{\partial r}\right) + \frac{1}{r^2}\frac{\partial^2 T}{\partial \theta^2} + \frac{\partial^2 T}{\partial z^2}\right] \qquad \textbf{(Eq 2 - 23)}$$

Spherical coordinates (r, θ, ϕ)

$$\rho c\left(\frac{\partial T}{\partial t} + v_r\frac{\partial T}{\partial r} + \frac{v_\theta}{r}\frac{\partial T}{\partial \theta} + \frac{v_\phi}{r\sin\theta}\frac{\partial T}{\partial \phi}\right) \qquad \textbf{(Eq 2 - 24)}$$

$$= k\left[\frac{1}{r^2}\frac{\partial}{\partial r}\left(r^2\frac{\partial T}{\partial r}\right) + \frac{1}{r^2\sin\theta}\frac{\partial}{\partial \theta}\left(\frac{\partial T}{\partial \theta}\right) + \frac{1}{r^2\sin^2\theta}\frac{\partial^2 T}{\partial \phi^2}\right]$$

2 - 3 Nondimensional Equations

To investigate the development of velocity field and temperature field of natural convective fluid induced by the buoyancy force, we need to identify the non-dimensional groups that govern this behavior. For this reason, we need to derive the non-dimensional form of the governing equations.

We non-dimensionalize these governing equations with respect to the reference quantities:

τ: the characteristic time for the final flow field / temperature field to develop; specifically, the time taken for the differential temperature between radially opposed thermocouples to reach 63% of its steady-state value.

r_i: the inner radius of concentric cylinders or concentric spheres

T_o: the temperature of outer cylinder or outer sphere

2 - 3.1 Cylindrical Case

2 - 3.1.1 Continuity Equation

The dimensional form of continuity equation for cylindrical case is,

$$\frac{1}{r}\frac{\partial(rv_r)}{\partial r} + \frac{1}{r}\frac{\partial v_\theta}{\partial \theta} + \frac{\partial v_z}{\partial z} = 0 \qquad \textbf{(Eq 2 - 25)}$$

$\frac{\partial v_z}{\partial z} = 0$ in our case since we assume an infinite horizontal cylinder, so it can be simplified to

$$\frac{\partial(rv_r)}{\partial r} + \frac{\partial v_\theta}{\partial \theta} = 0 \qquad \textbf{(Eq 2 - 26)}$$

which can be expanded to

$$\frac{v_r}{r} + \frac{\partial v_r}{\partial r} + \frac{1}{r}\frac{\partial v_\theta}{\partial \theta} = 0 \qquad \textbf{(Eq 2 - 27)}$$

Now put non-dimensional quantities,

$$\hat{r} = \frac{r}{r_i} \qquad \textbf{(Eq 2 - 28)}$$

$$\hat{v}_r = v_r\frac{\tau}{r_i}, \hat{v}_\theta = v_\theta\frac{\tau}{r_i} \qquad \textbf{(Eq 2 - 29)}$$

Therefore, the nondimensional form of the continuity equation is obtained,

$$\frac{\hat{v}_r}{\hat{r}} + \frac{\partial \hat{v}_r}{\partial \hat{r}} + \frac{\partial \hat{v}_\theta}{\partial \hat{r}} = 0 \qquad \textbf{(Eq 2 - 30)}$$

2 - 3.1.2 Equation of Motion

The dimensional form of equation of motion in r direction:

$$\rho\left(\frac{\partial v_r}{\partial t} + v_r\frac{\partial v_r}{\partial r} + \frac{v_\theta}{r}\frac{\partial v_r}{\partial \theta} - \frac{v_\theta^2}{r} + v_z\frac{\partial v_r}{\partial z}\right) \qquad \textbf{(Eq 2 - 31)}$$

$$= -\frac{\partial P}{\partial r} + \mu\left[\frac{\partial}{\partial r}\left(\frac{1}{r}\frac{\partial(rv_r)}{\partial r}\right) + \frac{1}{r^2}\frac{\partial^2 v_r}{\partial \theta^2} - \frac{2}{r^2}\frac{\partial v_\theta}{\partial \theta} + \frac{\partial^2 v_r}{\partial z^2}\right] + \rho\beta(T - T_o)g_r$$

it can be rewritten as:

$$\frac{\partial v_r}{\partial t} + v_r\frac{\partial v_r}{\partial r} + \frac{v_\theta}{r}\frac{\partial v_r}{\partial \theta} - \frac{v_\theta^2}{r} + v_z\frac{\partial v_r}{\partial z} \qquad \textbf{(Eq 2 - 32)}$$

$$= -\frac{1}{\rho}\frac{\partial P}{\partial r} + \frac{\mu}{\rho}\left[\frac{\partial}{\partial r}\left(\frac{1}{r}\frac{\partial (r v_r)}{\partial r}\right) + \frac{1}{r^2}\frac{\partial^2 v_r}{\partial \theta^2} - \frac{2}{r^2}\frac{\partial v_\theta}{\partial \theta} + \frac{\partial^2 v_r}{\partial z^2}\right] + \beta g(T - T_o)\cos\theta$$

since $\frac{\partial v_r}{\partial z} = \frac{\partial^2 v_r}{\partial z^2} = 0$, it can be simplified as:

$$\frac{\partial v_r}{\partial t} + v_r\frac{\partial v_r}{\partial r} + \frac{v_\theta}{r}\frac{\partial v_r}{\partial \theta} - \frac{v_\theta^2}{r} \qquad \textbf{(Eq 2 - 33)}$$

$$= -\frac{1}{\rho}\frac{\partial P}{\partial r} + \frac{\mu}{\rho}\left[\frac{\partial}{\partial r}\left(\frac{1}{r}\frac{\partial (r v_r)}{\partial r}\right) + \frac{1}{r^2}\frac{\partial^2 v_r}{\partial \theta^2} - \frac{2}{r^2}\frac{\partial v_\theta}{\partial \theta}\right] + \beta g(T - T_o)\cos\theta$$

Put the following nondimensional quantities (Eq 2 - 28), (Eq 2 - 29) and

$$\hat{t} = \frac{t}{\tau} \qquad \textbf{(Eq 2 - 34)}$$

$$\hat{P} = \frac{P}{\rho v^{*2}} = \frac{P}{\rho\left(\frac{r_i}{\tau}\right)^2} \qquad \textbf{(Eq 2 - 35)}$$

(Eq 2 - 32) becomes:

$$\frac{\partial \hat{v}_r}{\partial \hat{t}} + \hat{v}_r\frac{\partial \hat{v}_r}{\partial \hat{r}} + \frac{\hat{v}_\theta}{\hat{r}}\frac{\partial \hat{v}_r}{\partial \theta} - \frac{\hat{v}_\theta^2}{\hat{r}} \qquad \textbf{(Eq 2 - 36)}$$

$$= -\frac{\partial \hat{P}}{\partial \hat{r}} + \frac{\mu\tau}{\rho r_i^2}\left[\frac{\partial}{\partial \hat{r}}\left(\frac{1}{\hat{r}}\frac{\partial (\hat{r}\hat{v}_r)}{\partial \hat{r}}\right) + \frac{1}{\hat{r}^2}\frac{\partial^2 \hat{v}_r}{\partial \theta^2} - \frac{2}{\hat{r}^2}\frac{\partial \hat{v}_\theta}{\partial \theta}\right] + \beta g(T - T_o)\cos\theta\frac{\tau^2}{r_i}$$

Using nondimensional groups which are defined as:

Fourier number,

$$F_o = \frac{\tau\alpha}{r_i^2} \qquad \textbf{(Eq 2 - 37)}$$

Prandtl number,

$$Pr = \frac{\mu c}{k} = \frac{\mu}{\rho\alpha} \qquad \textbf{(Eq 2 - 38)}$$

where

$$\alpha = \frac{k}{\rho c} \qquad \textbf{(Eq 2 - 39)}$$

and

Grashof number,

$$Gr = \frac{\rho^2 r_i^3 g \Delta T \beta}{\mu^2} \qquad \textbf{(Eq 2 - 40)}$$

(Eq 2 - 36) can be then rewritten in terms of nondimensional groups of F_o, Gr and Pr,

$$\frac{\partial \hat{v}_r}{\partial \hat{t}} + \hat{v}_r \frac{\partial \hat{v}_r}{\partial \hat{r}} + \frac{\hat{v}_\theta}{\hat{r}} \frac{\partial \hat{v}_r}{\partial \theta} - \frac{\hat{v}_\theta^2}{\hat{r}} \qquad \textbf{(Eq 2 - 41)}$$

$$= -\frac{\partial \hat{P}}{\partial \hat{r}} + F_o Pr \left[\frac{\partial}{\partial \hat{r}} \left(\frac{1}{\hat{r}} \frac{\partial (\hat{r} \hat{v}_r)}{\partial \hat{r}} \right) + \frac{1}{\hat{r}^2} \frac{\partial^2 \hat{v}_r}{\partial \theta^2} - \frac{2}{\hat{r}^2} \frac{\partial \hat{v}_\theta}{\partial \theta} \right] + Gr F_o^2 Pr^2 \cos\theta$$

Similarly,

θ direction:

$$\rho \left(\frac{\partial v_\theta}{\partial t} + v_r \frac{\partial v_\theta}{\partial r} + \frac{v_\theta}{r} \frac{\partial v_\theta}{\partial \theta} + \frac{v_r v_\theta}{r} + v_z \frac{\partial v_\theta}{\partial z} \right) \qquad \textbf{(Eq 2 - 42)}$$

$$= -\frac{1}{r} \frac{\partial P}{\partial \theta} + \mu \left[\frac{\partial}{\partial r} \left(\frac{1}{r} \frac{\partial (r v_\theta)}{\partial r} \right) + \frac{1}{r^2} \frac{\partial^2 v_\theta}{\partial \theta^2} + \frac{2}{r^2} \frac{\partial v_r}{\partial \theta} + \frac{\partial^2 v_\theta}{\partial z^2} \right] + \rho \beta (T - T_o) g_\theta$$

where it can be rewritten as:

$$\frac{\partial v_\theta}{\partial t} + v_r\frac{\partial v_\theta}{\partial r} + \frac{v_\theta}{r}\frac{\partial v_\theta}{\partial \theta} + \frac{v_r v_\theta}{r} + v_z\frac{\partial v_\theta}{\partial z} \qquad \textbf{(Eq 2 - 43)}$$

$$= -\frac{1}{\rho r}\frac{\partial P}{\partial \theta} + \frac{\mu}{\rho}\left[\frac{\partial}{\partial r}\left(\frac{1}{r}\frac{\partial (r v_\theta)}{\partial r}\right) + \frac{1}{r^2}\frac{\partial^2 v_\theta}{\partial \theta^2} + \frac{2}{r^2}\frac{\partial v_r}{\partial \theta} + \frac{\partial^2 v_\theta}{\partial z^2}\right] + \beta g(T - T_o)\sin\theta$$

since $\frac{\partial v_\theta}{\partial z} = \frac{\partial^2 v_\theta}{\partial z^2} = 0$, the above equation can then be written as:

$$\frac{\partial v_\theta}{\partial t} + v_r\frac{\partial v_\theta}{\partial r} + \frac{v_\theta}{r}\frac{\partial v_\theta}{\partial \theta} + \frac{v_r v_\theta}{r} \qquad \textbf{(Eq 2 - 44)}$$

$$= -\frac{1}{\rho r}\frac{\partial P}{\partial \theta} + \frac{\mu}{\rho}\left[\frac{\partial}{\partial r}\left(\frac{1}{r}\frac{\partial (r v_\theta)}{\partial r}\right) + \frac{1}{r^2}\frac{\partial^2 v_\theta}{\partial \theta^2} + \frac{2}{r^2}\frac{\partial v_r}{\partial \theta}\right] + \beta g(T - T_o)\sin\theta$$

Putting nondimensional quantities defined in (Eq 2 - 28), (Eq 2 - 29) and (Eq 2 - 33), (Eq 2 - 35) the above equation becomes:

$$\frac{\partial \hat{v}_\theta}{\partial \hat{t}} + \hat{v}_r\frac{\partial \hat{v}_\theta}{\partial \hat{r}} + \frac{\hat{v}_\theta}{\hat{r}}\frac{\partial \hat{v}_\theta}{\partial \theta} + \frac{\hat{v}_r \hat{v}_\theta}{\hat{r}} \qquad \textbf{(Eq 2 - 45)}$$

$$= -\frac{1}{\hat{r}}\frac{\partial \hat{P}}{\partial \theta} + \frac{\mu}{\rho}\frac{\tau}{r_i^2}\left[\frac{\partial}{\partial \hat{r}}\left(\frac{1}{\hat{r}}\frac{\partial (\hat{r}\hat{v}_\theta)}{\partial \hat{r}}\right) + \frac{1}{\hat{r}^2}\frac{\partial^2 \hat{v}_\theta}{\partial \theta^2} + \frac{2}{\hat{r}^2}\frac{\partial \hat{v}_r}{\partial \theta}\right] + \beta g(T - T_o)\sin\theta\frac{\tau^2}{r_i}$$

Again, using nondimensional groups of (Eq 2 - 37), (Eq 2 - 38), and (Eq 2 - 39), (Eq 2 - 40), the above equation can be written as:

$$\frac{\partial \hat{v}_\theta}{\partial \hat{t}} + \hat{v}_r\frac{\partial \hat{v}_\theta}{\partial \hat{r}} + \frac{\hat{v}_\theta}{\hat{r}}\frac{\partial \hat{v}_\theta}{\partial \theta} + \frac{\hat{v}_r \hat{v}_\theta}{\hat{r}} \qquad \textbf{(Eq 2 - 46)}$$

$$= -\frac{1}{\hat{r}}\frac{\partial \hat{P}}{\partial \theta} + F_o Pr\left[\frac{\partial}{\partial \hat{r}}\left(\frac{1}{\hat{r}}\frac{\partial (\hat{r}\hat{v}_\theta)}{\partial \hat{r}}\right) + \frac{1}{\hat{r}^2}\frac{\partial^2 \hat{v}_\theta}{\partial \theta^2} + \frac{2}{\hat{r}^2}\frac{\partial \hat{v}_r}{\partial \theta}\right] + Gr(F_o)^2(Pr)^2\sin\theta$$

There is no component for velocity in z direction for momentum equation of cylindrical case.

2 - 3.1.3 Energy Equation

The dimensional form of energy equation is,

$$\rho c\left(\frac{\partial T}{\partial t}+v_r\frac{\partial T}{\partial r}+\frac{v_\theta}{r}\frac{\partial T}{\partial \theta}+v_z\frac{\partial T}{\partial z}\right)=k\left[\frac{1}{r}\frac{\partial}{\partial r}\left(r\frac{\partial T}{\partial r}\right)+\frac{1}{r^2}\frac{\partial^2 T}{\partial \theta^2}+\frac{\partial^2 T}{\partial z^2}\right] \qquad \textbf{(Eq 2 - 47)}$$

which can be rewritten as:

$$\frac{\partial T}{\partial t}+v_r\frac{\partial T}{\partial r}+\frac{v_\theta}{r}\frac{\partial T}{\partial \theta}+v_z\frac{\partial T}{\partial z}=\alpha\left[\frac{1}{r}\frac{\partial}{\partial r}\left(r\frac{\partial T}{\partial r}\right)+\frac{1}{r^2}\frac{\partial^2 T}{\partial \theta^2}+\frac{\partial^2 T}{\partial z^2}\right] \qquad \textbf{(Eq 2 - 48)}$$

where α is defined in (Eq 2 - 39).

since $\frac{\partial T}{\partial z}=\frac{\partial^2 T}{\partial z^2}=0$, it can be simplified as:

$$\frac{\partial T}{\partial t}+v_r\frac{\partial T}{\partial r}+\frac{v_\theta}{r}\frac{\partial T}{\partial \theta}=\alpha\left[\frac{1}{r}\frac{\partial}{\partial r}\left(r\frac{\partial T}{\partial r}\right)+\frac{1}{r^2}\frac{\partial^2 T}{\partial \theta^2}\right] \qquad \textbf{(Eq 2 - 49)}$$

Put nondimensional quantities $\hat{r}$, $\hat{v}_r$, $\hat{v}_\theta$, $\hat{t}$ defined in (Eq 2 - 28)(Eq 2 - 29)(Eq 2 - 33), and

$$\hat{T}=\frac{T}{T_o} \qquad \textbf{(Eq 2 - 50)}$$

(Eq 2 - 48) is non-dimensionalized to

$$\frac{\partial \hat{T}}{\partial \hat{t}}+\hat{v}_r\frac{\partial \hat{T}}{\partial \hat{r}}+\frac{\hat{v}_\theta}{\hat{r}}\frac{\partial \hat{T}}{\partial \theta}=\frac{\alpha\tau}{r_i^2}\left[\frac{1}{\hat{r}}\frac{\partial}{\partial \hat{r}}\left(\hat{r}\frac{\partial \hat{T}}{\partial \hat{r}}\right)+\frac{1}{\hat{r}^2}\frac{\partial^2}{\partial \theta^2}\hat{T}\right] \qquad \textbf{(Eq 2 - 51)}$$

Using nondimensional group F_o,

The above equation can be written as:

$$\frac{\partial \hat{T}}{\partial \hat{t}}+\hat{v}_r\frac{\partial \hat{T}}{\partial \hat{r}}+\frac{\hat{v}_\theta}{\hat{r}}\frac{\partial \hat{T}}{\partial \theta}=F_o\left[\frac{1}{\hat{r}}\frac{\partial}{\partial \hat{r}}\left(\hat{r}\frac{\partial \hat{T}}{\partial \hat{r}}\right)+\frac{1}{\hat{r}^2}\frac{\partial^2}{\partial \theta^2}\hat{T}\right] \qquad \textbf{(Eq 2 - 52)}$$

2 - 3.2 Spherical Case

The corresponding solution for the case of concentric spheres is derived in Appendix I, and also depends on the three non-dimensional groups, Pr, Gr and F_o.

2 - 4 Examination of the Governing Dimensionless Numbers

The first of the non-dimensional groups, the Prandtl number Pr, is a property of the working fluid. Specifically, it is the ratio of the fluid's ability to transport momentum to its ability to transport heat. The Prandtl number for air, the only working fluid to have been discussed in the prior literature, is about 0.7. Liquid metals, such as mercury, have much lower values of Pr, while most liquids have values higher than one; Pr for water, for example, is about 5.4.

The second non-dimensional group, the Grashof number Gr, shows the ratio of the buoyancy forces that would create natural convection to the viscous forces opposing fluid motion. It is sometimes used in combination with the Prandtl number to create the Rayleigh number, $Ra = GrPr$. Prior research has established correlations between the value of Rayleigh number and the relative importance of convection and conduction. Kuehn and Goldstein (1976), for example, present a plot of 'equivalent conductivity', the ratio of heat transfer via convection to the heat transfer expected from pure conduction, versus Rayleigh number, showing that the increase in heat transfer due to convection is only a few percent for Rayleigh numbers less than 100. For comparison, the Rayleigh number for the accelerometer chip studied in Chapter 5, "Experimental Studies", under a 1g acceleration and using air as the working fluid, is about 0.0001. So the accelerometer chip operates in the conduction-dominated regime.

Nevertheless, although conduction is the main mechanism by which heat is lost from the heater, it is the small amount of convective flow that is responsible for the temperature difference between the detectors, and hence for the operation of the accelerometer.

The third non-dimensional number, the Fourier number F_o, governs the time taken for the temperature difference between radially opposite points to develop once an acceleration has been imposed. No prior literature exists on this topic, since the initial conditions -- a pre-existing temperature field and a suddenly imposed acceleration -- are the reverse of the transient case usually considered, of a body in an existing gravity field suddenly being heated. The correlations needed to predict the Fourier number from the Grashof and Prandtl numbers will be developed in Chapter 4, "The Concentric-Cylinders Model: Transient Analysis", and Chapter 7, "The Concentric Spheres Model: Transient Analysis".

In addition to the three dimensionless numbers mentioned, there is a fourth parameter, R, the ratio of the radius of the inner cylinder or sphere to that of the outer cylinder or sphere. Establishing the effect of this parameter on the device sensitivity and response time will permit evaluation of the effects of shrinking or expanding the heater for a given cavity size.

In this chapter, we have set out the assumptions used to model the microthermal accelerometer, set up the equations describing convective flow and heat transfer within the accelerometer cavity, and derived the non-dimensional parameters governing device performance. In the following chapters, we will construct computational fluid dynamic (CFD) models based on the equations derived here and conduct a literature review of theoretical and experimental studies of free-convection laminar flow, seeking correlations that will permit prediction of device performance.

Chapter 3 The Concentric-Cylinders Model: Steady-State Analysis

In this chapter we will use the CFD package 'FLOTRAN' to solve the equations developed in the previous chapter. Our objective is not to predict the performance of any one device, but to establish correlations that will allow us to predict the effects of changing the working fluid or the device size on sensitivity and response time.

The characteristic operating regime of the accelerometer results in a very small temperature differential between the thermocouples, of the order of 10^{-3} K compared with absolute value of ambient temperature at 300 K; to predict this difference accurately, the level of precision in the model needs to be of the same order. This requires great care in building the model.

To ensure that the correlations obtained from the model are valid, we perform a series of checks on the model predictions:

- Internal consistency: are the predictions independent of details of the modeling, such as mesh size? (This is investigated in Appendix III)
- Consistency with literature: can the model reproduce the experimental and analytic results derived in the prior literature? (This is done in the current chapter).
- Consistency with experiment: are the predicted effects of choice of working fluid consistent with experimental results? (This will be checked following the description of experimental work in Chapter 5.)

The above-mentioned temperature differential was smaller than 0.1K reported in Chapter 1, it can be explained that the simulations use lower value of $\Delta T = 10\text{K}$ between heater temperature and ambient temperature rather than 100 K in the real operation, and

this was done to match the assumption of Hodnett that $(T_i - T_o)/T_o \ll 1$.

3 - 1 FLOTRAN Concentric-Cylinders Model

3 - 1.1 FLOTRAN Model Specifications

A FLOTRAN model was set up with the following specifications:

- Model consists of the fluid in the annulus bounded by two concentric cylinders;
- Fluid properties set for air as shown in Table 3 - 1;

Table 3 - 1 Fluid properties of air

k	μ	ρ	c	β	Pr
W/mK	$Pa \cdot s$	kg/m^3	$J/(kg \cdot K)$	K^{-1}	
2.574×10^{-2}	1.813×10^{-5}	1.1768	1.004×10^3	0.0033	0.7072

- Inner cylinder temperature maintained at $T_i = 310\,K$, and the outer at $T_o = 300\,K$.
- The radius of inner cylinder set to 100 microns, that of outer set to 1000 microns, corresponding to $R = 10$. Other values of R can be realized by changing the radius of inner cylinder.
- Acceleration set at 10 m/s^2, corresponding to $Ra = 0.001$.
- For steady-state FLOTRAN analysis at this stage, radially symmetric mesh is chosen. The mesh refinement study reported in Appendix III shows that 20 divisions in radial direction and 72 divisions in circumferential direction can provide sufficient level of accuracy.

- Iterative method used to solve temperature and pressure fields until convergence was obtained, convergence criteria used are:

$$\sum_{i=1}^{n} \frac{\left|T_i^k - T_i^{k-1}\right|}{\left|T_i^k\right|} < 10^{-8}$$

$$\sum_{i=1}^{n} \frac{\left|p_i^k - p_i^{k-1}\right|}{p_i^k} \leq 10^{-6}$$

3 - 1.2 FLOTRAN Modeling Procedure

The procedure for modeling and meshing of concentric cylinders is as follows:

1. Create a partial annulus centered at (0, 0), with inner radius of 0.0001m, outer radius of 0.001m, from 90° to 270°;
2. Mesh the area with 0.00005m division on straight lines and 5° division on arc lines;
3. Reflect meshed area in Y, Z plane on the other half of X axis;
4. Coincide the nodes on the same boundary shared by the original area and the reflected areas.
5. Apply load: temperature on inner circle set to 310K, temperature on outer circle set to 300K; velocity on all boundaries set to 0 m/s; gravity in x direction set to 10 m/s^2.
6. Set up simulation control, the simulation runs to 1000 iterations, with convergence criteria set as specified in the previous section.
7. The velocity solver is Tri-Diagonal Matrix Algorithm (TDMA); for the incompressible pressure equation, pressure solver is Preconditioned Conjugate Gradient Method (PCG), and temperature solver is TDMA.

As mentioned above, the differential temperature between the detectors is a small difference between large quantities. Exceptional care therefore had to be taken in designing and refining the mesh used for the model. The details of this refinement are given in Appendix III to this thesis.

3 - 2 FLOTRAN Concentric-Cylinder Model Steady-State Analysis

We begin concentric-cylinder model steady-state analysis with a review of the prior literature in the area of convective laminar flow between the enclosure of concentric cylinders, which will be used to validate the results of FLOTRAN modeling.

A review given by Kuehn and Goldstein (1976) covers the experimental and theoretical studies of natural convection between horizontal concentric cylinders up to that date.

3 - 2.1 Experimental Studies

Experimental investigation of natural convection between horizontal concentric isothermal cylinders was first carried out by Beckmann (1931), using fluids such as air, hydrogen and carbon dioxide to obtain overall heat-transfer coefficients. Then, Voigt & Krischer (1932) carried out a similar experiment using air. Their result was further extended by Kraussold (1934) to larger Prandtl numbers, using water, transformer oil and machine oil and obtaining correlations for the overall heat-transfer coefficients. In the experiments carried out by Liu, Mueller & Landis (1961), radial temperature profiles of air, water and a silicone fluid were measured and qualitative flow characteristics were described for each fluid. Photographic techniques were developed by Bishop & Carley

(1966) and Bishop, Carley & Powe (1968) using smoke to observe the flow pattern. Different flow regimes also were pictured by Powe, Carley & Bishop (1969) for a range of Rayleigh numbers and diameter ratios. A more complete experimental investigation for natural convection within a horizontal annulus was carried out by Kuehn and Goldstein (1976), in which velocity and temperature distributions were presented. Since our interests on experimental work is more focused on velocity and temperature distributions, we will explore their findings in the next section.

3 - 2.1.1 Experimental Investigation by Kuehn and Goldstein

In this section, we will include some details of findings of Kuehn and Goldstein studies (1976) on experimental investigation of natural convection within a horizontal annulus.

Apparatus

A schematic diagram of apparatus built by Kuehn and Goldstein for testing natural convection within concentric cylinders is sketched in Figure 3 - 1.

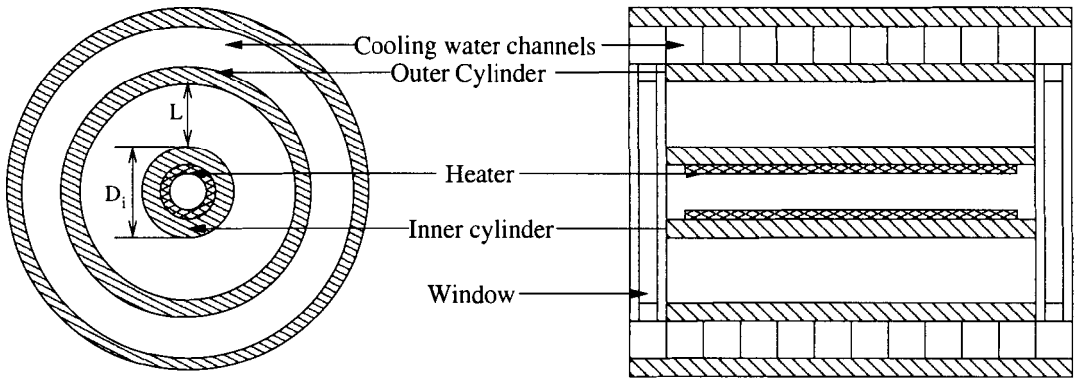

Figure 3 - 1 Schematic diagram of experimental apparatus for natural convection within concentric cylinders

The apparatus consisted of two cylinders: inner cylinder and outer cylinder. It was heated by passing direct current to a resistor held in the center of the cylinder. Six thermocouples, four in the mid plane set at 90° apart and one at each end, were used to measure the temperature at the outer surface of the inner cylinder. Another set of six thermocouples were positioned similarly to measure the temperature at the inner surface of outer cylinder. The cooling water was maintained isothermal between outer cylinder and water jacket. A Mach-Zehnder interferometer capable of using air at atmospheric pressure as well as liquid was used in their test apparatus, to record the temperature distribution between the cylinders. The flow pattern could be conveniently observed through windows at the end of cylinders.

The entire apparatus was first insulated and left overnight to come to thermal equilibrium, the system was then adjusted to a predetermined setting by circulating the cooling water to the outer cylinder and heating the inner cylinder. The apparatus was then left to reach a steady state.

Results

In Kuehn & Goldstein's experiments, the steady state temperature distribution (isotherm) resulting from buoyancy could be interpreted from the fringes of interferograms. Three interferograms using air or water were presented for the natural convectional flow within the enclosure of horizontal concentric cylinders at different Rayleigh number. The Rayleigh number, $Ra^* = \frac{\rho g \beta (r_o - r_i)^3 (T_i - T_o)}{\mu \alpha}$, based on the gap width $L = r_o - r_i$, varied from 2.11×10^4 to 9.76×10^5. From these interferograms, three regions of the natural convectional flow can be generally observed: inner cylinder boundary layer, outer cylinder boundary layer and the central core region between the two boundary layers. The hot fluid flows up in a boundary layer near the inner cylinder and forms a buoyant plume above the inner cylinder and then impinges upon the outer cylinder

and separates at the top, and this warmer fluid moves in a boundary layer adjacent to the outer cylinder towards the bottom, forming a fluid flow loop. This fluid flow loop appears symmetrical along the vertical plane of cylindrical axis. As Rayleigh number Ra^* of the fluid flow increase, this inner boundary layer and outer boundary layer becomes more defined and the temperature gradient increases; and the central core region becomes larger. Their results also shows that the fluid flow becomes unsteady at higher Rayleigh number $Ra^* > 10^5$.

These experimental results presented by Kuehn and Goldstein are not immediately applicable to our problem since the Rayleigh number is higher than that of interest to us. However, it still provides us much useful information in understanding qualitatively the nature of the problem, and modeling work as well.

First, our problem is constrained in a much smaller scale, in micron level. A possible approach to experimental work, would be to scale the system up, constructing a apparatus similar to Kuehn and Goldstein's. To keep the Rayleigh number at the level of our interest, a high-viscosity fluid, such as glycerine would be used.

Second, the experimental work of Kuehn and Goldstein confirms that Rayleigh number, Prandtl number and radius ratio are the three important characteristics that determine the behavior of buoyancy-driven fluid flow. For example, as the Rayleigh number increases, the significance of buoyancy increases until the flow becomes unsteady. On the other hand, for the small Rayleigh numbers of our application, we would expect a more conduction-dominated steady flow, refer to Figure 6. "*Influence of Rayleigh number on local equivalent conductivity*" and Figure 7. "*Mean equivalent conductivity as a function of Rayleigh numbe*r" in Kuehn and Goldstein (1976). These figures show the equivalent conductivity is within a few percent of the actual conductivity for $Ra^* < 100$. Hence, we can qualitatively determine the flow of our problem to be a natural convective laminar flow, but in the conduction-dominated region.

Moreover, some important observations from the isotherm obtained by Kuehn and Goldstein are as follows:

- the flow is invariant along the axis of the cylinders,
- the fluid flow is symmetrical about the vertical plane of the cylindrical axis.

These observations can provide some guides to simplify our model of the problem. The theoretical studies in their work, which were compared with their experimental results, will be more directly applicable to our problem. Those results will be discussed in Section 3 - 2.1.2, and will be compared with results of FLOTRAN steady-state analysis.

3 - 2.1.2 Numerical Studies by Kuehn and Goldstein

Natural convection laminar flow within the enclosure between concentric cylinders has been studied theoretically using numerical method by Kuehn and Goldstein (1976). Here, we review some of their findings.

Their analysis was simplified by the following approximations:

- First, the flow is assumed as steady laminar flow for small Rayleigh numbers.
- Second, since the flow is invariant along the axis of the cylinders, and the flow in the vertical central plane is symmetrical, a two-dimensional representation of one side of the system is used.
- Third, the fluid properties are assumed constant, hence, Boussinesq approximation can be used in governing equations.

Kuehn and Goldstein's static solution is simplified and solved by introducing new variables such as stream function and vorticity, and then these simplified equations are solved numerically by finite-difference method.

In the following sections, Kuehn and Goldstein's results for stream function and temperature distribution will be presented here for comparison with FLOTRAN results.

Here, we briefly explain the concepts of streamline and stream functions based on Cartesian coordinates, and give definition of stream function in cylindrical coordinates.

Streamline

A streamline is defined as a line such that the tangent to the line at any point is the direction of the fluid velocity at that point. From this definition, it follows that the mathematical equations of a streamline are

$$\frac{dx}{v_x} = \frac{dy}{v_y} = \frac{dz}{v_z} \qquad \textbf{(Eq 3 - 1)}$$

Stream Function

For a two-dimensional irrotational flow of an incompressible fluid, the stream function ψ can be defined mathematically in the following relations which hold true:

such that

$$\frac{\partial^2 \psi}{\partial x^2} + \frac{\partial^2 \psi}{\partial y^2} = 0 \qquad \textbf{(Eq 3 - 2)}$$

Thus the stream function is a solution of the Laplace equation in its two-dimensional form.

From the equations for a streamline:

$$v_y dx - v_x dy = 0 \qquad \textbf{(Eq 3 - 3)}$$

then it follows that

$$\frac{\partial \psi}{\partial x} dx + \frac{\partial \psi}{\partial y} dy = d\psi = 0 \qquad \textbf{(Eq 3 - 4)}$$

Hence, ψ = constant, i.e., the stream function is constant along a stream line.

In cylindrical coordinate, the stream function is defined as:

$$v_r = r^{-1}\frac{\partial \psi}{\partial \theta} \text{ and } v_\theta = \frac{-\partial \psi}{\partial r} \qquad \textbf{(Eq 3 - 5)}$$

Their solutions were obtained for $Pr = 0.7$ and $(r_o - r_i)/(2r_i) = 0.8$ with Rayleigh number Ra^* varying from 10^2 to 10^5. For the range of Rayleigh number studied by Kuehn and Goldstein, the flow can be divided into several regimes, among which regime 1 and 2 are of interest to us. In the following we discuss the results of these two regimes, and we compare with the result of FLOTRAN analysis later.

1. For flows with Rayleigh number Ra^* below 10^2, the convection is relatively small compared with conduction, hence the heat transfer was mainly conduction. Within this regime, the velocities are too small to affect the temperature distribution, so the isotherms remain essentially concentric circles. The flow in the top and bottom portions of the annulus is symmetric about the horizontal axis. This is the regime in which we believe the accelerometer operates.

2. For flows with Rayleigh number Ra^* between 10^2 and 3×10^4, a transition region exists. The convection flow remains in essentially the same pattern but it becomes strong enough to influence the temperature field. The isotherms become eccentric circles at Rayleigh number Ra^* near 10^3 as can be seen in Figure 3 - 2. The center of stream lines moves upwards.

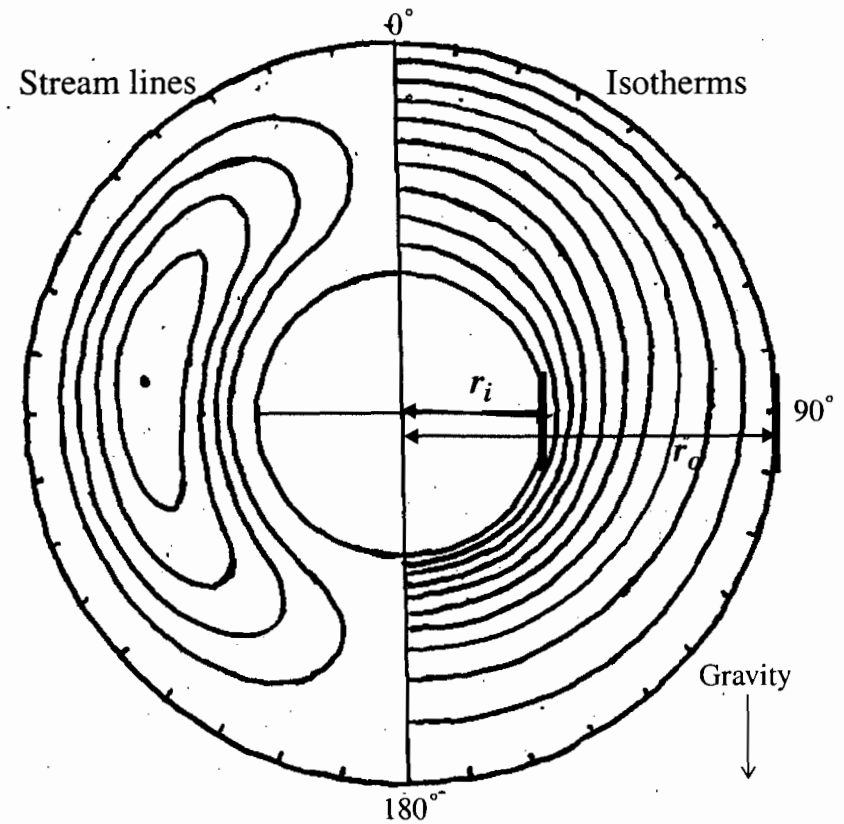

Figure 3 - 2 Sketched streamlines and isotherms in transition region for Ra^*=1000, Pr=0.7 and $(r_o-r_i)/(2r_i)$=0.8 (based on Kuehn and Goldstein 1976, for comparison)

Kuehn and Goldstein's experimental results for temperature were found to agree with their theoretical studies; they made no experimental measurements of fluid velocity.

In the scope of our studies in design and analysis of microthermal accelerometer, we are mainly interested in the laminar convective flow with small Rayleigh number, below 10^3, as above classified regimes 1 and 2, since it is only in these regimes that the maximum differential temperature is proportional to the applied acceleration. Hence, the results quoted in Figure 3 - 2 along with the qualitative discussion of experimental results (see Section) provide some useful information to check on the validity of our model and steady-state FLOTRAN results for cylinder case.

3 - 2.2 Comparison with Kuehn and Goldstein Experimental Results

The result of our FLOTRAN concentric cylinders model were compared with the results of Kuehn and Goldstein, quoted in Figure 3 - 2 for the same characteristic numbers such as Rayleigh number Ra, Prandtl number $Pr = 0.7$ and radius ratio R. It should be noticed that for the case shown in Figure 3 - 2, the characteristic numbers are: $Ra^* = 10^3$, $Pr = 0.7$, and $(r_o - r_i)/(2r_i) = 0.8$, it can be readily calculated that:

since $\frac{r_o - r_i}{2r_i} = 0.8$, therefore, $R = \frac{r_o}{r_i} = 2.6$

meanwhile, since $\frac{r_i}{r_o - r_i} = \frac{1}{1.6}$

therefore,

$$Ra = \frac{r_i^3}{(r_o - r_i)^3} Ra^* = \frac{1}{(1.6)^3} Ra^* = \frac{10^3}{4.096} = 244.$$

In making this comparison, we have scaled down from the dimensions used by kuehn and Goldstein (1976) to a smaller scale, (we have retained the assumption of infinite cylinder length), such that the radius of inner cylinder is set for 0.01m, the radius of outer cylinder is set such that $R = 2.6$, air is used for the fluid in the enclosure, so $Pr = 0.7$, and other parameters are adjusted such that $Ra = 244$. The other specifications are as given in 3 - 1.1.

The contour plots of stream function and temperature field from FLOTRAN simulation for the case of $Ra^* = 10^3$, $Pr = 0.7$ and $R = 2.6$, is shown in Figure 3 - 3. Comparison with the sides of Figure 3 - 2 provides qualitative verification of the FLOTRAN concentric cylinders model.

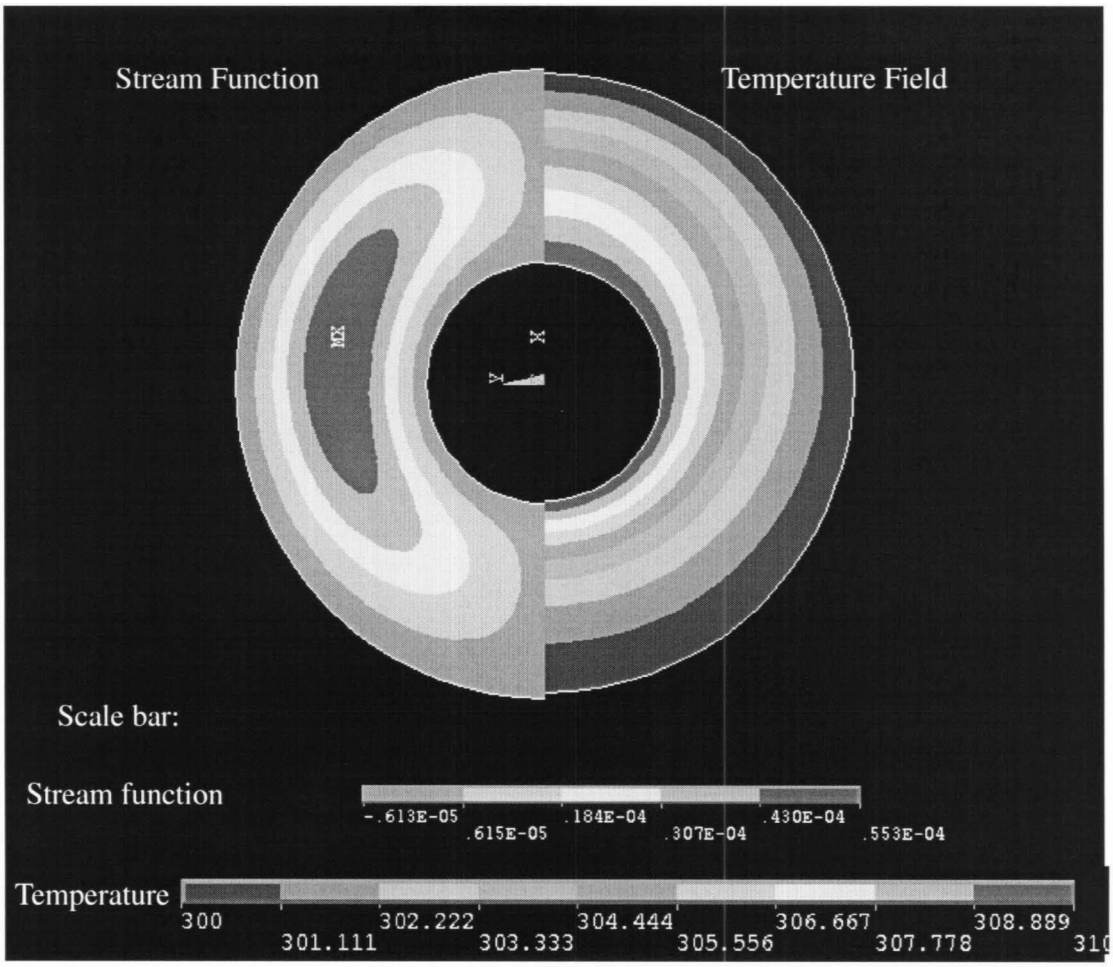

Figure 3 - 3 Stream function and temperature isotherm results for FLOTRAN concentric cylinder model, Ra^*=1000, Pr=0.7 and R=2.6

3 - 2.3 Temperature Distribution by Steady-State FLOTRAN Analysis

For the particular case specified in Section 3 - 1.1 steady-state FLOTRAN analysis gives the temperature distribution shown in Figure 3 - 4. The acceleration is applied in upward direction. This temperature distribution for Ra = 0.001 is concentric contours, the temperature asymmetry caused by the acceleration applied, via buoyancy, is almost

invisible from this picture, this agrees with previous experimental observation by Kuehn and Goldstein (1976) described in Section 3 - 2.1.1 of this thesis, flow regime one. However, the applied acceleration ***does*** cause a temperature asymmetry, which is shown as a differential temperature profile in Figure 3 - 7 of this chapter.

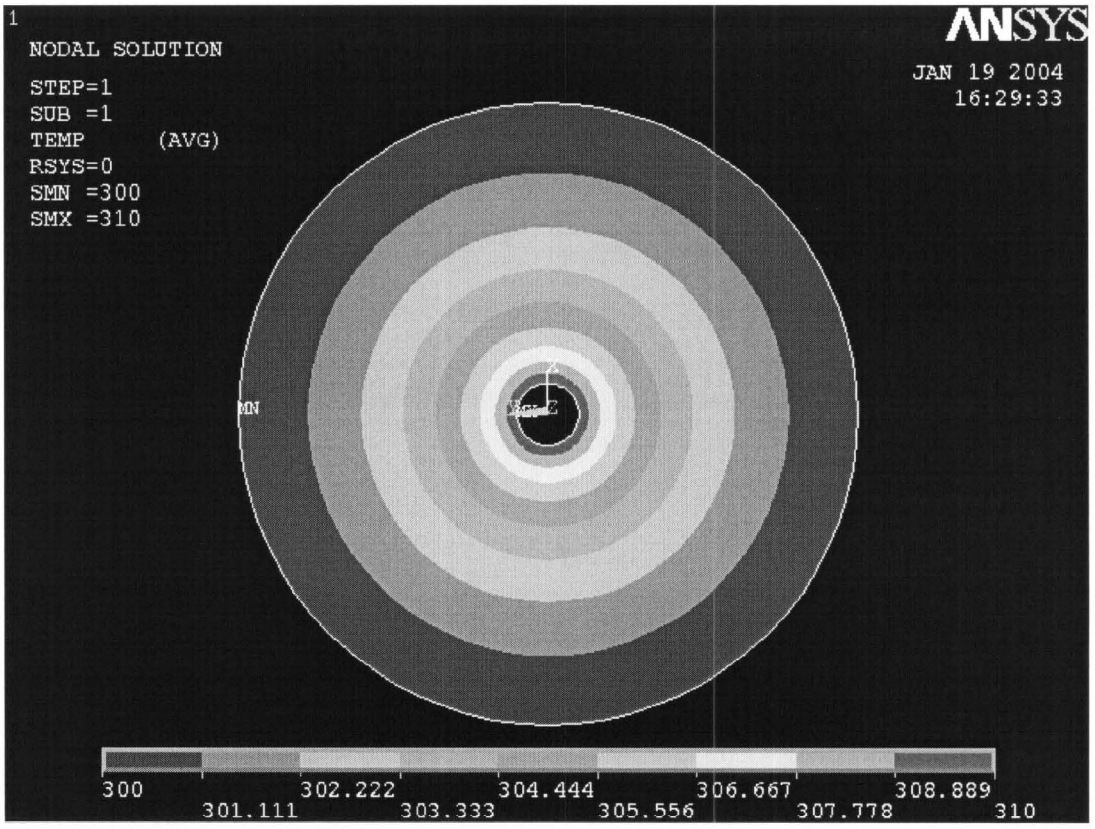

Figure 3 - 4 Temperature distribution for FLOTRAN concentric cylinders model *Ra*=0.001, *Pr*=0.7 and *R*=10

3 - 2.4 Velocity Distribution by Steady-State FLOTRAN Analysis

The velocity distribution for the case described in Section 3 - 1.1 is shown in Figure 3 - 5. The acceleration is applied in upwards direction. Convective fluid flow

caused by buoyancy is obvious in this graph. The hotter fluid flows from the hotter surface of inner cylinder and moves up and separates from the top of outer cylinder and flows down to the bottom of the outer cylinder, there flows up again to the inner cylinder to form a loop. The flow is symmetric about the vertical axis.

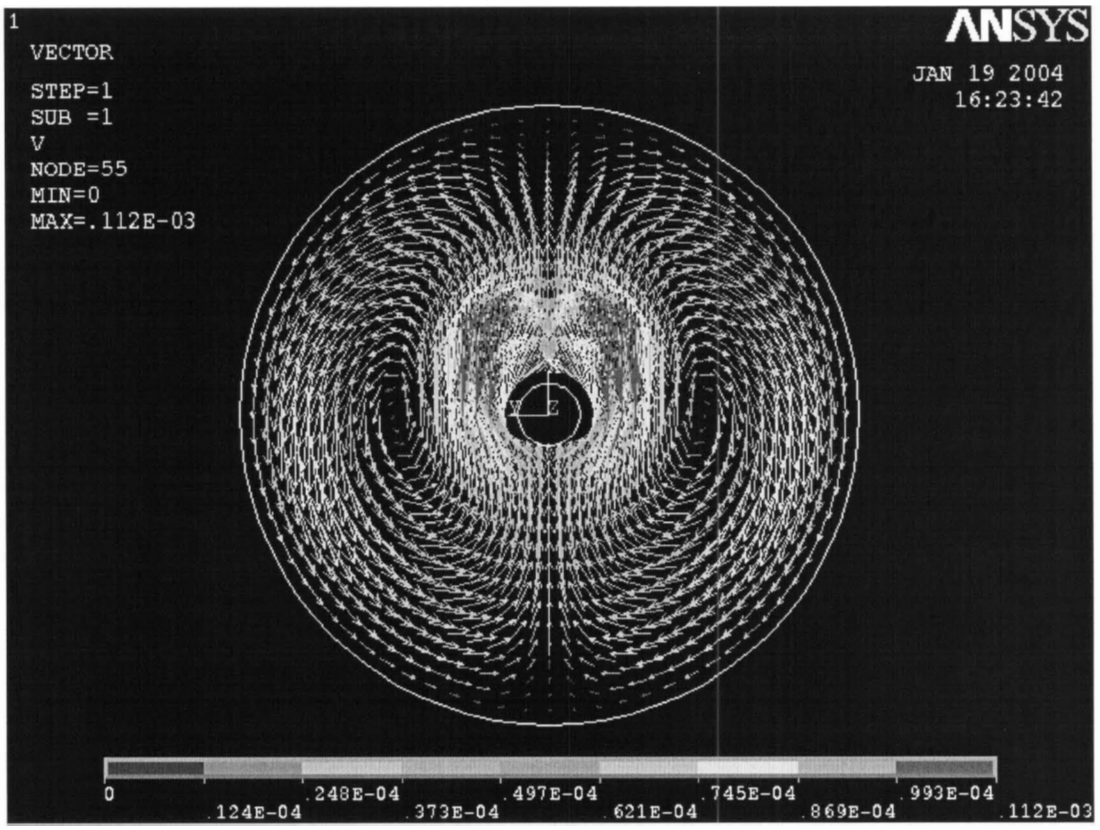

Figure 3 - 5 Velocity distribution for FLOTRAN concentric cylinders model Ra=0.001, Pr=0.7 and R=10

3 - 2.5 Analytic Studies

Analytical solutions for temperature distribution valid at small Rayleigh number have been obtained in the literature. Mack & Bishop (1968) solved the problem with a power-series expansion, the solution valid for small values of Ra and R, the ratio of the

radii of the cylinders, specifically, $Ra < 10^4$, and $1.15 < R < 4.15$. A more general case of an inner solid heat-conducting cylinder has been solved by Rotem (1972). Hodnett (1973) presented an analytical solution to the same problem using the perturbation method. His solution is valid for the conduction-dominated regime, and the limit of validity as a function of R was also established. This solution is of interest because it is valid for the range of Ra within which the accelerometer operates and within which the accelerometer response is linear. In the following Section 3 - 2.5.1, we will present some details of Hodnett's approximate analytical solution and compare the results with the numerical solution obtained using FLOTRAN analysis.

3 - 2.5.1 Hodnett's Analytic Solution

In this section, we will look at the analytical solution by Hodnett (1973) that can then be used to validate the results of FLOTRAN Model.

Coordinate System

Hodnett presented an analytical treatment of the natural convection between the space of concentric cylinders. The schematic graph Figure 3 - 6 is used to illustrate the model of the problem and the coordinate system used.

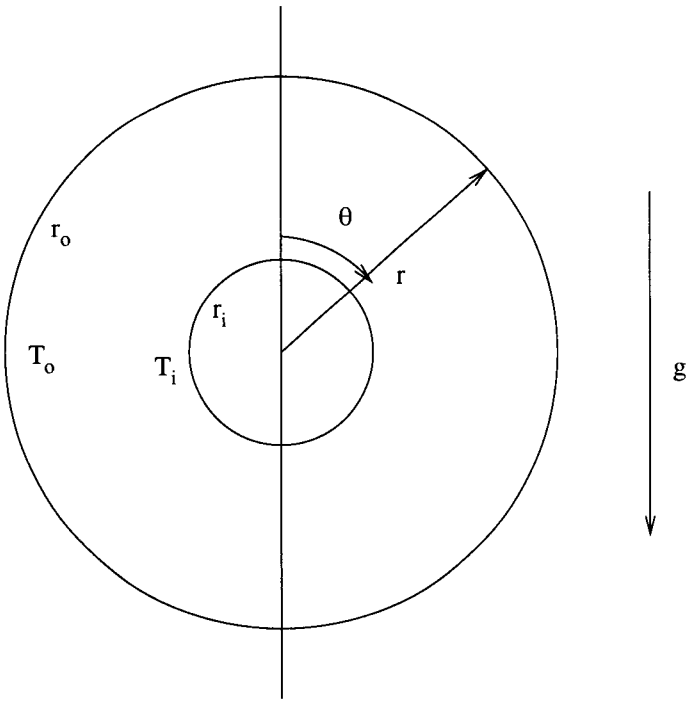

Figure 3 - 6 Concentric cylinders model and coordinate system

In this coordinate system:

r is the radial distance,

θ is the angle between a given radius and the axis of acceleration

Also, G is gravity number, defined as $G = \frac{\rho^2 r_i^3 g}{\mu^2}$.

Prandtl number $Pr = \frac{\mu c}{k}$

Rayleigh number $Ra = \frac{c\rho^2 r_i^3 g \Delta T \beta}{\mu k}$

Solution

Hodnett solved the governing equations of this problem using perturbation method

with the following assumptions:

- the inner cylinder radius is small enough so that $G \ll 1$.
- the temperature difference $(T_i - T_o)/T_o = \varepsilon \ll 1$

and obtained the following solution for the temperature distribution:

$$\frac{T}{T_o} = 1 + \varepsilon f_1(r) + m\varepsilon^2 f_2(r) + Ra\varepsilon f_3(r)\sin(\theta) + o(m\varepsilon^2, Ra\varepsilon) \qquad \textbf{(Eq 3 - 6)}$$

where

m is the parameter in $k \propto T^m$, k is the conductivity of the fluid. We assume $m = 0$.

R is the radius ratio, $R = \frac{r_o}{r_i}$.

And $f_1(r), f_2(r), f_3(r)$ are functions of r:

$$f_1(r) = 1 - (\ln r / \ln R) \qquad \textbf{(Eq 3 - 7)}$$

$$f_2(r) = \frac{1}{2}\frac{\ln r}{\ln R}\left[1 - \frac{\ln r}{\ln R}\right] \qquad \textbf{(Eq 3 - 8)}$$

$$f_3(r) = \left\{L_1 r + M_1 r^{-1} + \ln^{-1} R\left[\frac{1}{2}A_1 r \ln r - \frac{1}{2}B_1 r^{-1}\ln r + \frac{1}{8}C_1 r^3 \right.\right. \qquad \textbf{(Eq 3 - 9)}$$

$$\left.\left. + \frac{1}{4}D_1 \ln r\left((\ln r - 1) - \left(r^3 \ln\left(r - \frac{3}{4}\right)\right)/(128 \ln R)\right)\right]\right\}$$

where

$$M_1 = \ln^{-1} R(R^2 - 1)^{-1}\left[\frac{1}{2}A_1 R^2 \ln R - \frac{1}{2}B_1 \ln R + \frac{1}{8}C_1 R^2(R^2 - 1) + \right. \qquad \textbf{(Eq 3 - 10)}$$

$$\left. \frac{1}{4}D_1 R^2 \ln R(\ln R - 1) - R^2\left(R^2 \ln R - \frac{3}{4}R^2 + \frac{3}{4}\right)/(128 \ln R)\right]$$

and

$$L_1 = -\ln^{-1}R(R^2-1)^{-1}\left[\frac{1}{2}A_1R^2\ln R - \frac{1}{2}B_1\ln R + \frac{1}{8}C_1(R^4-1) + \frac{1}{4}D_1R^2\ln R(\ln R - 1) - \left(R^4\ln R - \frac{3}{4}R^4 + \frac{3}{4}\right)/(128\ln R)\right] \quad \textbf{(Eq 3 - 11)}$$

$$A_1 = \frac{C_0R^2}{16\Delta}[-R^6 + R^4 + R^2 - 1 - 2(R^2-1)^2\ln R + 8R^4(\ln R)^2] \quad \textbf{(Eq 3 - 12)}$$

$$B_1 = \frac{C_0R^4}{16\Delta}[(R^2-1)^2 - 4R^2(\ln R)^2] \quad \textbf{(Eq 3 - 13)}$$

$$C_1 = \frac{C_0R^2}{16\Delta}[(R^2-1)^2 + 2(R^2-1)^2\ln R - 4R^4(\ln R)^2] \quad \textbf{(Eq 3 - 14)}$$

$$D_1 = \frac{C_0R^2(R^2-1)}{8\Delta}(R^4 - 1 - 4R^2\ln R) \quad \textbf{(Eq 3 - 15)}$$

$$\Delta = 4R^2((R^2-1)^2 - (R^4-1)\ln R) \quad \textbf{(Eq 3 - 16)}$$

$$C_0 = (\ln R)^{-1} \quad \textbf{(Eq 3 - 17)}$$

The temperature differential, δT, measured by the accelerometer corresponds to the fourth term in (Eq 3 - 6), $Ra\varepsilon f_3(r)\sin\theta$.

The differential temperature for radially opposite points at a given r is:

$$\delta T = 2RaT_o\varepsilon f_3(r) \quad \textbf{(Eq 3 - 18)}$$

where we multiply the fourth term by T_o to obtain the actual, rather than the dimensionless temperature.

Hodnett does not include the complete set of equations (Eq 3 - 12)-(Eq 3 - 17) in his paper, but they are given by Mack and Bishop (1968) (equation (26) through (30) and by Rotem (1972) (equation (19) through (24)).

3 - 2.6 Comparison with Hodnett's Analytical Solution

3 - 2.6.1 Differential Temperature Profiles

In Figure 3 - 7, the differential temperature profile along the axis of acceleration predicted by steady-state FLOTRAN analysis for the case set up in Section 3 - 1.1 is compared with the result of Hodnett's (Eq 3 - 6) calculated for the same problem. Good agreement is seen between analytical and numerical solution. (The radial distance is calculated as zero at outer cylinder to inner cylinder).

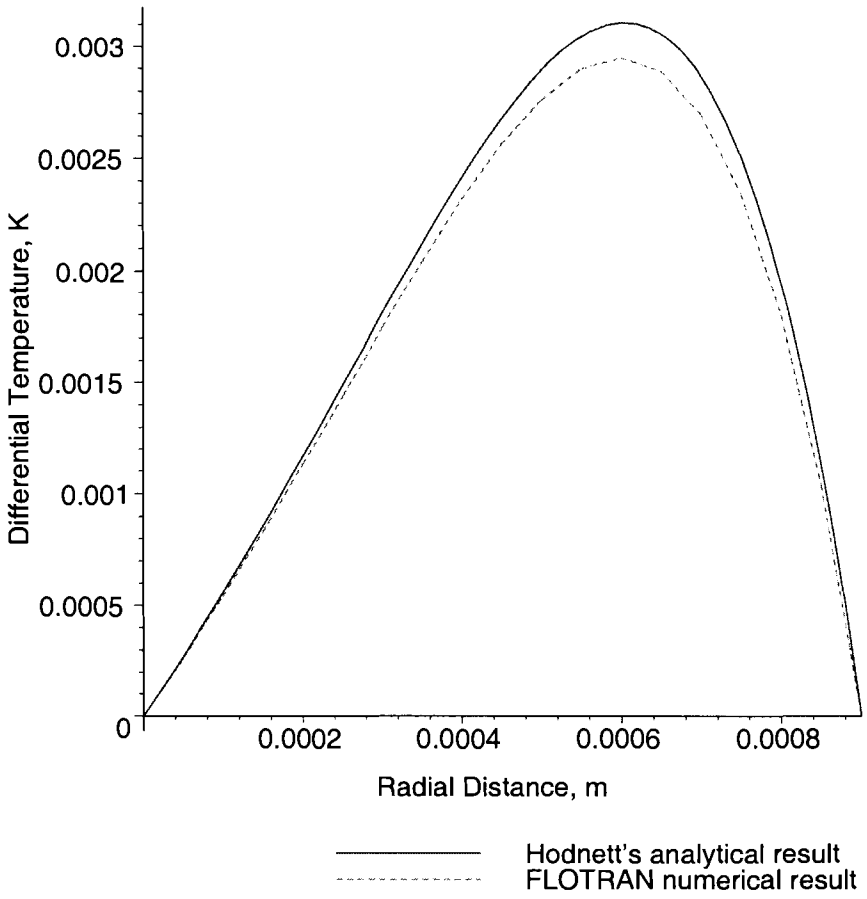

Figure 3 - 7 Dimensional differential temperature for concentric cylinders model Ra=0.001, Pr=0.7 and R=10, comparison between Hodnett's analytical and FLOTRAN numerical result

3 - 2.7 Limits to Validity

Mack and Bishop (1968) state that their analysis is valid for values of R between 1.15 and 4.15 for values of Ra limited by two equations:

For $E_1 \leq R \leq 4.15$

$$A_{lim} = E_2 + E_3 \times 10^{3-(\ln(R-1))/(\ln E_4)} \quad \textbf{(Eq 3 - 19)}$$

and for $1.15 \leq R \leq E_1$,

$$A_{lim} = \exp(E_5) R^{E_6} \quad \textbf{(Eq 3 - 20)}$$

where the constants $E_1 - E_6$, tabulated in Mack and Bishop (1968), are weak functions of the Prandtl number. Their solution is claimed to be accurate to within about 10% for values of Ra up to half A_{lim}.

Hodnett (1973) notes the necessity of establishing limits to the validity of (Eq 3 - 6) for higher values of R.

And if R, ratio of radii, is large, the limit of Rayleigh number scales as

$$Ra_{lim} \propto \log(R)/R^3 \quad \textbf{(Eq 3 - 21)}$$

Thus, the literature has offered us two criteria for the validity of (Eq 3 - 6): Mack and Bishop's for $1.15 \leq R \leq 4.15$, and Hodnett's for large R. In Section 3 - 2.8, these two criteria will be checked for consistency and compared with numerical solution.

3 - 2.8 Linearity Limits on *Ra*

As mentioned in Section 3 - 2.7 the literature offers two criteria for the validity of (Eq 3 - 6): Mack and Bishops' for $1.15 \leq R \leq 4.15$, and Hodnett's for large R. To see if these criteria are consistent, and to fill in the intermediate values of R, we conducted

numerical studies. We compared the predictions of (Eq 3 - 18) with a numerical solution for a range of values of R and of Ra and noted the "limiting Rayleigh number", that is the highest value of Ra for which the temperature difference between radially opposite points is predicted to within 5% accuracy by (Eq 3 - 18). The results are shown in Figure 3 - 8. We take the constant of proportionality in (Eq 3 - 21) to be 60.

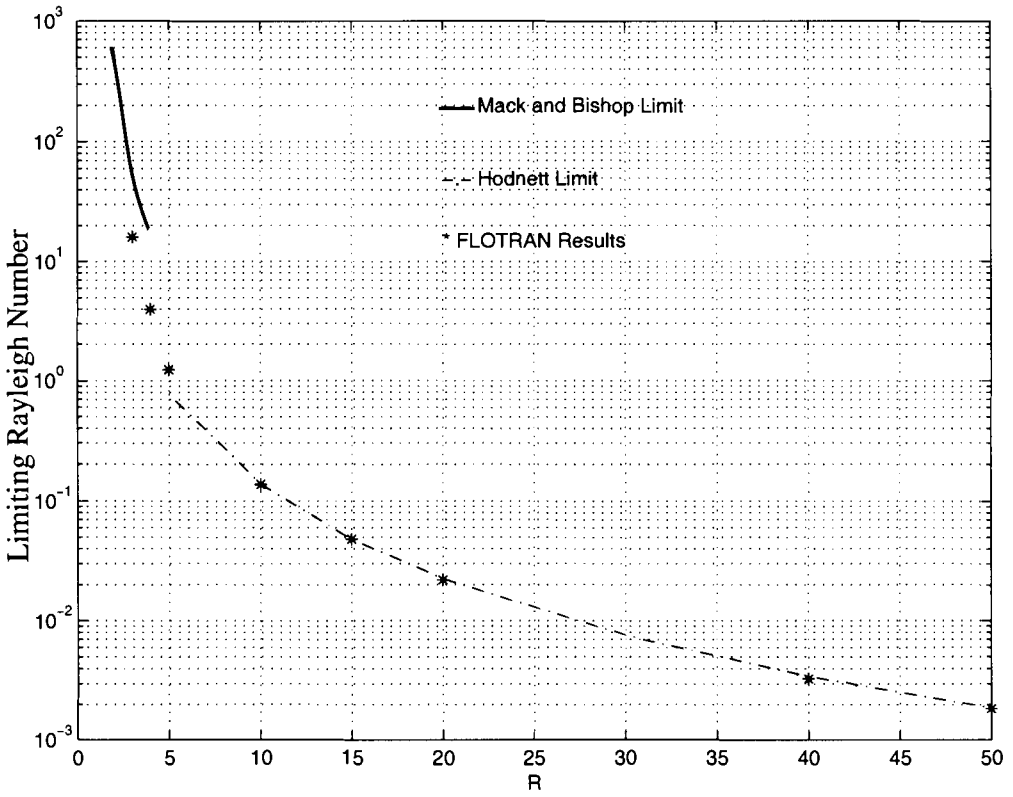

Figure 3 - 8 Linearity Limit on *Ra* as a function of *R*

This graph does not only show the limit of validity of Mack and Bishop's and Hodnett's results; it also shows the highest value of Ra for which the accelerometer signal is a linear function of acceleration, and hence establishes an upper bound on the accelerometer's operating range.

3 - 3 Conclusion

In this chapter, a CFD model of convective flow within the space enclosed by concentric cylinders has been constructed, based on the equations derived in Chapter 2. The internal consistency of this model has been established by careful mesh refinement, described in detail in Appendix III. The results of the FLOTRAN concentric-cylinders model for the steady-state case have been compared with the experimental results of Kuehn and Goldstein (1976) and the analytic results of Hodnett (1973), good qualitative agreement has been achieved with Kuehn and Goldstein's work and excellent quantitative agreement has been achieved with Hodnett's analytical solution. (Eq 3 - 18) is recommended as a guide to design work, Figure 3 - 8 establishes an upper bound on the operating range of the microthermal accelerometer.

Chapter 4 The Concentric-Cylinders Model: Transient Analysis

For microthermal accelerometer applications as discussed in Chapter 1, the response time of the accelerometer is an important performance parameter. This response time results from two factors: the time taken for the differential temperature to establish itself, and the time taken for the thermocouples to respond to this differential. In this chapter, we will study the transient behavior of the natural convective laminar flow within the space enclosed by concentric cylinders to determine correlations that can be used to predict the development of the temperature differential. To provide these correlations, we use the same FLOTRAN model developed in the previous chapter, but run it as a transient rather than as a static problem. We have again established internal consistency by mesh refinement studies, reported in Appendix III. We will then establish a formula for the thermocouple response time.

4 - 1 Transient Response Time

The problem of solving for response time differs from the transient case that has been studied in the prior literature in that the transient in the case of the accelerometer develops due to the suddenly imposed acceleration rather than the heating of one boundary surface. The transient case of sudden imposed heating of the inner surface in a pre-existing gravity field has been discussed in Kuebleck, Merker and Straub (1980), Castrejon and Spalding (1988), Tsui and Tremblay (1984), and Vafai and Ettefagh (1990). No prior researcher has discussed the transient case of interest to us. The correlations derived from the modeling can therefore not be validated against results from the literature, but will be compared with the results of the experimental work to be described in Chapter 5

"Experimental Studies".

We define the transient response time τ as the time required for the differential temperature to reach 63% of its steady-state value. It is shown by dimensional analysis in Chapter 2 that the transient development of the temperature difference is given by an expression of the form $F_o = f(Ra, Pr, R)$.

Possible working fluids for the microthermal accelerometer fall into three categories:

- low-Prandtl-number fluids, such as mercury;
- intermediate-Prandtl-number fluids, including air and other gases
- high-Prandtl-number fluids, such as oil.

FLOTRAN simulations of fluids with a range of Prandtl number show that the development of the fluid temperature field consists of two stages: development of the buoyancy-induced flow field, and the consequent development of a modified temperature field. For the low Rayleigh numbers of interest to us, the fluid temperature field differs by only a few percent from the original, pre-acceleration field, so the second-order effect of the changing temperature field on the velocity field is negligible.

The results of numerous simulations of fluids with different Prandtl numbers show that the relative time scales for the development of the velocity and temperature fields depend on Prandtl number. For fluids with Prandtl numbers much less than unity, the development of the velocity field is relatively slow compared with the development of the temperature field, while for fluids with Prandtl numbers much greater than unity, the velocity field develops very much more rapidly than the temperature field.

The latter case is illustrated in Figure 4 - 1, which shows the results of a simulation of convective laminar flow within space enclosed by concentric cylinders of inner radius of 100 microns and outer radius of 1000 microns.The imposed acceleration was 10 m/s^2,

and the fluid properties were as shown in Table 4 - 1. Note that *any* high-Prandtl-number fluid would give results similar to those shown in Figure 4 - 1; this particular fluid is just used as an illustration.

Table 4 - 1 Fluid properties of a high-Prandtl-number fluid, *Pr*=15.6

k	μ	ρ	c	β	Pr
W/mK	$Pa \cdot s$	kg/m^3	$J/(kg \cdot K)$	K^{-1}	
2.574×10^{-2}	4.0×10^{-4}	1.1768	1.004×10^3	0.0033	15.6

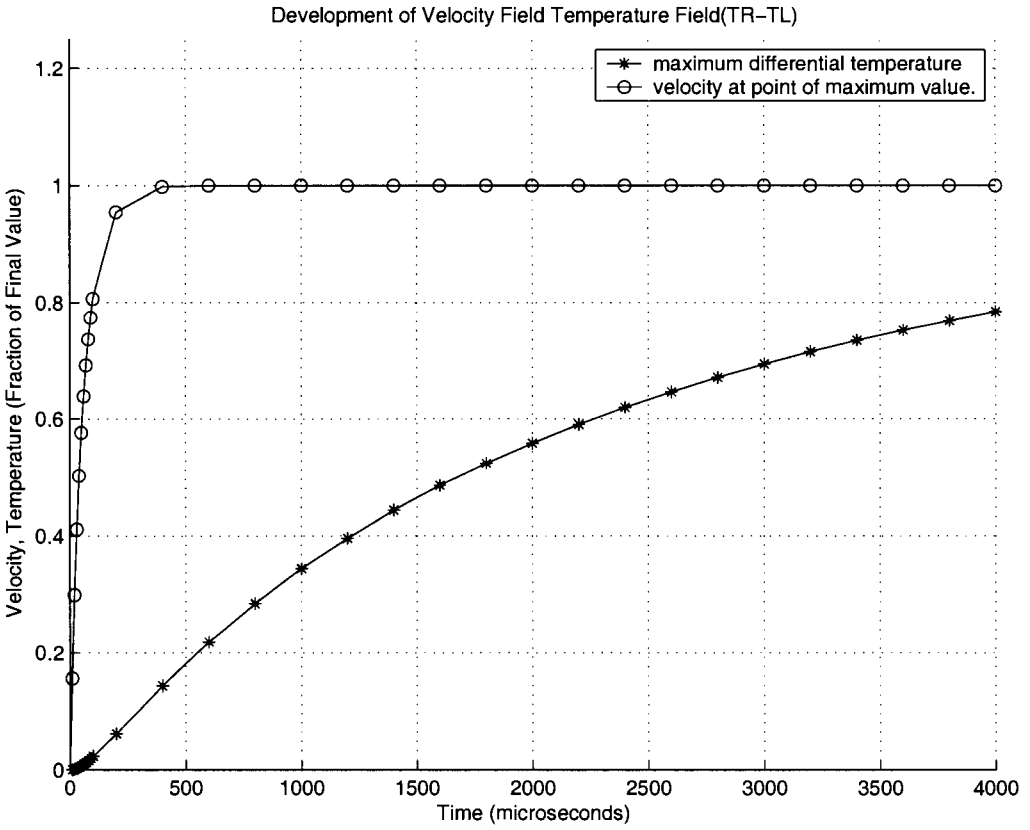

Figure 4 - 1 Development of velocity and temperature fields for concentric cylinders model, *Pr*=15.6 and *R*=10

In Figure 4 - 1, the development of fluid velocity has been shown as a function of time and as a fraction of maximum velocity in the direction parallel to the imposed

acceleration. The velocity reaches 63% of its final, steady state, value in approximately 59 microseconds, and the differential temperature reaches 63% of its steady state value in approximately 2500 microseconds.

For comparison, the development of velocity and temperature field of the fluid of air, of which Prandtl number is 0.7, has been shown in Figure 4 - 1. The imposed acceleration was 10 m/s^2. The fluid properties of air, were as shown in Table 4 - 2.

Table 4 - 2 Fluid properties of air, *Pr*=0.7

k	μ	ρ	c	β	Pr
W/mK	$Pa \cdot s$	kg/m^3	$J/(kg \cdot K)$	K^{-1}	
2.574×10^{-2}	18.53×10^{-6}	1.1768	1.004×10^3	0.0033	0.7

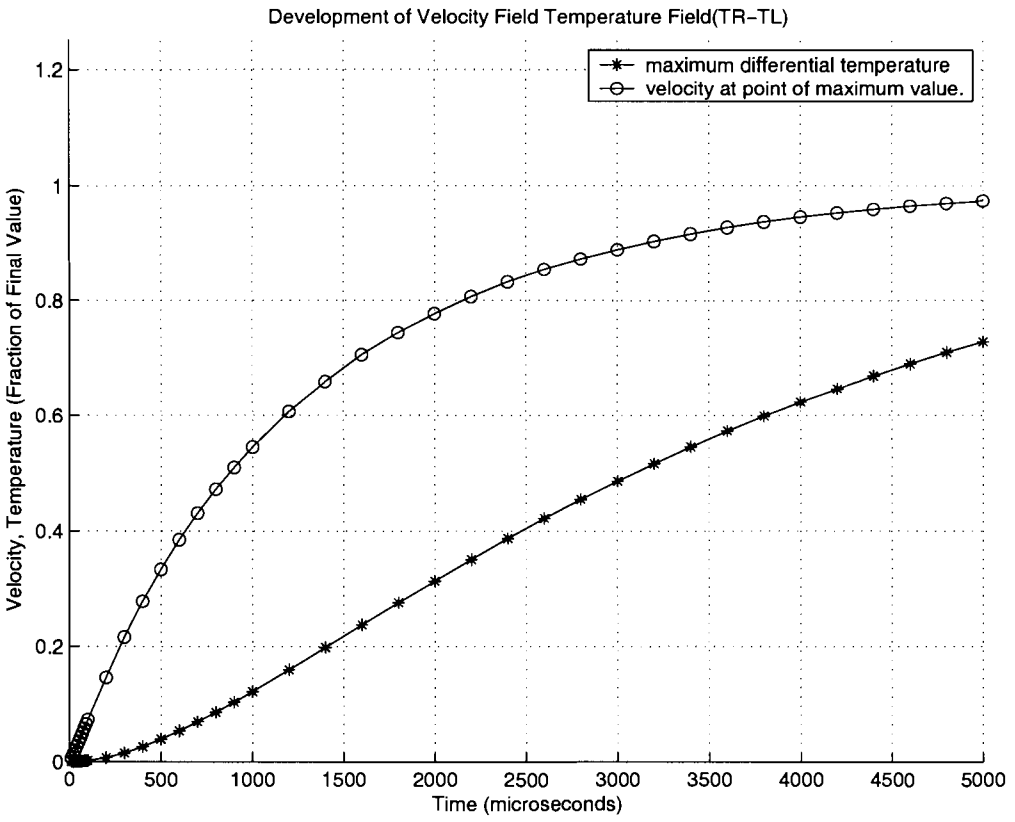

Figure 4 - 2 Development of velocity and temperature fields for concentric cylinders model, *Pr*=0.7 and *R*=10

In Figure 4 - 1, for a fluid of air, Prandtl number is 0.7, the development of fluid velocity has been shown as a function of time and as a fraction of maximum velocity in the direction parallel to the imposed acceleration. The velocity reaches 63% of its final, steady state, value in approximately 1354 microseconds, much longer than the previous case of high-Prandtl-number fluid of 15.6, and the differential temperature reaches 63% of its steady state value in approximately 4055 microseconds.

Furthermore, for the fluids, of which the Prandtl number is much less than unity, the development of velocity would experience a even longer time than that of fluid of air, consequently followed by much quicker development of its temperature field.

We deduce from these figures, and from the large number of other simulations performed, that the main determinant of the time taken for the differential temperature to reach its final value is, for low-Prandtl-number fluids, the establishing of the buoyancy-induced flow field; and, for high-Prandtl-number fluids, the establishing of the temperature field resulting from the buoyancy-induced flow. For intermediate-Prandtl-number fluids, such as air, the two processes overlap, and both contribute to the overall response time.

FLOTRAN simulation also shows that the response time does not appear to be a function of Ra, at least within the range of values of interest to us. However, it is a function of R, the ratio of the radii of inner and outer cylinders. In order to be able to predict the response time for any fluid, therefore, we need three correlations, giving F_o as a function of R and Pr for high-, low-, and intermediate-Prandtl number fluids.

(In prior literature, the Fourier number is often defined in terms of radius of inner cylinders: $F_o = \tau\alpha/r_i^2$. However, FLOTRAN simulation shows that the response is more strongly determined by the radius of the outer cylinder than that of inner cylinder. Therefore, in this thesis, the Fourier number is defined based on the radius of the outer cylinder, which is also called the effective Fourier number $F_o/R^2 = (\tau\alpha)/r_o^2$)

4 - 2 Empirical Correlations

4 - 2.1 Empirical Correlations: High Prandtl Number

A series of FLOTRAN simulation shows that F_o/R^2 varies with R as shown in Figure 4 - 3.

This graph can be approximated by the function

$$F_o/R^2 = \exp\left(-2.234524 - \frac{2.410128}{R} - 0.185096\ln(R)\right) \qquad \textbf{(Eq 4 - 1)}$$

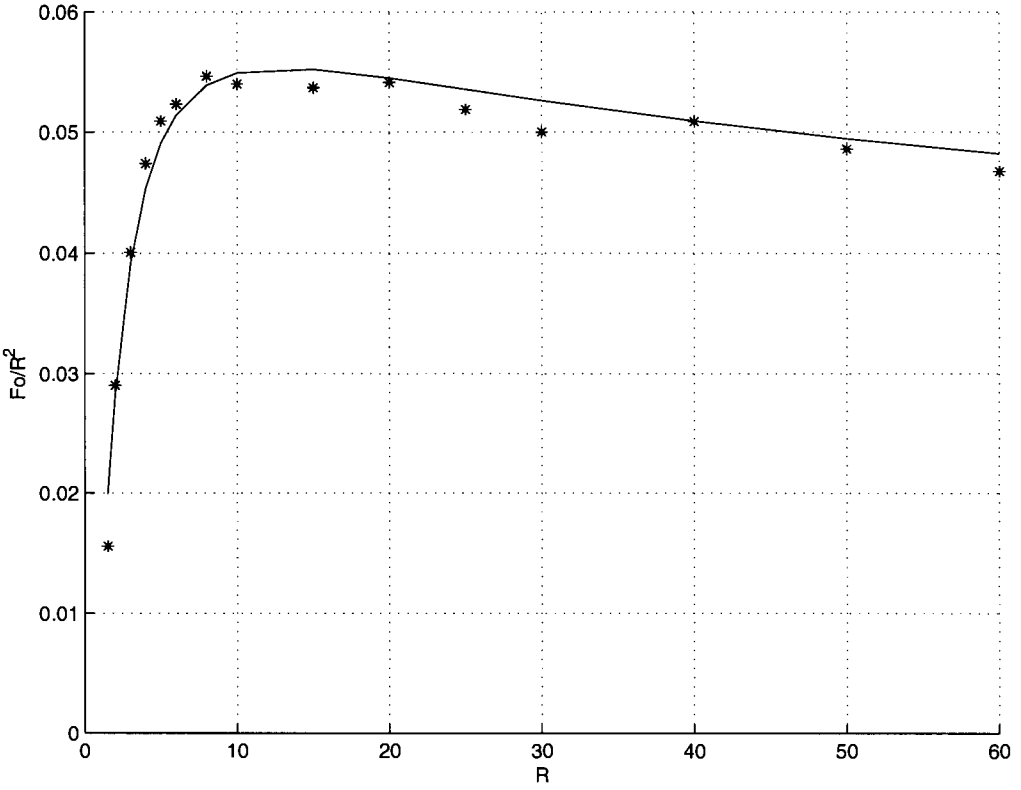

Figure 4 - 3 F_o/R^2 versus R, high-Prandtl-number fluids, concentric cylinders case

4 - 2.2 Empirical Correlations: Low-Prandtl-Number

A series of FLOTRAN simulations shows that the product $F_o Pr/R^2$ varies with R as shown in Figure 4 - 4.

This graph can be approximated by the function

$$F_o Pr/R^2 = \exp\left(-3.716597 - \frac{2.618219}{R} + 0.025842\ln(R)\right) \qquad \textbf{(Eq 4 - 2)}$$

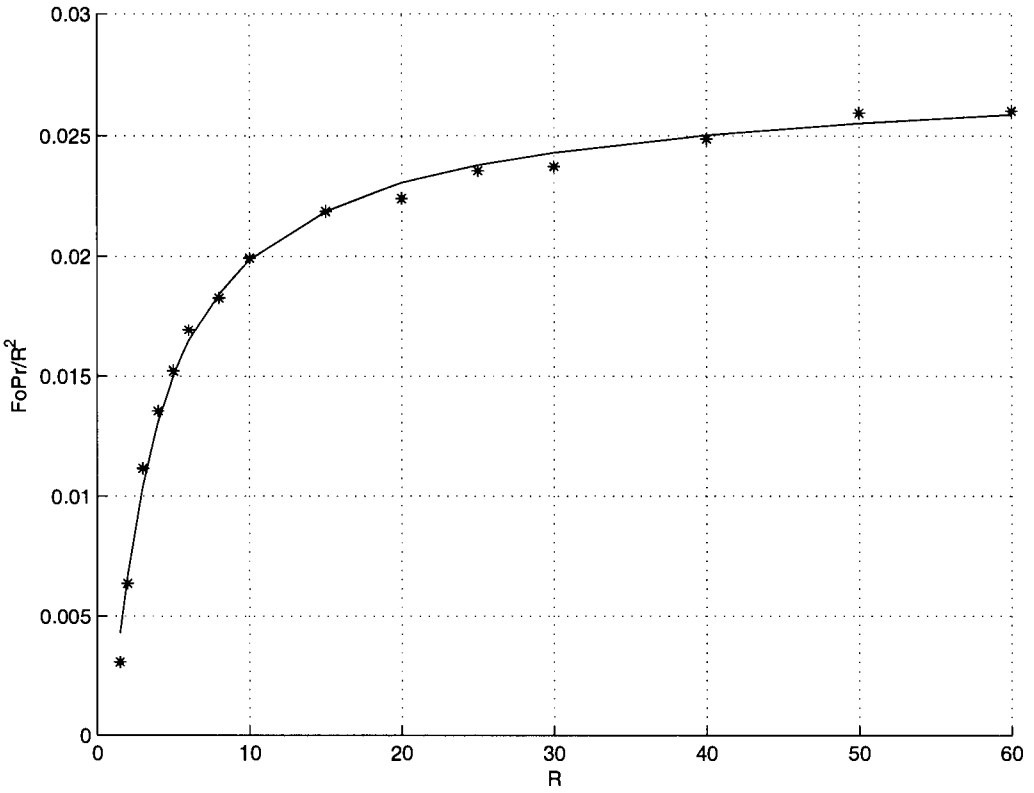

Figure 4 - 4 $F_o Pr/R^2$ versus R, low-Prandtl-number fluids, concentric cylinders case

4 - 2.3 Empirical Correlations: Intermediate-Prandtl-Number

A series of simulations was carried out representing the working fluid as having a Prandtl number of 0.7, leading to the relationship between F_o/R^2 and R shown in Figure 4 - 5

This graph can be approximated by the function

$$F_o/R^2 = \exp\left(-1.91326 - \frac{2.69773}{R} - 0.09997\ln(R)\right) \qquad \textbf{(Eq 4 - 3)}$$

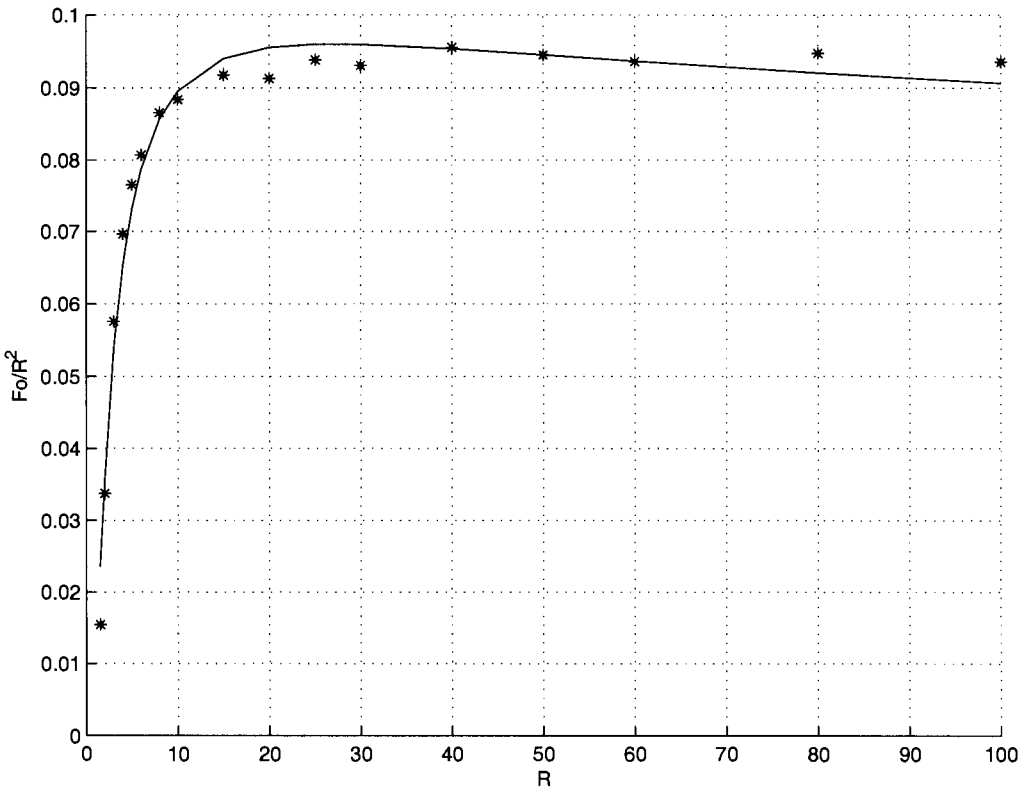

Figure 4 - 5 F_o/R^2 versus R, intermediate-Prandtl-number fluids, Pr=0.7, concentric cylinders case

4 - 3 Accelerometer Response Time

The response time of a microthermal accelerometer results from two factors: the time taken for the differential temperature to establish itself, and the time taken for the thermocouples to respond to this differential. In this section, we will calculate typical values of both response times, to show which dominates.

4 - 3.1 Thermal Response Time

From the empirical correlation obtained from previous section, we can deduce the thermal response time: the time taken for the differential temperature to establish itself. We will look at the two working fluid to be investigated in Chapter 5, air and isopropanol.

Air is an intermediate-Prandtl-number fluid ($Pr = 0.7$), so from Figure 4 - 5, F_o/R^2 takes the value 0.095 for $R = 50$. For air $\alpha = 0.22 \times 10^{-4}\,\mathrm{m^2/s}$, and $r_o = 0.001$ m. So $\tau_{air} = 4.3$ milliseconds.

Isopropanol is a high-Prandtl-number fluid ($Pr = 36.3$), so from Figure 4 - 3, for $R = 50$, F_o/R^2 is about 0.05. For isopropanol, $\alpha = 0.9 \times 10^{-7}\,\mathrm{m^2/s}$. So $\tau_{iso} = 0.5$ seconds.

4 - 3.2 Response Time of Thermocouples

The response time for a thermocouple is determined by (Incropera, DeWitt, 1996)

$$\tau_c = \frac{\rho_c V_c c_c}{h A_c} \qquad \textbf{(Eq 4 - 4)}$$

where ρ_c is the density of the thermocouple material, V_c its volume, c_c its specific heat, A_c its area, and h the convective heat transfer coefficient, which can be

calculated from Nusselt number Nu by its definition.

Here Nusselt number Nu is defined as $Nu = hd_c/k_f$, where h is the heat transfer coefficient for convection to be sought, d_c is the diameter of thermocouple, and k_f is the thermal conductivity of the fluid at the "film" temperature $T_f = (T_m + T_a)/2$. T_m is the mean thermocouple cylinder temperature, and T_a is the ambient temperature of the fluid. The physical interpretation of Nusselt number is ratio of convective heat transfer to conduction.

h should be calculated from the Nusselt number obtained from Kramers' correlation, (Kramers, 1946),

$$Nu = 0.42(Pr)^{0.26} + 0.57(Pr)^{0.53}(Re)^{0.5} \quad \textbf{(Eq 4 - 5)}$$

Here, Re is the Reynolds number, defined as $Re = \frac{\rho_f v_f d_c}{\mu_f}$. The physical interpretation of Reynolds number is the ratio of inertial to viscous force. ρ_f is the fluid density, v_f is the free stream velocity, and u_f is the fluid viscosity. Pr is Prandtl number.

The velocity of the fluid is estimated from FLOTRAN simulation at 10^{-3} m/s.

For the accelerometer chip, the thermocouples used in this chip consist of metal film contained in strips of silicon approximately $3\mu m$ by $20\mu m$. If air is used as fluid, the calculated τ_c for these detectors is of the order of 2 milliseconds. If a liquid, such as isopropanol, is used as working fluid, the calculated τ_c for these detectors is reduced to the order of sub milliseconds.

The total response time of the accelerometer will be the sum of the thermal response time and the response time of thermocouples. Therefore, for the air-filled accelerometer, the thermal response time and thermocouple response time both contribute comparably to the overall response time. Whereas for liquid-filled accelerometer chip, the thermocouple response time can be neglected, and the thermal response time dominates.

4 - 4 Conclusion

In this chapter, the CFD model of convective flow within the space enclosed by concentric cylinders that was constructed and validated in Chapter 3 "The Concentric-Cylinders Model: Steady-State Analysis" has been extended to model the transient following the application of an acceleration. The results of this modeling have been used to derive correlations between response time, fluid properties and device geometry. Overall response time has been estimated based on these correlation results for air and isopropanol used as working fluid and on the response time of the thermocouples used to measure the differential temperature. It has been shown that the thermocouple response time contributes significantly to the overall response time of the air-filled accelerometer chip, but made a negligible contribution to the response time for the alcohol-filled chip. The correlations derived in this chapter will be used in Chapter 5 "Experimental Studies" and Chapter 8 "Size Limitations, Design Implications, and Future Work" to predict the effect of the choice of working fluid on response time.

Chapter 5 Experimental Studies

The current prototype microthermal accelerometer uses air as working fluid. The basic structure and the operational principle has been presented in Section 1 - 2. In this thesis, we tested air and isopropanol as working fluids. The purpose of using a liquid, such as isopropanol, as the working fluid is to increase the signal level. The output signal from the air-filled accelerometer is at 100 microvolts level; the formulas and simulation results, discussed in Chapter 3 "The Concentric-Cylinders Model: Steady-State Analysis", suggest that by using a liquid as the working fluid, for example, isopropanol, because of its higher density, theoretically the signal output can be increased by several hundred times.

Experiments have been carried out using isopropanol as the working fluid. First, we constructed a liquid-filled microthermal accelerometer based on a supplied prototype air-filled accelerometer, then an amplification circuit was built to amplify the output signal for both air-filled and liquid-filled types. Steady state response was then done by measuring the chip's response to gravity change, finally dynamic response was measured by testing the chip on a vibration table.

5 - 1 Construction of Liquid-Filled Accelerometer

5 - 1.1 Prototype Air-Filled Accelerometer

The MEMSIC corporation supplied us with a number of accelerometer chips designed for use with air as a working fluid. The photograph of a supplied microthermal accelerometer has been shown in Figure 1 - 5. A sketch of cross-section of one of these chips is shown in Figure 5 - 1. The cavity is 970 microns across in the direction parallel

to the heater, and 915 microns across in the orthogonal direction. Eight (T09W03 or T21W03 series) or eleven (T06W03 or T18W03 series) pairs of thermocouples are symmetrically positioned to either side of the heater bridge, which is 20.6 microns wide and 3 microns deep. The depth of the etched cavity below the plane of the heater and detectors was 230 microns. The cavity was unsealed above the plane, but was covered by a metal cap giving about 1000 microns clearance above the heater plane.

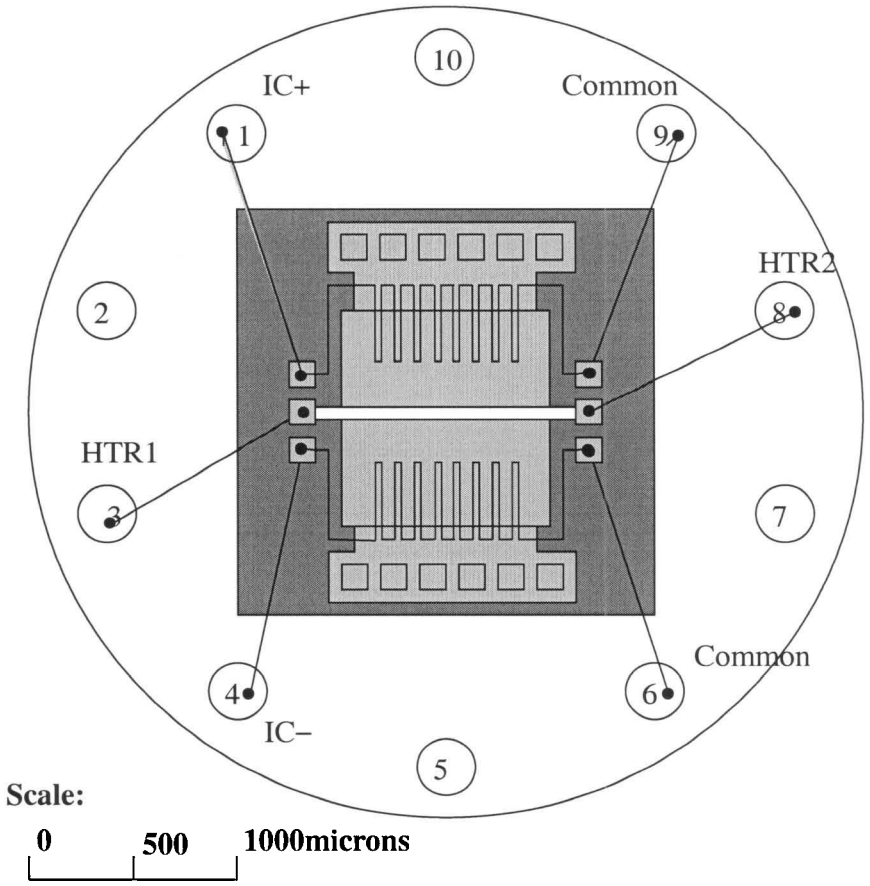

Figure 5 - 1 A sketch of cross-section of a prototype air-filled accelerometer

5 - 1.2 Operation of Prototype Air-Filled Accelerometer

This prototype microthermal accelerometer chip was contained in a ten-pin-can package as shown in Figure 5 - 1. Six out of ten pins are in use. Pin 3 (HTR1) and Pin 8

(HTR2) are connected to the heater. Pin 1 (IC+) and Pin 9 (common ground) are two terminals for upper group of thermocouples, and Pin 4 (IC-) and Pin 6 (common ground) are two terminals for lower group of thermocouples.

To measure the acceleration in the direction perpendicular to the long axis of the heater, the chip was supplied with power of 5 to 10 mW between HTR1 and HTR2, common mode signals can be measured between IC+ and ground, as well as between IC- and ground. The desired differential signal can be measured between IC+ and IC-. For the air-filled accelerometer supplied with 5 volts, the differential signal in response to a 1 g acceleration of a bare chip without amplification circuitry is approximately 200 microvolt for T09W03, T21W03 series and 100 microvolt for T06W03, T18W03 series as listed in Table 5 - 1. Acceleration can be deduced from the differential signal measured. Meanwhile, the approximate values of common mode signal of each series are also listed, from which we can deduce the average temperature at the detectors by characteristic of the detector with temperature.

Table 5 - 1 Response of bare chip to 1 g acceleration change

Accelerometer Series	Differential signal millivolt	Common mode signal millivolt
T09W03	0.2	90
T21W03	0.2	90
T06W03	0.1	50
T18W03	0.1	50

5 - 1.3 Amplification Circuit

The differential signal generated by the thermocouples for 1-g acceleration was of the order of 100 microvolts for the air-filled chip. Such a small signal is rather difficult to

measure using regular devices such as digital multimeter and oscilloscope. Hence, it was necessary to construct an amplification circuit.

Knowing that our input differential signal is at 100 microvolts level, while common mode signals are at the 50 to 100 millivolts level, the requirements of the amplification circuit are quite high; to list a few, it requires high gain at 1000, to increase differential signal from 100 microvolts to 100 millivolts; high common mode rejection; low noise, low offset; and a matched high input impedance.

Therefore we use a high quality instrumentation amplifier for its desirable features such as high AC (DC) common-mode rejection, low offset voltage and offset voltage drift, a matched, high-input impedance, low input bias, low noise, and low nonlinearity. It was found more effective to use an instrumental amplifier to amplify microvolt-level signal while simultaneously rejecting volts of common-mode at its inputs. (Kitchin and Counts, Analog Devices, Inc., 2000)

We hence constructed a two-stage amplifier circuit using instrumentation amplifiers AD620 and AD625 as shown in Figure 5 - 2. First stage of AD620 achieves gain of 10, and second stage of AD625 achieves gain of 100, for a total gain of 1000. Meanwhile, the amplification circuit was designed in such a way that each stage of amplification could be used independently, to provide a gain of 10 or 100. For the value of gain resistors, refer the data sheets of AD620 and AD625 (Analog Device, Inc. 2003).

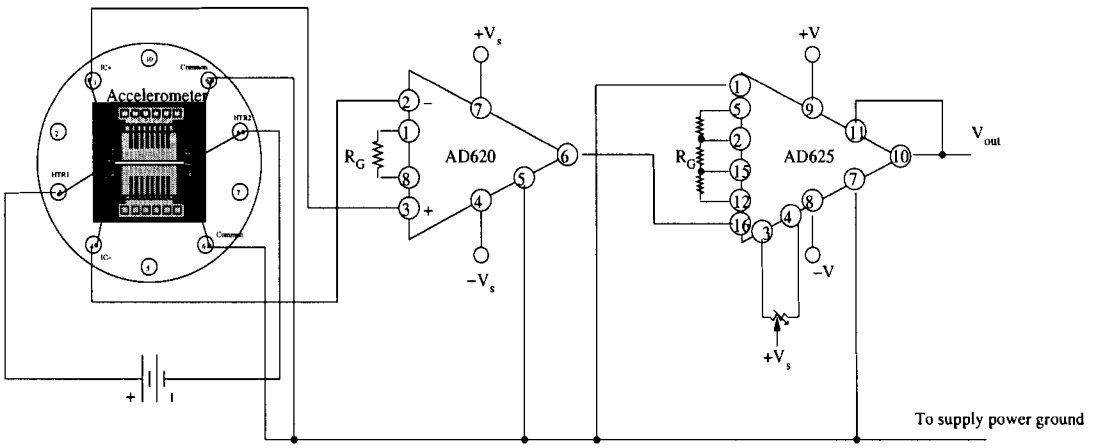

Figure 5 - 2 Diagram of amplification circuit

5 - 1.4 Noise

One important issue in building amplification circuits is handling the noise problem. There are many sources of noise in the environment, specifically light source at 60Hz, high-frequency noise at 50MHz and other random triggered noise. With such high gain of amplification circuit, noise can be easily picked up and amplified and then overwhelm the signal. Without proper handling of the noise problem, the circuit will not work.

To reduce interference, the amplification circuit and accelerometer first needed to be properly grounded; coaxial cables were used to connect the differential signal from sensor to the amplifiers and output signal to oscilloscope; more important, the whole circuitry which includes the accelerometer sensor and amplification circuit was carefully shielded by a metal box from noise, as shown in Figure 5 - 3

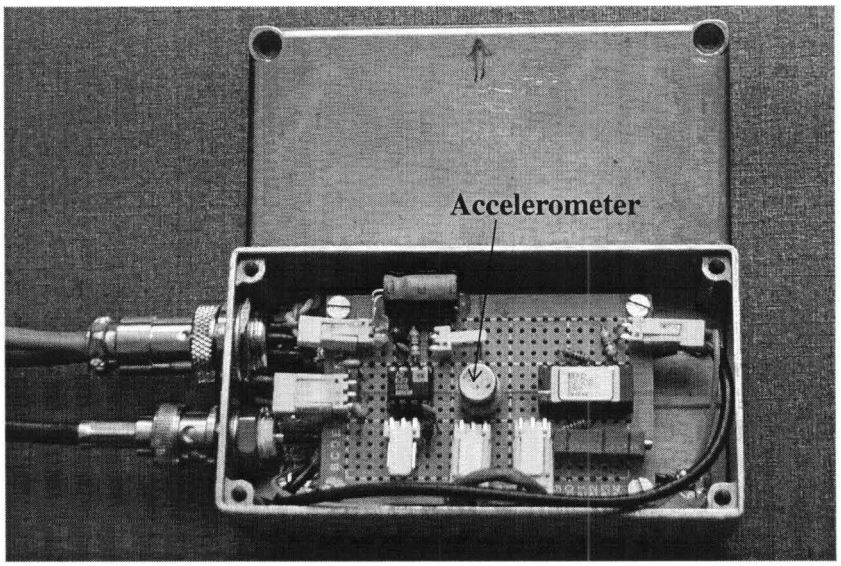

Figure 5 - 3 Accelerometer circuitry encapsulated by a metal box

5 - 1.5 Construction of Fluid-filled Accelerometer

After removing the chip's metal cap, we found it relatively straightforward to fill the chip cavity with isopropanol, using a fine syringe. Microscopic inspection of the chip with this operation didn't detect any bubbles of trapped air. The cap was then separately filled with isopropanol and placed over the chip. While not vapor-proof, this arrangement was found adequate to keep the chip charged with isopropanol for about 24 hours. For liquid-filled accelerometer, the gain of amplification circuit was selected at 100.

5 - 1.6 Temperature Characteristics of the Heater of the Accelerometer

In analyzing the effect of filling an accelerometer with fluid, we would like to know the temperature characteristics of the heater of the accelerometer; for example, the

temperature difference between detectors, and the temperature of the heater.

To allow us to determine the temperature at the heater during operation, we placed the chip in an environmental chamber and heated it by stages from 20°C to 100°C, measuring the resistance of the heater at each stage. As shown in Figure 5 - 4, the resistance changes versus temperature for chip T060304, the change can be well-fitted with a straight line.

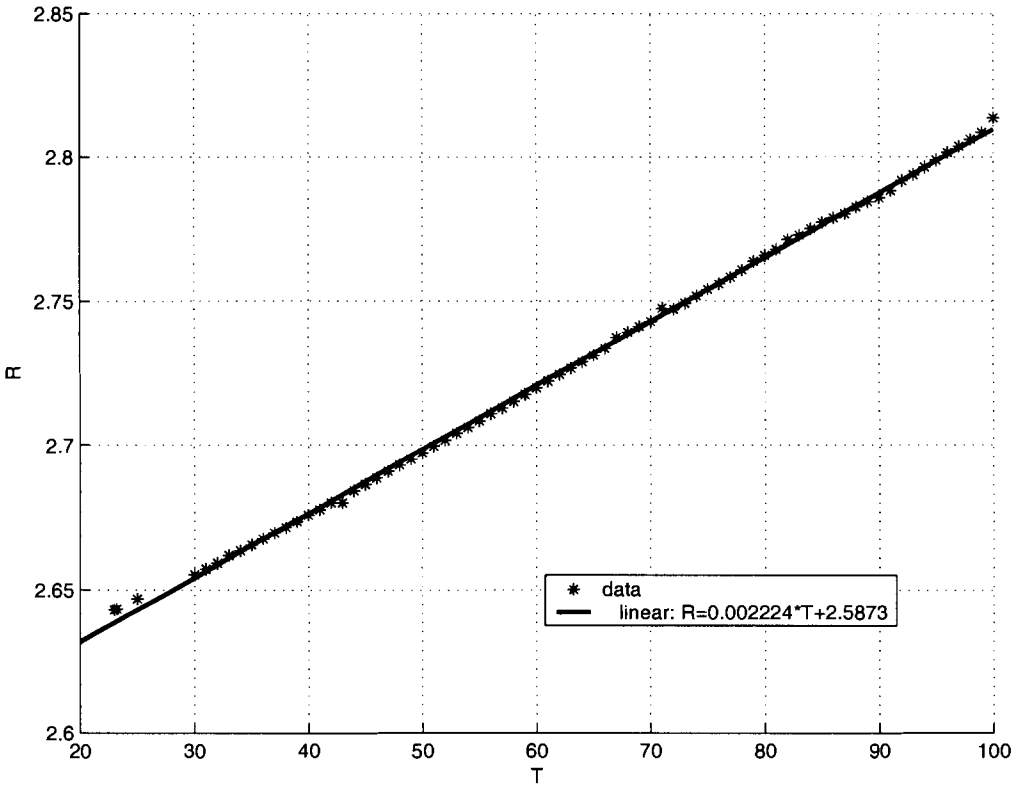

Figure 5 - 4 Resistance of heater vs. temperature

From the relationship between resistance and temperature, the temperature of the heater can be estimated.

5 - 2 Steady-State Response

5 - 2.1 Steady-State Response of Air-Filled Accelerometer Chip

We took an air-filled chip and increased the voltage across the heater by stages, from 0 to 5 volt. The heater temperature was estimated at each stage by measuring its electrical resistance, as shown in Table 5 - 2; for example, a voltage of 5V corresponded to an average heater temperature of 143°C, and the steady-state response to 1 g acceleration change was about 100 mV after 1000 times amplification.

Table 5 - 2 Heater resistance vs. voltage across for air-filled accelerometer

Voltage across (Volt)	Current measured (mA)	Heat Power mW	Resistance calculated KΩ	Temperature Estimated °C	Response to 1g (amp=1000) mV
0.5	0.189	0.0945	2.6455	26.5	0
1	0.374	0.3740	2.6738	39.3	0
1.5	0.559	0.8385	2.6834	43.7	1
2	0.741	1.4820	2.6991	50.8	3
2.5	0.921	2.3025	2.7144	57.8	9
3	1.093	3.2790	2.7447	71.6	19
3.5	1.258	4.4030	2.7822	88.6	34
4	1.419	5.6760	2.8189	105.3	49
4.5	1.575	7.0875	2.8571	122.7	74
5	1.723	8.6150	2.9019	143.0	108

5 - 2.1.1 Sensitivity of Air-filled Accelerometer

The maximum differential temperature measured by the accelerometer at a given

radial position was predicted in Section 3 - 2.5.1 to be:

$$\frac{\delta T}{T_o} = 2R_a \varepsilon f_3(r) \qquad \textbf{(Eq 5 - 1)}$$

where

$$\varepsilon = (T_i - T_o)/T_o \qquad \textbf{(Eq 5 - 2)}$$

hence

$$\delta T = 2\Delta T R_a f_3(r) \qquad \textbf{(Eq 5 - 3)}$$

where

$$\Delta T = T_i - T_o \qquad \textbf{(Eq 5 - 4)}$$

where $f_3(r)$ is defined as in (Eq 3 - 9).

(Eq 5 - 3) implies that the sensitivity of the air-filled accelerometer, which is directly proportional to δT, increases as $(\Delta T)^2$, since Ra includes a second ΔT factor, and hence as the square of the power supplied. However, in Figure 7 of (Leung, Jones, Czyzewska, Chen, and Pascal, 1997) and in this experiment, see Table 5 - 2, we see an approximately linear increase in device sensitivity with heater power, as shown in Figure 5 - 5. This apparent contradiction can be resolved by noting the increase in heater power leads to an increase in the mean temperature T of the contained air. From the tabulated properties of air over the relevant temperature range, we find that the product $(c\beta)/(\mu k)$ and hence Ra, is proportional to $1/T^{2.67}$. Including this in (Eq 5 - 3), modifies the dependence of δT on power to an approximately linear relationship, consistent with experiment. This is illustrated by plotting column 3 versus column 6 in Table 5 - 2, graphed in Figure 5 - 5.

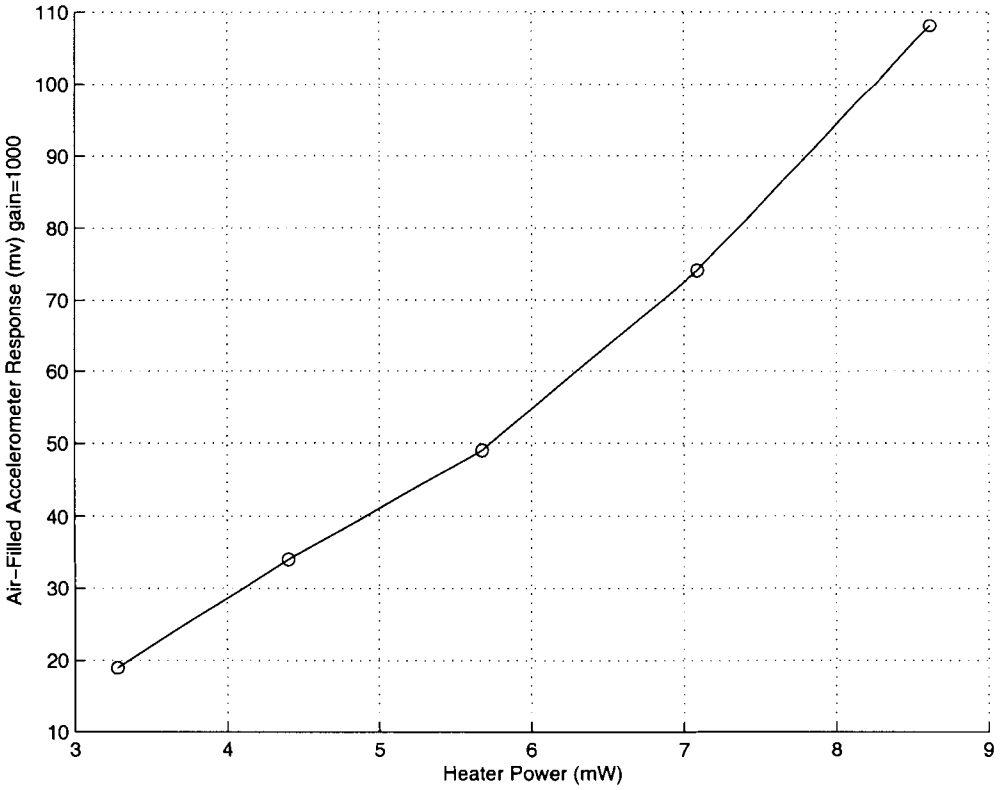

Figure 5 - 5 Air-filled accelerometer sensitivity with heater power

5 - 2.1.2 Linearity Test of Air-filled Accelerometer

Measuring the amplified differential signal from the detectors (gain=1000) as the imposed acceleration was gradually increased from -1g to 1 g confirmed that this signal increased linearly with acceleration as shown in Figure 5 - 6.

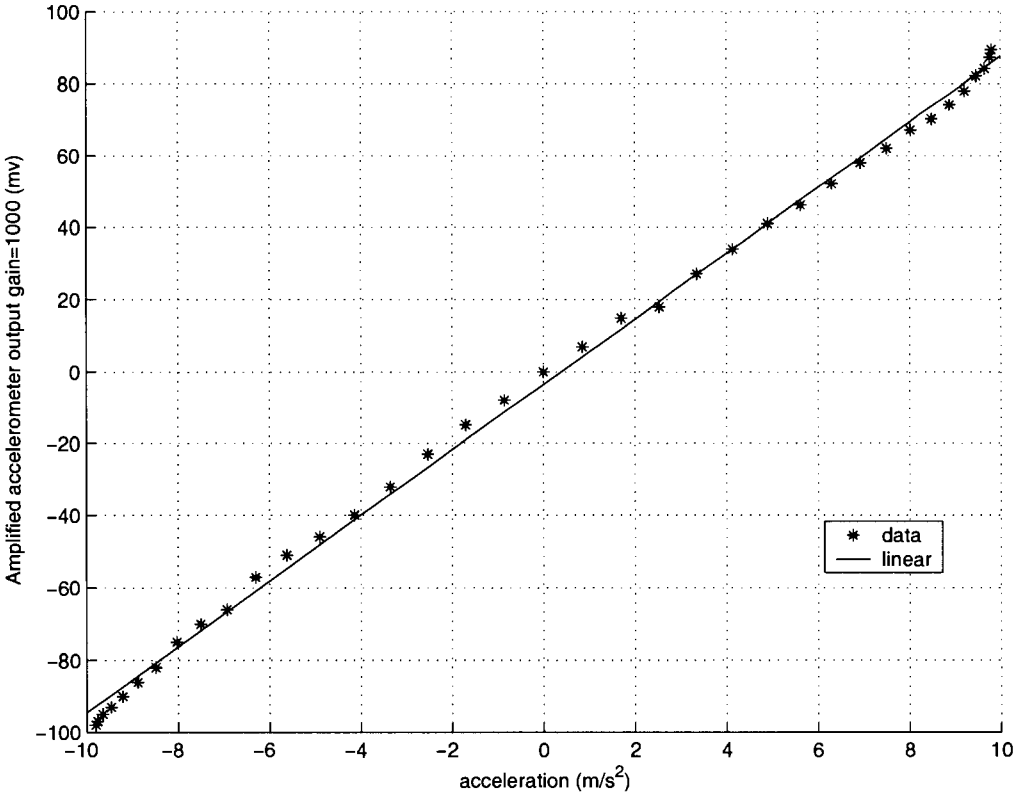

Figure 5 - 6 Linearity test of air-filled accelerometer, output signal amplified with gain=1000.

5 - 2.2 Steady-State Response of Liquid-Filled Accelerometer Chip

5 - 2.2.1 Measurement of Heater Resistance Versus Voltage Applied

A gradually increasing voltage was then put across the heater of the same chip filled with isopropanol. Due to the greater thermal conductivity of isopropanol, the heater temperature corresponding to a given voltage was lower than for the air-filled chip: a voltage of 5V corresponded to an average heater temperature of 59.8 °C , as listed in Table

5 - 3.

Table 5 - 3 Heater resistance vs. voltage across for liquid-filled accelerometer

Voltage across (Volt)	Current measured (mA)	Heat Power mW	Resistance calculated KΩ	Temperature Estimated °C	Response to 1g (amp=100) mV
3	1.122	3.366	2.6738	39.3	90
4	1.484	5.936	2.6954	49.1	280
5	1.839	9.195	2.7189	59.8	630
6	2.18	13.08	2.7523	75.0	1320
7	2.52	17.64	2.7778	86.6	2090
8	2.84	22.72	2.8169	104.4	2990
9	3.15	28.35	2.8571	122.7	4170
10	3.44	34.4	2.9070	145.3	5360

5 - 2.2.2 Microscope Observation During Operation

A close observation has been made under microscope for the liquid-filled accelerometer chip powered with gradually increasing voltage.

First, the cavity of the chip was filled with isopropanol, and then power supply was applied with the voltage increasing in the range from 1V to 10 V, the bare chip is observed under microscope without metal cap.

Our detailed observations were that:

- From 1 V to 5 V, it can be observed that the liquid stays quite stable on the top of cavity and around the heater bridge; no obvious drying can be observed and no obvious bubble appears.

- At 6 V, one or two bubbles start to appear; liquid gets thinner around heater bridge after a while; when we switch power on and off, we can observe the bubble moves, but spherical liquid body does not move much.
- At 7 V, we can observe bubble stably appear above the heater and as we switch the power on and off we could observe movements of liquid body, liquid obviously gets thinner as power is on and start to dry up.
- At 8 V, a steady bubble appears on the top of the heater and enlarges and creates a stable cavity around heater, which persists even after turning off the power, the bubble may burst and liquid start to dry up quickly. After refilling with liquid, a new bubble appears soon and form a big one again around the heater.
- At 9 V, as soon as we refill, the liquid gets thinner, and steady bubbles appear around heater, enlarge until blow and dry.
- At 10 V, obvious boiling of the liquid occurs. First of all, right after filling with the liquid, and before applying the power, because of the liquid surface tension, there existed a half sphere of liquid over the upper part of cavity. As soon as power was applied, this spherical body of liquid started shaking, a few bubbles appear right on the top of the heater bridge, and then combine as a bigger bubble forms around the heater, and expands, eventually bursting, then liquid get thinner, eventually, cavity dry up.

The above observations can be explained as follow:

- When liquid is heated up by the power supplied to the heater, as the supplied voltage is increased from 1 to 5 V, the liquid stays safely below boiling point, (82 °C for isopropanol). Hence no movement of liquid can be observed at this stage. This can also be verified by the temperature estimated by measuring the resistance as shown in Table 5 - 3.

- As the voltage is increased from 6 V to 7 V, the liquid is heated up close to the boiling point, hence we start to observe bubble appearing.
- As the voltage is increased to 7 V and above, the liquid is soon heated up to boiling, hence, we observe obvious bubbles, and the liquid dry up.

It can also be concluded from the above observations and measurements, for this liquid-filled accelerometer, to avoid the liquid being boiled, we should carefully chose the applied voltage below 6 V, for a more repeatable and reliable operation. Alternatively, the chip could be sealed and allowed to increase in internal pressure.

5 - 2.2.3 Linearity Test

By gradually tilting the accelerometer from the horizontal to a vertical plane, a linearity test for accelerometer chip filled with liquid was also performed at each applied voltage from 1 V to 10 V. The accelerometer signal was amplified 100 times and measured by the digital multimeter, in the meantime, the signal was monitored by the oscilloscope. For supplied voltage to the heater of 1 V, the signal output doesn't change much with the increment of acceleration, while the signal output can't be measured stably at above 7 V supplied voltage due to the frequent ripples in the signal, which can be observed in the oscilloscope. As suggested by the previous observations under microscope and estimated temperature after supplied voltage increased to 7 V and above, these ripples are caused by the heating of the working fluid above the boiling point as bubbles form in the boiling liquid. In the next figure, we present the linearity test of accelerometer chip filled with liquid with supplied voltage at 3 V, 4 V, 5 V, and 6 V.

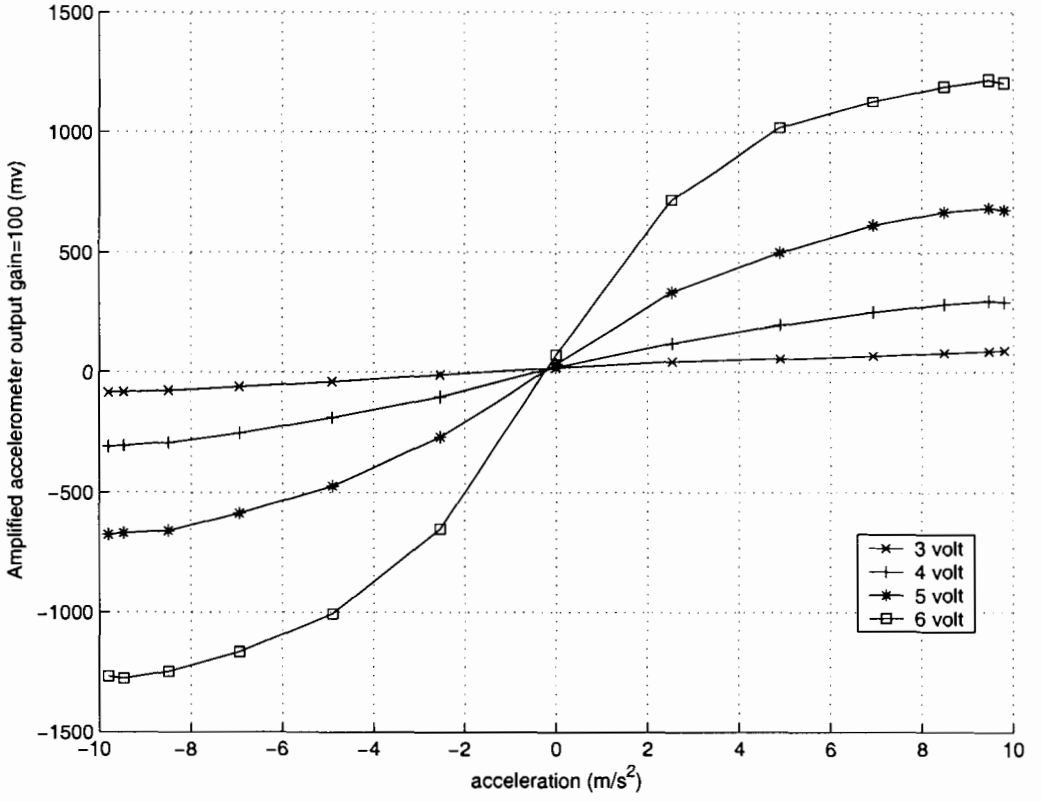

Figure 5 - 7 Linearity test of liquid-filled accelerometer, output signal amplified with gain=100.

It can be observed that as the supplied voltage increases, the response to the acceleration becomes nonlinear.

According to (Eq 5 - 3), the differential temperature between the detectors at a given acceleration should be proportional to $(\Delta T)^2$. This can be confirmed by plotting column 3 versus column 6 in Table 5 - 3, as graphed in Figure 5 - 8.

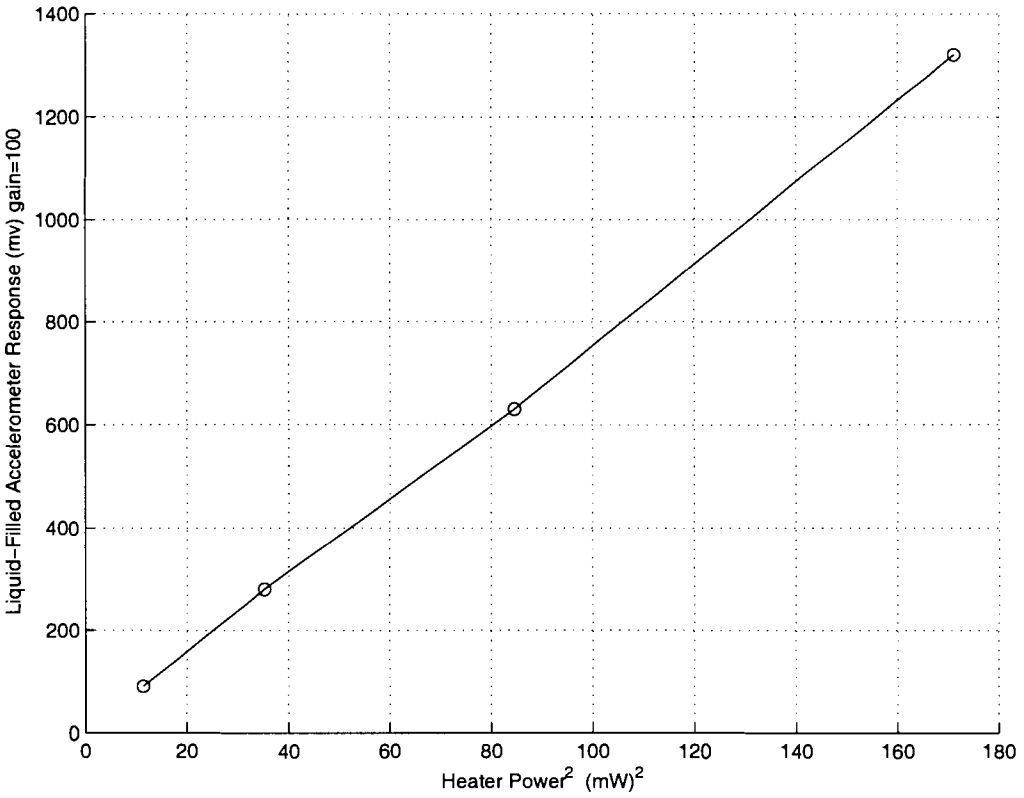

Figure 5 - 8 Liquid-filled accelerometer sensitivity with heater power

Hence, we can use this relationship to normalize the response curve of the accelerometer shown in Figure 5 - 7 at applied voltage of 3 V, 4 V, 5 V and 6 V. The resulting graph is shown in Figure 5 - 9.

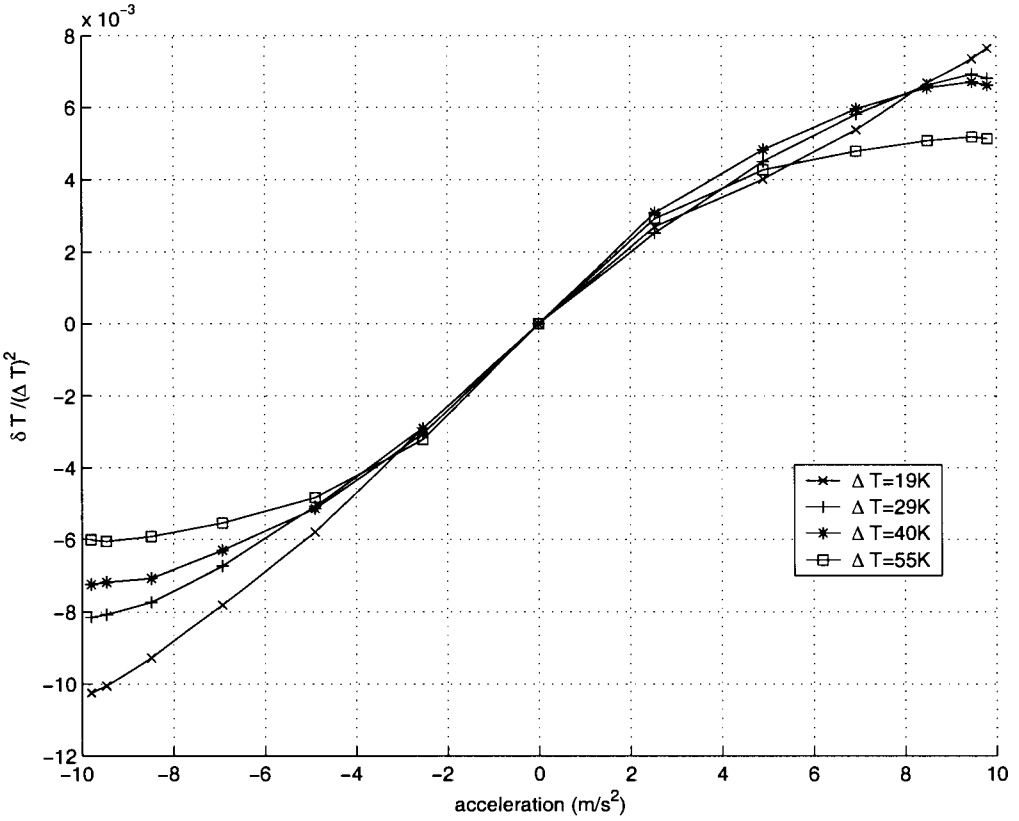

Figure 5 - 9 Saturation of response with increasing acceleration for liquid-filled accelerometer

It may be seen that the response is initially linear, becoming sub-linear before reaching 1 g. The higher the value of ΔT, the lower the value of acceleration at which the response becomes sub-linear, and this is due to device saturation.

5 - 2.3 Comparison between Air-Filled Chip and Liquid-Filled Chip

The steady state response of the liquid-filled chip to 1-g acceleration change at a series of heater temperatures was then compared with the steady state response of an

identical air-filled chip, the results are shown in Figure 5 - 10. Here, MDT stands for maximum differential temperature measured between two differential thermocouples.

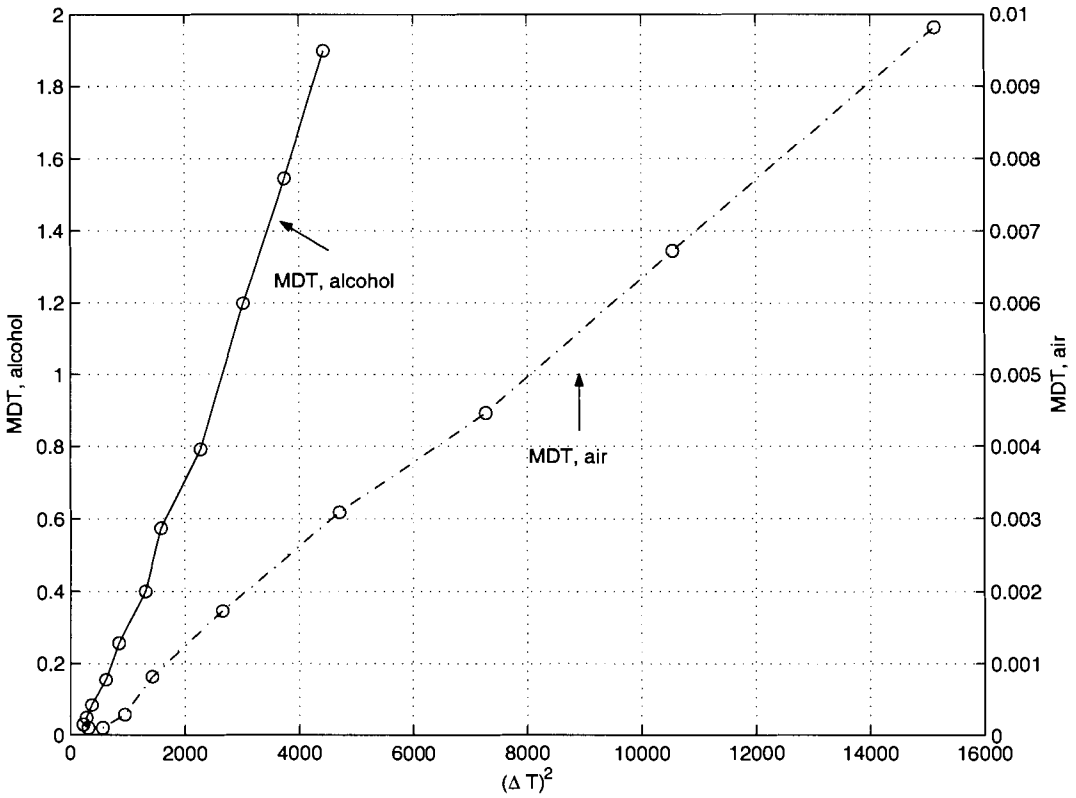

Figure 5 - 10 Differential temperature as a function of $(\Delta T)^2$.

Over this range, the sensitivity of the liquid-filled accelerometer is approximately 700 times that of the air-filled accelerometer. This ratio is consistent with (Eq 5 - 3), which predicts that the sensitivities of the air and liquid-filled chips should be in the ratio:

$$\frac{\delta T_{liq}}{\delta T_{air}} = \frac{(\rho_{liq})^2 \beta_{liq} c_{liq} k_{air} \mu_{air}}{(\rho_{air})^2 \beta_{air} c_{air} k_{liq} \mu_{liq}} = \frac{790^2 \times 62 \times 2440 \times 26 \times 2}{1^2 \times 330 \times 1000 \times 119 \times 177} = 700 \qquad \textbf{(Eq 5 - 5)}$$

where the subscripts "liq" and "air" denote the properties of liquid of isopropanol and air respectively.

5 - 3 Transient Response

To measure the transient response of the accelerometer chip, it was mounted on a Brüel & Kjær PM vibration Exciter Type 4808 (shaker) (Brüel & Kjær Co. 2003) and subjected to a sinusoidally varying acceleration at a frequency gradually increasing from 1Hz to 1kHz. This sinusoidal wave is generated by a functional generator and amplified by a stereo power amplifier to control the shaker's vibration frequency and displacement.

5 - 3.1 Vibration Exciter and Acceleration Estimated

In order to calculate the transient response of the accelerometer chip, we first need to estimate the acceleration generated by the vibration exciter for the measured output vibration amplitude at each frequency.

In our experiments, the payload, including the accelerometer chip, and amplification circuitry enclosed within a metal box plus the coaxial connection cable, and mounting devices, weighs about 441grams. Within the safe range of operation, the displacement limit (maximum displacement peak to peak for all frequency) of the vibration can range from 4mm to 8mm.

The acceleration can be estimated by measuring the displacement and frequency of vibration.

Since shaker vibration is controlled by sinusoidal signal described as:

$$A\sin(2\pi ft) \qquad \textbf{(Eq 5 - 6)}$$

where A is the amplitude, and f is the frequency of the control signal from signal generator.

The position of the table at time t can be written as:

$$\frac{D}{2}\sin(2\pi ft) \qquad \textbf{(Eq 5 - 7)}$$

Here D is the to be measured vibration displacement from peak to peak at specific frequency f.

Take first derivative of (Eq 5 - 7), velocity is obtained as:

$$\frac{D}{2}\times 2\pi f\cos(2\pi ft) \qquad \textbf{(Eq 5 - 8)}$$

Take second derivative ((Eq 5 - 7), acceleration is obtained as:

$$-\frac{D}{2}\times(2\pi f)^2\sin(2\pi ft) \qquad \textbf{(Eq 5 - 9)}$$

Therefore the shaker's acceleration amplitude can be estimated as:

$$\frac{D}{2}(2\pi f)^2 \qquad \textbf{(Eq 5 - 10)}$$

In Figure 5 - 11, the acceleration data, labelled by '.' were estimated by using (Eq 5 - 10) from our measurement of shaker's vibration displacement for a range of frequency from 1 to 100Hz, (during the measurement, the shaker's displacement limit was set to 5mm), and compared with those acceleration obtained from product data sheet (Brüel & Kjær Co. 2003), (the payload curve was taken by interpolation and by proportion of $5/12.7$), labeled as '*' and product data, which is then corresponding to 5 mm displacement limit, the agreement is good. Therefore, in subsequent dynamic experiments, (Eq 5 - 10) is used to estimate the acceleration for the shaker operated at specific displacement and at specific frequency.

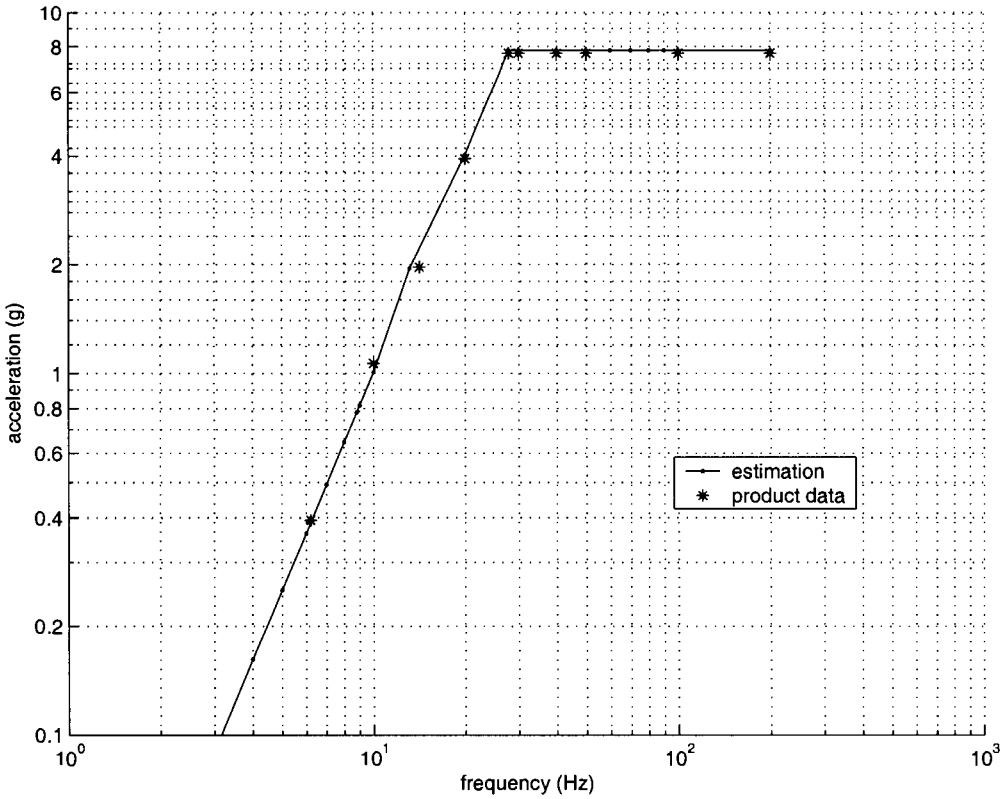

Figure 5 - 11 Acceleration of a payload on the Brüel & Kjær exciter as a function of frequency; comparison of product data and (Eq 5 - 10)

In using vibration table for dynamic test of the air-filled and isopropanol-filled chips, we first measure the displacement at each specific frequency after mounting the metal box on the vibration table, these measurements will be used to estimate the acceleration using (Eq 5 - 10); then the system is maintained at the same setting, the amplitude of output signal of the chip is measured and recorded for the same frequency.

5 - 3.2 Transient Response of Air-Filled Accelerometer Chip

Figure 5 - 12 shows normalized frequency response of an air-filled accelerometer chip. The normalized response at each specific frequency is obtained by taking the

measurement and dividing it by the product of steady state value of 1 g and estimated imposed acceleration.

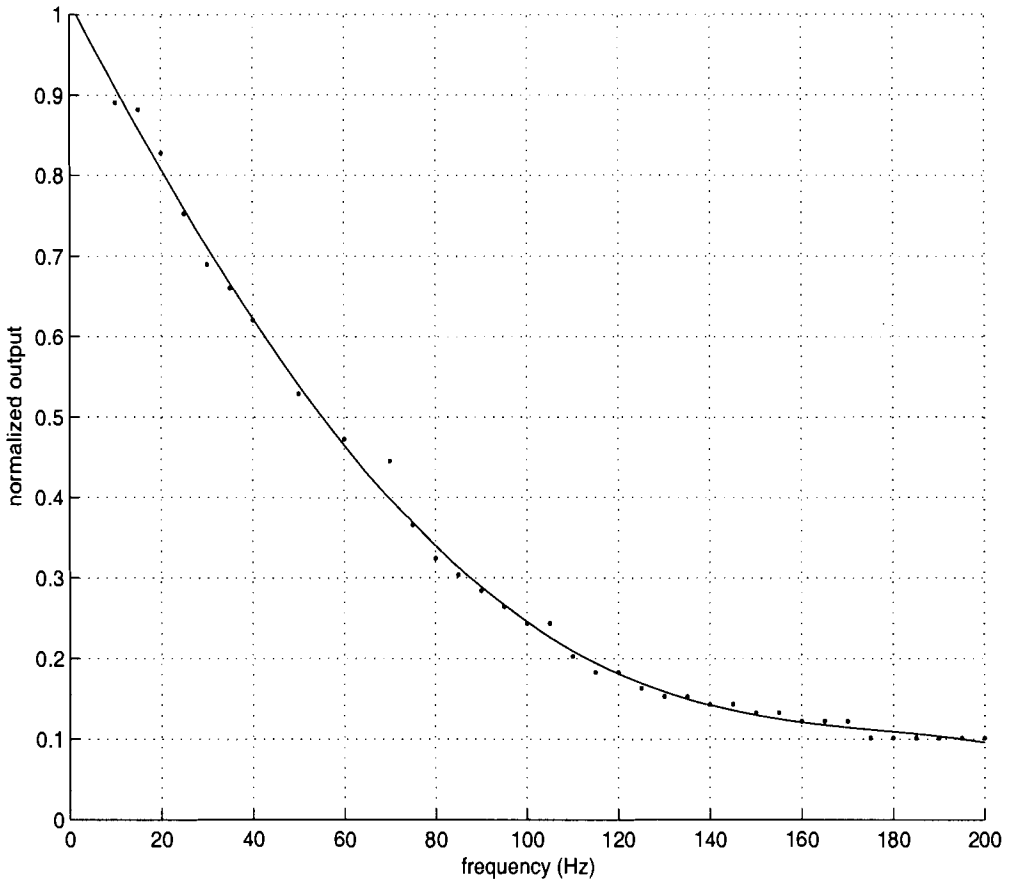

Figure 5 - 12 Normalized frequency response of air-filled chip

For air-filled accelerometer chip, the chip output signal followed the imposed acceleration, but its amplitude fell off after a certain point. As defined in Section 4 - 1 for τ, from Figure 5 - 12, where normalized output at 63% of its total value, hence response time deduced is τ = 25 millisecond for this particular air-filled chip.

5 - 3.3 Transient Response of Liquid-filled Accelerometer Chip

Figure 5 - 13 shows normalized frequency response of a liquid-filled accelerometer chip. Again, the normalized response at each specific frequency is obtained by taking the measurement and dividing it by the product of steady state value of 1 g and estimated imposed acceleration.

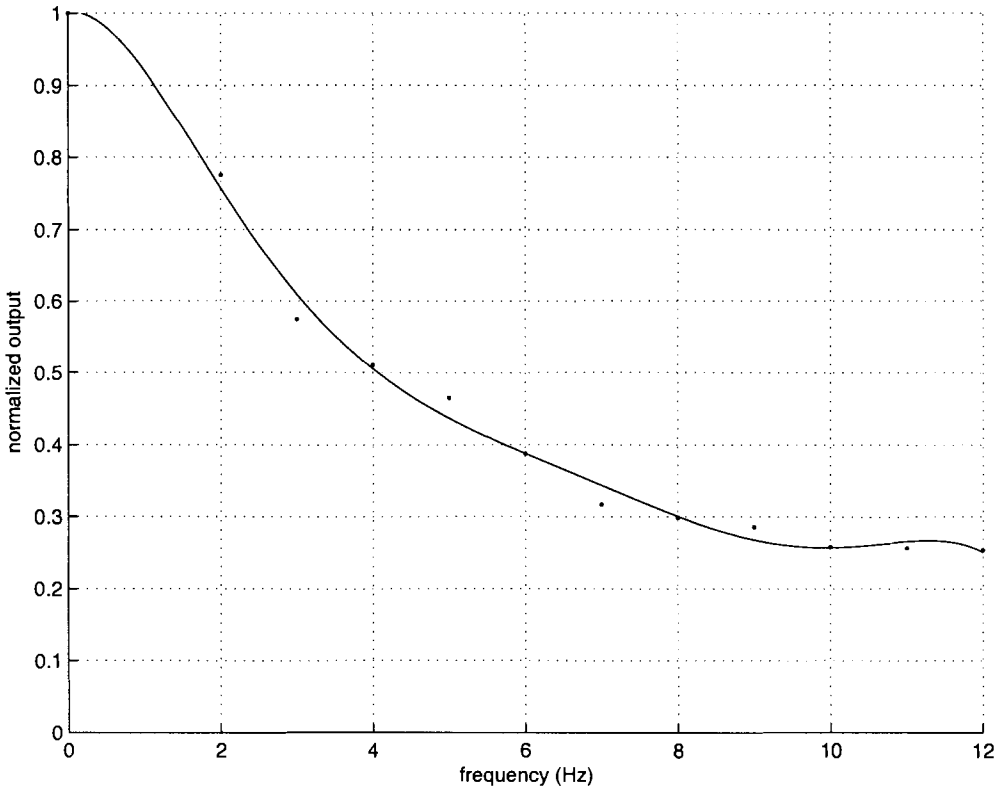

Figure 5 - 13 Normalized frequency response of liquid-filled chip

As defined in Section 4 - 1 for τ, from Figure 5 - 13, where normalized output at 63% of its total value, hence the response time deduced is about $\tau = 0.4$ second for this particular isopropanol-filled chip.

A comparison of frequency response between air-filled chip and liquid-filled chip is shown in Figure 5 - 14.

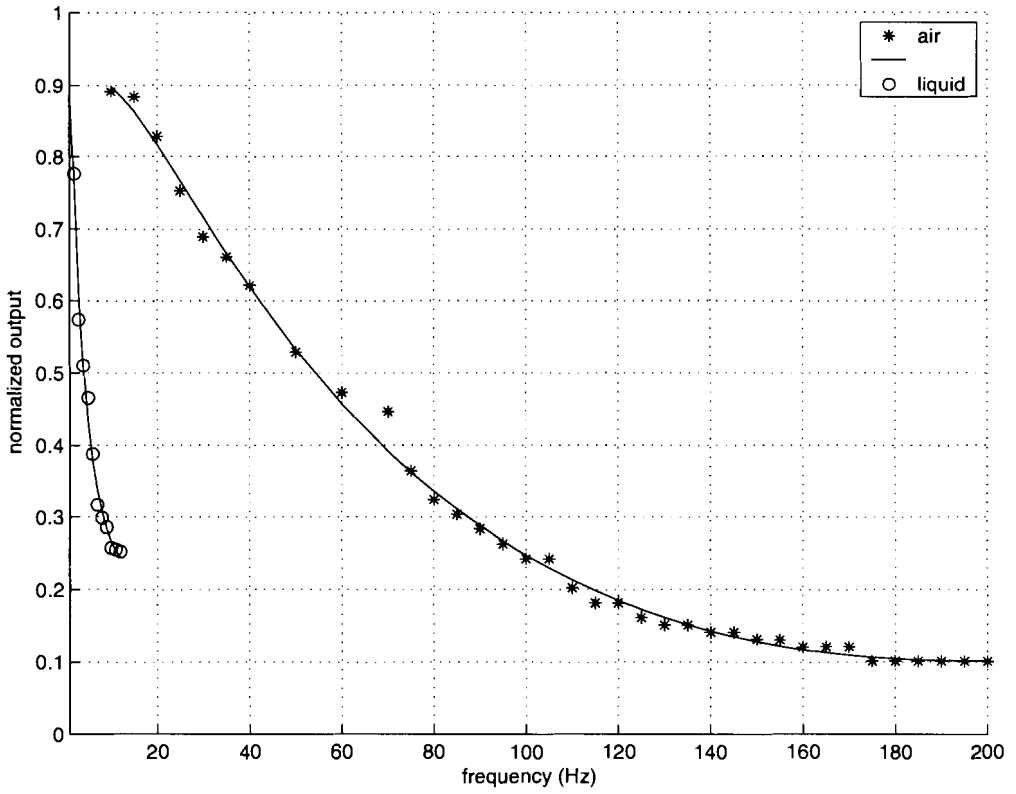

Figure 5 - 14 Comparison of frequency response between air-filled chip, and liquid-filled chip

5 - 3.4 Comparison between Experiment and Theoretical Correlation

The experimental results may be compared with the correlations developed in Section 4 - 2.

As calculated in Section 4 - 3, the air-filled accelerometer response time takes into account both thermal response time and thermocouple response time. Air is an intermediate-Prandtl number fluid, so from Figure 4 - 5, F_o/R^2 takes the value 0.095 for $R = 50$. For air $\alpha = 0.22 \times 10^{-4}\ \mathrm{m^2/s}$, and $r_o = 0.001$ m. So thermal response time is

τ_{air} = 4.3 milliseconds, whereas the response time of thermocouples for air-filled chip is in the order of 2 milliseconds. The total calculated response time for air-filled chip is about 6.3 milliseconds. For air-filled chip in our experiments, the response time is about 25 milliseconds, hence, we observed a longer response time than the calculated total response time. This may due to differences between the idealized geometry of the model used to develop correlation and the actual chip used in experiments as well as the difference of thermocouple size used in the estimation and the actual thermocouple size in the chip.

For air-filled accelerometer, to improve the response time, some techniques can be considered. For instance, reducing the dimension of the thermocouple will decrease the thermocouple response time. Also a typical method used in industry to increase the frequency response is to use a frequency compensation circuit.

For liquid-filled chip, alcohol is a high-Prandtl-number fluid, so from Figure 4 - 3, for $R = 50$, F_o/R^2 is about 0.05. For isopropanol, $\alpha = 0.9 \times 10^{-7}\,\mathrm{m^2/s}$. So the thermal response time is τ_{iso} = 0.5 seconds. The thermocouple response time is in the order of sub milliseconds, hence it is negligible. The total response time of liquid-filled chip is about 0.5 seconds. For isopropanol-filled chip, we observed slightly shorter response time than that of theory, this is may due to the geometry difference between experimental chip and the idealized geometry of concentric cylinders used to develop the correlation.

In general, the response time of experimental work agree with those predicted by the correlation curve. In practice, we do observe longer response time for isopropanol-filled chip than air-filled chip.

During these measurements, care had to be taken to ensure that the amplifier circuitry was not picking up an electrical signal generated by the vibration table itself. This was achieved by very careful shielding of the circuits. We confirmed that the signal measured was indeed generated by the differential temperature at the detectors by

switching off the power to the heater at intervals during the experiment: the output signal then quickly faded, confirming that we were measuring accelerometer output rather than electrical noise.

5 - 4 Conclusion

In this chapter, we have carried out the experimental work as a supplement to our theoretical study of using an alternative working fluid, such as liquid. We have first constructed an liquid-filled accelerometer, using isopropanol as working fluid. We then carried out static and dynamic tests on this chip. Comparing with the performance of air-filled chip, the sensitivity of liquid-filled chip has been increased by 700 times, at a cost of longer response time, these results also agree with the theoretical results obtained in previous chapter. In conclusion, we have successfully demonstrated the feasibility of using liquid as working fluid, and the results of our experimental work have verified our theoretical result of FLOTRAN steady state and transient study. This will also provide a basis for future identification of a more suitable working fluid to improve the performance on both sensitivity and response time.

Chapter 6 The Concentric-Spheres Model: Steady-State Case

In this chapter we will use the CFD package 'FLOTRAN' to solve the steady-state version of the equations developed in Appendix I for the concentric-spheres model. Considering the spherical case in addition to the cylindrical case, allows us to estimate the performance of the two-axis variant of the accelerometer. It also sets a bound on the performance of the single-axis accelerometer in the case where the heated region of the heater is a peak rather than a plateau (see Appendix II). Our objective is not to predict the performance of any one device, but to establish correlations that will allow us to predict the effects of changing the working fluid or the device size on sensitivity. To ensure that these correlations are valid, we perform a series of checks on the model predictions:

- Internal consistency: are the predictions independent of details of the modeling, such as mesh size?
- Consistency with literature: can the model reproduce the experimental and analytic results derived in the prior literature?

6 - 1 FLOTRAN Concentric Spheres Model

6 - 1.1 FLOTRAN Concentric Spheres Model Specifications

FLOTRAN concentric sphere model was set up with the following specifications:

- Model consists of two concentric spheres;
- Inner sphere temperature maintained at T_i = 310 K, and the outer at T_o = 300 K;

- Initially, the radius of inner sphere is set to 100 microns, that of outer set to 1000 microns, corresponding to $R = 10$; the radius of the inner sphere was later varied to investigate a range of values from $R = 2$ to $R = 50$;
- Acceleration at 10 m/s^2, corresponding to $Ra = 0.001$;
- Mesh is to be determined;
- Iterative method used to solve temperature and pressure fields until convergence was obtained, convergence criteria used are:

$$\sum_{i=1}^{n} \frac{\left|T_i^k - T_i^{k-1}\right|}{\left|T_i^k\right|} < 10^{-8}$$

$$\sum_{i=1}^{n} \frac{\left|p_i^k - p_i^{k-1}\right|}{p_i^k} \leq 10^{-6}$$

The refinement of the mesh used in the model to yield results of adequate precision was a lengthy process, requiring great care. This process is described in Appendix IV - 1 to the thesis, in which we have concluded that if a regular-volume-mesh is used in FLOTRAN steady state analysis of concentric spheres model, mesh size of (0.0005m, 5°, 5°) should be the appropriate choice, that is 20, 72, 36 divisions in the radial, circumferential and azimuthal directions respectively.

6 - 1.2 FLOTRAN Steady State Analysis of Concentric Sphere Model Procedure

A complete procedure of FLOTRAN steady state analysis of concentric-spheres model, involving modeling and meshing using regular-volume-mesh, includes the following steps:

1. Create partial annulus with center at (0, 0), inner radius of 0.0001m, outer radius of 0.001m, from 90° to 270°. This corresponding to $R = 10$. Other

radius ratio can be realized by adjusting the inner sphere radius.

2. Mesh the area with regular mesh with 20 divisions on straight line and 72 division on circumferential curve.
3. Extrude the meshed area 180° about the Y axis to create a volume consisting of volume segments at 5° apart.
4. Apply load: temperature on inner sphere: 310K, on outer sphere 300K; velocity V_x, V_y, V_z on all the boundaries of inner sphere and outer sphere to 0 m/s, V_z set to 0 m/s on the plane face of the hemisphere; acceleration on x direction set to $10 m/s^2$.
5. Set up simulation control, the simulation run to 1000 iteration, with convergence criteria set to 10^{-6} for pressure and 10^{-8} for temperature.
6. The velocity solver is Tri-Diagonal Matrix Algorithm (TDMA); for the incompressible pressure equation, the solver is Preconditioned Conjugate Gradient Method (PCG); and temperature solver is TDMA.

6 - 2 Experimental and Theoretical Studies of Laminar Free Convection between Concentric Spheres

We begin our concentric-spheres model steady-state analysis by review of prior work on laminar free convection between concentric spheres, which has been summarized by Chu and Lee (1993)

6 - 2.1 Experimental Studies of Laminar Free Convection between Concentric Spheres

Natural convection in the annulus between two concentric spheres has been investigated experimentally by Bishop et al.(1964), (1966), Scanlan et al. (1970) and by Yin et al. (1973). Three types of flow pattern in the annuli between concentric spheres were observed for various radius ratios, Prandtl numbers and Rayleigh numbers. They were crescent, kidney-shaped flows and falling-vortices. Temperature profiles were measured in these experiments.

The experimental work done by Bishop et al. (1966), though its results are not directly applicable to the problem of interest to us, does however present some relevant information on possible experimental apparatus set up, flow patterns, and temperature distribution, which would help us understand the underlying physics that can not be obtained otherwise. Therefore, we present a brief description of their work here.

6 - 2.2 Experimental Work by Bishop et. al.

Bishop, Mack and Scanlan (1966) carried out an experimental investigation concerning natural convection of air enclosed between two isothermal concentric spheres of various radius ratios ranging from 1.19 to 3.14. Results of a visual study, which indicated three distinct types of flow patterns, crescent, kidney-shaped flow and falling-vortices, were summarized. Measured temperature profiles vs. radius were analyzed. The Grashof number based on gap thickness ranged from 10^4 to 3.6×10^6, and therefore the Rayleigh number based on gap thickness ranged from 7×10^3 to 2.5×10^5.

6 - 2.2.1 The Heat Transfer Apparatus

The heat-transfer apparatus used by Bishop et. al, (1964), (1966), shown schematically in Figure 6 - 1, consisted of two concentric spheres enclosed in a water jacket. A single outer sphere of 10 inch diameter was used in conjunction with inner spheres of 4, 5, 6, and 8 inch diameters. All spheres were of 1/16 inch thick copper.

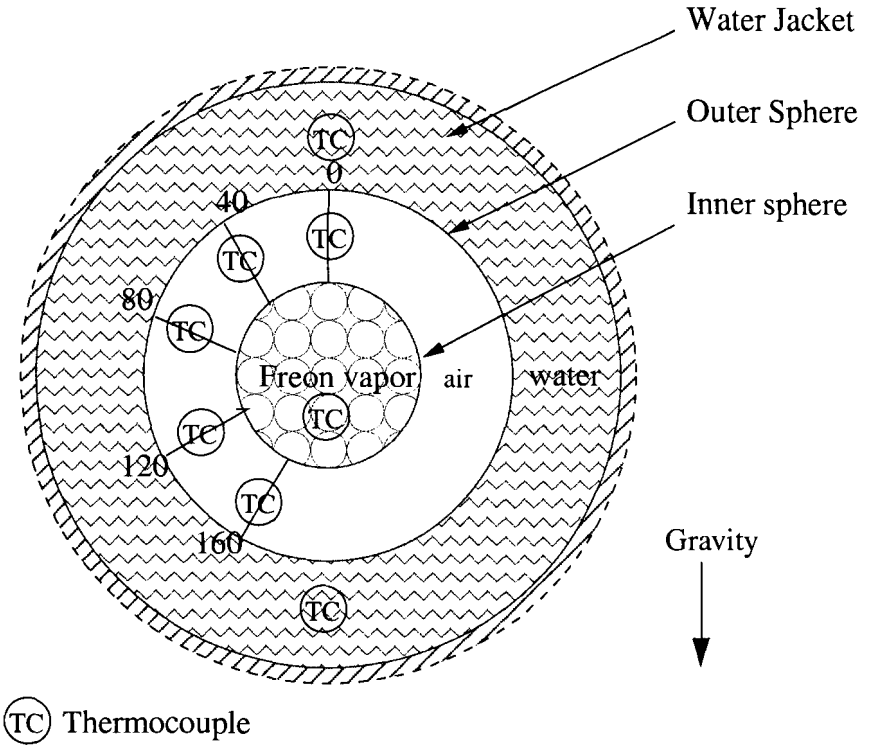

Figure 6 - 1 Schematic diagram of heat-transfer apparatus

Five thermocouple probes were located in a common vertical plane through the center of the spheres. They were spaced at 40° intervals beginning with a probe on the upward vertical axis.

6 - 2.2.2 Flow Patterns

A transparent apparatus was constructed similar to the metallic apparatus

described above by Bishop et. al. to allow visual observation of the flow. Three distinct types of flow: the crescent-eddy type, the Kidney-Shaped Eddy type, the falling vortices type, were observed in the ranges of L/r_i and ΔT investigated, among them, the crescent-eddy is of interest to us due to its low Rayleigh number of this type of flow.

The Crescent-Eddy Type

The "crescent-eddy" type, the most common pattern observed by Bishop et. al, is illustrated in Figure 6 - 2. It occurs at a low temperature difference, and a low Rayleigh number. The graph shows that a thin boundary layer consisting of rapidly moving fluid exists very close to each sphere, while the central crescent eddy consists of slowly moving fluid. The upward velocities adjacent to the inner sphere were considerably greater than the downward velocities along the outer sphere. In the lower region essentially the entire gap between the spheres was filled with relatively stagnant fluid. At the top of the inner sphere the high-speed flow separated from the inner sphere, leaving a corner eddy adjacent to the intersection of the surface of the inner sphere with the vertical axis of symmetry.

In the experimental work done by Bishop, Mack and Scanlan (1966), temperature profiles were also presented for the cases of three flow patterns.

Again, since the scale of the problem of our interests are in micron level, one method for us to study the underlying physics experimentally would be to scale up the system and construct a similar apparatus to observe the flow pattern and temperature distribution, using a high-viscosity fluid to obtain a suitably low Rayleigh number.

A quick analysis shows that Rayleigh number of the system of interest to us is below 10^3. In Bishop et. al.'s experimental work, although the flow was classified by the parameters L/r_i and ΔT, the overall Rayleigh number ranged from 0.7×10^4 to 2.5×10^5, hence the results are not directly applicable to the problem of interest to us.

However, since the Rayleigh number is generally larger than that of our problem,

we would expect our accelerometer to display more steady conduction-dominated buoyant fluid flow, similar to the "crescent-eddy" shaped fluid flow. Also it can be observed that the flow is axi-symmetrical.

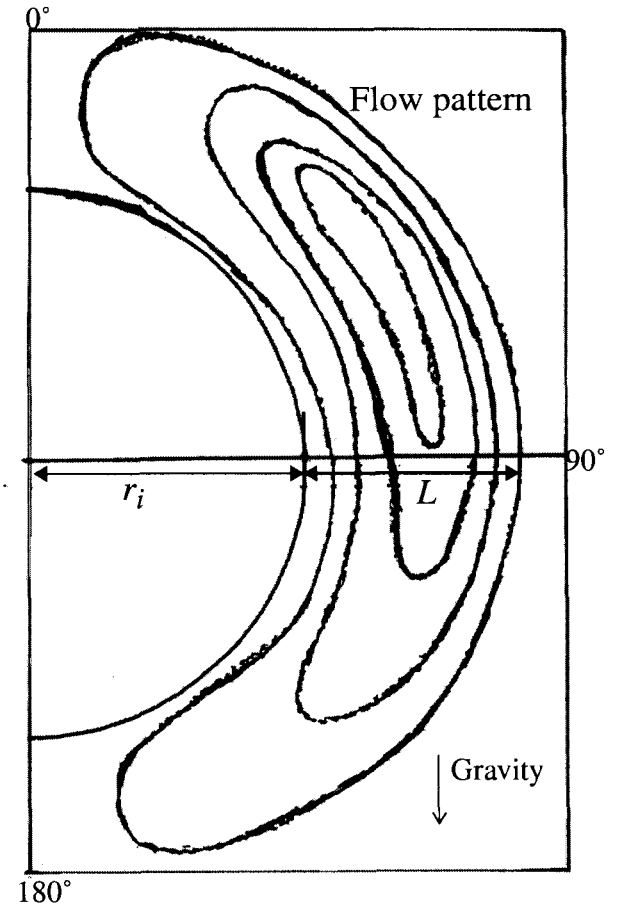

Figure 6 - 2 Sketched crescent-eddy flow pattern for L/r_i=0.72, ΔT=8.3°C, (based on Bishop et. al 1966, for comparison)

6 - 2.3 Analytical Studies

Based on the experiments done previously by Bishop et. al, (1964), (1966), Mack and Hardee(1968) obtained an approximate analytical solution of natural convection in annuli between two isothermal concentric spheres, the inner surface being hotter, using

perturbation method to determine the temperature and fluid flow field. The details of the mathematical work of this analytical solution were presented in Hardee (1966). This analytical solution will be studied carefully in section 6 - 2.4. The same problem has been studied numerically by Brown (1967) using finite-difference scheme, allowing the problem to be solved with a much larger range of Prandtl and Grashof numbers. It has been claimed that the same problem can be solved with a greater range of Rayleigh number by Shaughnessy et al. (1978) using spectral expansions technique, however the accurate solutions that could be obtained were very limited. Astill (1980) et al. again solve this problem for Prandtl numbers between 0.7 and 5.0 by using the finite difference method. More related work was presented in the following references: (Caltagirone, Combarnous and Mojtabi, 1980), (Wright and Douglass, 1986), (Ingham, 1981), (Mojtabi and Caltagirone, 1982) (Singh and Chen, 1980), (Geoola and Cornish, 1982), and (Huang and Yang, 1984).

6 - 2.4 Analytical Steady State Response (Mack & Hardee's Solution)

We begin by examing an analytical solution, as we will use this to validate the FLOTRAN concentric spheres model.

Mack & Hardee (1968), using Boussinesq approximation, obtained an analytical solution for steady axi-symmetric natural convection between isothermal concentric spheres.

As reviewed in section 6 - 2.1, although Bishop et. al. (1964), (1966) observed unsteady flows under certain conditions, their experimental work indicated that the flow is axi-symmetric and steady for sufficiently low Rayleigh numbers. Guided in their assumptions by the experimental results, Mack and Hardee gave an analysis of natural

convection in the enclosure between concentric spheres for low Rayleigh numbers. They discussed the range of reliability of the solution, the configuration of the streamlines, the velocity and temperature distributions.

6 - 2.4.1 Solution

Mack and Hardee solved the problem to its third approximations of nondimensional temperature $\tilde{T} = (T - T_o)/(T_i - T_o)$ and stream function ψ, which can be expressed as:

$$\tilde{T} = \tilde{T}_0 + Ra\tilde{T}_1 + Ra^2\tilde{T}_2 + Ra^3\tilde{T}_3 \qquad \textbf{(Eq 6 - 1)}$$

$$\psi = Ra\psi_1 + Ra^2\psi_2 + Ra^3\psi_3 \qquad \textbf{(Eq 6 - 2)}$$

where

$$\tilde{T}_0 = -(R-1)^{-1} + R(R-1)^{-1}r^{-1} \qquad \textbf{(Eq 6 - 3)}$$

which gives the well known temperature distribution for pure conduction.

and

$$\psi_1 = \frac{R}{8(R-1)}(B_1 r^4 + r^3 + B_2 r^2 + B_3 r + B_4 r^{-1})\sin^2\theta \qquad \textbf{(Eq 6 - 4)}$$

where

$$B_1 = (2R^7 - 6R^6 + 4R^5 + 4R^4 - 6R^3 + 2R^2)/\Delta \qquad \textbf{(Eq 6 - 5)}$$

$$B_2 = (2R^9 - 12R^7 + 10R^6 + 10R^5 - 12R^4 + 2R^2)/\Delta \qquad \textbf{(Eq 6 - 6)}$$

$$B_3 = (-3R^9 + 8R^8 - 5R^7 - 5R^4 + 8R^4 - 3R^3)/\Delta \qquad \textbf{(Eq 6 - 7)}$$

$$B_4 = (R^9 - 4R^8 + 6R^7 - 4R^6 + R^5)/\Delta \qquad \textbf{(Eq 6 - 8)}$$

$$\Delta = -4R^8 + 9R^7 - 10R^5 + 9R^3 - 4R^2 \qquad \textbf{(Eq 6 - 9)}$$

$$\tilde{T}_1 = f_1(r)\cos\theta \qquad \textbf{(Eq 6 - 10)}$$

$$\psi_2 = f_2(r)\sin^2\theta\cos\theta \qquad \textbf{(Eq 6 - 11)}$$

$$\tilde{T}_2 = f_3(r)(3\cos^2\theta - 1) + f_4(r) \qquad \textbf{(Eq 6 - 12)}$$

$$\psi_3 = f_5(r)(5\sin^2\theta\cos^2\theta - \sin^2\theta) + f_6(r)\sin^2\theta \qquad \textbf{(Eq 6 - 13)}$$

$$\tilde{T}_3 = f_7(r)(5\cos^3\theta - 3\cos\theta) + f_8(r)\cos\theta \qquad \textbf{(Eq 6 - 14)}$$

Each function $f_k(r)$, $1 \le k \le 8$ is a sum of a number of terms, each of the form $r^m(\ln r)^n$. The coefficients of these terms depend on the parameter R and, in general, on Pr.

The expressions for the f_k can be found in the Ph.D dissertation of Hardee (1966). These expressions themselves are lengthy and complicated. In our current work, by using Maple (Kamerich, 1999), a symbolic computing working sheet was constructed based on Hardee's solution listed above in his thesis work, and calculations were carried out to obtain the temperature distribution and stream functions at given Rayleigh number, Prandtl number, and Ratio of Radius. Since $\tilde{T}_2$ is symmetric in θ, it makes no contribution to the differential temperature measured between radially opposite points. Hence, the differential temperature can be simplified as, without using term $\tilde{T}_3$:

$$\delta\tilde{T} = 2Ra\tilde{T}_1 = 2Raf_1(r) \qquad \textbf{(Eq 6 - 15)}$$

Because of the length and complexity of the section (Eq 6 - 1) to section (Eq 6 - 14), the Maple working sheet was very carefully checked against figures from Hardee's thesis to confirm that it correctly represented the equations. This checking process is described in Appendix V. We now use this Maple working sheet to provide analytical solutions for the appropriate cases at given values of Rayleigh number, Prandtl number

and Radius Ratio, and compare these analytic solutions with the FLOTRAN numeric solutions.

6 - 3 FLOTRAN Steady State Analysis Results

We proceed using the concentric spheres model to solve problems of interest to us, as described in section 6 - 1, we first solve the case of $r_i = 0.0001\,\text{m}$, $r_o = 0.001\,\text{m}$, hence, $R = 10$, for air as working fluid, $Pr = 0.7$ and $Ra = 10^{-3}$.

6 - 3.1 Temperature Distribution

The steady state solution for temperature distribution for this case of $R = 10, Pr = 0.7, Ra = 10^{-3}$ in the plane $z = 0$, is given in Figure 6 - 3. The temperature distribution is visually indistinguishable from concentric spheres, though there is in fact an asymmetry, shown in Figure 6 - 3.

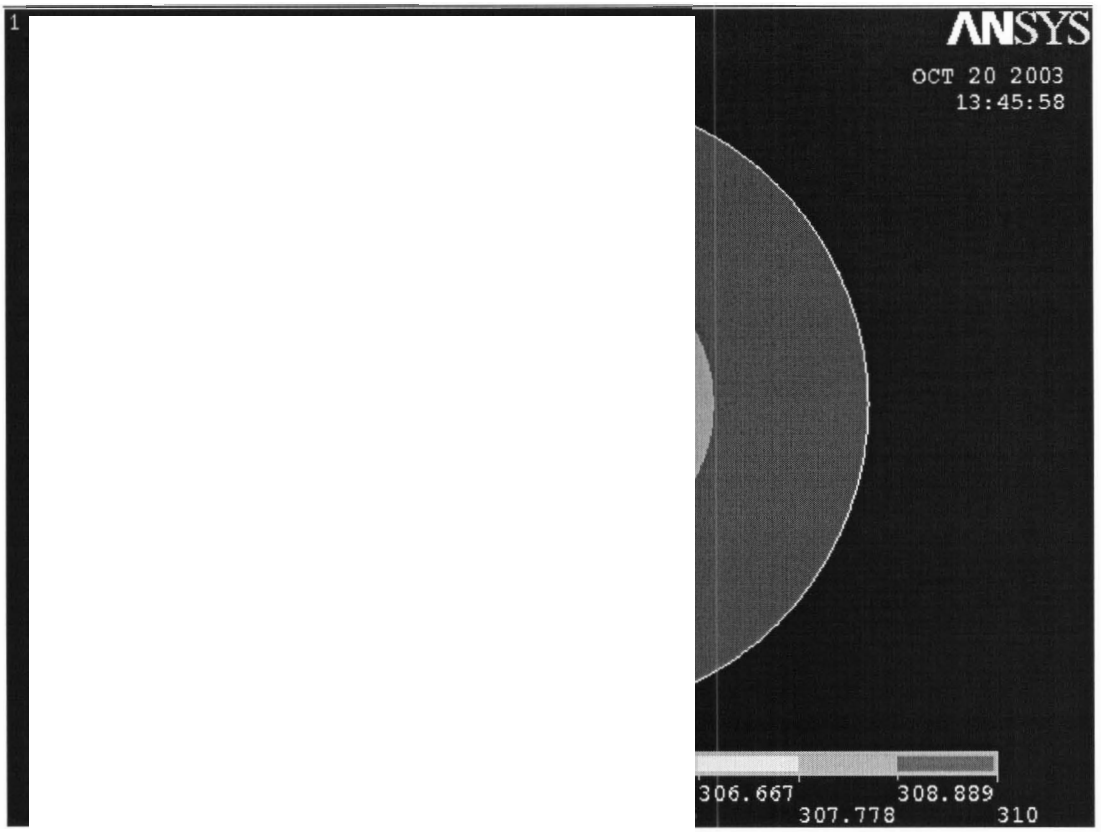

Figure 6 - 3 Temperature distribution for FLOTRAN concentric spheres model *Ra*=0.001, *Pr*=0.7 and *R*=10

6 - 3.1.1 Velocity Distribution

The steady state solution from FLOTRAN simulation for velocity distribution for concentric spheres model for case of $R = 10$, $Pr = 0.7$, $Ra = 10^{-3}$ is given in Figure 6 - 4. It resembles the crescent-type flows described in section 6 - 2.2.2

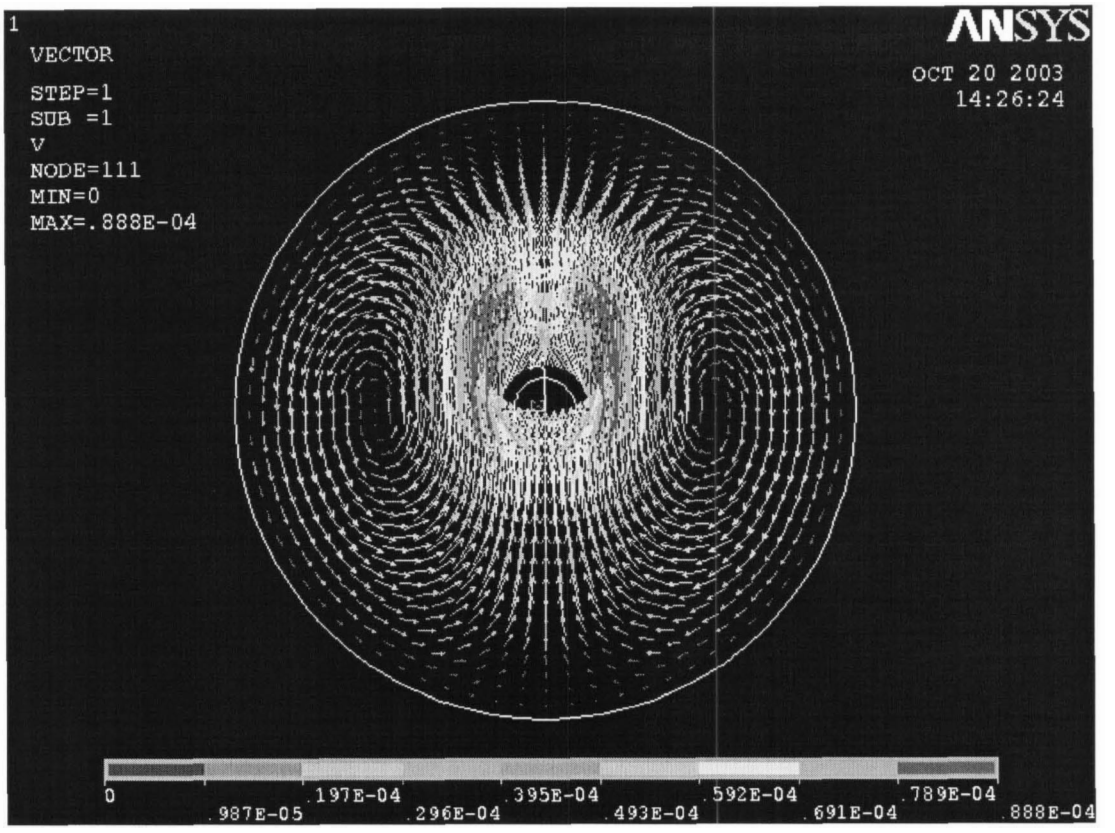

Figure 6 - 4 Velocity distribution for FLOTRAN concentric spheres model Ra=0.001, Pr=0.7 and R=10

6 - 3.1.2 Temperature Difference

The differential temperature profile along the axis of acceleration predicted by FLOTRAN analysis for the case set up in section 6 - 1.1 was compared with the result of (Eq 6 - 1) predicted by Hardee's formula for the same problem. The differential temperature profiles for $Ra = 10^{-3}$, $Pr = 0.7$, $R = 10$ for both results are shown in Figure 6 - 5, good agreement has been shown between analytical and numerical solution.

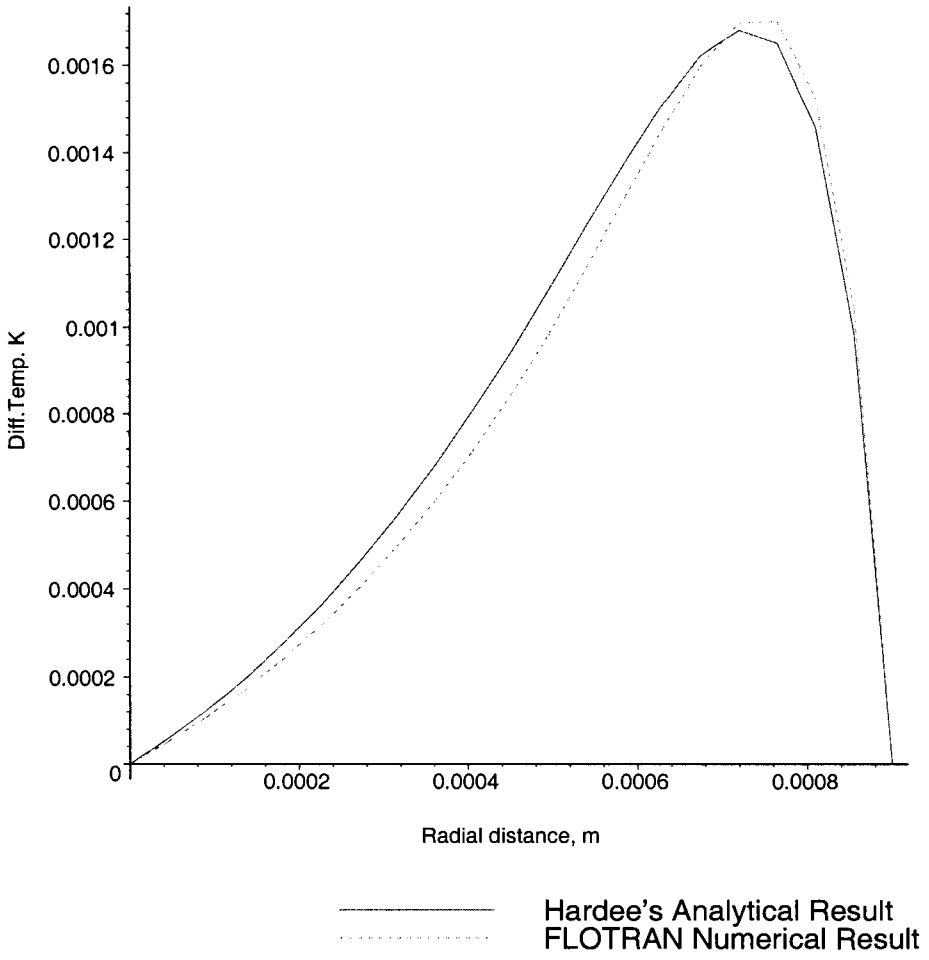

Figure 6 - 5 Dimensional differential temperature for concentric spheres model Ra=0.001, Pr=0.7 and R=10, comparison between Hardee's analytical and FLOTRAN numerical result.

6 - 4 Conclusion

In this chapter, a series of steady-state analyses have been done for convective laminar flow within the enclosure between concentric spheres. Mesh studies have been performed to ensure that our models are sufficiently precise to resolve the magnitude and

timing of the accelerometer signal. The results of the analysis have been compared with analytical results from the prior literature, and good agreement found. Hence, the results derived in this chapter can be used to predict the magnitude of the maximum temperature differential and its location for the geometry of concentric spheres. In the following chapter, we will extend these models for FLOTRAN transient analysis to obtain empirical correlations for the Fourier number as a function of radius ratio and Prandtl number. These correlations will be used to predict the effect of accelerometer geometry and choice of working fluid on response time.

Chapter 7 The Concentric Spheres Model: Transient Analysis

In this chapter we will use the 'FLOTRAN' model developed in the previous chapter to solve the time-dependent form of the equations developed in Appendix I. Our objective is not to predict the performance of any one device, but to establish correlations that will allow us to predict the effects of changing the working fluid or the device size on response time.

Appendix IV - 2 includes a description of the refinement of the mesh required to ensure adequate precision in the prediction of response time.

7 - 1 Prior Work on Transient Concentric-Spheres Study

As it has been mentioned for transient analysis of concentric-cylinder model in Chapter 4, the problem of solving response time for natural convection between concentric spheres differs from the transient cases discussed in the literature in that the accelerometer transient develops due to the suddenly imposed acceleration rather than the heating of one boundary surface.

Previous work concerning transient behavior due to sudden change of boundary condition has been presented in the following references. Ozoe et al. (1987) and Mochimaru (1989) studied transient natural convection both numerically and experimentally in a spherical/hemispherical enclosure after a step change in the spherical wall temperature. Fujii et al. (1984) obtained a numerical solution of two-dimensional laminar natural convection in annuli between two concentric spheres for radius ratio at

Prandtl number of 0.7 and Rayleigh number of 100, then for the range of Prandtl numbers $Pr = 0.7 - 120$ (1987). A three-dimensional numerical transient analysis of natural convection in a spherical annulus between two concentric spheres under nonsymmetrical thermal boundary conditions was performed by Ozoe et al. (1985) with Rayleigh number at 500 and Prandtl number at 1.0. Transient natural convection between concentric spheres has been also studied numerically by Chu & Lee (1993) using the finite difference method. The transient behavior of the flow field and its subsequent effect on the temperature distribution of different Rayleigh numbers and radius ratios are analyzed in their work. Since no previously published work is directly relevant to the operating condition of the accelerometer, we perform our own numerical study in the following sections.

7 - 2 FLOTRAN Concentric-Spheres Model Transient Analysis

Following a similar procedure to that developed for transient analysis for concentric-cylinder model, we proceed to transient analysis of concentric-sphere model.

7 - 2.1 Development of Fluid Flow and Temperature Field

As we mentioned earlier for cylindrical case, possible working fluids for the microthermal accelerometer fall into three categories:

- low-Prandtl-number fluids, such as mercury;
- intermediate-Prandtl-number fluids, including air and other gases
- high-Prandtl-number fluids, such as oil.

The dimensional analysis in Appendix I shows that the transient development of

the temperature difference is given by an expression of the form $F_o = f(Ra, Pr, R)$.

From simulation of fluids in each of these categories, we find that the chief determinant of the accelerometer response time is, for low-Prandtl-number fluids, the time taken for the velocity field to develop, while for high-Prandtl-number fluids, it is the time taken for the subsequent development of the temperature field. For intermediate values of Prandtl number, the two processes overlap, and the correlation between F_o and R must be found separately for each particular value of Pr.

The high-Prandtl case is illustrated by Figure 7 - 1, which shows the results of a simulation of convective laminar flow of high-Prandtl-number fluid within the space enclosed by concentric spheres of inner radius of 100 microns, and outer radius of 1000 microns. The imposed acceleration was $10 m/s^2$. The high-Prandtl-number fluid properties used are as listed in Table 4 - 1, with $Pr = 15.6$. (As in the concentric cylinders case, these fluid properties are used only as an illustration; we have verified that any high-Prandtl fluid would give qualitatively similar results.)

In Figure 7 - 1, the development of velocity has been shown as a function of time and as the fraction of its maximum value in the direction parallel to the imposed acceleration; and development of temperature field, in term of maximum differential temperature, has been show as a function of time. For this particular case, the time taken for the velocity field to reach 63% of its steady state value is approximately 53 microseconds, and 1200 microseconds for the maximum differential temperature to reach 63% of its steady state value.

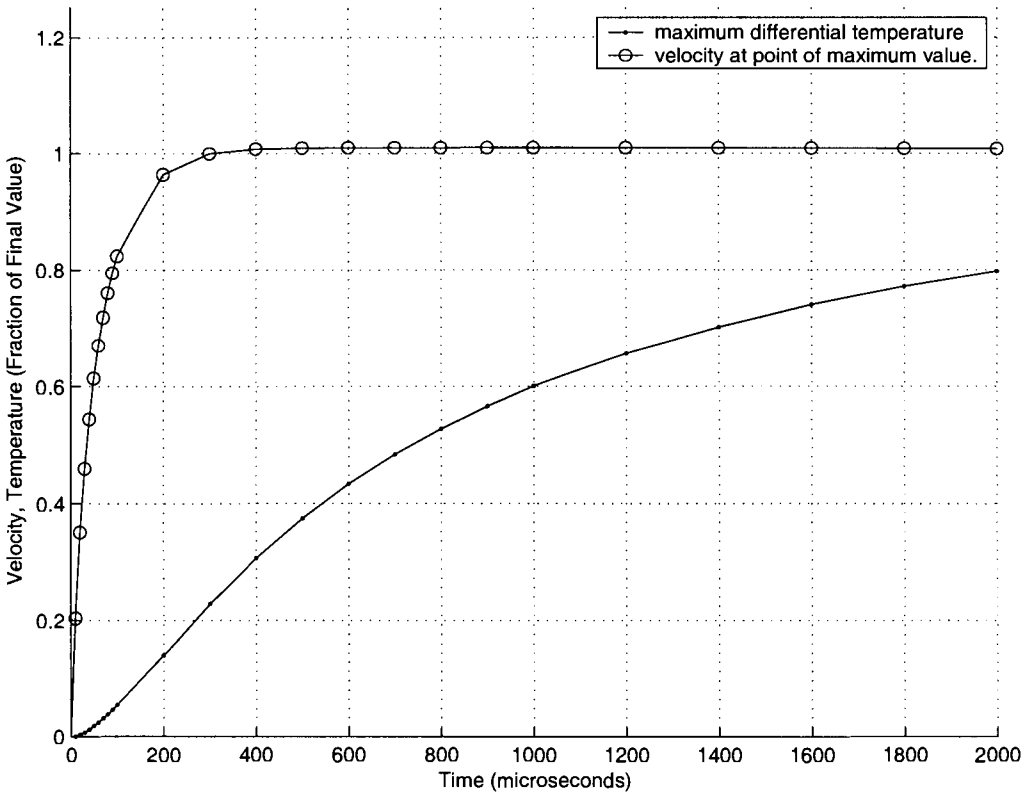

Figure 7 - 1 Development of velocity and temperature field for concentric spheres model *Pr*=15.6 and *R*=10

7 - 2.2 Empirical Correlations for Concentric Spheres Case

On the basis of these qualitative results, we conclude that the correlations determining Fourier number will take different forms for each of the three categories mentioned. We therefore simulate each category separately, then obtain the approximate form of the dependency by curve-fitting to the results of numerical simulation.

(In prior literatures, the Fourier number is often defined in terms of radius of inner sphere, $F_o = \frac{\tau\alpha}{r_i^2}$. However, FLOTRAN simulation shows that the response is more strongly determined by the radius of outer sphere than that of inner sphere. Therefore, in

this thesis, Fourier number is defined based on radius of outer sphere, which is also called the effective Fourier number $F_o/R^2 = (\tau\alpha)/(r_i^2 R^2) = F_o/R^2$.)

7 - 2.2.1 Empirical Correlations for Low-Prandtl-Number Fluids

A series of FLOTRAN simulations shows that the product $F_o Pr$ varies with R as shown in Figure 7 - 2.

This graph can be approximated by the function

$$F_o Pr/R^2 = \exp\left(-3.18237 - \frac{3.58728}{R} - 0.19985\ln(R)\right) \qquad \textbf{(Eq 7 - 1)}$$

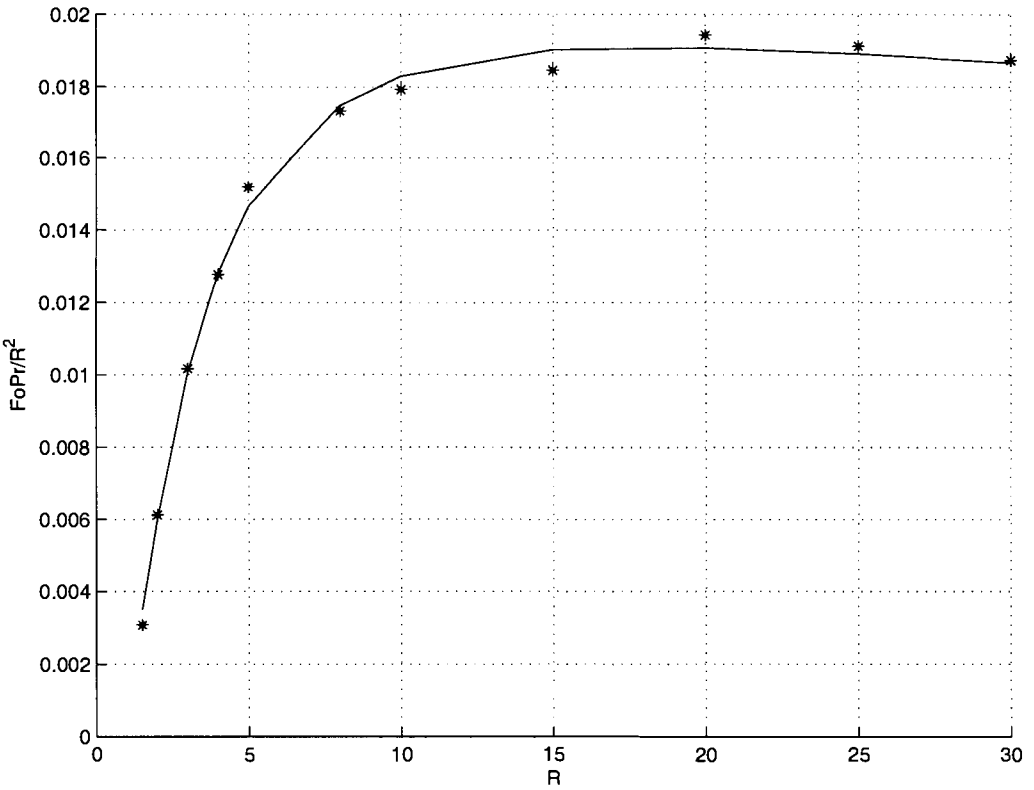

Figure 7 - 2 $F_o Pr/R^2$ versus R, low-Prandtl number fluids for concentric spheres model

7 - 2.2.2 Empirical Correlations for Intermediate-Prandtl-Number Fluids

A series of simulations was carried out representing the working fluid as having a Prandtl number of 0.7, leading to the relationship between F_o/R^2 and R shown in Figure 7 - 3

This graph can be approximated by the function

$$F_o/R^2 = \exp\left(-0.985343 - \frac{3.807484}{R} - 0.612383\ln(R)\right) \qquad \textbf{(Eq 7 - 2)}$$

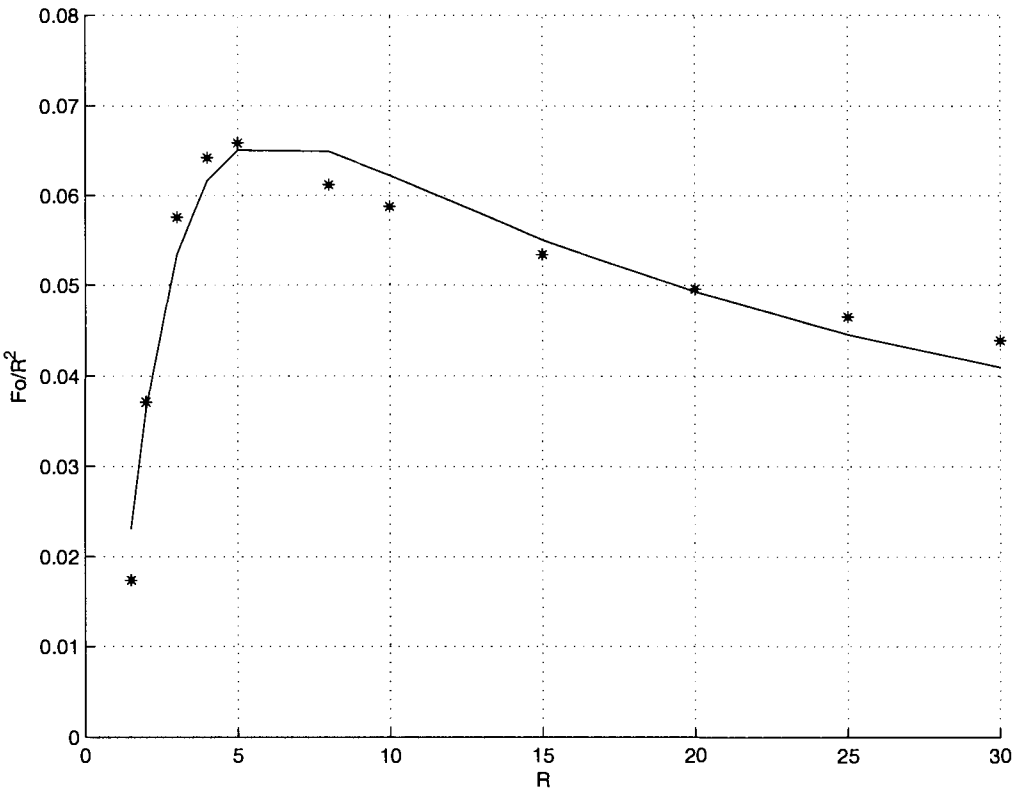

Figure 7 - 3 F_o/R^2 versus R, intermediate-Prandtl-number fluid Pr=0.7, concentric-spheres model

7 - 2.2.3 Empirical Correlation for High-Prandtl-Number Fluids

A series of FLOTRAN simulations shows that F_o/R^2 varies with R as shown in Figure 7 - 4.

This graph can be approximated by the function

$$F_o/R^2 = \exp\left(-0.106154 - \frac{5.541604}{R} - 1.399878\ln(R)\right) \qquad \textbf{(Eq 7 - 3)}$$

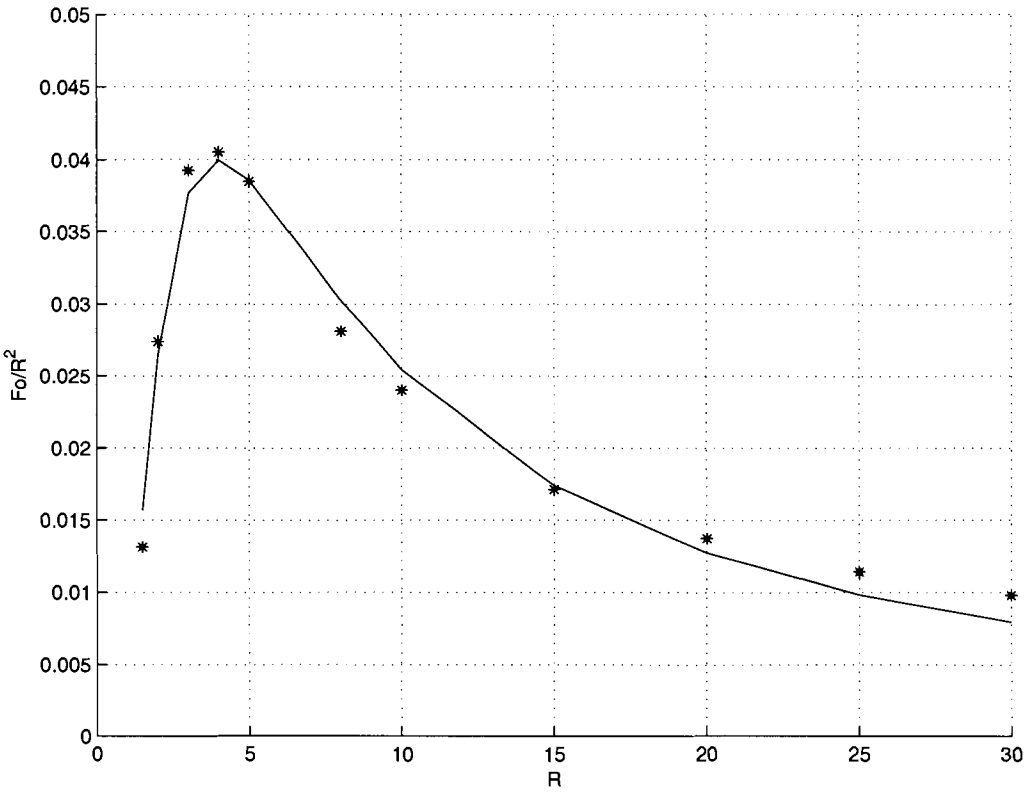

Figure 7 - 4 F_o/R^2 versus R, high-Prandtl-number fluids, concentric-spheres model

7 - 3 Conclusion

In this chapter, transient analyses have been done for convective laminar flow within the enclosure between concentric spheres. We have first determined that the form of the correlation between the thermal response time and the radius ratio and fluid properties takes different forms for low, intermediate and high values of Pr. We next perform FLOTRAN transient analysis to obtain empirical correlations for the Fourier number as a function of radius ratio R and Prandtl number for each of these categories of fluid. These correlations can be used to predict the effect of accelerometer geometry and choice of working fluid on response time.

Chapter 8 Size Limitations, Design Implications, and Future Work

In this chapter, we will complete the definition of the performance envelope for the microthermal accelerometer by establishing upper and lower bounds on device size. We will then explore the implications of the results obtained in this thesis for accelerometer design, re-visit our comparison with other accelerometer designs in the light of these results, and discuss possible future work.

8 - 1 Bounds on Device Size

8 - 1.1 Lower Bounds

It is probably possible to construct accelerometers at least an order of magnitude smaller than the examples studied in Chapter 5, "Experimental Studies". We consider two questions: firstly, as the device size is reduced, at what point do the assumptions on which the analysis in this thesis is based become invalid; secondly, within the range of validity of our analysis, what is the smallest accelerometer that would be of practical use?

8 - 1.1.1 Validity of Analysis

An underlying assumption of our analysis is that the working fluid can be treated as a continuum, that is, we can ignore the fact that the fluid is composed of individual molecules with a range of speeds. This assumption is justified as long as the dimensions of the device are large compared with the mean free path of a fluid molecule. We can

calculate the mean free path length as follows:

For air used as working fluid, air can be thought of as a mixture of N_2 and O_2 molecules, the mean free path length λ can be calculated from:

$$\lambda = \frac{kT}{\sqrt{2}\sigma P} \qquad \textbf{(Eq 8 - 1)}$$

where k is Boltzmann constant, $k = 1.38 \times 10^{-23} \text{J/K}$, σ is the collision cross-sections, it is $0.31\,(\text{nm})^2$ for N_2 molecules and $0.27\,(\text{nm})^2$ for O_2 molecules and P is the pressure of the air. Therefore, for molecules in air, the mean free path length calculated by (Eq 8 - 1) is approximately 100 nm ($1\text{nm} = 1 \times 10^{-9}\text{m}$).

For a liquid used as working fluid, such as isopropanol, the mean free path is about the same size as the isopropanol molecules. The diameter of isopropanol molecules is approximately 600 pm ($1\text{pm} = 1 \times 10^{-12}\text{m}$).

From the above analysis, we can see that the dimensions of our devices are at least an order of magnitude greater than the mean free path length, for air or liquid used as working fluid, therefore, the assumptions for the model hold.

8 - 1.1.2 Thermal Noise

The accelerometer works by measuring a fluid temperature, if the temperature of the gas is measured with a sufficiently small detector over a short time interval, a relatively small number of gas molecules will come into contact with the detector, and the mean kinetic energy of this small sample may differ from the mean kinetic energy of the gas as a whole. This will introduce noise into the measurements, and the noise will be greater as the size of the detector decreases.

Origins of the Noise

According to gas kinetics, the temperature of a gas is a measure of the mean kinetic energy of the gas molecules. However, not all the molecules of the gas have the same kinetic energy; rather, their velocities are distributed according to the expression

$$p(v) = 4\pi\left(\frac{m}{2\pi kT}\right)^{3/2} v^2 \exp\left(\frac{-mv^2}{2kT}\right) \qquad \textbf{(Eq 8 - 2)}$$

Where $p(v)dv$ is the probability that a randomly chosen molecule will have a velocity in the range v to $v+dv$, m is the mass of a gas molecule and k is Boltzmann's constant.

v_m is the root-mean-square velocity of the gas molecules, its value is given by:

$$v_{\text{rms}} = \left(\frac{3kT}{m}\right)^{1/2} \qquad \textbf{(Eq 8 - 3)}$$

And the mean speed of the gas molecules is given by

$$v_m = \int_0^\infty v p(v) dv = \left(\frac{8kT}{\pi m}\right)^{1/2} \qquad \textbf{(Eq 8 - 4)}$$

We represent the velocity of a gas molecule selected at random by

$$v = v_{\text{rms}} + \Delta v \qquad \textbf{(Eq 8 - 5)}$$

When Δv is the difference between the root-mean-square velocity and the velocity of the selected molecule.

Δv can be either positive or negative, so its *mean* value will be close to zero. $(\Delta V)^2$, the mean value of $(\Delta v)^2$ is given by

$$(\Delta V)^2 = \left(\frac{kT}{m}\right)\left(3 - \frac{8}{\pi}\right) \qquad \textbf{(Eq 8 - 6)}$$

From this we can calculate the mean temperature fluctuations of a system made up

of a single molecule. This has been calculated at about 50K. Since 95% of the measurements of a random variable lies within 2 standard deviations of its mean value, therefore, for air at room temperature, it can be expected that 95% of molecules selected will have velocities corresponding to temperatures within 100K of room temperature.

By the Central Limit Theorem, the mean temperature fluctuations of an ensemble of N molecules scale as $1/(\sqrt{N})$. The temperature fluctuations measured by the thermocouple are of size

$$\Delta T_t = \frac{\Delta T_g c_g m_g}{c_t m_t + c_g m_g} \qquad \textbf{(Eq 8 - 7)}$$

where c is specific heat, m is mass, and the subscripts t and g denote the detector and the gas ensemble respectively. (Eq 8 - 7) attains its maximum value when the thermal mass of the gas ensemble we are considering is comparable with that of the detector.

A cylindrical detector made of silicon, radius 0.1 microns, length 500 microns, has a thermal mass of about 10^{-10} J/K. This corresponds to an ensemble of 2×10^{12} air molecules. The fluctuations measured by the detector will therefore be about 10^{-6} times smaller than the temperature fluctuations of a single air molecule, that is, 0.1 milliKelvin or smaller.

For comparison, the temperature differential between the detectors of the accelerometer investigated in Chapter 5 is about 0.1 K for a 1-g acceleration when the working fluid is air, and about 10K for a liquid (isopropanol). Hence, we conclude that the assumptions in our analysis will remain valid until the detector mass is reduced by 100 times.

8 - 1.1.3 Practical Limits

The sensitivity of the accelerometer falls rapidly with reduced size. We have

established that sensitivity is proportional to Rayleigh number, which is proportional to the cube of the cylinder or sphere radius. So if the smallest acceleration measurable by the prototype air-filled accelerometer studied in Chapter 5 is at the order of 0.1g, the smallest acceleration that an air-filled accelerometer one-tenth this size would be able to measure is 100g. This sensitivity could be improved by approximately a thousand times by using a liquid in place of air. A robust accelerometer that could measure accelerations in this range might be used to study the firing and impact of projectiles.

8 - 1.2 Upper Bounds

The practical upper bound on accelerometer size is the point at which the induced temperature difference ceases to be a linear function of Rayleigh number; further acceleration will change the value of the difference, but sensitivity will be reduced. This limit is established by Figure 3 - 8. We have seen that the isopropanol-filled accelerometer investigated in Chapter 5 approaches this limit under an imposed 1-g acceleration, and, from the scaling rules established, an air-filled accelerometer would approach the same limit if the cavity diameter were scaled up to about 1 cm. There is probably no point in considering accelerometers larger than this for terrestial application, as the acceleration due to gravity would induce a permanent distortion of the temperature field, and, for sufficiently large cavities, set up a turbulent flow which would induce unpredictable temperature fluctuations. However, for orbital or space-based applications, it might be possible to obtain extremely high sensitivities by building comparatively large accelerometers based on the buoyancy principle.

8 - 2 Design Implications

We now explore a few design implications, such as optimum location of detectors for geometries of concentric-cylinders and concentric-spheres model.

8 - 2.1 Optimum Location of Detectors

The optimum location for the symmetrical thermal detectors will be at the radial distance from the heater at which the differential temperature reaches its maximum value. This may be found from (Eq 3 - 18), in the case of cylindrical geometry, and from the formula (Eq 6 - 15) in the case of spherical geometry.

8 - 2.1.1 Optimum Location of Detectors for Cylindrical Geometry

Figure 8 - 1 shows the radial position at which the differential temperature reaches a maximum for different values of R for cylindrical geometry. The vertical axis, rmax/R, varies from 0, corresponding to the surface of the inner cylinder, to 1, corresponding to the surface of the outer cylinder. The graph was obtained by keeping the radius of the inner bounding surface constant while increasing the radius of the outer surface. For low values of R, the optimum position is close to the outer bounding surface. As R increases, the optimum position moves closer to the inner surface, reaching a limiting value of about $0.3R$.

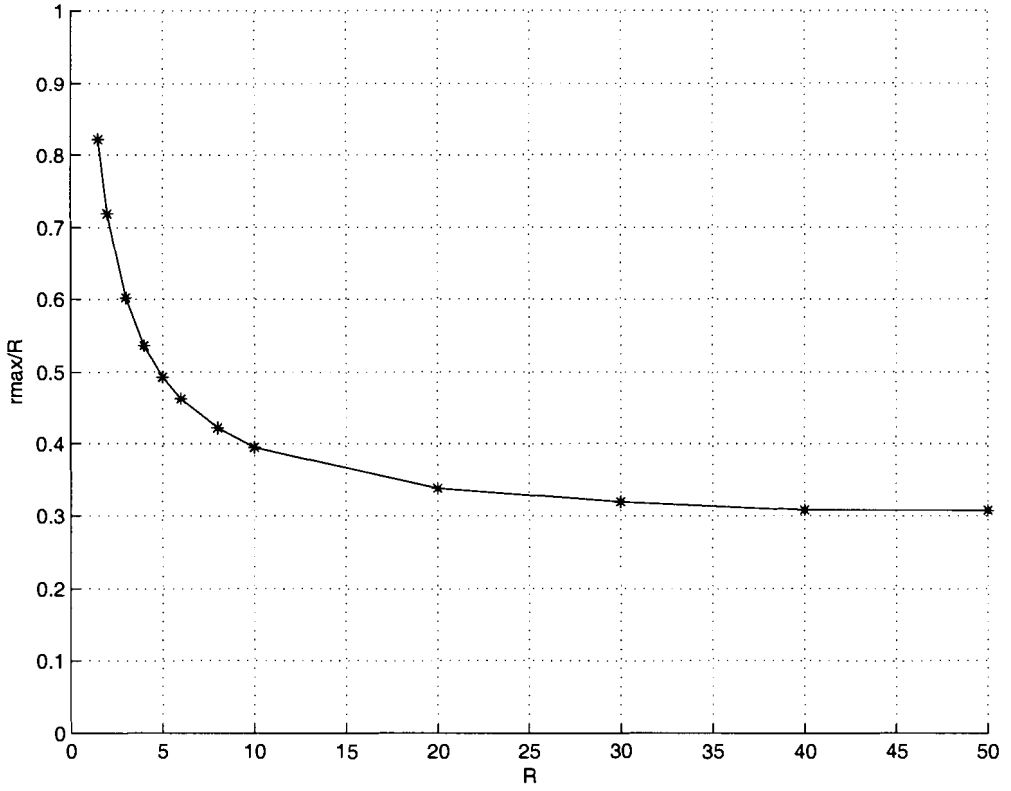

Figure 8 - 1 Optimum location of detectors as a function of R for cylindrical case

8 - 2.1.2 Optimum Location of Detectors for Spherical Geometry

Similarly, Figure 8 - 2, shows the radial position at which the differential temperature reaches a maximum for different values of R for spherical geometry. The vertical axis, rmax$/R$, varies from 0 -- corresponding to the surface of the inner sphere-- to 1 corresponding to the surface of the outer sphere. Again, the graph was obtained by keeping the radius of the inner bounding surface constant while increasing the radius of the outer surface. As R increases, from $0.4R$, the optimum position moves closer to the inner surface, reaching a limiting value of about $0.1R$ for concentric spheres.

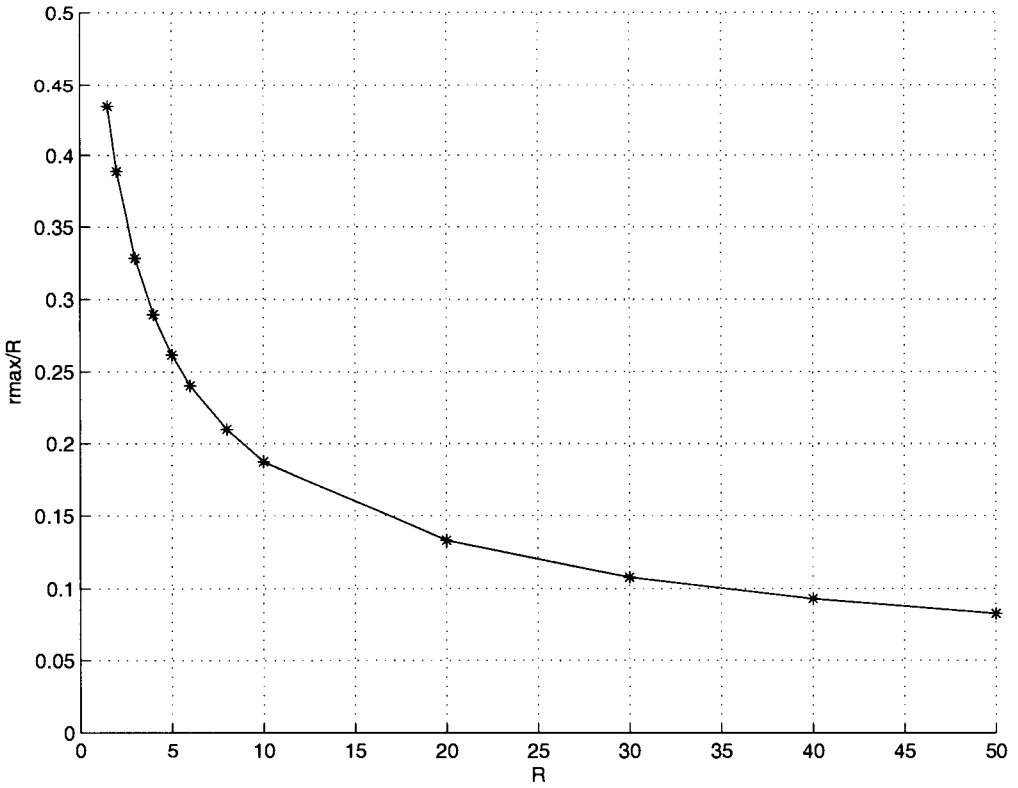

Figure 8 - 2 Optimum location of detectors as a function of R for spherical geometry

8 - 2.2 Trading Sensitivity for Response Time

It has been shown that the isopropanol-filled chip is approximately 1000 times as sensitive as the air-filled chip, but also approximately 100 times slower to respond to an acceleration change. If we reduce r_i and r_o for this chip by a factor of 10, the Rayleigh number will be reduced by a factor of 1000, as will the differential temperature signal. The response time of the shrunken isopropanol chip will be reduced by 100 times as a result of the shrinkage, which will make it slightly faster than the air-filled chip.

So we can trade off increased sensitivity against response time to get an

isopropanol-filled chip that is as sensitive, as fast and ten times smaller than an air-filled chip.

Meanwhile, if a gas under high pressure is used for working fluid, the sensitivity will be increased at the cost of longer response time. (Eq 3 - 18) and our correlation (Eq 4 - 3) will allow us to calculate the effect of this on sensitivity and response time. For instance, if the pressure of air is doubled, the density will be doubled correspondingly, and the Rayleigh number Ra will be increased by 4 times, hence, the sensitivity will be increased by 4 times. From the correlation (Eq 4 - 3), we can deduced that response time will be twice as long.

8 - 2.3 Temperature Sensitivity

One weakness of the microthermal accelerometer which we have not so far discussed results from the change in the properties of potential working fluids with temperature. We have shown that the device sensitivity is proportional to Rayleigh number, which in turn is proportional to the product $\rho^2\beta c/\mu k$.

We evaluate this product for several fluids at 300 K and at 350 K:

Table 8 - 1 Temperature Sensitivity

Fluid	Temp. K	ρ kg/m^3	β K^{-1}	c J/kgK	k W/mK	μ Pa • s	$\rho^2\beta c/\mu k$	change of $\rho^2\beta c/\mu k$
air	300	1.177	1/300	1005.7	0.0262	0.00001983	0.893874×10^7	
air	350	0.998	1/350	1009.0	0.0300	0.00002075	0.461259×10^7	48.40%
water	300	997	0.00018	4180.0	0.614	0.001	0.121807×10^{10}	
water	350	974	0.00018	4196.0	0.668	0.0010364	0.103496×10^{10}	15.03%

Table 8 - 1 shows that the calibration of the accelerometer will change with the ambient temperature. While it is possible to add circuitry to measure the ambient

temperature and compensate for this, it is an undesirable complication. This suggests that further work would be justified to identify fluids for which the product $\rho^2\beta c/\mu k$ changed only slightly with temperature.

8 - 3 Strengths and Weaknesses

Revisiting our comparison of the microthermal accelerometer with its competitors, we have identified some additional strengths and some novel weaknesses. Specifically, we have demonstrated that the sensitivity of the microthermal accelerometer can be increased almost a thousandfold by the use of isopropanol as the working fluid, and have provided theoretical reasons for thinking that even greater increases are possible with the use of other fluids. Moreover, this increase in sensitivity is obtained without compromising the robustness of the accelerometer; a liquid-filled device should be as or more resilient than an air-filled one.

Comparing with its competitor, one weakness of microthermal accelerometer is the slower response time. We have seen that for the air-filled accelerometer, two factors are about equally responsible for the response time: the time taken for the temperature differential to become established, and the time taken for the thermocouple to respond to this. So both of these would need to be improved to reduce the overall response time. The first factor might be improved by making the accelerometer smaller, by using air at reduced pressure as the working fluid, or by replacing the air with a lighter gas, such as helium. However, each of these changes would reduce sensitivity. The second factor could be improved by using a more conductive working gas, such as helium, or by reducing the mass of the thermocouples; again, the former change would reduce sensitivity, while the second would reduce robustness.

Response times for the liquid-filled accelerometer are almost two orders of

magnitude longer than for an air-filled accelerometer of the same dimensions -- of the order of 0.5 seconds for the accelerometer studied in Chapter 5. This is so slow as to rule out certain applications, such as the air-bag trigger. However, as noted in Section 4 - 2.1, these times may be improved by scaling down the liquid-filled version.

A second weakness is stability -- if an accelerometer has been calibrated at a particular temperature, its calibration will be inaccurate at other temperatures, because of the change in the thermophysical properties of the fluid. This might be compensated for either by adding a compensating circuit, or by careful choice of working fluid.

8 - 3.1 Potential Applications

In light of this discussion, the applications to which the microthermal accelerometer is best suited will be those in which the combination of high sensitivity and great robustness is needed. This will include applications in which the accelerometer is subject to very high accelerations (and required to measure relatively small accelerations). For example, it might form part of an instrumentation package for a spacecraft that must survive the accelerations of launch and re-entry, and perhaps a hard landing on a planetary surface. Or it could be used to record the accelerations experienced by an artillery shell on firing and on impact. For the most extreme applications, the liquid-filled accelerometer will be preferable to the air-filled design, since it is much more sensitive while equally robust.

Applications for which the microthermal accelerometer is *not* suited will include those in which the accelerometer will experience a wide range of temperature fluctuations. Liquid-filled accelerometers, in particular, cannot be used under conditions where the working fluid might freeze or boil.

8 - 4 Future Work

In this thesis, we have explored the possibility of using working fluids such as liquid, (more specifically, isopropanol) rather than air in microthermal accelerometer. The effect on performance has been studied theoretically and experimentally, and we have observed that isopropanol gives increased sensitivity, however with longer response time.

It is possible that a systematic survey of possible working fluids would identify other options with further improvements in performance.

Here, by using the formula developed in Chapter 3, 4, 6, and 7 we can evaluate the performance of some different working liquids in the microthermal accelerometer -- their effects on sensitivity and response time.

Some particular fluids of interests are

- high-pressure gases
- glycerine
- liquid metal, such as mercury
- water

In the following sections, the results of using the fluids above mentioned will be discussed.

8 - 4.1 Properties of Possible Working Fluids

Some possible working fluids and their properties are listed in Table 8 - 2.

Table 8 - 2 Properties of possible working fluids

Fluids	k W/(m • K)	μ Pa • s	ρ kg/m^3	c J/(kg • K)	β K^{-1}	α m^2/s	Pr
air	26.07e-3	18.13e-6	1.1768	1.004e3	0.0033	0.2201e-4	0.7153
glycerine	0.286	1.5	1260	2400	0.0005	0.9458e-7	12587
mercury	8.141	0.0017	13595	139	0.000182	0.4308e-5	0.029
water	0.617	0.0007971	1000	4179	0.00018	0.1476e-6	5.3988
Isopropanol	0.119	0.00177	932	2440	0.00062	0.7e-7~0.9e-7	36.3

Concentric Cylinders Geometry

Assume concentric cylinders geometry is used for the accelerometer chip design, with the inner cylinder of $r_i = 0.000020\,\text{m}$ and outer cylinder of $r_o = 0.001\,\text{m}$, hence $R = 50$.

The inner cylinder, i.e. heater, is kept at isothermal at $T_i = 310K$, and the outer cylinder is kept at $T_o = 300K$.

The imposed acceleration imposed is set to 1 g.

8 - 4.2 Predicted Performance Parameters for Accelerometer Chip Filled with Possible Working Fluids

The performance parameters for an accelerometer filled with each of several possible working fluids has been predicted and is given in Table 8 - 3.

Table 8 - 3 Predicted performance parameters for accelerometer chip filled with possible working fluids for the given design geometry

Fluids	*Gr*	*Ra*	MTD K	Sensitivity ratio to air-filled chip	Response Time s	Response time ratio to air-filled chip
air	0.1075e-4	0.7694e-5	0.2371e-2		0.0063	
glycerine	0.2822e-9	0.3553e-5	0.1095e-2	0.46	0.53	84
mercury	0.9311e-2	0.2703e-3	0.083	35	0.21	33
water	0.2266e-3	0.1223e-2	0.3771	160	0.34	54
isopropanol	0.988e-4	0.358e-2	1.1052	500~700	0.5	100

8 - 4.2.1 Glycerine-Filled Accelerometer Chip

If a high-Prandtl number fluid, such as glycerine, is used as the working fluid, the performance parameters can be predicted for the same geometry, as shown Table 8 - 3.

The predicted MTD for glycerine-filled accelerometer chip is 0.001K.

And the sensitivity compared with that of air-filled chip,

$$\frac{\delta T_{gly}}{\delta T_{air}} = \frac{(\rho_{gly})^2 \beta_{gly} c_{gly} k_{air} \mu_{air}}{(\rho_{air})^2 \beta_{air} c_{air} k_{gly} \mu_{gly}} \quad \text{(Eq 8 - 8)}$$

$$= \frac{(1260)^2 \times 50 \times 2400 \times 26 \times 18.53e-6}{(1)^2 \times 330 \times 1000 \times 286 \times 1.5} = 0.46$$

Therefore, compared with air-filled chip, glycerine filled chip would lose some sensitivity due to high viscosity. Hence, glycerine is not an appropriate choice of working fluid.

Since glycerine is high-Prandtl number fluid, the response time to the acceleration changes can be estimated by the correlation developed in section 4 - 2.1 $F_o/R^2 = \frac{\tau\alpha}{r_o^2} = 0.05$, $\alpha = 0.9457e-7\ m^2/s$. such that $\tau = 0.53$ sec.

So a glycerine-filled chip would be both slower and less sensitive than an air-filled chip.

8 - 4.2.2 Mercury-Filled Accelerometer Chip

For low-Prandtl number fluid, such as mercury, the performance parameters can also be predicted, as shown in Table 8 - 3.

The maximum differential temperature predicted is approximately 0.083K

For this low-Prandtl-number fluid, $\alpha = 0.4308e-5\ m^2/s$.

Empirical correlation developed in section 4 - 2.2 shows that $F_o Pr/R^2 = 0.026$, hence, the predicted response time is 0.21 seconds.

Hence the mercury can be considered as a candidate for the working fluid, though it is slower, but it is much more sensitive than air-filled chip.

8 - 4.2.3 Water-Filled Accelerometer Chip

For intermediate-Prandtl number fluid, such as water, the predicted performance parameters are as listed in Table 8 - 3.

It can be seen that the predicted maximum differential temperature for water-filled chip is much higher than that of air-filled chip, more than 160 times higher, and the response time is predicted as: 0.34 seconds.

Comparing the performance parameters of fluid-filled chip with three possible working fluids: glycerine, mercury and water, and with that of air-filled chip, we can see that glycerine is not a preferable choice because it is both slower and less sensitive, whereas mercury and water filled chips are more sensitive but slower in response. It may need some further work to identify a more suitable fluid that can lead to a more sensitive

and rapidly responding accelerometer chip.

8 - 4.3 Practicality of Constructing Liquid-Filled Accelerometers

How practical is it to construct a liquid-filled version of the accelerometer? First, it has been demonstrated in our experiments reported in Chapter 5 that we have succeeded in filling a chip with liquid when the chip was not even designed with this purpose in mind. This experiment suggests that the liquid-filled version can not be that difficult to make. Secondly, one of the points in the production process in which the accelerometers tend to break is when they are dried after etching: the capillary forces of the drying liquid stress the bridges. Therefore, using a liquid-filled chip, it would never be necessary to dry the chip, only to replace the etching fluid with the working fluid. So manufacturing a liquid-filled chip might actually be easier.

In this section, based on our theoretical and experimental results obtained in this thesis, a preliminary study for a few possible working fluids has been given, illustrating the possibility of using different working fluid and their effects on sensitivity and response time.

To conclude, from this point, we can proposed for the future work that a wide range of possible fluids could be explored to find a more suitable working fluid for the purpose to improve sensitivity of the device and response time as mentioned; as well as to improve the stability with temperature, in particular, investigating the temperature dependence of their thermophysical properties, to find fluids for which the Rayleigh number at a given acceleration does not change much with changes in temperature.

Chapter 9 Conclusion

Our major motivation in this thesis has been to establish a basis for the design of microthermal accelerometers. In particular, we want to be able to predict the effect on sensitivity and response time of using working fluids other than air, including liquids. This has been pursued by literature search, by CFD modeling, and by experiment. Here we give a summary of the thesis.

We have first introduced the microthermal accelerometer and made a preliminary comparison with traditional electro-mechanical accelerometers and conventional MEMS capacitive accelerometers. This comparison was re-visited in Chapter 8, after we had established the formulae governing performance.

We next defined a set of assumptions which would allow us to model the accelerometer. We considered two idealizations of the device geometry: concentric cylinders and concentric spheres. These approximately correspond to two possible accelerometer designs, the single-axis and two-axis accelerometer. By considering the heater temperature profile in Appendix II, we suggested that the cylindrical and spherical models bracketed the actual temperature profile of practical accelerometers.

On the basis of these assumptions, the governing equations have been derived, the non-dimensional numbers governing performance have been identified, and CFD models of convective flow in the space enclosed by concentric cylinders and concentric spheres have been built. Both steady-state solution and transient solutions have been sought to establish limits on sensitivity and on response time for both geometries.

To verify these solutions, we have first established their internal consistency by mesh refinement, reported in Appendices III and IV. Exceptional care was needed for this, as the solution sought is the small difference between two large quantities.

The steady-state solutions have been verified quantitatively against prior analytical solutions. Good agreement has been demonstrated with prior literature for both geometries. These steady-state results have also been validated qualitatively against prior experimental work. In the course of these comparisons, closed-form (though lengthy) expressions have been identified which can be used as a guide to subsequent design work.

The transient performance of the accelerometer cannot be predicted from the existing literature, since the initial conditions do not match those of any prior problem. Therefore, guided by the results of dimensional analysis, we have sought novel correlations between Fourier number, Prandtl number and the ratio of radii which can be used to predict the response time of the accelerometer. It has been shown that three different regimes exist, corresponding to low, intermediate and high Prandtl-number working fluids, and separate correlations have been developed for each of these regimes and each of the idealized geometries.

The overall response time of the accelerometer has been estimated based on these correlation results and on the response time of the thermocouples used to measure the differential temperature. It has been shown that the thermocouple response time contributes significantly to the overall response time of the air-filled accelerometer chip, but makes a negligible contribution to the response time for the alcohol-filled chip.

To validate these theoretical analyses, we have constructed a liquid-filled accelerometer and performed static and dynamic tests for both air-filled and liquid-filled accelerometers. Their performance parameters such as sensitivity and response time have been compared and found consistent with the results of our theoretical analysis. We have confirmed that by using a liquid, such as isopropanol, we can increase the accelerometer sensitivity by a factor of 700, though at a cost in response time. Using the formulae established in the thesis, we have shown that even greater performance enhancement may be obtained by the use of other liquids.

Based on these results, we have extended our comparison of the microthermal accelerometer with its competitors, in particular, the capacitive MEMS, accelerometer. We concluded that microthermal accelerometers have many desirable features over traditional electro-mechanical accelerometers and conventional MEMS capacitive accelerometers, such as compact design, light weight, low manufacturing cost, and the combination of sensitivity to small acceleration with high resistance to mechanical shock. On the other hand, we also noted some weaknesses of the microthermal accelerometer, in particular, a relatively slow response time when liquids are used as the working fluid, and, depending on the working fluid used, a change in accelerometer sensitivity with ambient temperature. A systematic survey of possible working fluids to identify a proper working fluid which may reduce these weaknesses has been suggested.

Appendix I Governing Equations with Boussinesq Approximation: Spherical Case

In this appendix, we derive the non-dimensional form of the governing equations for the case of concentric spheres, using the Boussinesq approximation. With Boussinesq approximation, variations in ρ are ignored, except insofar as they give rise to a gravitational force. This closely parallels the derivation of the cylindrical case given in Chapter 2.

For convective laminar flow within enclosure of concentric spheres, the experimental studies (Bishop, Kolflat, Mack and Scanlan 1964) (Bishop, Mack and Scanlan 1966) indicated the flow is both steady and axisymmetric for sufficient low temperature difference. Therefore, spherical coordinates can be used and it can be assumed that all quantities are independent of the longitude and the velocity has no longitudinal component.

The governing equations can be derived into their nondimensional form in a similar manner as for the cylindrical case.

I - 1 Governing Equations

I - 1.1 Continuity Equation

The dimensional form for spherical case is,

$$\frac{1}{r^2}\frac{\partial(r^2 v_r)}{\partial r} + \frac{1}{r\sin\theta}\frac{\partial(v_\theta \sin\theta)}{\partial\theta} + \frac{1}{r\sin\theta}\frac{\partial v_\phi}{\partial\phi} = 0 \qquad \textbf{(Eq I - 1)}$$

Since $\frac{\partial v_\phi}{\partial\phi} = 0$, it can be simplified to,

$$\frac{1}{r^2}\frac{\partial(r^2 v_r)}{\partial r} + \frac{1}{r\sin\theta}\frac{\partial(v_\theta \sin\theta)}{\partial\theta} = 0 \qquad \textbf{(Eq I - 2)}$$

Put nondimensional quantities similarly defined as:

$$\hat{r} = \frac{r}{r_i} \qquad \textbf{(Eq I - 3)}$$

$$\hat{v}_r = v_r\frac{\tau}{r_i},\ \hat{v}_\theta = v_\theta\frac{\tau}{r_i} \qquad \textbf{(Eq I - 4)}$$

The nondimensional form of continuity equation becomes:

$$\frac{2}{\hat{r}^2}\hat{v}_r + \frac{\partial\hat{v}_r}{\partial\hat{r}} + \frac{1}{\hat{r}}\frac{\cos\theta}{\sin\theta}\hat{v}_\theta + \frac{1}{\hat{r}}\frac{\partial\hat{v}_\theta}{\partial\theta} = 0 \qquad \textbf{(Eq I - 5)}$$

I - 1.2 Equation of Motion

The dimensional form of equation of motion in r direction is:

$$\frac{\partial v_r}{\partial t} + v_r\frac{\partial v_r}{\partial r} + \frac{v_\theta}{r}\frac{\partial v_r}{\partial\theta} + \frac{v_\phi}{r\sin\theta}\frac{\partial v_r}{\partial\phi} - \frac{v_\theta^2 + v_\phi^2}{r} \qquad \textbf{(Eq I - 6)}$$
$$= -\frac{1}{\rho}\frac{\partial P}{\partial r} + \frac{\mu}{\rho}\left(\nabla^2 v_r - \frac{2v_r}{r^2} - \frac{2}{r^2}\frac{\partial v_\theta}{\partial\theta} - \frac{2v_\theta\cot\theta}{r^2} - \frac{2}{r^2\sin\theta}\frac{\partial v_\phi}{\partial\phi}\right) + \beta g(T - T_o)\cos\theta$$

Since $v_\phi = 0$, $\frac{\partial v_r}{\partial\phi} = \frac{\partial^2 v_r}{\partial\phi^2} = 0$, $\frac{\partial v_\phi}{\partial\phi} = 0$, it can be simplified as:

$$\frac{\partial v_r}{\partial t} + v_r\frac{\partial v_r}{\partial r} + \frac{v_\theta}{r}\frac{\partial v_r}{\partial \theta} - \frac{v_\theta^2}{r} \tag{Eq I - 7}$$

$$= -\frac{1}{\rho}\frac{\partial P}{\partial r} + \frac{\mu}{\rho}\left(\frac{1}{r^2}\frac{\partial}{\partial r}\left(r^2\frac{\partial v_r}{\partial r}\right) + \frac{1}{r^2\sin\theta}\frac{\partial}{\partial\theta}\left(\sin\theta\frac{\partial v_r}{\partial\theta}\right) - \frac{2v_r}{r^2} - \frac{2}{r^2}\frac{\partial v_\theta}{\partial\theta} - \frac{2v_\theta\cot\theta}{r^2}\right)$$

$$+ \beta g(T - T_o)\cos\theta$$

Put nondimensional quantities $\hat{r}$, $\hat{v}_r$, $\hat{v}_\theta$ defined in (Eq I - 3)(Eq I - 4), and

$$\hat{t} = \frac{t}{\tau} \tag{Eq I - 8}$$

$$\hat{P} = \frac{P}{\rho v^{*2}} = \frac{P}{\rho\left(\frac{r_i}{\tau}\right)^2} \tag{Eq I - 9}$$

It becomes:

$$\frac{\partial \hat{v}_r}{\partial \hat{t}} + \hat{v}_r\frac{\partial \hat{v}_r}{\partial \hat{r}} + \frac{\hat{v}_\theta}{\hat{r}}\frac{\partial \hat{v}_r}{\partial\theta} - \frac{\hat{v}_\theta^2}{\hat{r}} \tag{Eq I - 10}$$

$$= -\frac{\partial \hat{P}}{\partial \hat{r}} + \frac{\mu}{\rho}\frac{\tau}{r_i^2}\left(\frac{1}{\hat{r}^2}\frac{\partial}{\partial \hat{r}}\left(\hat{r}^2\frac{\partial v_r}{\partial r}\right) + \frac{1}{\hat{r}^2\sin\theta}\frac{\partial}{\partial\theta}\left(\sin\theta\frac{\partial \hat{v}_r}{\partial\theta}\right) - \frac{2\hat{v}_r}{\hat{r}^2} - \frac{2}{\hat{r}^2}\frac{\partial \hat{v}_\theta}{\partial\theta} - \frac{2\hat{v}_\theta\cot\theta}{\hat{r}^2}\right)$$

$$+ g\beta(T - T_o)\cos\theta\frac{\tau^2}{r_i}$$

Using nondimensional groups defined as:

$$F_o = \frac{\tau\alpha}{r_i^2} \tag{Eq I - 11}$$

$$Pr = \frac{\mu c}{k} = \frac{\mu}{\rho\alpha} \tag{Eq I - 12}$$

where

$$\alpha = \frac{k}{\rho c} \tag{Eq I - 13}$$

and

$$Gr = \frac{\rho^2 r_i^3 g \Delta T \beta}{\mu^2} \qquad \textbf{(Eq I - 14)}$$

The nondimensional form for equation of motion in r direction becomes:

$$\frac{\partial \hat{v}_r}{\partial \hat{t}} + \hat{v}_r \frac{\partial \hat{v}_r}{\partial \hat{r}} + \frac{\hat{v}_\theta}{\hat{r}} \frac{\partial \hat{v}_r}{\partial \theta} - \frac{\hat{v}_\theta^2}{\hat{r}} \qquad \textbf{(Eq I - 15)}$$

$$= -\frac{\partial \hat{P}}{\partial \hat{r}} + F_o Pr \left(\frac{1}{\hat{r}^2} \frac{\partial}{\partial \hat{r}} \left(\hat{r}^2 \frac{\partial v_r}{\partial r} \right) + \frac{1}{\hat{r}^2 \sin\theta} \frac{\partial}{\partial \theta} \left(\sin\theta \frac{\partial \hat{v}_r}{\partial \theta} \right) - \frac{2\hat{v}_r}{\hat{r}^2} - \frac{2}{\hat{r}^2} \frac{\partial \hat{v}_\theta}{\partial \theta} - \frac{2\hat{v}_\theta \cot\theta}{\hat{r}^2} \right)$$

$$+ Gr(F_o)^2 (Pr)^2 \cos\theta$$

Similarly,

θ direction:

$$\frac{\partial v_\theta}{\partial t} + v_r \frac{\partial v_\theta}{\partial r} + \frac{v_\theta}{r} \frac{\partial v_\theta}{\partial \theta} + \frac{v_\phi}{r \sin\theta} \frac{\partial v_\theta}{\partial \phi} - \frac{v_r v_\theta}{r} - \frac{v_\phi^2 \cot\theta}{r} \qquad \textbf{(Eq I - 16)}$$

$$= -\frac{1}{\rho} \frac{1}{r} \frac{\partial P}{\partial \theta} + \frac{\mu}{\rho} \left(\nabla^2 v_\theta + \frac{2}{r^2} \frac{\partial v_r}{\partial \theta} - \frac{v_\theta}{r^2 \sin^2\theta} - \frac{2\cos\theta}{r^2 \sin^2\theta} \frac{\partial v_\phi}{\partial \phi} \right) + \beta g (T - T_o) \sin\theta$$

Since $v_\phi = 0$, $\frac{\partial v_\theta}{\partial \phi} = \frac{\partial^2 v_\theta}{\partial \phi^2} = 0$, $\frac{\partial v_\phi}{\partial \phi} = 0$, it can be simplified as:

$$\frac{\partial v_\theta}{\partial t} + v_r \frac{\partial v_\theta}{\partial r} + \frac{v_\theta}{r} \frac{\partial v_\theta}{\partial \theta} - \frac{v_r v_\theta}{r} \qquad \textbf{(Eq I - 17)}$$

$$= -\frac{1}{\rho} \frac{1}{r} \frac{\partial P}{\partial \theta} + \frac{\mu}{\rho} \left(\frac{1}{r^2} \frac{\partial}{\partial r} \left(r^2 \frac{\partial v_\theta}{\partial r} \right) + \frac{1}{r^2 \sin\theta} \frac{\partial}{\partial \theta} \left(\sin\theta \frac{\partial v_\theta}{\partial \theta} \right) + \frac{2}{r^2} \frac{\partial v_r}{\partial \theta} - \frac{v_\theta}{r^2 \sin^2\theta} \right)$$

$$+ \beta g (T - T_o) \sin\theta$$

Put nondimensional quantities: $\hat{r}$, $\hat{t}$, $\hat{v}_r$, $\hat{v}_\theta$, $\hat{P}$ defined earlier, the above equation becomes:

$$\frac{\partial \hat{v}_\theta}{\partial \hat{t}} + \hat{v}_r \frac{\partial \hat{v}_\theta}{\partial \hat{r}} + \frac{\hat{v}_\theta}{\hat{r}} \frac{\partial \hat{v}_\theta}{\partial \theta} - \frac{\hat{v}_r \hat{v}_\theta}{\hat{r}} \qquad \textbf{(Eq I - 18)}$$

$$= -\frac{1}{\hat{r}} \frac{\partial \hat{P}}{\partial \theta} + \frac{\mu}{\rho} \frac{\tau}{r_o^2} \left(\frac{1}{\hat{r}^2} \frac{\partial}{\partial \hat{r}} \left(\hat{r}^2 \frac{\partial \hat{v}_\theta}{\partial \hat{r}} \right) + \frac{1}{\hat{r}^2 \sin\theta} \frac{\partial}{\partial \theta} \left(\sin\theta \frac{\partial \hat{v}_\theta}{\partial \theta} \right) + \frac{2}{\hat{r}^2} \frac{\partial \hat{v}_r}{\partial \theta} - \frac{\hat{v}_\theta}{\hat{r}^2 \sin^2\theta} \right)$$

$$+ g\beta(T - T_o) \sin\theta \frac{\tau^2}{r_o}$$

Using dimensional variables, F_o, Pr, Gr defined earlier, the nondimensional form in θ direction becomes,

$$\frac{\partial \hat{v}_\theta}{\partial \hat{t}} + \hat{v}_r \frac{\partial \hat{v}_\theta}{\partial \hat{r}} + \frac{\hat{v}_\theta}{\hat{r}} \frac{\partial \hat{v}_\theta}{\partial \theta} - \frac{\hat{v}_r \hat{v}_\theta}{\hat{r}} \qquad \textbf{(Eq I - 19)}$$

$$= -\frac{1}{\hat{r}} \frac{\partial \hat{P}}{\partial \theta} + F_o Pr \left(\frac{1}{\hat{r}^2} \frac{\partial}{\partial \hat{r}} \left(\hat{r}^2 \frac{\partial \hat{v}_\theta}{\partial \hat{r}} \right) + \frac{1}{\hat{r}^2 \sin\theta} \frac{\partial}{\partial \theta} \left(\sin\theta \frac{\partial \hat{v}_\theta}{\partial \theta} \right) + \frac{2}{\hat{r}^2} \frac{\partial \hat{v}_r}{\partial \theta} - \frac{\hat{v}_\theta}{\hat{r}^2 \sin^2\theta} \right)$$

$$+ Gr(F_o)^2 (Pr)^2 \sin\theta$$

Velocity has no component in the ϕ direction.

I - 1.3 Energy Equation

The dimensional form of energy equation is

$$\rho c \left(\frac{\partial T}{\partial t} + v_r \frac{\partial T}{\partial r} + \frac{v_\theta}{r} \frac{\partial T}{\partial \theta} + \frac{v_\phi}{r \sin\theta} \frac{\partial T}{\partial \phi} \right) \qquad \textbf{(Eq I - 20)}$$

$$= k \left[\frac{1}{r^2} \frac{\partial}{\partial r} \left(r^2 \frac{\partial T}{\partial r} \right) + \frac{1}{r^2 \sin\theta} \frac{\partial}{\partial \theta} \left(\frac{\partial T}{\partial \theta} \right) + \frac{1}{r^2 \sin^2\theta} \frac{\partial^2 T}{\partial \phi^2} \right]$$

it can be rewritten as:

$$\frac{\partial T}{\partial t} + v_r \frac{\partial T}{\partial r} + \frac{v_\theta}{r}\frac{\partial T}{\partial \theta} + \frac{v_\phi}{r\sin\theta}\frac{\partial T}{\partial \phi} \qquad \textbf{(Eq I - 21)}$$

$$= \alpha\left[\frac{1}{r^2}\frac{\partial}{\partial r}\left(r^2\frac{\partial T}{\partial r}\right) + \frac{1}{r^2\sin\theta}\frac{\partial}{\partial\theta}\left(\frac{\partial T}{\partial\theta}\right) + \frac{1}{r^2\sin^2\theta}\frac{\partial^2 T}{\partial\phi^2}\right]$$

Since $\frac{\partial T}{\partial \phi} = \frac{\partial^2 T}{\partial \phi^2} = 0$, it is simplified as,

$$\frac{\partial T}{\partial t} + v_r \frac{\partial T}{\partial r} + \frac{v_\theta}{r}\frac{\partial T}{\partial \theta} = \alpha\left(\frac{1}{r^2}\frac{\partial}{\partial r}\left(r^2\frac{\partial T}{\partial r}\right) + \frac{1}{r^2\sin\theta}\frac{\partial}{\partial\theta}\left(\frac{\partial T}{\partial\theta}\right)\right) \qquad \textbf{(Eq I - 22)}$$

Put the nondimensional quantities $\hat{r}$, $\hat{t}$, $\hat{v}_r$, $\hat{v}_\theta$ and

$$\hat{T} = \frac{T}{T_o} \qquad \textbf{(Eq I - 23)}$$

it becomes,

$$\frac{\partial \hat{T}}{\partial \hat{t}} + \hat{v}_r \frac{\partial \hat{T}}{\partial \hat{r}} + \frac{\hat{v}_\theta}{\hat{r}}\frac{\partial \hat{T}}{\partial \theta} = \frac{\alpha\tau}{r_o^2}\left[\frac{1}{\hat{r}^2}\frac{\partial}{\partial \hat{r}}\left(\hat{r}^2\frac{\partial \hat{T}}{\partial \hat{r}}\right) + \frac{1}{\hat{r}^2\sin^2\theta}\frac{\partial^2}{\partial\theta^2}\hat{T}\right] \qquad \textbf{(Eq I - 24)}$$

and using nondimensional groups F_o, the nondimensional form is obtained as:

$$\frac{\partial \hat{T}}{\partial \hat{t}} + \hat{v}_r \frac{\partial \hat{T}}{\partial \hat{r}} + \frac{\hat{v}_\theta}{\hat{r}}\frac{\partial \hat{T}}{\partial \theta} = F_o\left[\frac{1}{\hat{r}^2}\frac{\partial}{\partial \hat{r}}\left(\hat{r}^2\frac{\partial \hat{T}}{\partial \hat{r}}\right) + \frac{1}{\hat{r}^2\sin^2\theta}\frac{\partial^2}{\partial\theta^2}\hat{T}\right] \qquad \textbf{(Eq I - 25)}$$

We have so far completed the derivation of nondimensional form of governing equations for natural convective laminar flow within the enclosure of concentric spheres.

It can be concluded that from the dimensional analysis that the Fourier number can be calculated from the values of Grashof number Gr, Prandtl number Pr and radius ratio R; however, to determine the exact form of this dependence, we have to do experiments or simulations.

I - 2 Definitions

There are a few definitions that have been used in this appendix:

I - 2.1 The Partial Time Derivation $\frac{\partial f}{\partial t}$

This is the partial time derivative of $f(x, y, z, t)$, where f is any continuum property (e.g. density, velocity, temperature, concentration, etc.).

It represents the change of f with time at a fixed position in space. In other words, $\frac{\partial f}{\partial t}$ is change of f with t as seen by a stationary observer.

I - 2.2 Total Time Derivative $\frac{df}{dt}$.

This is the total time derivative which can be related to the partial time derivative as follows:

$$\frac{df}{dt} = \frac{\partial f}{\partial t} + \frac{dx}{dt}\frac{\partial f}{\partial x} + \frac{dy}{dt}\frac{\partial f}{\partial y} + \frac{dz}{dt}\frac{\partial f}{\partial z} \qquad \textbf{(Eq I - 26)}$$

where $\frac{dx}{dt}, \frac{dy}{dt}, \frac{dz}{dt}$ are the components of the velocity of a moving observer. Therefore, $\frac{df}{dt}$ is the change of f with time as seen by the moving observer.

I - 2.3 Substantial Time Derivative $\frac{Df}{Dt}$.

This derivative is a special kind of total time derivative where the velocity of the observer is just the same as the velocity of the stream, i.e., the observer drifts along with the current:

$$\frac{Df}{Dt} = \frac{\partial f}{\partial t} + u\frac{\partial f}{\partial x} + v\frac{\partial f}{\partial y} + w\frac{\partial f}{\partial z} \qquad \textbf{(Eq I - 27)}$$

where u, v, w are the component of the local fluid velocity $\boldsymbol{V}$. The substantial time derivative is also called the derivative following the motion. The operator $\frac{D}{Dt}$ can also be expressed in vector form:

$$\frac{D}{Dt} = \frac{\partial}{\partial t} + (\boldsymbol{V} \bullet \nabla) \qquad \textbf{(Eq I - 28)}$$

which can then be expressed in the following coordinate systems:

rectangular coordinates (x, y, z):

$$\frac{D}{Dt} = \frac{\partial}{\partial t} + u\frac{\partial}{\partial x} + v\frac{\partial}{\partial y} + w\frac{\partial}{\partial z} \qquad \textbf{(Eq I - 29)}$$

cylindrical coordinates (r, θ, z):

$$\frac{D}{Dt} = \frac{\partial}{\partial t} + v_r\frac{\partial}{\partial r} + \frac{v_\theta}{r}\frac{\partial}{\partial \theta} + v_z\frac{\partial}{\partial z} \qquad \textbf{(Eq I - 30)}$$

spherical coordinates (r, θ, ϕ)

$$\frac{D}{Dt} = \frac{\partial}{\partial t} + v_r\frac{\partial}{\partial r} + \frac{v_\theta}{r}\frac{\partial}{\partial \theta} + \frac{v_\phi}{r\sin\theta}\frac{\partial}{\partial \phi} \qquad \textbf{(Eq I - 31)}$$

Appendix II Longitudinal Temperature Distribution in the Heater

In this Appendix, we will calculate closed-form expression for the longitudinal temperature profile in heaters of two types:

- long heater, the heater is heated all along its length.
- central heater, the heater is heated in the center.

Then, we will study the shape of the temperature profiles by plotting some typical dimensions and material properties characteristic of the accelerometer,

It will be shown that for the dimensions and material properties characteristic of the accelerometer, the shape of the profile depends critically on the heater dimension.

Depending the shape of the heater temperature profile, we can approximate the accelerometer using either the concentric-cylinder model or concentric-spheres model.

II - 1 Longitudinal Temperature Distribution in the Long Heater

This heater is modeled as a prism with cross-section of arbitrary shape, attached to the wall of the cavity at one end. The boundary condition at the other end is obtained from symmetry considerations. The air within the cell and the cell walls are considered to be at the same temperature T_0. Heater is generated per unit volume of the heater at a rate $q\ \mathrm{W/m^3}$. The temperature is considered to be uniform over any cross-section of the heater. Radiative heat losses are ignored. We consider that the heater has reached equilibrium.

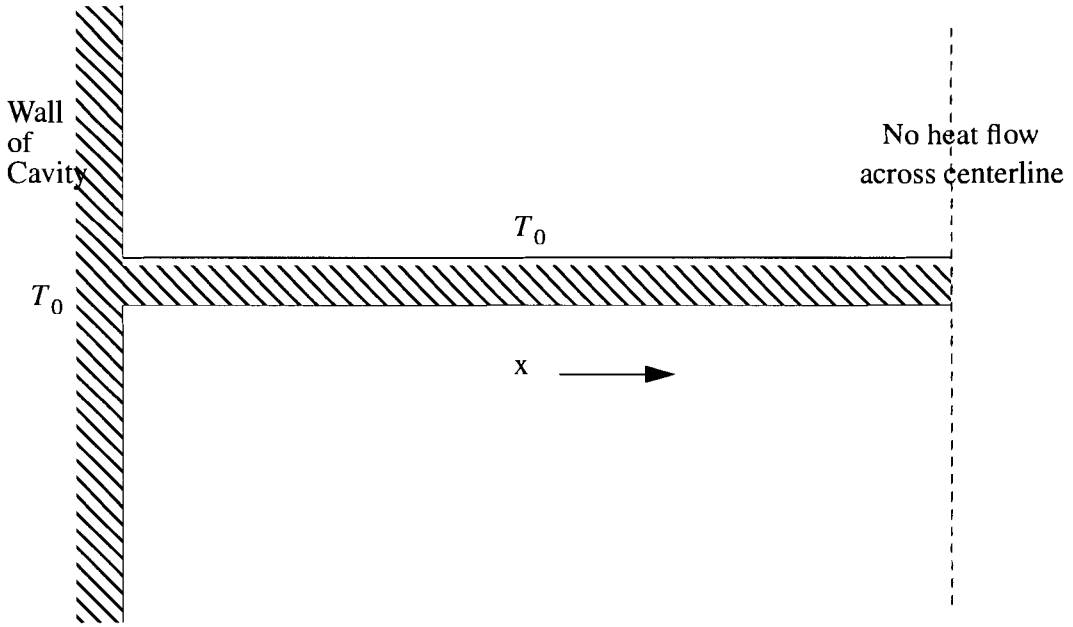

Figure II - 1 Sketch of a long heater

Under these conditions, the temperature is a function of x only, given by the equation

$$\frac{d^2T}{dx^2} - \frac{hP}{kA}(T - T_0) + \frac{q}{k} = 0 \qquad \textbf{(Eq II - 1)}$$

where h is the convective heat transfer coefficient, k is the conductivity of the heater material, P is the perimeter of the heater cross-section, and A is the area of the heater cross-section.

We divide the equation by T_0 and substitute $\theta = (T - T_0)/T_0$ to get:

$$\frac{d^2\theta}{dx^2} - \frac{hP}{kA}\theta + \frac{q}{(kT_0)} = 0 \qquad \textbf{(Eq II - 2)}$$

We multiply the equation by L^2, where L is the half-length of the heater, and put $X = x/L$:

$$\frac{d^2\theta}{dX^2} - \frac{hPL^2}{kA}\theta + \frac{qL^2}{(kT_0)} = 0 \qquad \textbf{(Eq II - 3)}$$

Now we put $m^2 = \frac{hPL^2}{kA}$ and $a = \frac{qL^2}{kT_0}$ to get

$$\frac{d^2\theta}{dX^2} - m^2\theta + a = 0 \qquad \textbf{(Eq II - 4)}$$

This has boundary condition:

$\theta = 0$ at $X = 0$

and

$\frac{d\theta}{dX} = 0$ at $X = 1$.

Integrating the equation, we get

$$\theta = \frac{a}{m^2} + c_1 e^{mX} + c^2 e^{-mX} \qquad \textbf{(Eq II - 5)}$$

Using the boundary conditions to solve for the constants c_1 and c_2, we get

$$\theta = \frac{a}{m^2}\left(1 - e^{mX} + e^m \frac{\sinh(mX)}{\cosh(m)}\right) \qquad \textbf{(Eq II - 6)}$$

It can be seen that from this expression that the shape of the temperature profile depends only on m, not on a, that is the shape is independent of the rate of heat generation or ambient temperature.

We plot this profile for several representative values:

1. Let $h = 10\,\mathrm{W/(m^2K)}$, $k = 20\mathrm{W/(mK)}$ (typical of steel or silicon), $L = 0.001\mathrm{m}$, P = 0.000024 m, $A = 20 \times 10^{-12}\mathrm{m}$. This corresponds to a cavity 2mm across, with a rectangular 2 micron by 10 micron heater cross-section. For this geometry, $m = 0.7$ .This is plotted in Figure II - 2.

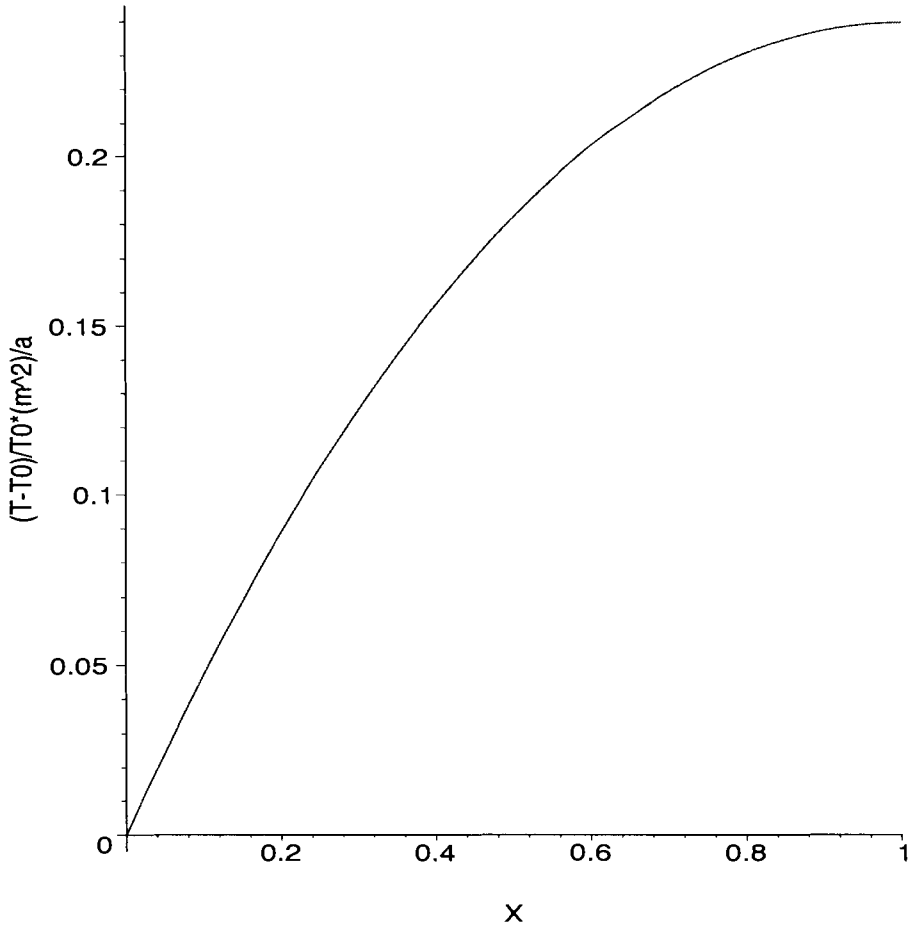

Figure II - 2 Longitudinal temperature profile in the long heater

In the above figure, the x axis is the nondimensional distance $X = x/L$ from 0 to 1, the y axis product of $\theta = (T - T_0)/T_0$ and a constant of m^2/a. This graph has shown that the temperature profile yields a central peak and bounding slopes.

2. To get a more 'plateau-like' profile, we would need to increase m, for example, if we use a lower-conductivity material for the heater, we can get $k = 1\text{W}/(\text{mK})$. We reduce the heater thickness to 0.5 microns. Now $m = 6.5$. This is plotted in Figure II - 3.

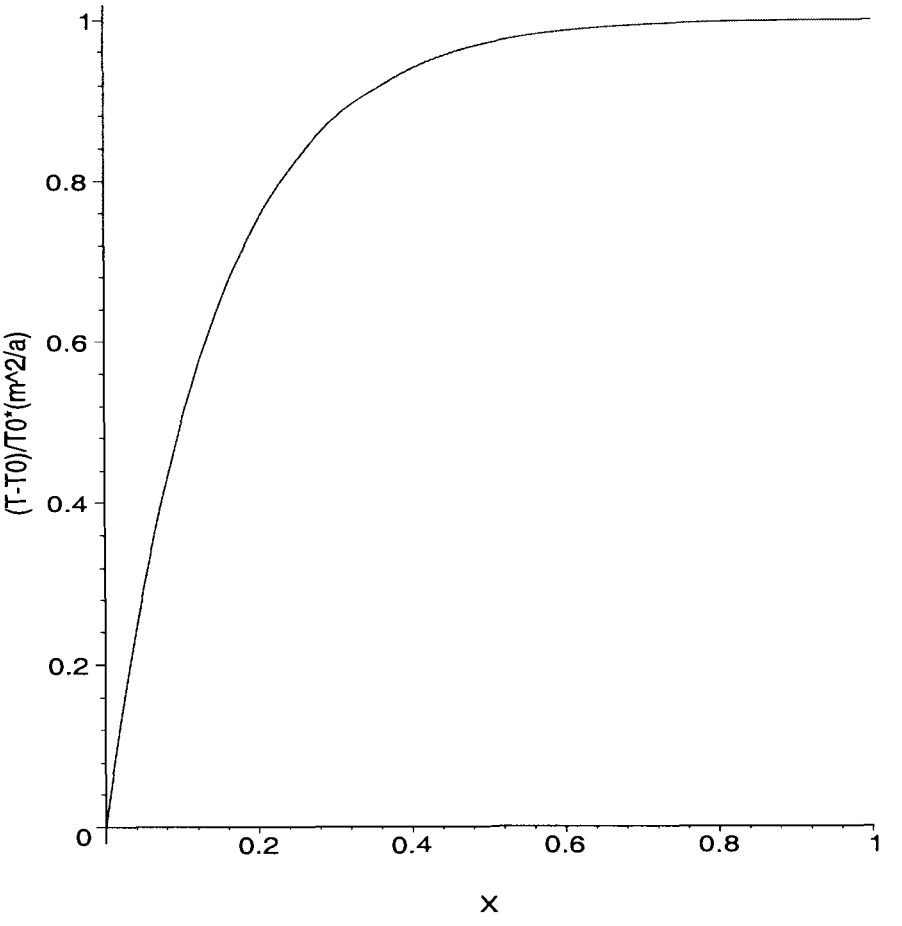

Figure II - 3 Longitudinal temperature profile for a long heater with increased m $m = \sqrt{\frac{hPL^2}{kA}}$.

In the graph the variables being plotted on the x and y axis are the same as in Figure II - 2

The profile is best modeled using the concentric-cylinder model.

It can be seen that m is directly proportional to L, the cavity width. Thus, narrowing the cavity will result in a less plateau-like temperature profile.

II - 2 Longitudinal Temperature Distribution in a Point-Source Heater

In this section, a closed-form expression for the longitudinal temperature distribution in a heater in which all the heat is generated in a small region at the center, as sketched in Figure II - 4.

The heater is modeled as a prism with cross-section of arbitrary shape, attached to the wall of the cavity at one end. The boundary condition at the other end is obtained from symmetry considerations. The air within the cavity and the cavity walls are considered to be at the same temperature, T_0. Heat is generated in a small region at the end of the prism distance from the wall at rate $2q$ watts. The temperature is considered to be uniform over any cross-section of the heater. Radiative heat losses are ignored. We consider the heater to have reached equilibrium.

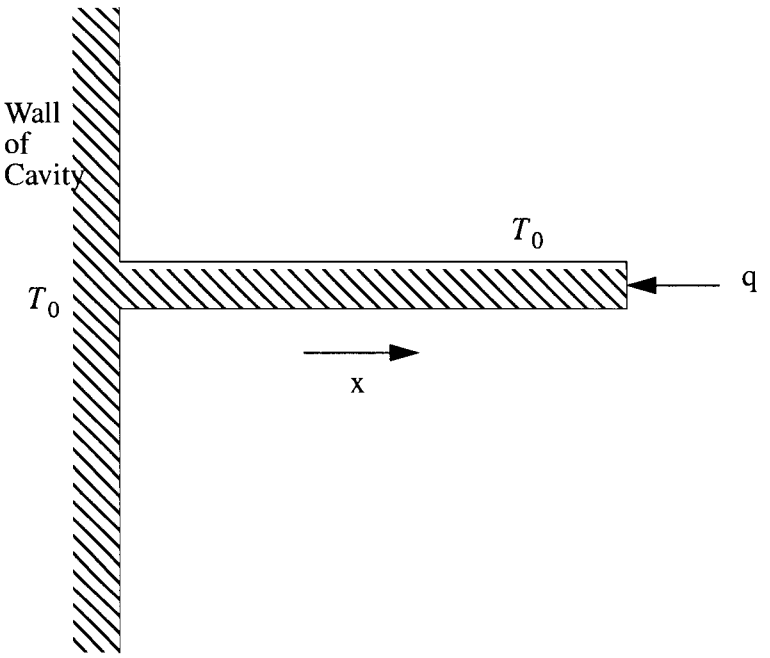

Figure II - 4 Sketch of a central heater

Under these conditions, the temperature is a function of x only, given by the

equation

$$\frac{d^2T}{dx^2} - \frac{hP}{kA}(T - T_0) = 0 \qquad \textbf{(Eq II - 7)}$$

where h is the convective heat transfer coefficient, k is the conductivity of the heater material, P is the perimeter of the heater cross-section, and A is the are of the heater cross-section.

We divide the equation by T_0 and substitute $\theta = (T - T_0)/T_0$ to get:

$$\frac{d^2\theta}{dx^2} - \frac{hP}{kA}\theta = 0 \qquad \textbf{(Eq II - 8)}$$

We multiply the equation by L^2, where L is the half-length of the heater, and put $X = x/L$:

$$\frac{d^2\theta}{dX^2} - \frac{hPL^2}{kA}\theta = 0 \qquad \textbf{(Eq II - 9)}$$

Now, we put $m^2 = \frac{hPL^2}{kA}$ to get

$$\frac{d^2\theta}{dX^2} - m^2\theta = 0 \qquad \textbf{(Eq II - 10)}$$

This has boundary conditions:

$\theta = 0$ at $X = 0$

and

$\frac{d\theta}{dX} = (qL)/(T_0kA)$ at $X = 1$.

Let $Q = (qL)/(T_0kA)$.

Integrating the equation, we get

$$\theta = c_1e^{mX} + c_2e^{-mX} \qquad \textbf{(Eq II - 11)}$$

Using the boundary conditions to solve for the constants c_1 and c_2, we get

$$\theta = \frac{Q\sinh(mX)}{m\cosh(m)} \qquad \textbf{(Eq II - 12)}$$

From above equation, it can be seen that the shape of temperature profiles depends only on m, not on Q. That is, the shape is independent of the rate of heat generation or ambient temperature.

Now, we plot this profile for several representative values:

1. Let $h = 10\,\mathrm{W/(m^2K)}$, $k = 20\mathrm{W/(mK)}$ (typical of steel or silicon), $L = 0.001\mathrm{m}$, P = 0.000024 m, $A = 20 \times 10^{-12}\,\mathrm{m}$. This corresponds to a cavity 2mm across, with a rectangular 3 micron by 20 micron heater cross-section. For this geometry, $m = 0.8$ .This is plotted in Figure II - 5.

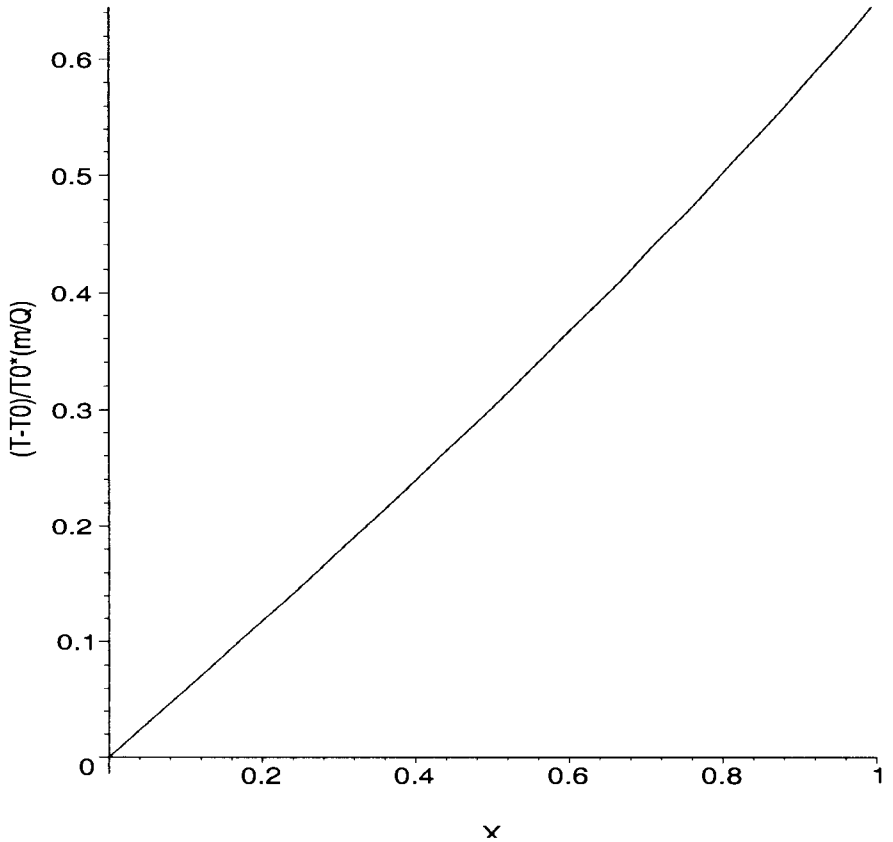

Figure II - 5 Longitudinal temperature profile for a central heater

In Figure II - 5, the x axis is the nondimensional distance $X = x/L$ from 0 to 1, the y axis product of $\theta = (T - T_0)/T_0$ and a constant of m/Q.

2. To get a less 'Fujiyama-like' profile, we would need to increase m for example, if we use a lower-conductivity material for the heater, we can get $k = 1\text{W}/(\text{mK})$. We reduce the heater thickness to 0.5 microns. Now $m = 6.9$. This is plotted in Figure II - 6

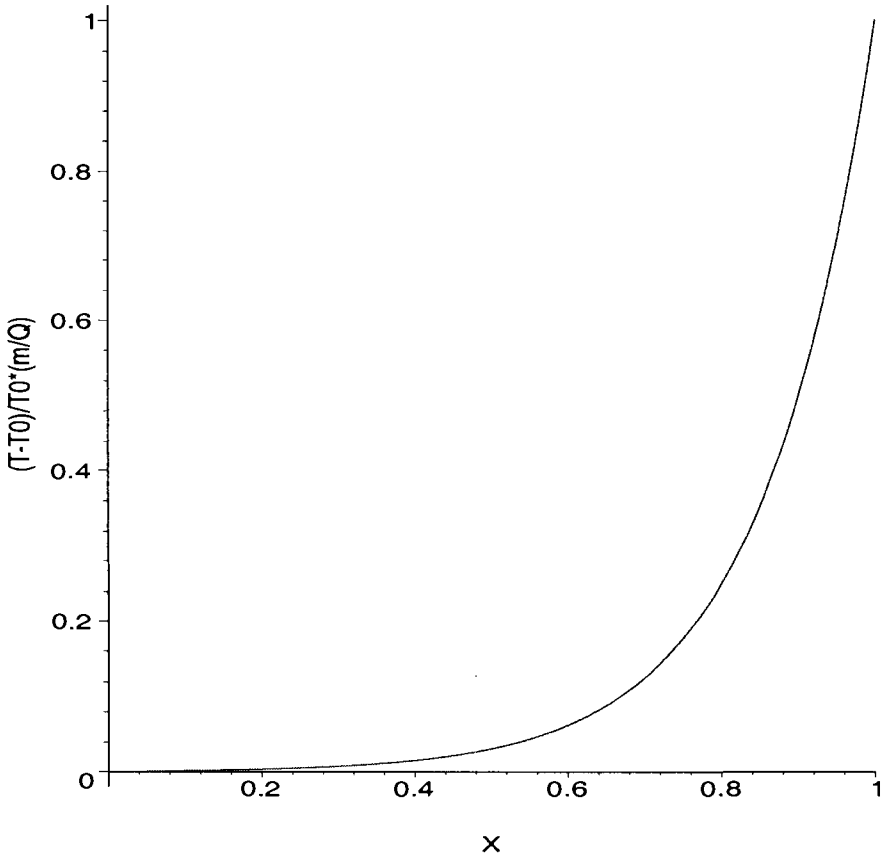

Figure II - 6 Longitudinal temperature profile for a central heater with increased m $m = \sqrt{\frac{hPL^2}{kA}}$

In the graph the variables being plotted in x and y axis are the same as in Figure II - 5.

It can be seen that m is directly proportional to L, the cavity width. Thus, narrowing the cavity will result in a less Fujiyama-like temperature profile. The heater

profiles in both Figure II - 5 and Figure II - 6 are best modeled using the concentric-spheres model.

Hence, from above analysis in this appendix, the range of heater profiles is bounded by the concentric-cylinders model at one end, and the concentric spheres model at the other. Equations II-6 and II-12 can be used to determine which is the better approximation to a given device.

Appendix III Mesh Refinement for the Concentric Cylinders Model

III - 1 Mesh Studies for Steady-State Case

A regular unscaled radially symmetric mesh is used in steady-state FLOTRAN analysis for concentric cylinders model. A suitable mesh size was arrived at mesh refinement studies.

III - 1.1 Study of the Effect of Mesh Size

Simulations with a range of mesh sizes were used to determine the sufficient mesh size. The maximum temperature differential outputs corresponding to each mesh size are listed in Table III - 1.

Table III - 1 Effect of unscaled size, FLOTRAN steadystate analysis of concentric cylinders model

Model mesh size (radial, circumferential)	Number of nodes	Max. Diff. Temp. K
0.00020m, 5°	432	0.00222033
0.00010m, 5°	740	0.00262246
0.00005m, 5°	1406	0.00278191
0.00003m, 5°	2294	0.00281313
0.00002m, 5°	3404	0.00282402
0.00001m, 5°	6734	0.00282901

The effect of mesh size can be observed more clearly in graphic form, shown in

Figure III - 1. For a data point in the graph, the value on the x axis is the total number of nodes generated by meshing with particular mesh size shown in Table III - 1, the value on the y axis is the solution of maximum temperature differential by using that mesh setting. It can be seen that the maximum temperature differential of the concentric cylinders model is bounded when the mesh is getting finer. The optimal mesh size is arrived at by increasing the number of mesh divisions until no mesh-dependent changes were seen in the solution; for current concentric cylinders model, this was achieved with 20 radial divisions and 72 circumferential division, i.e., mesh size in the radial direction at 0.00005m and 5° in the circumferential direction, corresponding to a total of 1406 nodes in the model.

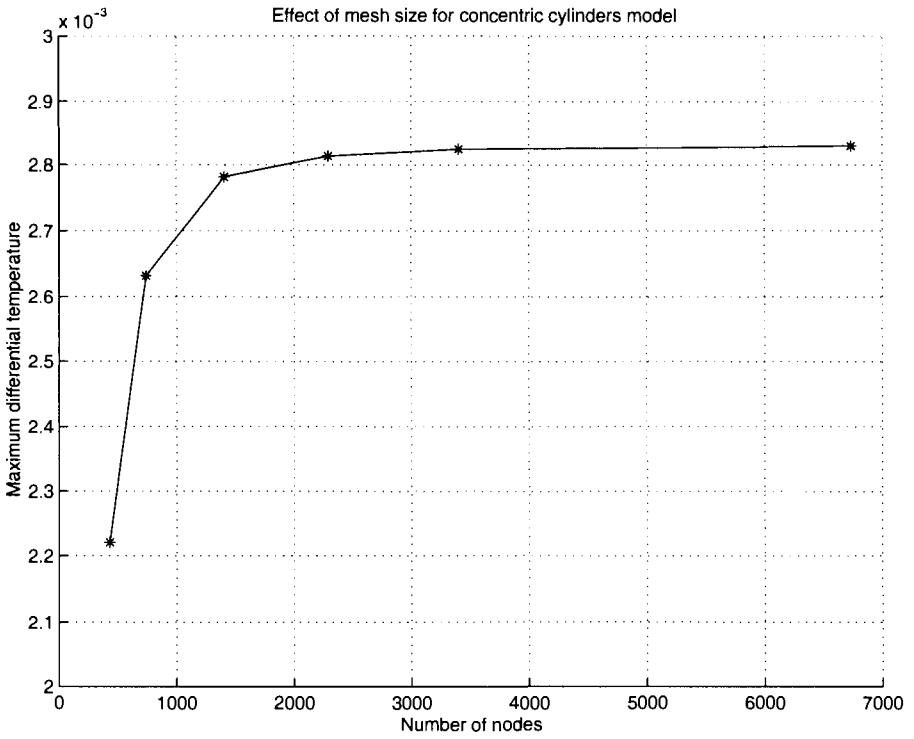

Figure III - 1 Effect of mesh size for FLOTRAN steady-state analysis of concentric cylinder model

III - 1.2 Mesh

The optimal mesh arrived from study of effect of mesh refinement on steady-state solution MTD is shown as Figure III - 2.

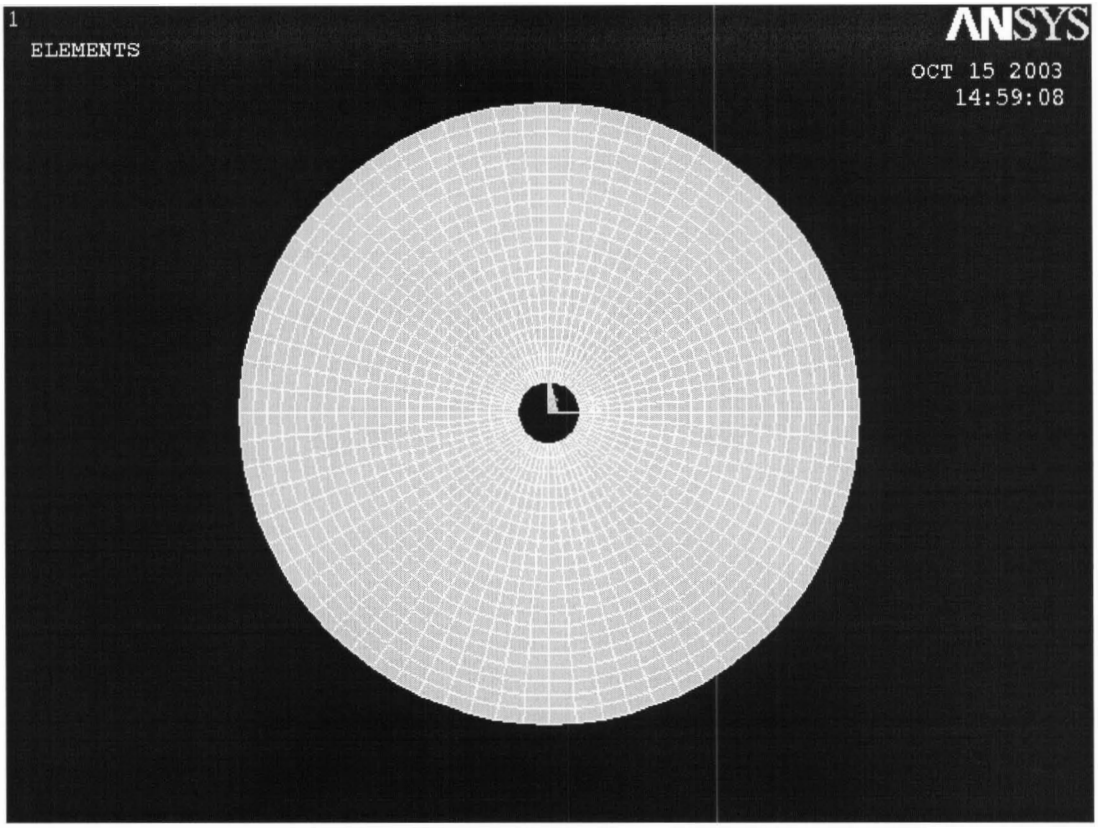

Figure III - 2 Radially symmetric unscaled mesh for concentric cylinders model, mesh size 0.00005m, 5°

III - 2 Scaled Mesh Studies for Transient Case

Transient studies at high-Prandtl-number fluid and high radius ratio place higher demand on the computation efficiency and accuracy. Therefore, in transient analysis for the cylindrical case, to derive the empirical correlation of response time with a wide range

of radius ratio from 1.5 to 80, FLOTRAN concentric-cylinders models were built using a scaled mesh, and mesh refinement studies were repeated to ensure that the predicted temperature difference and response time were mesh-independent.

III - 2.1 Scaled Mesh

A scaled mesh for concentric-cylinders model of $R = 50$ is illustrated in the Figure III - 3, in which the radial divisions are adjusted with space ratio such that more nodes are distributed in the area close to the inner cylinders, since there are more temperature gradient and velocity changes occurring in this area.

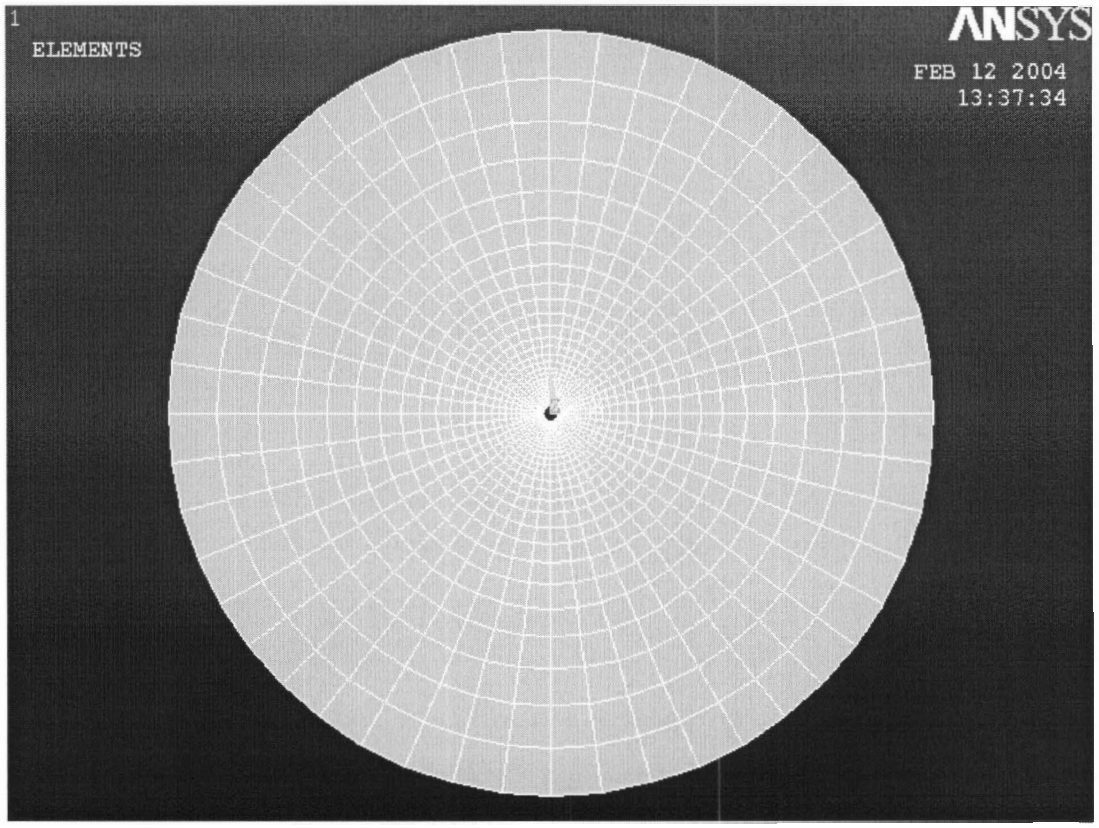

Figure III - 3 Radially symmetric scaled mesh for concentric cylinders model for R=50, total 1550 nodes

III - 2.2 Study of Scaled Mesh Refinement

To obtain the optimal number of divisions in the radial and circumferential directions, the effect of mesh refinement was studied. In this section, we present the effect of refining a scaled mesh for the concentric cylinders case.

The particular FLOTRAN model under investigation is natural convection between concentric cylinders. The working fluid is a high-Prandtl-number fluid, $Pr = 15.6$. The radius of inner cylinder is 20 microns and the radius of outer cylinder is 1000 microns. This is a case of high radius ratio ($R = 50$), therefore, it is more appropriate to use scaled mesh. By defining a scaling ratio of $1/R$ between the radial extent of the innermost and outermost element, we ensure each element in the mesh is approximately square.

The effect of mesh size on the predicted time taken for the velocity and temperature fields to develop, τ_v and τ_T respectively, is shown in Figure III - 4. From this figure, we can observe that both τ_v and τ_T converge as the mesh is refined in the radial direction from 10 to 35 divisions, and the circumferential mesh is set at division of 10°, 9°, 7.5°, 6°, 5° apart. τ_v settles between 75 and 76 microseconds, while τ_T settles between 2230 and 2315 microseconds.

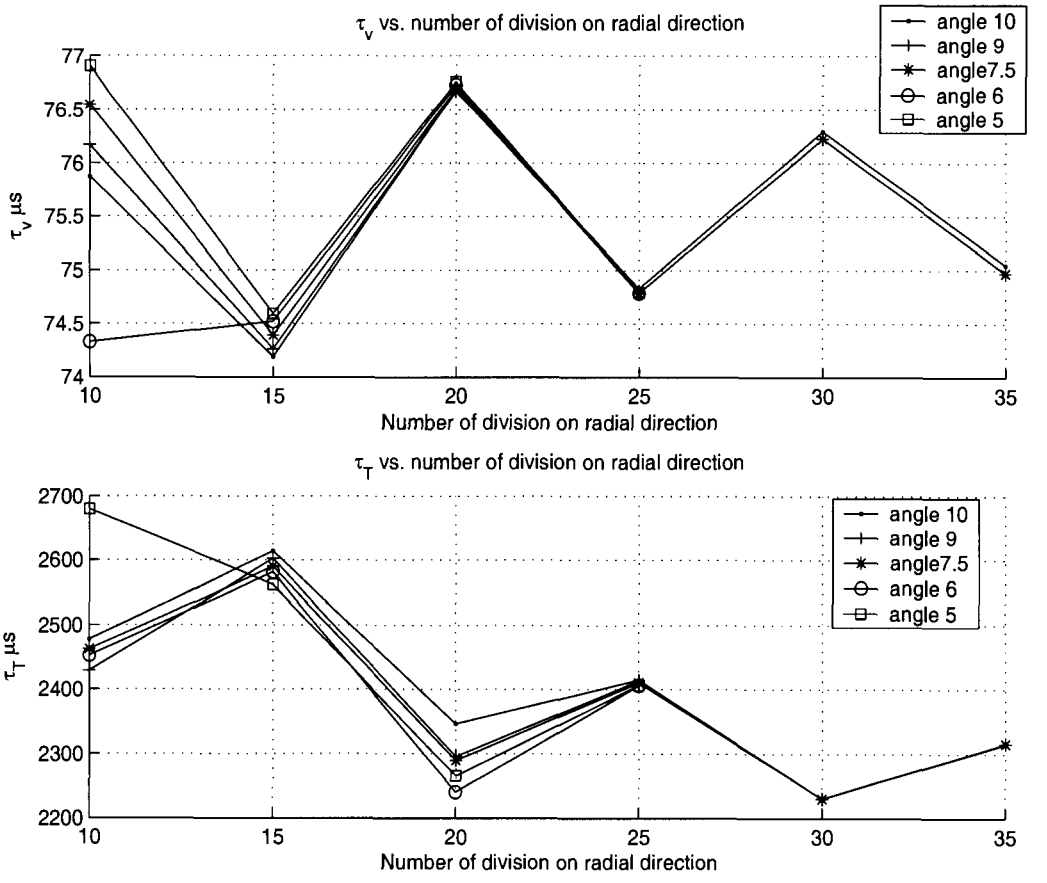

Figure III - 4 Scaled mesh study for FLOTRAN transient study of concentric cylinders model

As the conclusion of this study, the optimal mesh size arrived at is 30 divisions in the radial direction and 7.5° apart, that is 48 divisions in the circumferential direction, this corresponds to a total of 1550 nodes in the model, this optimal mesh is as shown in Figure III - 3. This spacing has been used in all FLOTRAN simulations of transient behavior of concentric cylinders model.

Appendix IV Mesh Refinement for the Concentric Spheres Model

In our FLOTRAN analysis of the concentric-spheres model, at preprocess mesh mapping stage, a few alternative volume meshings have been explored, including free-volume mesh, regular unscaled volume mesh, and scaled mesh, to establish the internal consistency of the model, that is to ensure mesh size does not affect the solution. After detailed evaluation of these three meshing options, the appropriate mesh and mesh size are chosen to solve current problem.

IV - 1 Volume Meshing in FLOTRAN Steady-State Analysis of Concentric Spheres Model

IV - 1.1 Free - Volume Mesh Study

An initial attempt at solving steady-state solution of concentric spheres model using FLOTRAN involved meshing the concentric-sphere-model with a free-volume mesh.

Free-volume meshing is an automated process of generating a mesh with tetrahedral FLOTRAN 3D elements on the solid model. The user sets a single parameter to control the level of meshing from coarse to fine.

IV - 1.1.1 Free - Volume - Mesh Procedure

FLOTRAN steady-state analysis of concentric-spheres model using free-volume-

mesh, involves the following steps:

1. Create partial annulus with center at 0, 0, inner radius of 0.0001m, outer radius of 0.001m, from 90° to 270°. This corresponds to the radius ratio $R = 10$. Other radius ratios can be realized by changing the inner sphere radius.
2. Mesh the area with *regular* mesh with M divisions on straight line and N division on circumferential curve.
3. Extrude the meshed area 90° about the Y axis to create a volume.
4. Now, mesh the volume using *free-volume-mesh*. FLOTRAN will ensure that the nodes of the regular mesh coincide with the nodes of the free-volume mesh at the annular surfaces.
5. Reflect meshed volume on Y, Z plane on the other half of X axis.
6. Coincide those nodes on the same boundary which belong to both volumes.
7. Apply loads: temperature on inner sphere: 310K, on outer sphere: 300K; velocity V_x, V_y, V_z on all the boundaries of inner sphere and outer sphere to 0 m/s, V_z set to 0 m/s on the area of center plane of the hemisphere; acceleration on x direction set to 10 m/s^2.
8. Set up simulation control, let the simulation run to 1000 iteration, with convergence criteria set to 10^{-6} for pressure and 10^{-8} for temperature.
9. The velocity solver is Tri-Diagonal Matrix Algorithm (TDMA); for the incompressible pressure equation, the solver is Preconditioned Conjugate Gradient Method (PCG); and temperature solver is TDMA.

A series of models were set up following the above procedure, using successively finer free meshes, expecting to find a optimal mesh size.

Figure IV - 1 shows irregular free-volume mesh generated by this free-volume-mesh procedure. Note that one of the exposed annular surfaces displays a regular mesh,

though the column is meshed with tetrahedral elements.

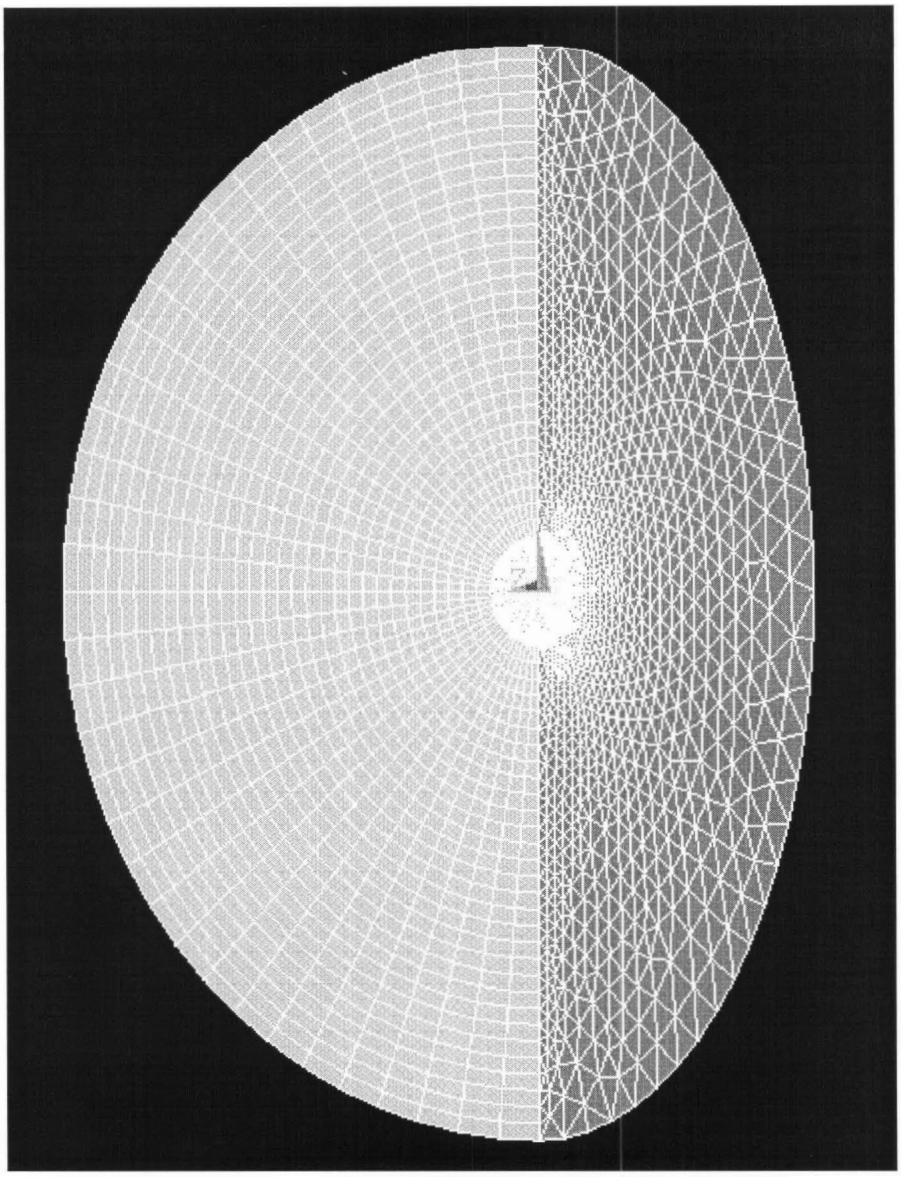

Figure IV - 1 Free -volume mesh, FLOTRAN concentric spheres modeling

IV - 1.1.2 Effect of Free-Volume Mesh Size Study

For our FLOTRAN analysis, we note that there is a particular difficulty of solving the maximum temperature differential (MTD), which is in fact a very small difference

between two large quantities at symmetrical points, so it requires those quantities to be calculated very precisely.

A study has been done, in which we increase the number of mesh nodes, and hence mesh elements, from coarse, medium to fine. In Figure IV - 1 the mesh shown is the irregular medium free-volume mesh. This particular mesh contains a total of 10,342 mesh nodes for a quarter of a sphere.

A series of simulations on the effect of mesh size shows that as we increase the number of nodes, and hence number of elements, the steady-state solution of maximum temperature differential (MTD) of two symmetrical nodes on the central path line diminishes, as shown Figure IV - 2.

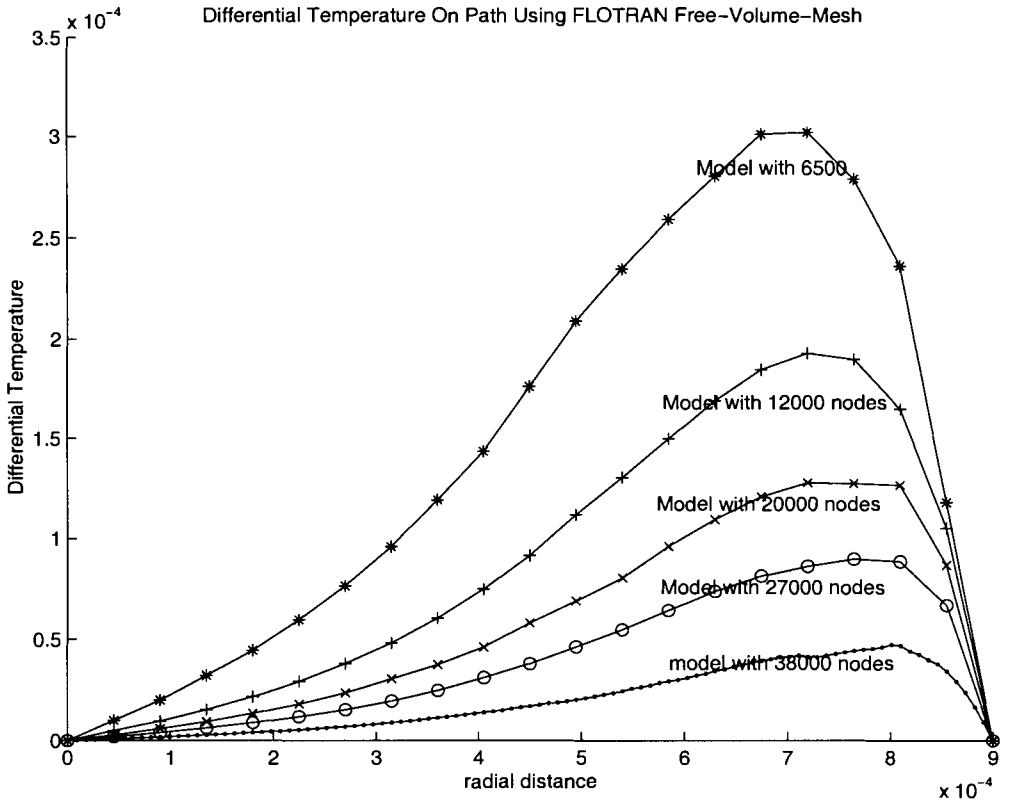

Figure IV - 2 Effect of free-volume mesh size, FLOTRAN concentric spheres modeling

It can be seen that the free-volume-mesh is not appropriate in solving our

concentric sphere model problem, because the simulation results of interest to us are dependent on the mesh size, and there is no sign of the results approaching an asymptotic limit as the mesh is refined. Hence, the mesh built by free-volume-mesh process can not satisfy our requirement for the modeling. We must search for a more appropriate meshing process, it will be discussed in the following sections.

IV - 1.2 Regular-Volume-Mesh Study

The second mesh mapping scheme evaluated in FLOTRAN steady-state analysis of the concentric spheres problem is regular volume mesh mapping. The major difference between free-volume-mesh and regular-volume-mesh is the mapping generated, irregular for the free-volume mesh, and regular for the latter.

IV - 1.2.1 Regular-Volume-Mesh Procedure

The regular-volume-mesh is created as follows:

1. Create partial annulus with center at (0, 0), inner radius of 0.0001m, outer radius of 0.001m, from 90° to 270°.
2. Mesh the area with regular mesh with M divisions on straight line and N division on circumferential curve.
3. Extrude the meshed area 180° about the Y axis to create a volume consisting of volume segments at L° apart.

Remaining steps as for free-volume mesh.

Using the above procedure, a regular volume mesh was generated, as shown in Figure IV - 3.

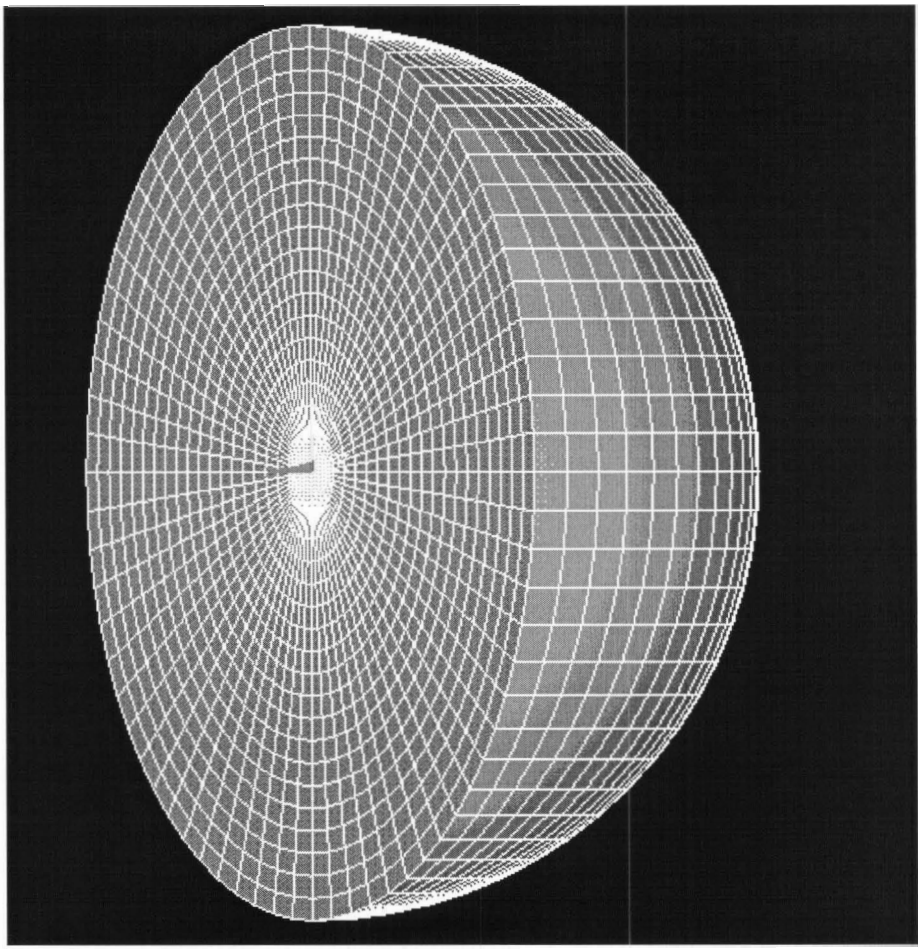

Figure IV - 3 Regular Volume Mesh, 20, 72, 36 divisions in radial, circumferential and azimuthal directions respectively, FLOTRAN concentric-spheres modeling

IV - 1.2.2 The Effect of Regular-Volume-Mesh Size

The effect of mesh size of regular-volume-mesh on the steady-state solution has also been studied. In this study, a series of FLOTRAN concentric-sphere models were built with regular mesh of different size for the case of $Pr = 0.7$, $R = 10$, corresponding to air as working fluid, the detail of modeling is listed in Table IV - 1

Table IV - 1 Effect of regular volume-mesh size for concentric-spheres model

Mesh Size	Total Nodes	Max. Diff. Temp
0.00015m, 15°,15°	1015	0.000683570
0.00010m, 10°,10°	3250	0.00134743
0.00005m, 5°,5°	24643	0.001629370
0.00003m, 3°,3°	111631	0.001701030

These data can be better presented in graphic format, as shown in Figure IV - 4.

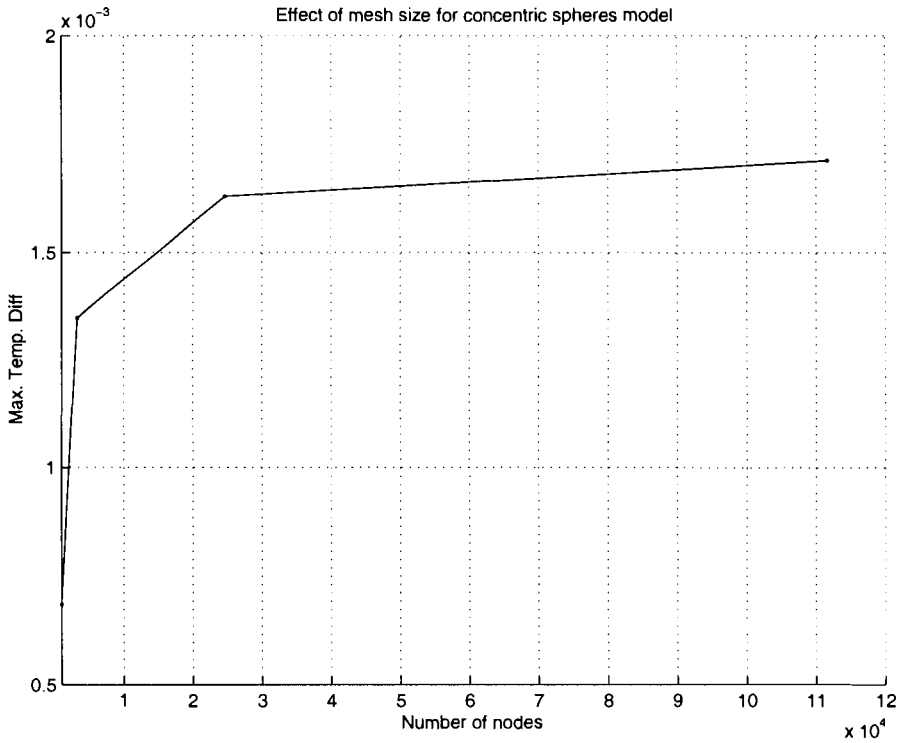

Figure IV - 4 Effect of regular volume-mesh size, FLOTRAN concentric spheres modeling

In Figure IV - 4, the MTD on the path has been plotted versus the total number of nodes for each mesh size. As the mesh gets finer, the MTD becomes relatively independent of mesh size. Compared with free-volume mesh, regular-volume-mesh is therefore a better choice. The finest mesh size used corresponded to a regular volume-

mesh size of (0.00003m, 3°, 3°): the hemisphere has 30 divisions in radial direction, 120 and 60 divisions in circumferential and azimuthal directions respectively. As shown in Table IV - 1, this fine mesh contains more than 100,000 nodes, and computation time of such fine mesh is prohibitive (100 hours on Sun Ultra 10). Hence, in FLOTRAN steady-state analysis of concentric spheres model using regular volume mesh, an optimal choice of mesh size of (0.0005m, 5°, 5°) can be arrived considering computation amount and accuracy. This mesh size corresponded to 20 divisions in the radial direction, and 72 and 36 divisions in the circumferential and azimuthal direction respectively. Such regular volume meshing result is shown in Figure IV - 3.

IV - 1.3 Scaled Regular-Volume Mesh Study

In transient analysis for concentric sphere problem, as we discussed in Section 7 - 2, to derive the correlation for a range of radius ratio from 1.5 to 50, due to the nature of the problems, especially for high-Prandtl-number fluid and high radius ratio cases, a scaled mesh is more computationally efficient than the regular mesh.

In this section, we first discuss the scaled mesh refinement on steadystate solution.

IV - 1.3.1 Scaled Regular-Volume Mesh Versus Unscaled Mesh

A *scaled* regular-volume mesh is generated by following the regular-volume mesh procedure given in Section IV - 1.2.1 except for radial division, the space ratio option is turned on and set to the reciprocal of radius ratio of the model. The effect of this change is to make each of the mesh element more nearly cubic.

The following figures show the comparison between unscaled mesh (Figure IV - 5) and scaled mesh (Figure IV - 6) for the same number of divisions in the radial direction (20 divisions), circumferential direction (72 divisions, 5 ° apart), and azimuthal direction

(36 divisions, 5 ° apart).The model being shown is of radius ratio $R = 20$. The meshed plane shown in both figures is the central plane at $z = 0$ of the sphere. It can be seen that with the scaled mesh, the elements in the region near the inner sphere are closer to cubic shape than those with the unscaled mesh.

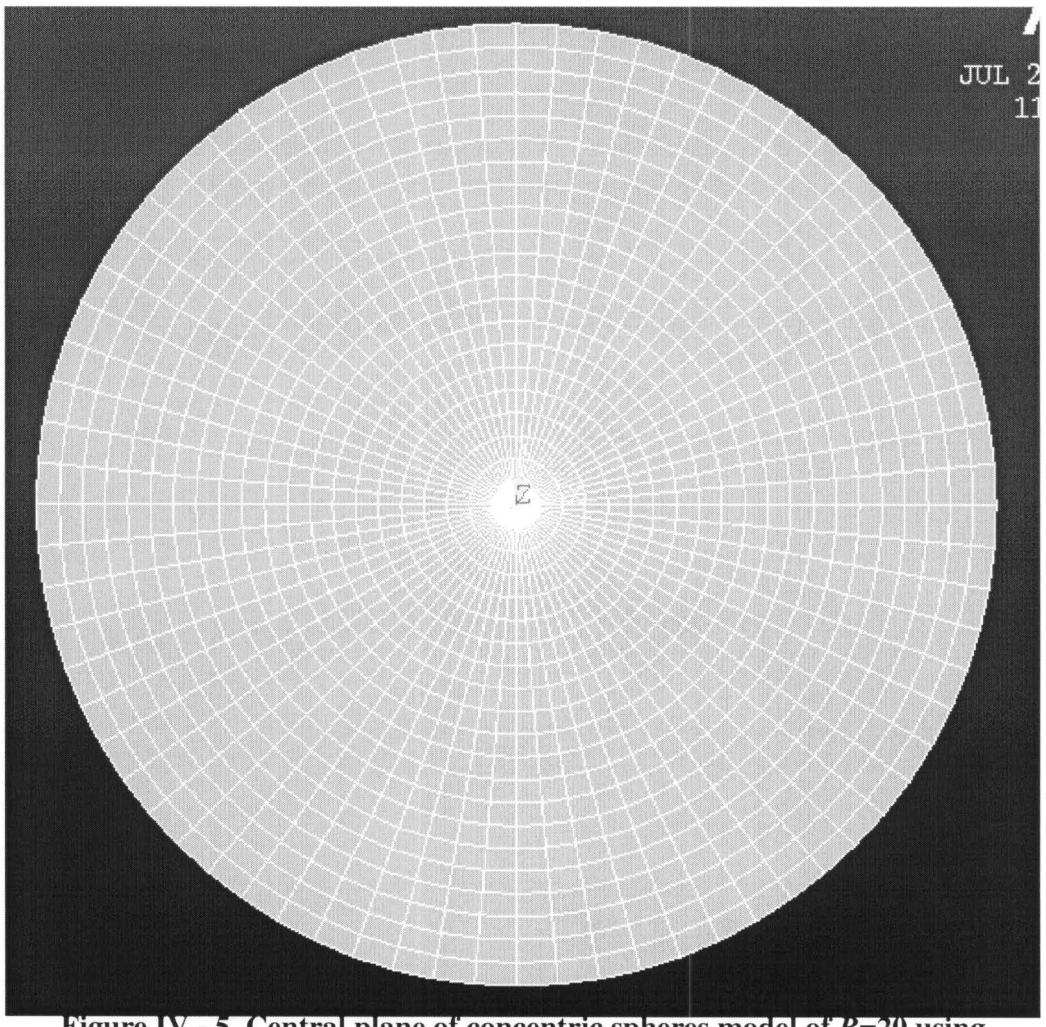

Figure IV - 5 Central plane of concentric spheres model of R=20 using unscaled regular mesh, 20, 72, 36 divisions in the radial, circumferential, and azimuthal direction respectively.

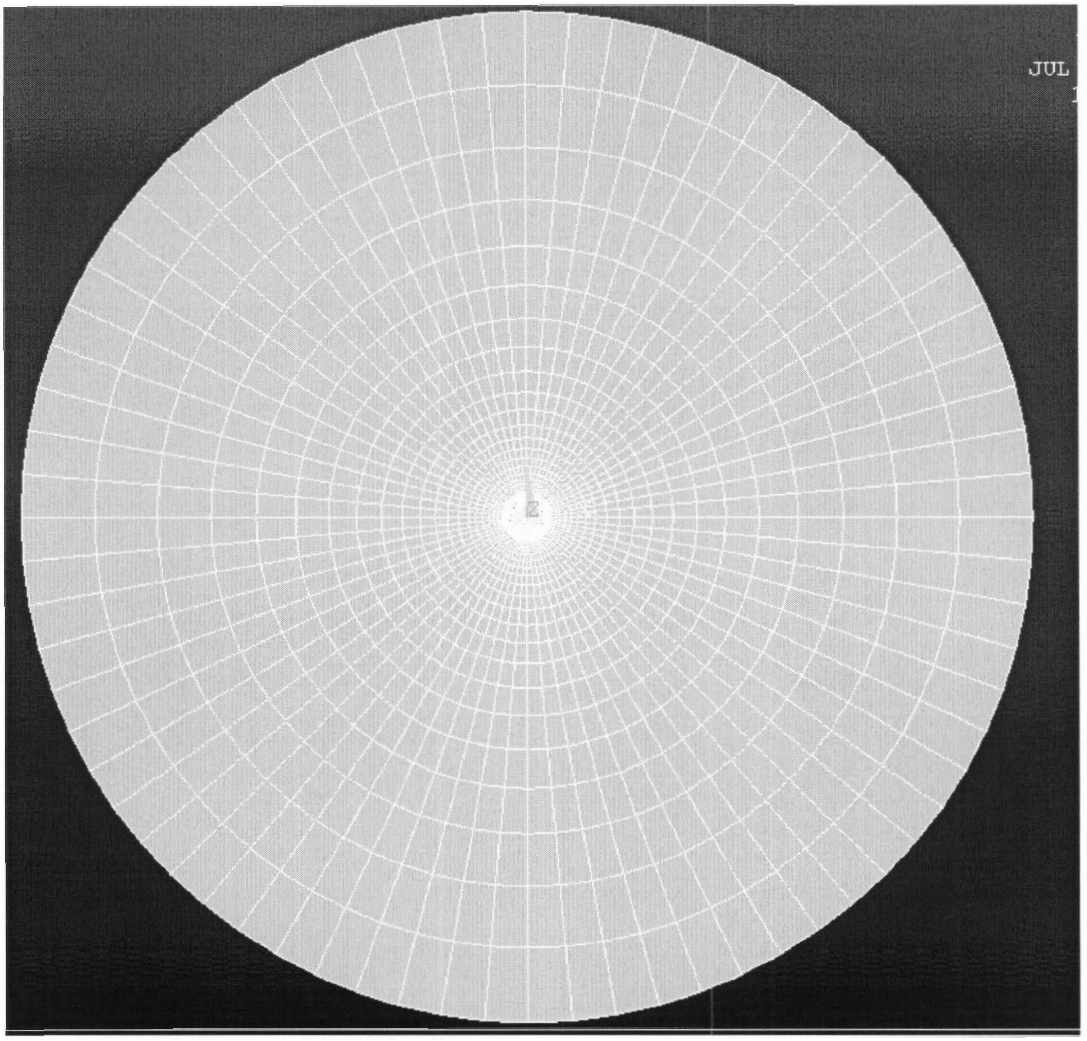

Figure IV - 6 Central plane of concentric spheres model R=20 using scaled regular volume mesh, space ratio: 1/20, 20, 72, 36 divisions in the radial, circumferential, and azimuthal direction respectively

IV - 1.3.2 Ratio of Measured Quantities to Model Artifacts for Scaled Mesh

In our FLOTRAN concentric-spheres modeling, due to the low values of Ra, the absolute value of maximum temperature differential and maximum velocity is small, as will be shown later, numerical artifact becomes an important issue. To illustrate the

concept of numerical artifact, we take a more obvious example, if a FLOTRAN concentric-spheres model is built with the most coarse mesh setting of 10 divisions, 10°, 10°, we are unable to detect the maximum temperature differential (showing negative value) with acceleration set at $10\mathrm{m}/\mathrm{s}^2$.

Apparently it was overshadowed by numerical artifacts at this mesh size. We therefore undertook a series of studies in which the required quantities such as maximum temperature differential (MTD) and maximum velocity and the values of their numerical artifacts were all recorded. By monitoring the ratio of these quantities to their corresponding artifacts at each mesh setting, we found it was possible to increase the accuracy of computing by increasing the value of the imposed acceleration, hence decreasing relative size of artifacts.

The specific case under investigation is the FLOTRAN concentric-spheres model built by scaled regular-volume mesh, the radius ratio of $R = 20$, with radius of inner sphere 50 microns and radius of outer sphere 1000 microns, the division adjustment parameter - the space ratio - is set as $SR = 1/R = 0.05$ in radial direction. The working fluid is high-Prandtl-number fluid with $Pr = 15.6$, This is a difficult case to solve since the solutions take very low numerical values.

In Table IV - 2, a series of simulation results have been reported, steady-state simulations have been run for each case listed, here the acceleration value is listed as input and steady-state solutions of maximum temperature differential, and maximum velocity as output for each case. In the mean time, the results of analysis, including the calculated maximum velocity per g, the calculated MTD, the artifact of MTD and ratios of MTD to its artifacts for this scaled mesh 10 division, 10°, 10°, are reported.

Table IV - 2 Input acceleration and output result for FLOTRAN concentric spheres model, R=20, Pr=15.6, scaled mesh 10 division, 10°, 10°

acce. m/s^2	steadystate max.velo.	steady-state MTD	calc. max.velo. (per g)	calc. MTD (per g)	artifact of MTD	$\frac{\text{MTD}}{\text{artifact}}$ (per g)
0	0	-0.1056×10^{-3}	n/a	n/a	-0.1056×10^{-3}	n/a
10	0.2357×10^{-5}	-0.7787×10^{-4}	0.2357×10^{-5}	n/a	-0.1056×10^{-3}	0.29 estimate
100	0.2357×10^{-4}	0.2094×10^{-3}	0.2357×10^{-5}	0.2094×10^{-4}	0.9097×10^{-4}	2.01
1000	0.2358×10^{-3}	0.2968×10^{-2}	0.2358×10^{-5}	0.2968×10^{-4}	-0.1043×10^{-3}	28.46
10000	0.2367×10^{-2}	0.3075×10^{-1}	0.2367×10^{-5}	0.3075×10^{-4}	-0.1043×10^{-3}	294.82

Some important information can be recovered from this series of simulations. First, we noticed that the first simulation gives an output of MTD=-0.1×10^{-3}K even with acceleration input of zero. And by physical intuition, we know that the correct result should be zero when there is no acceleration imposed, therefore it can be concluded it is an numerical artifact.

Second, by analysis of steady-state results, we can estimate the MTD per g to be 0.3075×10^{-4}K, and the numerical artifact is estimated to be 0.1043×10^{-3}K for this particular mesh setting. From analysis of the ratio of MTD to its numerical artifact, it also explains that for acceleration input of 10m/s^2, this FLOTRAN model is unable to produce meaningful result for the quantity MTD because this ratio is less than 1. Hence, it can be seen that input of acceleration of 1000m/s^2 or above would be needed to raise the output above numerical "noise". Since this scaled mesh setting of 10 division, 10°, 10°, is the coarsest, hence the biggest artifact, it can be deduced that acceleration of 1000m/s^2 or above would be sufficient value for the rest of finer mesh setting to produce meaningful output result.

In Table IV - 3, a similar analysis made for mesh setting of 15 division, 10°, 10° is listed. For this mesh setting, input of 1000m/s^2, acceleration and above is necessary for

the simulation to deliver correct numerical result, hence, previous finding is confirmed. Comparing this result with Table IV - 2, we also see that, even after scaling up the input, there is still a mesh-dependent difference in the MTD predicated for this case.

Table IV - 3 Input acceleration and output results for FLOTRAN concentric spheres model, R=20, Pr=15.6, scaled mesh 15 division, 10°, 10°

acce. m/s^2	steadystate max.velo.	steadystate MTD	calc. max.velo per g	calc. MTD per g	artifact of MTD	$\frac{\text{MTD}}{\text{artifact}}$ per g
0	0	-0.1032×10^{-3}	n/a	n/a	-0.1032×10^{-3}	n/a
10	0.2659×10^{-5}	-0.7720×10^{-4}	0.2659×10^{-5}	n/a	-0.1032×10^{-3}	0.27 estimate
100	0.2659×10^{-4}	0.1811×10^{-3}	0.2659×10^{-5}	0.1811×10^{-4}	-0.9448×10^{-4}	1.75
1000	0.2660×10^{-3}	0.2688×10^{-2}	0.2660×10^{-5}	0.2688×10^{-4}	-0.1032×10^{-3}	26.03
10000	0.2664×10^{-2}	0.2783×10^{-1}	0.2664×10^{-5}	0.2783×10^{-4}	-0.1032×10^{-3}	269.56

IV - 1.3.3 The Effect of Mesh Size on Artifacts for Scaled Mesh

In this section, as it listed in the followingTable IV - 4, we will show that the size of the artifact is closely related to each specific mesh setting, but is independent of the input acceleration. As the mesh is getting finer, the artifact is getting smaller.

The specific spherical case under investigation is the FLOTRAN model built with a radius ratio of $R = 20$, with radius of inner sphere 50 microns and radius of outer sphere 1000 microns, the division adjustment parameter - the space ratio - is set as $SR = 1/R = 0.05$ in radial direction. The working fluid is high-Prandtl-number fluid with $Pr = 15.6$. By analysis of the effect of scaled mesh on simulation results, we can ensure the sufficient input level to minimize that artifact and its effect on steadystate solution.

The specific parameters under investigation are the number of divisions in radial,

circumferential and azimuthal direction.

The effect of mesh size for a series of scaled mesh models has been studied and listed in Table IV - 4.

In previous Section IV - 1.3.2, we have shown that sufficient high imposed acceleration is needed to ensure that the output quantities are larger than the numerical artifact. Therefore in the following simulations to study the effect of mesh size, the input acceleration is set to $1000 m/s^2$.

Table IV - 4 Effect of scaled mesh size on artifact, FLOTRAN steady-state analysis of concentric spheres model, R=20, Pr=15.6, input acceleration 1000m/s^2.

run	rad. div.	circ. azim div.	accel m/s^2	total nodes	artifact at accel.=0	MTD
1	10	10°, 10°	1000	3575	-0.1043×10^{-3}	0.2968×10^{-2}
2	15	10°, 10°	1000	5200	-0.1032×10^{-3}	0.2688×10^{-2}
3	20	10°, 10°	1000	6825	-0.1026×10^{-3}	0.2259×10^{-2}
4	10	9°, 9°	1000	4411	-0.6143×10^{-4}	0.3198×10^{-2}
5	15	9°, 9°	1000	6416	-0.6077×10^{-4}	0.2934×10^{-2}
6	20	9°, 9°	1000	9552	-0.6041×10^{-4}	0.2535×10^{-2}
7	10	7.5°, 7.5°	1000	6347	-0.2382×10^{-4}	0.3532×10^{-2}
8	15	7.5°, 7.5°	1000	9519	-0.2356×10^{-4}	0.3310×10^{-2}
9	20	7.5°, 7.5°	1000	12117	-0.2342×10^{-4}	0.2929×10^{-2}
10	10	6°, 6°	1000	9911	-0.7132×10^{-5}	0.3866×10^{-2}
11	15	6°, 6°	1000	14416	-0.7057×10^{-5}	0.3696×10^{-2}
12	20	6°, 6°	1000	19822	-0.7015×10^{-5}	0.3361×10^{-2}
14	15	5°, 5°	1000	20752	-0.2556×10^{-5}	0.3953×10^{-2}
15	20	5°, 5°	1000	27237	-0.2541×10^{-5}	0.3671×10^{-2}

The artifact of maximum temperature differential depends on specific mesh setting, and its value decreases as the mesh gets finer, especially in circumferential

direction, as shown in Figure IV - 7. Note mesh 10, 15, 20 in the legend corresponding to the number of divisions1 0, 15, 20 in radial direction respectively. It can be seen that a sufficient number of division in the circumferential direction is crucial to the accuracy of the simulation results. In the consideration of accuracy and computation amount, in solving the steady-state solution using scale mesh, a mesh size of 20 divisions in radial direction and 60 divisions (6° apart) in circumferential and azimuthal direction is the minimum requirement to minimize the numerical artifacts.

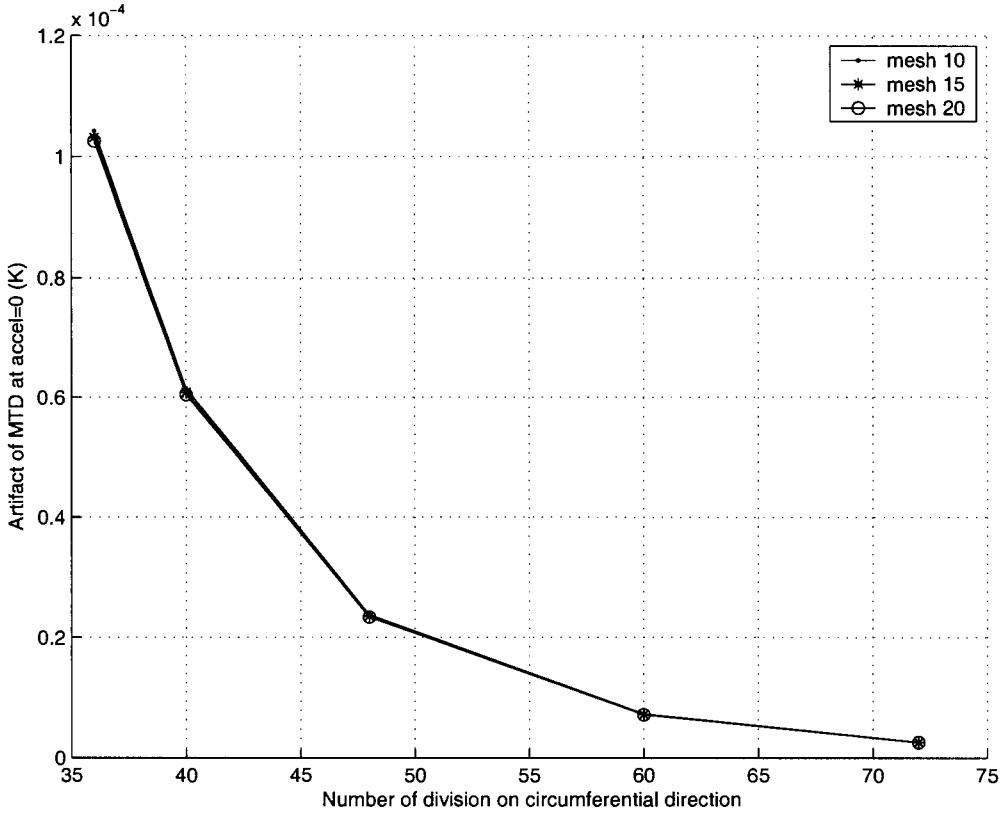

Figure IV - 7 Artifact of MTD versus number of division in circumferential direction, FLOTRAN concentric spheres modeling using scaled mesh

Meanwhile, In Figure IV - 8, it has been shown the MTD approaches a limit as mesh refines.

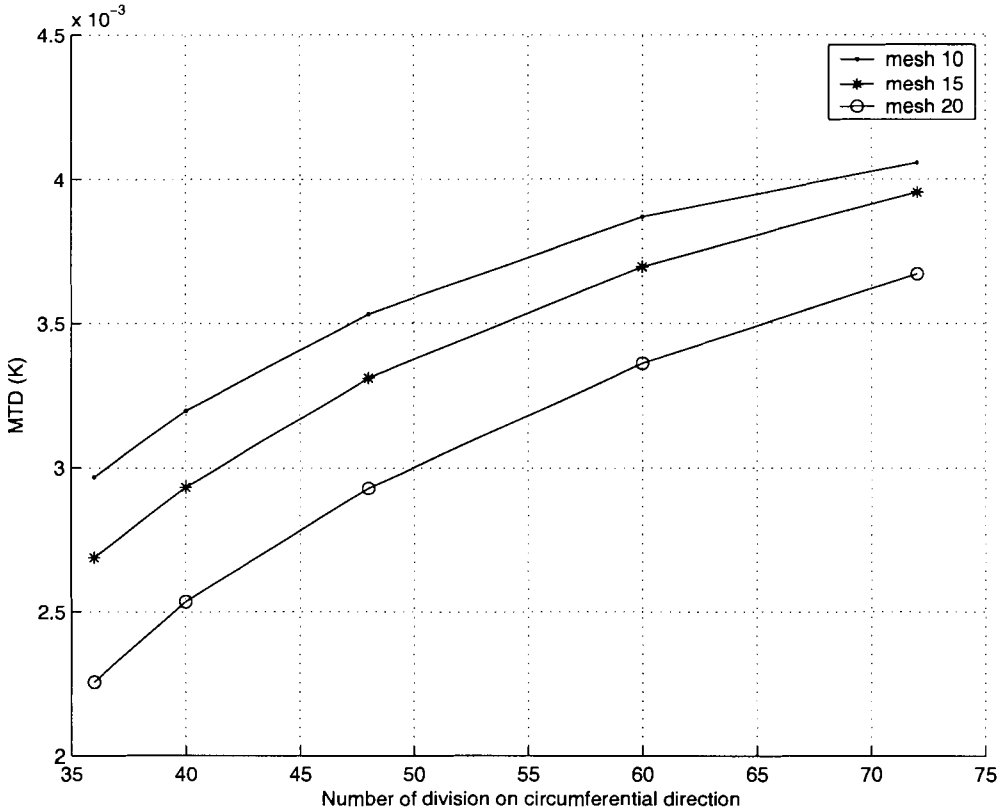

Figure IV - 8 MTD versus number of division in circumferential direction. FLOTRAN concentric spheres modeling using scaled mesh

IV - 2 Scaled Mesh Study for FLOTRAN Transient Analysis of Concentric Spheres Model

In searching for the numerical solution to transient natural convection between concentric spheres, a scaled meshing scheme has been adapted in the radial direction. The purpose of using scaled mesh is to optimize the simulation by using more nodes and elements to achieve accurate results in the region near the inner sphere where the greatest variation in velocity and temperature occurs, also to ensure that all elements have an

aspect ratio close to cubic.

IV - 2.1 Effect of Numerical Artifacts on Transient Results

In previous section, due to numerical artifacts corresponding to each mesh setting of scaled mesh studied, we have concluded that sufficient acceleration input (> $1000 m/s^2$) is needed to assure that numerical artifacts can be neglected for steady-state analysis.

In Table IV - 5, a series of transient simulation results have been reported using scaled mesh 10 division, 10°, 10°. The specific case under investigation is the FLOTRAN concentric-spheres model built by scaled regular-volume mesh, the radius ratio of $R = 20$, with radius of inner sphere 50 microns and radius of outer sphere 1000 microns, the division adjustment parameter - the space ratio - is set as $SR = 1/R = 0.05$ in radial direction. The working fluid is high-Prandtl-number fluid with $Pr = 15.6$. The acceleration value is listed as input and the transient solutions for τ_v and τ_T are listed as output for each acceleration input. Meanwhile, the results of steady-state analysis, including MTD, calculated MTD per g, the artifact of MTD, ratios of MTD to its artifacts are listed as reference.

Table IV - 5 Input acceleration and output response time, for transient analysis of spherical model of *R*=20, *Pr*=15.6, scaled mesh 10 division, 10°, 10°

acce. m/s^2	steadystate max.velo.	steady-state MTD	calc. MTD (per g)	artifact of MTD	$\frac{\text{MTD}}{\text{artifact}}$ (per g)	τ_v	τ_T
0	0	-0.1056×10^{-3}	n/a	-0.1056×10^{-3}	n/a	n/a	n/a
10	0.2357×10^{-5}	-0.7787×10^{-4}	n/a	-0.1056×10^{-3}	0.29 estimate	n/a	n/a
100	0.2357×10^{-4}	0.2094×10^{-3}	0.2094×10^{-4}	0.9097×10^{-4}	2.01	48.86	1148
1000	0.2358×10^{-3}	0.2968×10^{-2}	0.2968×10^{-4}	-0.1043×10^{-3}	28.46	48.89	621
10000	0.2367×10^{-2}	0.3075×10^{-1}	0.3075×10^{-4}	-0.1043×10^{-3}	294.82	49.26	603

In the table τ_v and τ_T are the response time of velocity field and temperature field defined in Section 4 - 1. By analysis of the transient results, it is shown that as we increase the value of acceleration from 100 to 10000m/s^2, the response time τ_T predicted by FLOTRAN simulation goes from 1147 microseconds to 602 microseconds. This also can be explained by the value of the initial artifact at time 0 and ratio of the eventual value of MTD to this artifact. At time 0, acceleration switches from 0 to designated value. Since the artifact gives a negative initial value of MTD, the lower the imposed acceleration, the longer time it takes for MTD to offset this value, and this period of time artificially extends τ_T; whereas, the predicted value of τ_v is not affected much since, at time 0, simulation gives relatively correct output for maximum velocity.

In Table IV - 6, a similar analysis made for mesh setting of 15 division, 10°, 10° is listed. For this mesh setting, input of 1000 m/s^2 acceleration and above is necessary for the simulation to deliver correct transient analysis result, hence, previous finding is confirmed.

Table IV - 6 Input acceleration and output transient results for spherical model of *R*=20, *Pr*=15.6, scaled mesh 15 division, 10°, 10°

acce.	steadystate max.velo.	steadystate MTD	calc.MTD per g	artifact of MTD	$\frac{\text{MDT}}{\text{artifact}}$ (per g)	τ_v	τ_T
0	0	-0.1032×10^{-3}	n/a	-0.1032×10^{-3}	n/a	n/a	n/a
10	0.2659×10^{-5}	-0.7720×10^{-4}	n/a	-0.1032×10^{-3}	0.27 estimate	n/a	n/a
100	0.2659×10^{-4}	0.1811×10^{-3}	0.1811×10^{-4}	-0.9448×10^{-4}	1.75	54.70	1171.2
1000	0.2660×10^{-3}	0.2688×10^{-2}	0.2688×10^{-4}	-0.1032×10^{-3}	26.03	54.71	645.1
10000	0.2664×10^{-2}	0.2783×10^{-1}	0.2783×10^{-4}	-0.1032×10^{-3}	269.56	54.88	620.6

IV - 2.2 The Effect of Mesh Size on Transient Results

The specific transient spherical case under investigation is the FLOTRAN model built with a radius ratio of $R = 20$, with radius of inner sphere 50 microns and radius of outer sphere 1000 microns, the division adjustment parameter - the space ratio - is set as $SR = 1/R = 0.05$ in radial direction. The working fluid is high-Prandtl-number fluid with $Pr = 15.6$. By analysis of the effect of scaled mesh on simulation results, we can derive the optimal scaled mesh setting.

The specific parameters under investigation are the number of divisions in radial, circumferential and azimuthal direction.

The effect of mesh size on transient results for a series of scaled mesh models has been studied and listed in Table IV - 7.

In previous Section IV - 1.3.3 and Section IV - 2, we have shown that sufficient imposed acceleration is needed to ensure the steady-state solutions and transient solutions are significantly larger than its numerical artifact. Therefore in the following simulations to study the effect of mesh size, the input acceleration is set to $1000\mathrm{m/s^2}$.

Table IV - 7 Effect of scaled mesh size on transient result, for spherical case of R=20, Pr=15.6, acceleration at 1000 m/s^2 .

run	rad. div.	circ. azim div.	accel m/s^2	total nodes	τ_v	τ_T	τ_{T0}	τ_T'
1	10	10°, 10°	1000	3575	48.89	620.53	44.82	575.71
2	15	10°, 10°	1000	5200	54.71	645.12	49.08	596.04
3	20	10°, 10°	1000	6825	56.93	660.65	53.39	607.26
4	10	9°, 9°	1000	4411	49.34	619.94	31.86	588.08
5	15	9°, 9°	1000	6416	54.75	633.69	34.08	599.62
6	20	9°, 9°	1000	9552	56.80	644.16	37.51	606.65
7	10	7.5°, 7.5°	1000	6347	50.14	628.76	18.20	610.57
8	15	7.5°, 7.5°	1000	9519	55.03	628.81	18.85	609.96
9	20	7.5°, 7.5°	1000	12117	56.87	633.15	19.89	613.26
10	10	6°, 6°	1000	9911	51.09	648.43	9.38	639.04
11	15	6°, 6°	1000	14416	55.46	631.51	9.55	621.96
12	20	6°, 6°	1000	19822	57.11	631.24	9.79	621.46
13	10	5°, 5°	1000	14267	51.66	656.51	8.05	648.46
14	15	5°, 5°	1000	20752	55.76	634.68	8.33	626.35
15	20	5°, 5°	1000	27237	57.31	632.25	8.44	623.82

Here in the column, τ_{T0} is the calculated time in microsecond for the MTD to recover from its artifact value to its accurate value of 0, it can be then used to correct the response time of τ_T by substracting τ_{T0} from it, that is τ'_{T0}.

From the above simulation results, it can be seen that τ_v converges as scaled mesh gets finer, as shown in Figure IV - 9, while τ_T convergence can be better presented in Figure IV - 10

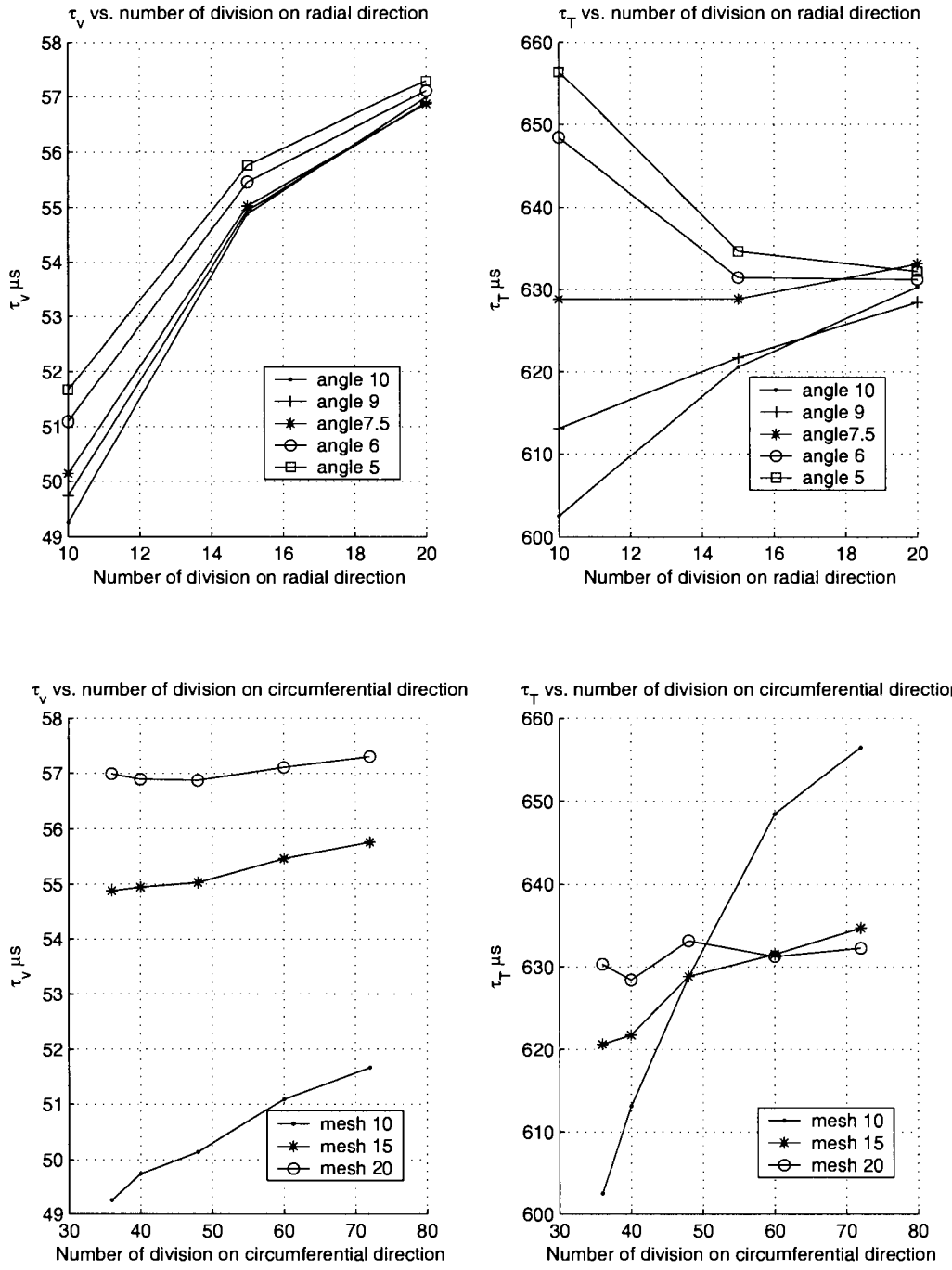

Figure IV - 9 τ_v and τ_T vs. scaled mesh for spherical model

Again, in the above figure, angle 10, 9, 7.5, 6, 5, correspond to number of division 36, 40, 48, 60,72 in the circumferential and azimuthal direction.

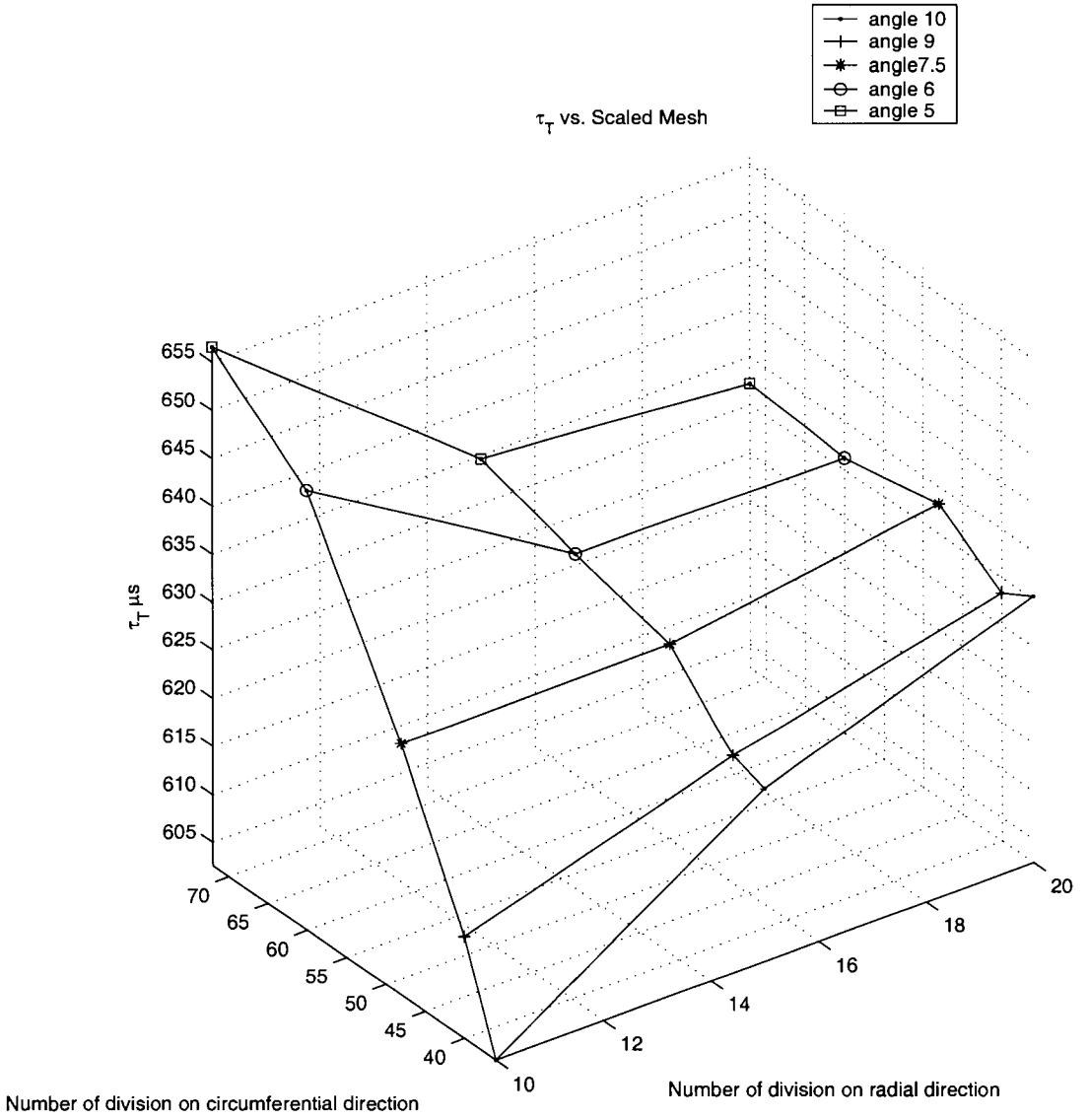

Figure IV - 10 Convergence of τ_T versus scaled mesh

Based on the above observations on the simulation results listed in previous section of Section IV - 1.3.3, with the consideration of computational expense, we concluded that with scaled mesh, 20 division in the radial direction with space ratio adjustment and 6° in circumferential and azimuthal directions would be sufficient for the transient spherical case simulation.

The FLOTRAN simulations for transient spherical cases on which the empirical correlations of transient response with radius ratio were based employed a scaled mesh scheme with 20 division in the radial direction and grid of 6° apart in the circumferential and azimuthal directions.

Appendix V MAPLE Form of Hardee's Solution

As mentioned in Section 6 - 2.4, though presented in explicit form, Hardee's solution consists of sets of extremely lengthy and complicated expressions. To make it easier to evaluate these expressions against the results of FLOTRAN analysis, they were typed into the symbolic math package 'MAPLE'. To ensure that these expression had been input correctly, it was necessary to validate Maple's calculation against the results from Hardee's thesis. In our work, this validation was done by two means. One way was by substituting the solution equations of each variable of $\tilde{T}_0, \tilde{T}_1, \tilde{T}_2$ and ψ_1, ψ_2 into their corresponding governing equations and boundary conditions respectively. Because of the extremely lengthy and complicated expressions for $\tilde{T}_3$ and ψ_3, these terms were not included in the calculation. Another way is to take a specific case with given Rayleigh number, Prandtl number and Ratio of radius, and compare the Maple-calculated results with those reported in Mack and Hardee (1968) and Hardee (1966).

First, a Maple working sheet was created based on the set of equations (Eq 6 - 1)-(Eq 6 - 14). In the following section, by symbolic computation, the stream function and temperature distribution of concentric spheres case with $Ra = 1000$, $Pr = 0.70$, $R = 2$ originally reported in Mack and Hardee (1968) and Hardee (1966) were reproduced in our current Maple working sheet, and compared with those originally reported.

V - 1 Stream Function

The stream function results for the case of $Ra = 1000, Pr = 0.70, R = 2$ originally presented as Fig 1 in Mack and Hardee (1968) have been reproduced using our current Maple working sheet, and the comparison with the original results is shown in Figure V - 1.

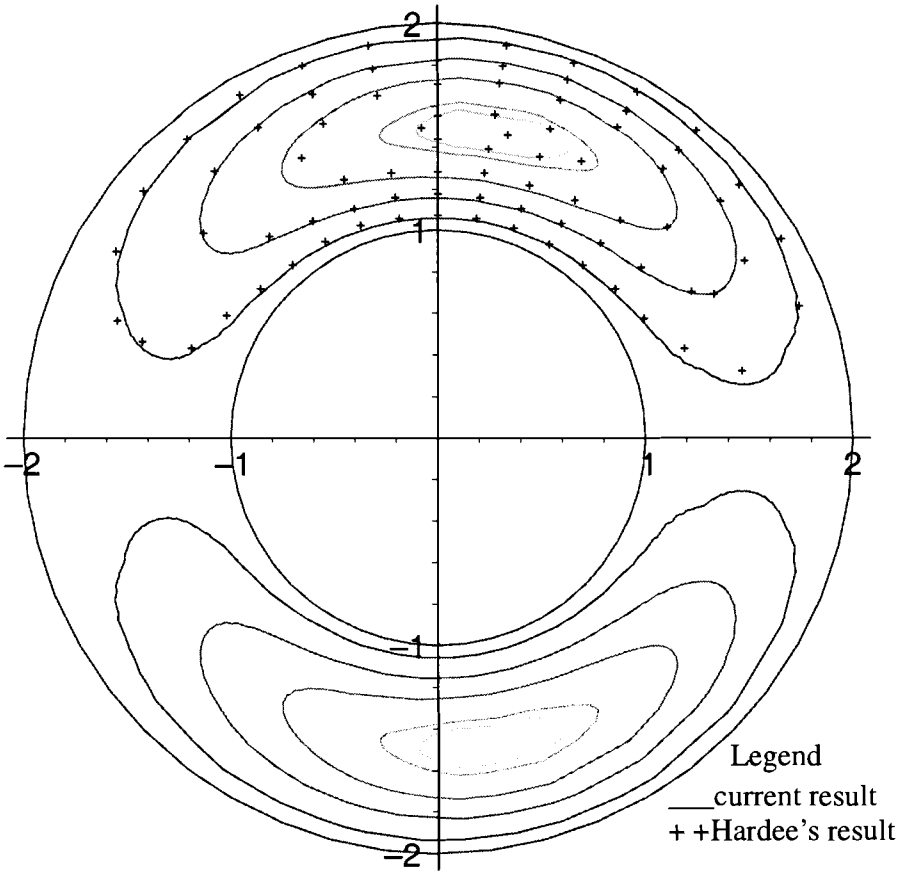

Figure V - 1 Comparison between the original reported Hardee's results and our current reproduced "MAPLE" result for stream function for concentric sphere model *Ra*=1000, *Pr*=0.7 and *R*=10

In the graph, Hardee's original reported results are depicted by the dots, while our current reproduced results are represented by the curve lines, at each value of ψ, it can be seen that our current reproduced results agrees with Hardee's original reported results. The gravity acceleration is applied in the x direction.

It can be seen that:

- Figure V - 1 shows a single cell of the "crescent-eddy" type which was photographed and described by Bishop et. al. (1964), (1966).

- The fluid flow is upward along the inner sphere and downward along the outer sphere.
- The center of the eddy, where ψ has its maximum value, is seen to lie in the upper half of the flow region at $\theta = 77°$ almost exactly half way between the two surfaces.

The creeping-flow solution $\psi^{(1)}$, applicable in the limit of infinitesimal Rayleigh number, places the center of the eddy at $\theta = 90°$ and $(r-1)/(R-1) = 0.49$; the effect of the finite Rayleigh number (1000) has been to move the center appreciably upward and very slightly outward. The upward and outward movement of the center of the eddy as the Rayleigh number is increased is in agreement with the experimental observations by Bishop et. al. (1964), (1966), as reviewed in Section 6 - 2.2.

V - 2 Velocity Distributions

The velocity components are related to the stream function by

$$V_r = (r^2 \sin\theta)^{-1} \frac{\partial \psi}{\partial \theta} \qquad \textbf{(Eq V - 1)}$$

and

$$V_\theta = -(r \sin\theta)^{-1} \frac{\partial \psi}{\partial \theta} \qquad \textbf{(Eq V - 2)}$$

Profiles of V_r and V_θ obtained by differentiating ψ in the above manner were originally reported for $Ra = 1000, P = 0.70, R = 2.00$ as Fig 2 in Mack and Hardee (1968).

For V_r the comparison is shown in Figure V - 2 (note: θ in this graph is in units of radian) and for V_θ, the comparison is shown in Figure V - 3. And again, the original results in Mack and Hardee (1968) are depicted by the dots, while our current reproduced

results are represented by the curved lines, and for V_r, at $r = 1.5 \times r_i$, as well as for V_θ, for each value of $\theta = 40^\circ, 80^\circ, 120^\circ, 160^\circ$, it can be seen that Hardee's results agree with current results.

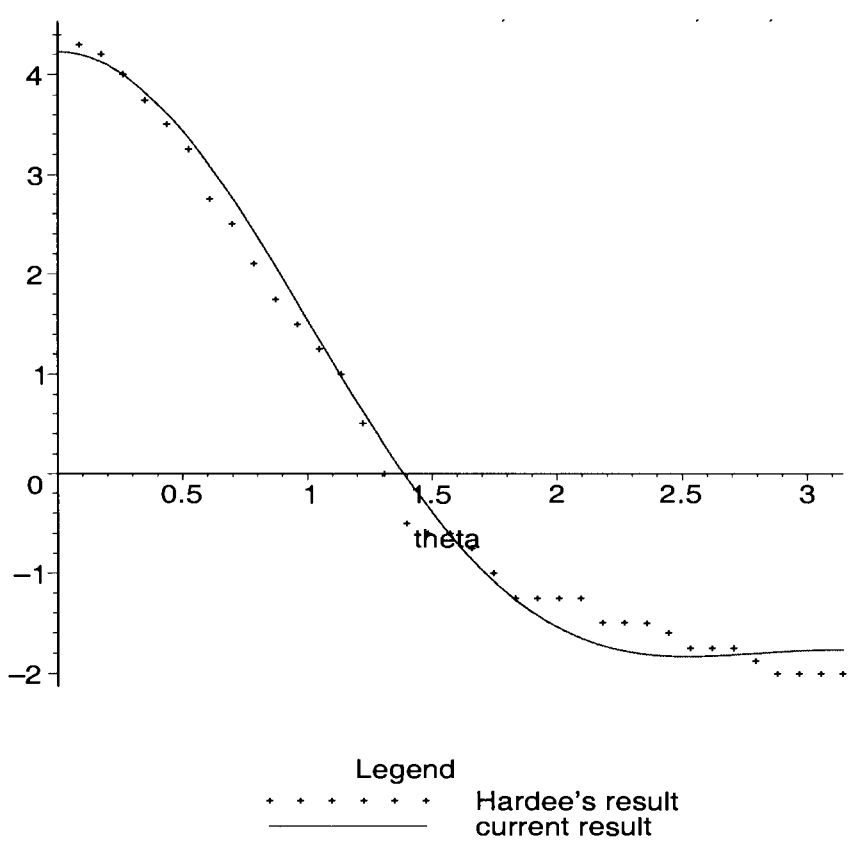

Figure V - 2 Comparison of the original reported Hardee's results and our current reproduced result for velocity distribution V_r at r=1.5r_i for concentric spheres model Ra=1000, Pr=0.7 and R=10

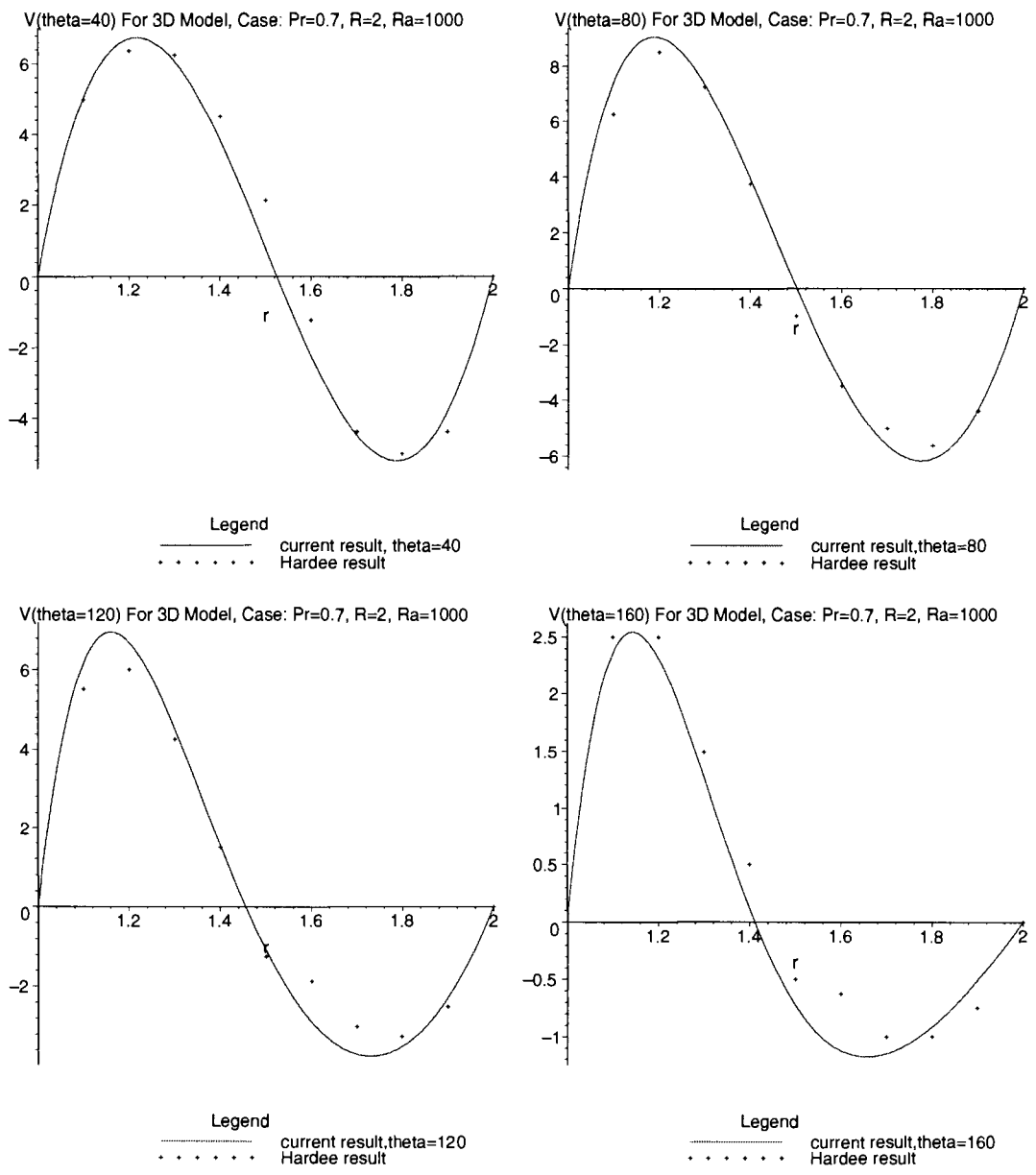

Figure V - 3 Comparison between the original reported Hardee's results and our current reproduced Maple result for velocity distribution V_θ at θ=40°, 80°, 120°, 160° for concentric spheres model *Ra*=1000, *Pr*=0.7 and *R*=10

V - 3 Temperature Profiles

For temperature profile for the case $Ra = 1000, Pr = 0.70, R = 2.00$ at $\theta = 40°, 80°, 120°, 160°$ as well as the temperature distribution $T = T_0$ for pure conduction were originally presented as Fig 3 in Mack and Hardee (1968).

We take the temperature profiles from Fig 3 in Mack and Hardee (1968), and compare them with those of the symbolic calculation in our current MAPLE working sheet, as shown in Figure V - 4.

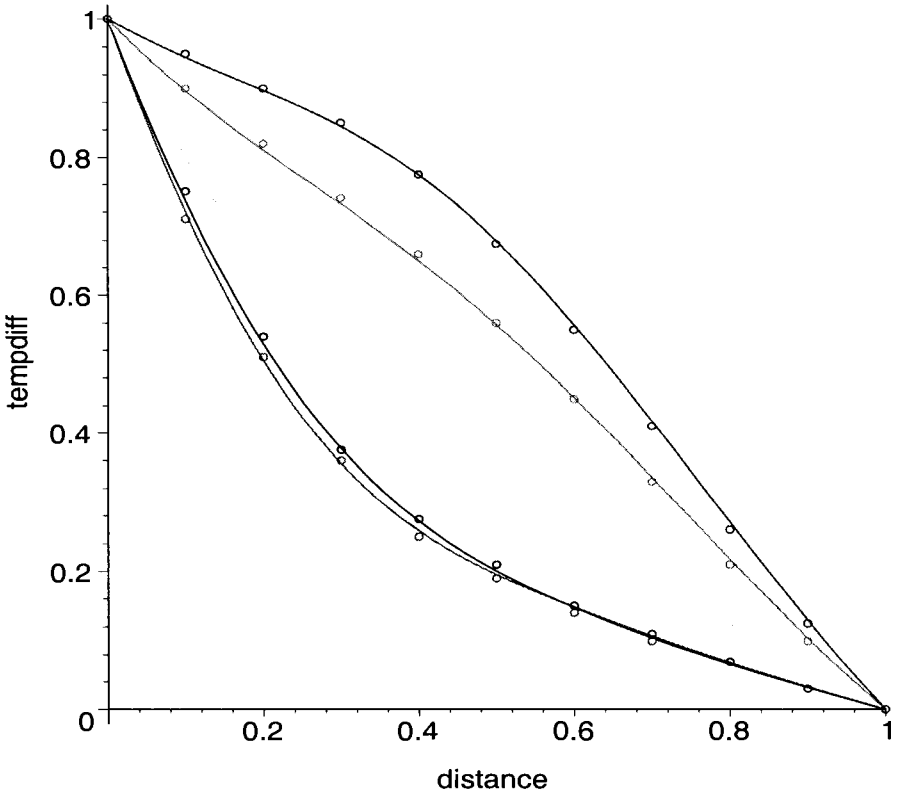

Figure V - 4 Comparison between Hardee's original results and our current reproduced result for temperature profiles for concentric sphere model *Ra*=1000, *Pr*=0.7 and *R*=10

Hardee's original results are depicted by the dots, while our current reproduced results are represented by the curved lines, at each value of $\theta = 40°, 80°, 120°, 160°$, it

can be seen that Hardee's results agree with our current results.

V - 4 Conclusion

In this Appendix, we have demonstrated that our current Maple working sheet which represents Hardee's equations (Eq 6 - 1) to (Eq 6 - 14) can reproduce Hardee's results for stream function, velocity distribution and temperature profiles for the case: $Pr = 0.7, R = 2, Ra = 1000$. Hence, the correspondence of the current Maple working sheet with (Eq 6 - 1) to (Eq 6 - 14) is verified, and we can use the output of the Maple working sheet to compare our numerical FLOTRAN results with Hardee's prior analytic solution.

Bibliography

1. Abbott, M.R., (1964). "A numerical method for solving the equations of natural convection in a narrow concentric cylindrical annulus with a horizontal axis". *Quart. J. Mech Appl. Math. 17,* pp. 471-481, 1964.

2. Analog Devices, Inc. (2003). *Data sheet: Programmable Gain Instrumentation Amplifier AD625.* Retrieved August 25, 2003 from http://www.analog.com/UploadedFiles/Data_Sheets/223795673AD625_d.pdf

3. Analog Devices, Inc. (2003). *Data sheet: Low cost, Low power Instrumentation Amplifier AD620.* Retrieved August 25, 2003 from http://www.analog.com/UploadedFiles/Data_Sheets/352971806086AD620_f.pdf

4. Astill, K. N., Leong, H., and Martorana, R., (1980). "A numerical solution for natural convection in concentric spherical annuli". *Proceedings of the 19th National Heat Transfer Conference, ASME HTD-Vol, 8,* pp. 105-113, 1980.

5. Babour, N., et al., (1996). "Micromechanical silicon instrument and systems development at Draper Laboratories". *AIAA Guidance, Navigation, and Control Conference, San Diego, CA, July 29-31, 1996.*

6. Bao, M.-H., (2000). *"Micro Mechanical Transducers, Pressure Sensors, Accelerometers and Gyroscopes".* Elsevier, 2000.

7. Beckmann, W., (1931). "Die Waermeuebertragung in zylinderischen Gasschichten bei naturlicher Konvektion". *Forsch. Geb. d. Ingenieurwesen, 2 (5),* pp. 165-178, 1931.

8. Bernard, A., Foulon, B., and Le Clerc, G.M., (1985). "Three-axis electrostatic accelerometer". *DGON Symposium Gyro Technology,* Stuttgart, 1985.

9. Bishop, E. H., and Carley, C. T., (1966). "Photographic studies of natural convection between concentric cylinders". *Proc.1966 Heat Transfer Fluid Mech. Inst.* pp. 63-78, 1966.

10. Bishop, E. H., Carley, C. T. and Powe, R. E. (1968). "Natural convective oscillatory flow in cylindrical annuli". *Int. J. Heat Mass Transfer, 11*, pp. 1741-1752, 1968.

11. Bishop, E. H., Kolflat, R. S, Mack, L.R., and Scanlan, J.A. (1964). "Convective heat transfer between concentric spheres." *Proc. 1964 Heat Transfer Fluid Mech. Inst.*, pp. 69-80, Berkeley, Stanford University Press, 1964.

12. Bishop, E. H., Mack, L.R., and Scanlan, J. A., (1966). "Heat transfer by natural convection between concentric spheres". *Int. J. Heat Mass Transfer 9*, pp. 649-662, 1966.

13. Blanco, J., and Geen, J., (1993). "Micromachined inertial sensor development at Northrop", *ION, Proc. 49th Annual Mtg, Cambridge, MA, June 21-23, 1993.*

14. Bower, D., Cracknell, M., and Harrison, A., (1987). "A high linearity SAW accelerometer". *Proc. IEEE 41st Annual Frequency Control Symposium*, pp. 544-547, 1987.

15. Brown, R. J., (1967). "Natural convection heat transfer between concentric spheres". *Ph.D. Dissertation.* University of Texas, Austin, 1967.

16. Brüel & Kjær Co. (2003). "Product data, PM Vibration Exciter-Type 4808". Retrieved August 25, 2003 from http://www.bksv.com/pdf/Bp0230.pdf

17. Caltagirone, J. P., Combarnous, M., and Mojtabi, A., (1980). "Natural convection between two concentric spheres: transition toward a multicelluar flow". *Numerical Heat Transfer 3,* pp. 107-114, 1980.

18. Carslaw, H.S., and Jaeger, J.D. (1959). *Conduction of Heat in Solids*, Second Edition, Oxford at the Clarendon press, 1959.

19. Castrejon, A., and Spalding, D., (1988). "An experimental and theoretical study of transient free-convection flow between horizontal concentric cylinders". *Int. J. Heat Mass Transfer, Vol. 31, No. 2,* pp. 273-284, 1988.

20. Cengel, Y.A., (1996). *Introduction To Thermodynamics And Heat Transfer.* The Mcgraw-Hill Series In Mechanical Engineering. Nov, 1996.

21. Chu, H. S., and Lee, T. S., (1993). "Transient natural convection heat transfer between concentric spheres". *International Journal of Heat and Mass Transfer. Vol, 36, No. 13*, pp 3159-3170, 1993.

22. Collis, D.C., and Williams, M.J., (1959). "Two dimensional convection from heated wire at low Reynolds Numbers". *J. Fluid Mech., Vol.6*, pp. 357-389, 1959

23. Crawford, L., and Lemlich, R., (1962). "Natural convection in horizontal concentric cylindrical annuli". *I.E.C. Fund. 1,* pp. 260-264, 1962.

24. Dao, R., (2003). "Mechanical shock test report, accelerometer model no. MXR7202ML", November, 2003. Retrieved January, 2004 from http:// www.memsic.com.

25. Fujii, M., Takamatsu, H., and Fujii, T., (1987). "A numerical analysis of free convection around an isothermal sphere (effects of space and Prandtl number)". *Proc. 1987 ASME-JSME Thermal Engineering Joint Conference, Vol. 4,* pp. 55-60, 1987.

26. Fujii, T., Honda, T., and Fujii, M., (1984). "A numerical analysis of laminar free convection around an isothermal sphere: finite-difference solution of the full Navier-Stokes and energy equations between concentric spheres". *Numerical Heat Transfer 7,* pp. 103-111, 1984.

27. Geoola, F., and Cornish, A. R. H., (1982). "Numerical simulation of free convective heat transfer from a sphere". *Int. J. Heat Mass Transfer 25,* pp. 1677-1687, 1982.

28. Hardee, H.C., Jr., (1966). "Natural convection between concentric spheres at low Rayleigh numbers". *Ph.D. Dissertation*, University of Texas, Austin. 1966.

29. Hartermann, P., Meunier, P.-L., and Jocobelli, A., (1985). "Elastic surface wave accelerometers". *U.S. Patent 4515016,* 7 May 1985.

30. Hodnett, P.F., (1973). "Natural convection between horizontal heated concentric circular cylinders". *J. Appl. Math. Phys. 24*, pp. 507-516, 1973.

31. Huang, J. S., and Yang, S. L., (1984). "A finite element solution for natural convection in spherical annuli". *J. CSME 5 (1),* pp. 9-18, 1984.

32. Incropera, F.P., DeWitt, D.P., (1996). *Introduction to Heat Transfer*, Third Edition, John Wiley & Sons, Inc. 1996.

33. Ingham, D. B., (1981). "Heat transfer by natural convection between spheres and cylinders". *Numerical Heat Transfer 4*, pp. 58-67, 1981.

34. Kamerich, E., (1999). *A guide to Maple,* Published New York: Springer, c1999

35. Kitchin, C., and Counts, L., Analog Devices, Inc., (2000). *A designer's guide to instrumentation amplifiers.* Retrieved August 25, 2003 from http:// www.analog.com/UploadedFiles/Associated_Docs 404101703557124232936 7appguide.pdf

36. Kramers, H., (1946). "Heat transfer from spheres to flowing media," *Physics,* vol. 12, pp. 61-80, 1946.

37. Kraussold, H., (1934). "Waermeabgabe von zylindeischen Fluessigkeitsschichten bei natuerlicher Konvektion". *Forsch. Geb. d. Ingenieurwesen, 5 (4),* pp. 186-191, 1934.

38. Kuebleck, K., Merker, G.P., and Straub, J., (1980). "Advanced numerical computation of two-dimensional time-dependent free convection in cavities". *Int. J. Heat Mass Transfer, Vol. 23,* pp. 203-217, 1980.

39. Kuehn, T. H., and Goldstein, R. J., (1976). "An experimental and theoretical study of natural convection in the annulus between horizontal concentric cylinders". *Journal of Fluid Mechanics, vol.74,* pp. 695-719, 1976.

40. Kuehnel, W., and Sherman, S., (1994). "A surface micromachined silicon accelerometer with onchip detection circuitry", *Sensors and Actuators A45,* pp. 7-16. 1994,

41. Lawrence, A., (1998). "*Modern inertial technology: navigation, guidance and control"*, Springer, 1998.

42. Leung, A., Jones, J., Czyzewska, E., Chen, J., and Pascal, M., (1997). "Micromachined accelerometer with no proof mass", *Technical Digest, International Electron Devices Meeting, Washington D.C., December 7-10, 1997*, pp. 899-902.

43. Liu, C. Y., Mueller, W.K., and Landis, F., (1961). "Natural convection heat transfer in long horizontal cylindrical annuli". *Int. Developments in Heat Transfer, A.S.M.E.* pp. 976-984, 1961.

44. Mack, L. R., and Hardee, H.C., (1968). "Natural convection between concentric spheres at low Rayleigh numbers". *Int. J. Heat Mass Transfer 11,* pp. 387-396, 1968.

45. Mack, L. R., and Bishop, E. H., (1968). "Natural convection between horizontal concentric cylinders for low Rayleigh numbers". *Quart. J. Mech. Appl. Math. 21*, pp. 223-241, 1968.

46. MEMSIC Inc. (2003) "Market Leader in Dual Axis Thermal Accelerometer Solutions". Retrieved August 20, 2003 from http://www.memsic.com.

47. MEMSIC Inc. (2004) "Application Note: Accelerometer Fundamentals". Retrieved January 8, 2004 from http://www.memsic.com.

48. Mochimaru, Y., (1989). "Transient natural convection heat transfer in a spherical cavity". *Heat Transfer-Jap. Res. 18,* pp. 9-19, 1989.

49. Mojtabi, A., and Caltagirone, J. P., (1982). "Natural convection between two concentric spheres for high Prandtl number". *Proceedings of the seventh International Heat Transfer Conference, München, Vol. 2*, pp. 245-249, 1982.

50. Ozoe, H., Kuriyama, H., and Takami, A. (1987). "Transient natural convection in a spherical and a hemispherical enclosure". *Proc. 1987 ASME -JSME Thermal Engineering Joint Conference, Vol. 4,* 1987

51. Ozoe, H., Fujii, K., Shibata, T., Kuriyama H., and Churchill, S. W., (1985). "Three-dimensional numerical analysis of natural convection in a spherical annulus". *Numerical Heat Transfer 8,* pp. 383-406, 1985.

52. Powe, R. E., Carley, C.T., and Bishop, E. H., (1969). "Free convective flow patterns in cylindrical annuli". *J. Heat Transfer, 91,* pp. 310-314, 1969.

53. Rotem, Z., (1972). "Conjugate free convection from horizontal conducting circular cylinders". *Int. J. Heat Mass Transfer, 15,* pp. 1679-1693, 1972.

54. Scanlan, J. A., Bishop, E. H. and Powe, R. E., (1970). "Natural convection heat transfer between concentric spheres". *Int. J. Heat and Mass Transfer 13,* pp. 1857-1872, 1970.

55. Shaughnessy, E. J., Custer, J., and Douglass, R.W., (1978). "Partial spectral expansion for problems in thermal convection." *J. Heat Transfer 100,* pp. 435-441, 1978.

56. Shibayama, S., and Mashimo, Y., (1968). "Natural convection heat transfer in horizontal concentric cylindrical annuli". *Papers J.S.M.E. Nat. Symp. no. 196,* pp. 7-20, 1968.

57. Singh, S.N., and Chen, J., (1980). "Numerical solution for free convection between concentric spheres at moderate Grashof numbers". *Numerical Heat Transfer 3,* pp. 441-459, 1980.

58. Tsui, Y.T., and Tremblay, B., (1984). "On transient natural convection heat transfer in the annulus between concentric horizontal cylinders with isothermal surfaces". *Int. J. Heat Transfer, Vol. 27, No. 1,* pp. 103-111, 1984.

59. Tveten, A.B., Dandrige, A., Davis, C.M., and Giallorenzi, T.G., (1980). "Fiber optic accelerometer". *Electronic Letters, 16, 22,* pp. 854-856, 12 Oct. 1980.

60. Vafai, K., and Ettefagh, J., (1990). "An investigation of transient three-dimensional buoyancy-driven flow and heat transfer in a closed horizontal annulus". *Int. J. Heat Mass Transfer, Vol 34, No. 10,* pp. 2555-2570, 1990.

61. Vigna, B., STMicroelectronics (2003). "MEMS Components Take Aim at Telecom Peripherals, Automotive and Consumer Markets", *Digital Consumer,* Retrieved August 20, 2003 from http://www.chipcenter.com/digitalconsumer/c006.html.

62. Voigt, H., and Krischer, O., (1932). "Die Waermeuebertragung in zylindrischen Lufschichten bei natuerlicher Konvektion". *Forsch. Geb. d. Ingenieurwesen, 3 (6),* pp. 303-306, 1932.

63. Wright, J. L., and Douglass, R.W., (1986). "Natural convection in narrow-gap spherical annuli". *Int. J. Heat Mass Transfer 29,* pp. 725-739, 1986.

64. Yin, S. H., Powe, R. E., Scanlan, J. A., and Bishop, E. H., (1973). "Natural convection flow patterns in spherical annuli". *Int. J. Heat Mass Transfer 16*, pp. 1785-1795, 1973.